NORTHWESTERN UNIVERSITY

# Reorganizing Defect Thermodynamics and Chemistry for Intuitive Exploratory Phase Stability Analysis

A DISSERTATION

SUBMITTED TO THE GRADUATE SCHOOL
IN PARTIAL FULFILLMENT OF THE REQUIREMENTS

for the degree

DOCTOR OF PHILOSOPHY

Field of Materials Science & Engineering

By

Shashwat Anand

EVANSTON, ILLINOIS

March 2021

Copyright ©2021 by Shashwat Anand

All rights reserved

# Abstract

Exploratory phase stability analysis in Materials Science has two primary goals: (a) Characterizing the evolution of the materials single phase field in composition space to identify solubility and electronic dopability limits and (b) Accelerated prediction of new phases of technological importance. In this thesis we reorganize defect theory — the thermodynamics and chemistry aspects — towards advancing both these goals significantly.

Although (a) can, in principle, be approached using computational as well as experimental techniques, both avenues can become quite prohibitive for phases in complex, multi-component composition space. Considering that a defect of interest (often the dominant defect) can often be chemically intuited based on the structure of a phase or similar compounds, it is often desirable to have strategies for solubility design requiring much less effort by relying entirely on thermodynamic intuition. The current thermodynamic rules of thumb (e.g. '$A$-rich conditions are suitable for solubility of $A$-interstitial defects') regarding defect solubility are limited only to interstitial and vacancy defects. We develop a thermodynamic visualization framework in composition space which applies to all defect-types (substitutional defects and paired defect complexes). This generalized framework, in-principle, *only* requires the defect type as the input to identify (i) chemical conditions leading to maximum solubility and (ii) the special cases in which two distinct chemical conditions will lead to equal solubility. These solubility guidelines explain why the varying reports of solubility limits in the thermoelectric $Mg_2Si$-$Mg_2Sn$ pseudobinary is thermodynamically impossible and correctly identify equilibrium yielding maximum solubility in Sn-doped ZnSb and Te-doped $Mg_3Sb_2$. The predictive nature of these thermodynamic guidelines can also help in warning against atypical pseudobinary systems in which the solubility limit can be quite dependent on chemical conditions. The thermoelectric LAST-type systems (like PbTe-$AgSbTe_2$) are identified, potentially, as one example of such systems.

The study of point defect thermodynamics in previous literature has thus far relied substantially on treating the reference chemical potential contributions to the defect energy by plotting them in chemical potential space. Thermodynamic analysis in chemical potential space can be quite abstract and is a relatively advanced concept not used regularly by the materials community. Considering the fact that defects impact all transport and thermochemical properties, the audience for defect thermodynamics is possibly much larger than the fraction of researchers well versed with analyzing stability in chemical potential space. By solving the defect solubility problem in composition space we bypass the need to work in chemical potential space entirely and provide a visualization scheme suitable for a very broad audience. Due to its simplicity, we expect our thermodynamic analysis to serve as an intermediate analysis step — for computationalists and experimentalists alike — before attempting (a).

Beside this general thermodynamic aspect of defects, we also focus on rationalizing the differences between the two very distinct physical chemistry and defect physics approaches for treating defects in semiconductors and insulators. While historically these approaches have been used for studying defects in ionic and electronic conductors separately, mixed conductors with applications as battery materials are now attracting the attention of researchers from both communities. Both approaches have their pros and cons. The pros for the physical chemistry approach is that (1) its data representation — characterized by plotting defect concentration against changing chemical potential in the so-called Brouwer diagrams — is more direct in communicating chemical control of defects and (2) it characterizes the defect formation with a single reaction equilibrium constant. The cons of this approach are that (1) it does not discuss the Fermi-level dependence of defect concentrations explicitly and (2) it often lacks a clear distinction between the behavior of paired and isolated components of complex defects, such as Schottky and Frenkel defects. An advantage of the defect physics approach is that it accounts for a Fermi-level dependence of defect energetics – connecting it to key properties such as electronic dopability and formation of deep defect states. The cons to this approach are that (i) the Fermi-level dependency is never studied with experimental techniques for verification of computational results and (ii) the Fermi-level dependency requires plotting the multi-dimensional data in separate panels, making visualization cumbersome. Using MgO, PbTe and $Mg_3Sb_2$ as example systems we address the cons in both the approaches and develop a composite language for defects in semiconductors and insulators.

The pursuit of (b) in modern exploratory phase stability analysis is often carried out using high-throughput first-principles computational approaches. The choices of structure and composition in approaches for discovery of semiconducting compounds are often based on chemical intuition from long-standing stability rules. While these rules reduce the computational cost significantly, they apply by default only to fixed stoichiometries *and* combination of elements, thereby favoring exploration in specific multi-component chemistries over others. Choosing the example of Heusler compounds, we show that these rules for stability of semiconductors nedd to apply to fixed stoichiometries or electron counts (as expected by the 18-electron rule for the $XYZ$ stoichiometry for example). We therefore develop the generalized valence balanced rule for stability of semiconductor Heuslers which now allows for a flexibility in the ground state composition by accounting for defects in the structure as well. We use this valence balanced rule be explain the semiconducting electronic structure of the thermodynamically stable ground state stoichiometries in $Nb_{0.8}CoSb$ (nominally 19-electron at NbCoSb), $Ti_{0.75}NiSb$ (nominally 19-electron at TiNiSb), and 24-electron $VFe_2Al$. By virtue of this rule, we predict over 150 new defective compounds — which includes over 100 low thermal conductivity quaternary double (e.g. $Ti_2FeNiSb_2$), triple and quadruple half-Heusler compounds — in multi-component chemistries which would have been inaccessible using the conventional 18-electron rule.

## Acknowledgements

I have just sat down to write the acknowledgments after completing most of my thesis. I understand that as with most other things in life, the way I say thanks will mean much more than the thanks itself. But with the deadline to my thesis submission fast approaching, I worry if I will be able to say thank you — if ever — in exactly the way I intend to.

I would like to thank my thesis advisor Prof. Jeff Snyder for his guidance through the past five years. Before coming to Northwestern, I had always wanted to work very close to the intersection of computational and experimental aspects of Materials Science. In Jeff's group I found that opportunity. Thanks to Jeff's advising style, I have always felt like I could take as much of his time as I wanted. I could walk in to his office anytime I saw the door open and a typical conversation with Jeff regarding my projects would at least be two hours long. In my interactions with Jeff, I have learnt a lot about scientific writing and choosing the right question to answer through my research. My PhD journey has surely not been without its ups an down. But I would like to thank Jeff for hanging in with me in my more scientifically stubborn periods. Towards the end of my PhD, Jeff very graciously extended my program duration when the job market froze as COVID-19 hit during the process of my job hunt. I remember this gesture giving me a lot of confidence, security and the much needed time to clear my head regarding what I wanted to do with my future.

My co-advisor Prof. Chris Wolverton for was very kind and supportive throughout my PhD research. Chris very graciously allowed me the freedom to sit on all group meeting and sub-group meetings of the group and learn as much as possible. I think Chris and I share a passion for materials thermodynamics; a passion that gradually grew in me after my first cluster expansion project under his guidance. Some of my most interesting scientific conversations at Northwestern have been with Chris regarding phase diagrams on which I could unfortunately not get to during my PhD. However, the fact that this thesis is on exploratory phase stability analysis is an accurate reflection I think of the knowledge I gained from his expertise and previous works.

I would like to thank Prof. Mercouri Kanatzidis for encouraging an environment of scientific freedom and collaboration. I have had the honor of collaborating with his group on several projects with his group during my PhD. I am also very grateful to him for spending the effort to write a reference letter for my postdoc application. I would also like to thank my committee member Prof. James Rondinelli for sharing his expertise, advice and encouragement. I remember his class on symmetry of materials as one of my favorite courses in the Materials Science department. I would also like to thank Prof. Sossina Haile for letting me audit her class in which I learnt a lot about Brouwer diagrams and transport in mixed conductors. Her class became one of the inspirations for chapter 4 of my thesis.

I would also like to thank my colaborators Dr. Eric Toberer, Dr. Vladan Stevanović, Dr. Prashun Gorai and Dr. Anuj Goyal from whom I have learnt a lot in our discussions.

Completing the thesis has been a daunting task and would not have been possible without James, Michael, Maddie and Ramya who read through various parts of the thesis and made the writing process very convenient by identifying parts which needed corrections.

The work in this thesis is entirely computational and for that I have my technical mentors to thank. Shiqiang trained me on my first cluster expansion project of the PhD. I always received a prompt reply for my e-mails to him throughout my PhD. Vinay guided me initially in projects involving high-throughput calculations. More importantly, he was always open for a chat and became a bouncing board for my ideas which eventually became Chapter 3 of my thesis. I felt great freedom in discussing my ideas with him and always knew that I would get a very curious audience in him. Jonathan was very helpful and set me up with the computational resources and defect calculations initially. Shahab, Jiangang, Vancho and Zhengpeng were also very patient in answering my questions initially. I would also like to thank Yi for his collaborative help in Chapter 8, Bi-Cheng and Koushik for chatting interesting ideas from time to time.

Over the past five years, everyone in the Snyder group have become very close friends and I am afraid that it would take me too long if I were to begin counting the ways in which they have enriched my PhD experience. Everyone from Matthias, Max Wood, Kazuki, Riley, Kent, Freddie, Ian, James, Ramya, Saneyuki, Stephen, Jimmy, Max Dylla, Michael, Maddie, Moath, Stefan Maier, Shuping, Umut Aydemir and Sam have just been fantastic. Some moments from my experience with the group stand out and I would like to mention them here. Matthias and Riley, thank you so much for being there for me during my surgery. In those tough days you guys made sure that I did not miss my family. Conversations with Max Wood during our stays at conferences in France and Arizona have helped me question my ideologies, helped me become, I think, a better person. Saneyuki and Stephen were among the first to graduate after I joined the group and remember learning a lot collaborating from them, their group meeting talks and their defense practice talks. Stephen's defense presentation was particularly inspirational; I learnt how to tie together all the projects from your PhD in a general fashion. Riley's excitement for science was incredible and if I may add at times also uncontainable! Discussions with him on his strain-induced-lattice-softening project became an inspiration for me to look into charge-carrier-driven lattice softening, a project which I later collaborated on with Tyler Slade in the Kantazidis group. This project is not contained in the thesis, but I am particularly proud of it.

Besides lake Michigan itself, my stay at Evanston was made extremely pleasant by Pooja Purohit, Koushik Pal, Ameet Morjaria, Tony Chung, Tom Cutler, Roger Larson, Emily Launer, Yash, Jeff, Freddie, Matthias, Sheema and Faez, Kent and Alisha, Xia, Aparajita, and the regular visitor and co-Evanston-lover Mr. Parth Aggarwal. My favorite times in Evanston besides the science was the squash, the board games, the kayaking, the swimming, the frisbee, the movies, the dinners and a bit of piano and badminton. You guys were a huge part of it. I also cannot forget my buddies from before Evanston Parth Ranjan, Apurv, Shubhendu, Utkarsh, Pahul, Chetan, Harshit, Chirayu, Kishore, Pranjal, Pratyush and Shiva too who have been an important part of my journey.

I am grateful to Prof. Umesh Waghmare, Prof. Dhananjai Pandey and Dr. Kanishka Biswas for their recommendations to my Northwestern applications. Prof. Waghmare is perhaps one of the kindest and most hard-working person I know. I have looked up to him since my time in his group at JNCASR. Prof. Pandey's energy and passion for science was a great inspiration during my undergrad days. I owe a huge part of my scientific journey to Prof. C. N. R. Rao's decision to give me an opportunity at JNCASR. His willingness to make time, interact and help young talent despite his scientific stature is an inspiration.

I would like thank my family members in the US: my Uncle in Mr. Sushil Mohan, my brother Vinay Singh, sister-in-law Neetu and Master Rajveer for their constant support.

In the time since our wedding and before it, my wife Pooja has become a pillar of strength. Her lifestyle, pro-activeness and preparedness are constant inspiration to me. Her advise on multiple occasions has prevailed as the voice of reason.

I would like to thank my parents Mrs. Madhu Sharma and Mr. Raj Kishore Singh for supporting me all the way. There is no achievement I could truly call my own because everything I am doing today is built on whatever my parents have selflessly done for me over the years. If I even have that right, I dedicate this thesis to my parents.

# Nomenclature

| | |
|---|---|
| $\Delta H_{CH}$ | Convex-hull distance. Energy distance with respect to the convex-hull |
| $\Delta H_{def}$ | Defect formation energy |
| $\Delta H_{eCH}$ | **Extended convex-hull distance** Energy distance with respect to common tangent planes of the convex-hull. |
| $\Delta H_f$ | Formation energy of the compound |
| $\Delta H_{Stability}$ | **Stability metric for high-throughput Thermodynamic analysis.** Energy distance of a phase with respect to a convex-hull (possibly even a *metastable* convex-hull) which is formed by excluding the structure of interest. |

# Contents

**1 Introduction** **39**

1.1 Thermodynamics of off-stoichiometry in solids . . . . . . . . . . . . . . . . . . 39

1.1.1 Finite Temperature . . . . . . . . . . . . . . . . . . . . . . . . . . . . . . 39

1.1.2 T = 0 K . . . . . . . . . . . . . . . . . . . . . . . . . . . . . . . . . . . . 41

1.1.3 Chemical potential diagram construction from the convex-hull . . . 42

1.1.4 Defect Energy . . . . . . . . . . . . . . . . . . . . . . . . . . . . . . . . . 44

1.2 Thermoelectric Properties . . . . . . . . . . . . . . . . . . . . . . . . . . . . 46

**2 Methodology** **50**

2.1 Density Functional Theory . . . . . . . . . . . . . . . . . . . . . . . . . . . . 50

2.2 Prediction of thermodynamic stability. Convex Hull Construction . . . . . . 52

2.3 Cluster Expansion . . . . . . . . . . . . . . . . . . . . . . . . . . . . . . . . . 54

2.4 Two-band Model for $VFe_2Al$ electrical transport . . . . . . . . . . . . . . . . . . 55

2.5 Double half-Heusler lattice thermal conductivity ($\kappa_L$) calculations . . . . . . 56

**3 Visualizing Defect Energetics** **59**

3.1 Overview . . . . . . . . . . . . . . . . . . . . . . . . . . . . . . . . . . . . . . 59

3.2 Context and Motivation . . . . . . . . . . . . . . . . . . . . . . . . . . . . 60

3.3 Results and Discussion . . . . . . . . . . . . . . . . . . . . . . . . . . . . 62

3.3.1 Graphical representation of point defect energies in convex-hulls . . . 62

3.3.2 Defining the “extended” convex-hull distance ($E_{eCH}$) . . . . . . . . . . 67

3.4 Conclusion . . . . . . . . . . . . . . . . . . . . . . . . . . . . . . . . . 69

**4 A Unified Understanding of Defects for Semiconductors and Insulators 71**

4.1 Context and Motivation . . . . . . . . . . . . . . . . . . . . . . . . . . . . 71

4.2 Results and Discussion . . . . . . . . . . . . . . . . . . . . . . . . . . . . 74

4.2.1 Mathematical Formulation for Building Brouwer Diagrams . . . . . . 74

4.2.2 Physics based approach to defects in semiconductors . . . . . . . . . 78

4.2.3 Experimental Demonstration of Fermi-level Dependence of [$V_{Pb}$] in PbTe 83

4.2.4 Understanding the Brouwer Diagram with Fermi-level dependence . 87

4.2.5 Isolated and Paired defect formation . . . . . . . . . . . . . . . . . . . 92

**5 Predicting Solubility in Complex Materials with Pen-and-Paper Drawings. 97**

5.1 Context and Motivation . . . . . . . . . . . . . . . . . . . . . . . . . . . . 97

5.2 Results and Discussion . . . . . . . . . . . . . . . . . . . . . . . . . . . . 99

5.2.1 Thermodynamic Solubility Guidelines for Multi-component Systems 99

5.2.2 Applying the Guidelines to previous examples . . . . . . . . . . . . . 103

5.2.3 Predicting Unusual Pseudobinary Phase Diagrams . . . . . . . . . . 110

5.2.4 Solubility of defect complexes . . . . . . . . . . . . . . . . . . . . . . 112

5.2.5 What if I do not know the phase diagram beforehand? . . . . . . . . . 112

5.2.6 Effects of Fermi-level dependency of defect energetic dependence of $\Delta H_{def}$ in semiconductors . . . 113

**6 A Valence Balanced Rule for Discovery of Defective half-Heulsers 115**

6.1 Overview . . . 115

6.2 Introduction to Chemistry of Heusler Thermoelectrics . . . 116

6.2.1 Zintl Chemistry perspective of half-Heuslers. A Valence Balanced Rule 117

6.3 Context and Motivation . . . 119

6.4 Results and Discussion . . . 121

6.4.1 Phase stability prediction *ignoring* any off-stoichiometry in $XYZ$ . . . 121

6.4.2 Nb-deficiency in NbCoSb structure . . . 122

6.4.3 Why Nb-vacancies? Extending the Valence Balanced rule to accommodate defects . . . 125

6.4.4 Predicted stability of $XYZ$ composition after considering cation vacancies . . . 126

6.4.5 Confirming the valence balanced rule from previously reported *nominally* VEC = 19 half-Heuslers . . . 126

6.4.6 Previously unknown compounds predicted stable using the valence balanced rule . . . 128

6.4.7 Semiconducting electronic structure driven stability . . . 129

6.4.8 Chemical Trends in stability of the *nominally* VEC = 19 half-Heusler family . . . 132

6.4.9 Experimental Verification . . . 136

6.5 Conclusion . . . 136

**7 Temperature-dependent $n$-type self-doping in *nominally* 19-electron half-Heusler thermoelectrics 138**

7.1 Overview . . . . . . . . . . . . . . . . . . . . . . . . . . . . . . . . . . . 138
7.2 Context and Motivation . . . . . . . . . . . . . . . . . . . . . . . . . . . 139
7.3 Results and discussion . . . . . . . . . . . . . . . . . . . . . . . . . . . 141
7.4 Conclusion . . . . . . . . . . . . . . . . . . . . . . . . . . . . . . . . . . 149

**8 Double half-Heulsers 150**

8.1 Overview . . . . . . . . . . . . . . . . . . . . . . . . . . . . . . . . . . . 150
8.2 Context and Motivation . . . . . . . . . . . . . . . . . . . . . . . . . . . 151
8.3 Results and Discussion . . . . . . . . . . . . . . . . . . . . . . . . . . . 155
  8.3.1 Locating double half-Heuslers in a pseudoternary phase space . . . . 155
  8.3.2 Enormous compositional phase space of quaternary *double*, *triple* and *quadruple* half-Heuslers. . . . . . . . . . . . . . . . . . . . . . . . . 156
  8.3.3 Stability prediction for selected double, triple and quadruple half-Heuslers. . . . . . . . . . . . . . . . . . . . . . . . . . . . . . . . . 159
  8.3.4 Guidelines for laboratory discovery . . . . . . . . . . . . . . . . . . 160
  8.3.5 Discovery of low $\kappa_L$ quaternary half-Heuslers . . . . . . . . . . . . . 160
  8.3.6 Subtle differences distinguishing Double half-Heuslers from half-Heusler compounds . . . . . . . . . . . . . . . . . . . . . . . . . . . . . 164
  8.3.7 Potential for exploration of low cost thermoelectrics in quaternary half-Heusler phase space . . . . . . . . . . . . . . . . . . . . . . . . . 165
8.4 Conclusion . . . . . . . . . . . . . . . . . . . . . . . . . . . . . . . . . . 166

**9 24-electron Full-Heulser $VFe_2Al$, Semi-metal or Semiconductor? 167**

9.1 Overview . . . . . . . . . . . . . . . . . . . . . . . . . . . . . . . . . . 167

9.2 Context and Motivation . . . . . . . . . . . . . . . . . . . . . . . . . . 168

9.3 Band-gap Estimation . . . . . . . . . . . . . . . . . . . . . . . . . . . 170

9.3.1 Weighted Mobility and Seebeck Mass . . . . . . . . . . . . . . . . . . . . 170

9.3.2 Temperature-Dependent Electrical Transport Analysis . . . . . . . . . 172

9.3.3 Modelling Room Temperature Bipolar Transport . . . . . . . . . . . . 173

9.4 Electronic Structure and Molecular Orbital Picture . . . . . . . . . . . . . 176

9.4.1 Rationalizing trends in weighted mobility with electronic structure analysis . . . . . . . . . . . . . . . . . . . . . . . . . . . . . . . . 185

**A Derivation for Graphical solution of $\Delta H_{def}$ 217**

A.0.1 Frenkel and Schottky Defects . . . . . . . . . . . . . . . . . . . . . . 218

A.0.2 Interstitial . . . . . . . . . . . . . . . . . . . . . . . . . . . . . . . . 218

A.0.3 Vacancy . . . . . . . . . . . . . . . . . . . . . . . . . . . . . . . . . . 220

A.0.4 Anti-site . . . . . . . . . . . . . . . . . . . . . . . . . . . . . . . . . 221

A.0.5 Interstitial defects in a ternary compound . . . . . . . . . . . . . . . . 223

A.0.6 Vacancy defects in a ternary compound . . . . . . . . . . . . . . . . . 223

A.0.7 Anti-site defects in a ternary compound . . . . . . . . . . . . . . . . . 224

**Vita** 225

# List of Figures

1.1 **Going from Experimental Phase diagrams to a $T$ = 0 K understanding of stability.** (a) Temperature-Composition phase diagram for a model binary system $A - B$ with three solid phases A, B and AB, and their adjoining two-phase regions. (b) Example free energy ($\Delta G_f$) models of the phases A (blue curve), B (red curve), AB (orange curve) at the temperature $T = T_0$ in panel (a). Thick black lines drawn at the common tangents between the stable phases represent the lowest energy surface and determine compositional limits of the phase boundaries. (c) At 0 K, the Gibbs curves in (b) collapse and $\Delta G_f$ for each compound becomes a point ($\Delta H_f$). Common tangents drawn between stable phases form the 0 K low energy surface, or convex-hull. 40

1.2 **Going from the convex-hull to chemical potential space representation of thermodynamic stability.** (a-c) A convex-hull construction for the hypothetical $A-B$ binary system (left column) with stable phases $A$, $B$, and $AB$ and metastable phase $AB_3$. (a) When phase $AB$ in in equilibrium with $A$ ($\Delta\mu_A = 0$), the change in elemental chemical potentials, $\Delta\mu_A$ and $\Delta\mu_B$, are directly read from the $y$ intercepts of the line connecting $AB$ and $B$ and plotted in chemical potential space (right column). (b) Shifting equilibrium from $AB$ and $A$ diverts $\Delta\mu_A$ and $\Delta\mu_B$ from their extrema until reaching equilibrium between $AB$ and $B$ (c), where $\Delta\mu_B = 0$. The line connecting every chemical potential between the two equilibria captures the entire range of accessible chemical potentials for $AB$. (d) When phase $AB_3$ become stable, the line representing its chemical potentials falls below that of phase $AB$ in chemical potential space. Phase equilibrium between $AB$ and $B$ is no longer possible, and is replaced by equilibrium between $AB$ and $AB_3$, reducing the range of $\Delta\mu_B$ accessible. . . . . . . . . . . . . . . . . . . . . . . . . . . . . 43

1.3 **Weighted Mobility for characterizing the electrical performace of thermoelectric materials.**Calculated Thermopower (|S|)-Conductivity ($\sigma$) relations (curves) using the single parabolic band (SPB) model with acoustic phonon scattering at two different values of weighted mobility ($\mu_w$). Multiple lines with constant power-factor values are plotted for a qualitative reference of device requirement for thermoelectric material. . . . . . . . . . . . . . . . 48

1.4 **Predicting maximum power factor with weighted mobility.** Optimized power factor value calculated using the single parabolic band (SPB) model under the acoustic phonon scattering assumption; plotted as a function of the weighted mobility value. . . . . . . . . . . . . . . . . . . . . . . . . . . . 49

2.1 (a) **Differentiating $E_{stability}$ from $E_{CH}$ in a model binary convex hull.** Formation enthalpy ($\Delta H_f$) of the structures with the compositions $A_3B$, $AB$, $AB_3$ with respect to lowest energy elemental phases A ($\mu_A$) and B ($\mu_B$). The convex hull of the $A-B$ binary phase space is given by the solid line. $E_{stability}$ of $AB$ is calculated by constructing a convex hull of all other phases (dashed line), and using the constant elemental chemical potentials ($\mu_A$ + $\Delta\mu_A$ and $\mu_B$ + $\Delta\mu_B$) associated with the metastable equilibrium $A_3B$-$AB_3$. The convex-hull distance is the energy distance with respect to the lowest energy convex-hull (which contains only the thermodynamically stable phases). When $E_{CH}$ > 0, $E_{stability}$ = $E_{CH}$ and when $E_{CH}$ = 0, $E_{stability} \neq E_{CH}$. . . . . . . . . . . . . . 58

3.1 **Visualizing defect energetics on a convex-hull.** (a-c) Graphical solutions for defect energy $\Delta H_{def}$ of (a) A interstitial, (b) A vacancy, and (c) $B_A$ antisite defects in the binary compound $AB$. Formation energy ($\Delta H_f$) of the defect-free $AB$ structure is given by the orange circle. $\Delta H_f$ of defective $AB$ structures are shown as filled hexagons for interstitials (a), empty hexagons for vacancy defects (b), or a combination for anti-sites (c). Defective structures with the same value of $\Delta H_{def}$ are shown by translucent symbols and fall on the 'defect line' (solid black line). The left and right columns correspond to $A$-rich and $B$-rich equilibrium, respectively. The chemical potentials of $A$ and $B$ corresponding to these equilibrium conditions (large, empty circles) are determined from intercepts of the common tangent lines (blue and red lines in the left and right columns respectively). $\Delta H_{def}$ is determined using intercept (for example $E_i$) between the defect line and the common tangent line on the $A$ and $B$-component axis. The sign of these quantities are are given by the direction of the arrows next to them (see grey box). The expression to calculate $\Delta H_{def}$ is given in each panel. The general expression for calculating $\Delta H_{def}$ for all defect types in is given in the grey box at the bottom where $\Delta N_i$ = 0 or 1 and $\Delta N_v$ = 0 or -1 depending on whether the number of atoms of a particular species is added (1), removed (-1) or unchanged (0) in the defect. . . . . . . . . . . . . . . . . . . . . . . . . . . . . . . . . . . . 63

3.2 **Visualizing Formation Enthalpy ($\Delta H_f$) of defective structures in a ternary convex-hull.** Convex-hull of the Nb-Co-Sb system calculated using [1] DFT. The $\Delta H_f$ of $Nb_{0.8}CoSb$ phase and the defects in it along the 1-dimensional composition slice CoSb-Nb are shown using blue circles in the figure on the right. . . . . . . . . . . . . . . . . . . . . . . . . . . . . . . . . . . . . . . 65

3.3 **Visualizing defect energetics of a ternary compound in a convex-hull.** Graphical solution for defect energy ($\Delta H_{def}$) of (a-b) C interstitial and (c-d) $C_B$ anti-site defects in the ternary compound $A_pB_qC_r$. The compound and the defective structures are represented by large orange and small red circles respectively. Panels a and c show the ternary convex-hulls in which the compound $A_pB_qC_r$ is in equilibrium with elements $A$, $B$ and $C$. Panels b and d show the $\Delta H_f$-composition convex-hull along the 1-D composition slice containing both the defect and the compound. The $\Delta H_{def}$ are shown for (a-b) C-rich ($A_pB_qC_r$-C two-phase region) and (c-d) B-poor ($A_pB_qC_r$-A-C three-phase region) conditions. Similar to the case of binary compounds (see Figure 3.1) $\Delta H_{def}$ is determined using intercept between the common tangent line and the defect line. The expression to calculate $\Delta H_{def}$ is given in each panel. The general expression for calculating $\Delta H_{def}$ for all defect types in is given in the grey box at the bottom where $\Delta N_i$ = 0 or 1 and $\Delta N_v$ = 0 or -1 depending on whether the number of atoms of a particular species is added (1), removed (-1) or unchanged (0) in the defect. . . . . . . . . . . . 66

3.4 **Graphical solution of $\Delta H_{def}$ on convex-hulls are exact.** Comparision of defect energies for 20 half-Heusler systems calculated graphically to those determined using conventional defect energy expression . . . . . . . . . . . . 67

3.5 **Sketch differentiating the convex-Hull distance ($E_{CH}$) from the extended convex-hull distance ($E_{eCH}$) in a model binary convex-hull.** . . . . . . . . 68

4.1 **Brouwer diagram example.** Typical Brouwer Diagram of a model oxide compound MO in which the vacancies $V_M''$ and $V_o^{\cdot\cdot}$ are the dominant point defect types. The $y$-axis gives log [], where [] represents concentration of the defect, and the $x$-axis gives log of the Oxygen partial pressure p$O_2$ (partial pressure). The Brouwer diagram can be broadly classified into three regions, separated by vertical dashed lines, with changing oxygen partial pressures. The slope of each defect and charge carrier concentrations in these regions are labelled next to them. In the extreme conditions (oxidizing and reducing), one of the point defects dominates ($V_M''$ and $V_o^{\cdot\cdot}$ respectively) causing a larger concentration of one of the carriers. In the intermediate conditions, neither of the vacancies clearly dominate and the charge carrier concentrations equal each other. The Brouwer approximations equating the dominant contributions to the charge neutrality condition in each region are mentioned above. . . . . . . . . . . . . . . . . . . . . . . . . . . . . . . . . . . 76

4.2 **Relating electronic properties and electronic structure to defect thermodynamics.** ((a) and (b)) Thermodynamics of the dominant intrinsic vacancy defects in the model insulator system MO determining its electronic dopability. The defect formation energeies ($\Delta H_{def}$) of the acceptor ($V_M^{-2}$) and donor ($V_O^{+2}$) defects depend on the Fermi-level ($E_f$) with a slope equal to their valence. The thermodynamic limit to the $E_f$ (dopability) under given temperature, pressure and chemical conditions is determined by the points where $\Delta H_{def}$ = 0 (a). This limit is shifted with changing chemical conditions (b). (c) The electronic density of states for the example of oxygen vacancy deep defect (defect level lies far from either band-edges) in MO. The defect level containing 2 states appears in a very narrow energy window indicating the localized nature of the states. At $E_f$ above the defect level, electronic charge equal to 2e localizes around the defect and the defect transitions from charge +2 to 0. The transition is observed as a change in slope of the $\Delta H_{def}$ versus $E_f$ plot for the defect. . . . . . . . . . . . . . . . . . . . . . . 81

4.3 **Schematic showing the procedure to obtain the defect diagram using experimental data.** In order to estimate the defect energetics accurately within a thermodynamic framework, the samples need to be annealed (and quenched subsequently) at the temperature of interest. The number of defects and number of carriers are presumed to be frozen from this annealing temperature. The $E_f$ dependence of $\Delta H_{Def}$ is calculated for the annealing temperature. Determining the equilibrium $E_f$ for each sample at the annealing temperature will also require the Seebeck effective mass from this temperature. . . . . . . . . . . . . . . . . . . . . . . . . . . . . . . . . 85

4.4 **The Fermi-level ($E_f$) dependence of $\Delta H_{def} - TS_{def}^{non-conf}$ (T = 973 K) for the $V_{Pb}^{-2}$ in PbTe determined from experimental data.** A solid line with a slope of -2 is shown for reference. . . . . . . . . . . . . . . . . . . . . . . 86

4.5 **Brouwer diagram for $Mg_3Sb_2$ with Fermi-level dependence of point defect energetics accounted for.** Concentration of important intrinsic charged defects and charge carriers in $Mg_3Sb_2$ calculated as a function of Mg-chemical potential. The defect energies (which implicitly also have a fermi-level dependence) and density of states masses are taken from Ref. [2]. The dominant defect types $\mathrm{Mg}_i^{+2}$ and $V_{Mg}^{-2}$ are both shallow defects. Despite the Fermi-level dependence, the plot resembles the one shown in Figure 4.1 with three distinct regions of Mg chemical potential dependencies separated by vertical lines which are drawn as guides to the eye. . . . . . . . . . . . . . . . . . . . . 89

4.6 **Presenting electronic dopability information on a Brouwer diagram.** Concentration of important intrinsic charged defects and charge carriers in $Mg_3Sb_2$ calculated as a function of Mg-chemical potential. The defect energies (which implicitly also have a fermi-level dependence) and density of states masses are taken from Ref. [2]. The $n$ and $p$-type dopabilities (red and blue lines) and are determined by the carrier concentrations from the $E_f$ at which $\Delta H_{def}$ of the $V_{Mg}^{-2}$ and $\mathrm{Mg}_i^{+2}$ defects becomes 0 eV. The VBM and CBM markers are determined by the carrier concentrations at the valence and conduction band edges. . . . . . . . . . . . . . . . . . . . . . . . . . . . 90

4.7 **Electrostatic and strain contributions to binding energy in the Schottky defect pair of PbTe.** (a) Defect energy (in eV/defect) of a Schottky defect in PbTe as a function of the distance between the vacancy pair in a 128 atom supercell. To estimate the electrostatic contributions to binding between the vacancy pair, we calculate the relaxed (blue circles) and unrelaxed (purple squares) separately. The electrostatic contribution from the unrelaxed calculations can be modelled with a 1/r dependence (solid blue line). (b) The energy gained from relaxing all degrees of freedom in the supercell as a function of the distance between the vacancy pair. This energy contribution is calculated by subtracting the relaxed energies from the unrelaxed energies shown in (a). . . . . . . . . . . . . . . . . . . . . . . . . . . . . . . . . . . 93

4.8 **Electrostatic and strain contributions to binding energy in the Schottky defect pair of MgO.** (a) Defect energy (in eV/defect) of a Schottky defect in MgO as a function of the distance between the vacancy pair in a 128 atom supercell. To estimate the electrostatic contributions to binding between the vacancy pair, we calculate the relaxed (blue circles) and unrelaxed (purple squares) separately. For the sake of verifying convergence in this low dielectric constant material we also calculate the unrelaxed energies in a 432 atom supercell (pink). The electrostatic contribution from the unrelaxed calculations can be modelled with a 1/r dependence (solid blue line). (b) The energy gained from relaxing all degrees of freedom in the supercell as a function of the distance between the vacancy pair. This energy contribution is calculated by subtracting the relaxed energies from the unrelaxed energies shown in (a). . . . . . . . . . . . . . . . . . . . . . . . . . . . . . . . 94

5.1 **Sketch summarizing the problem statement for this chapter.** Can we use available phase diagram information (experimental or computational) and combine it with our chemical intuition regarding the dominant defect to qualitatively predict the shape of the single phase region (and thereby the various limits to defect solubility)? As we deal with more complex materials, the answer to this question will come in handy. . . . . . . . . . . . . . . . . . . 99

5.2 **Building a visualization tool for predicting maximal solubility limit with simple pen-and-paper drawings.** (a) Ternary convex-hull of the model system $A$-$B$-$C$ containing a single stable compound $A_pB_qC_r$. The formation energy ($\Delta H_f$) of the compound $A_pB_qC_r$ and the $B$-interstitial defect ($B_i$) in it are shown by orange and blue filled circles respectively. The three common tangent planes representing compositions in which the $A_pB_qC_r$ phase will yield two impurity phases are numbered 1, 2 and 3. (b) Left: Ternary phase diagram of the model system $A$-$B$-$C$. Can also be visualized as the top view of (a). Right: side-view of (a) along the one-dimensional composition slice indicated in the left panel. (c) Sketch showing the directions along which the composition of the compound $A_pB_qC_r$ will change due to various point defects (or *defect directions*) or shown with orange arrows. The direction of the impurity phases with respect to $A_pB_qC_r$ (or *impurity phase directions*) are shown with purple arrows. The dominant defect direction and the impurity phase direction information is sufficient to qualitatively predict the region of maximal solubility. . . . . . . . . . . . . . . . . . . . . . . . . . . . . 101

5.3 **Rationalizing Ce$_i$ solubility in CoSb$_3$ prepared in varied chemical conditions.** (a) Ternary Co-Sb-Ce phase diagram zoomed in close to the ternary CoSb$_3$ phase (orange line) taken from Ref. [3]. The compositional regions which yield two impurity phases in CoSb$_3$ samples are numbered 1, 2 and 3. The relatively smaller regions which yield just one impurity phase lie in between these numbered regions. The impurity phases for the larger regions are labelled. (b) Sketch showing the dominant defect (Ce$_i$) direction and the impurity phase directions for CoSb$_3$. . . . . . . . . . . . . . . . . . . . . . . . 105

5.4 **Rationalizing chemical conditions of maximal Te$_{Sb}$ solubility in Mg$_3$Sb$_2$.** (a) $T$ = 0 K Mg-Sb-Te ternary phase diagram. The compositional regions which yield two impurity phases in Mg$_3$Sb$_2$ are numbered 1 and 2. (b) $T$ = 900 K Mg-Sb-Te ternary phase diagram zoomed-in close to the Mg$_3$Sb$_2$ phase [2]. The compositional region which yields no impurity phase in Mg$_3$Sb$_2$ phase is shown in grey. The unnumbered compositional regions yield one impurity phase (c) Schematic showing the dominant defect (Te$_{Sb}$) direction and the impurity phase directions for Mg$_3$Sb$_2$. . . . . . . . . . . . . . . . . . . 106

5.5 **Rationalizing Ni$_i$ solubility in TiNiSn prepared in varied chemical conditions.** (a) Ternary Ti-Ni-Sn phase diagram zoomed in close to the ternary TiNiSn phase (green line) taken from Ref [4]. The compositional regions which yield two impurity phases in half-Heusler TiNiSn samples are numbered 1, 2, 3 and 4. The compositions which yield just one impurity phase lie in between these numbered regions. The impurity phases are labelled in each case. (b) Sketch showing the dominant defect (Ni$_i$) direction and the impurity phase directions for TiNiSn. . . . . . . . . . . . . . . . . . . . . . . . 108

5.6 **Prediction of unusual pseudobinary solid-solution phase diagram.** Sketch for a possible Temperature-Composition phase diagram (right) for the model pseudobinary system $AD-BCD_2$. The $x$-axis represents the composition between the $AD$ and $BCD_2$ *phases* (instead of the exact compositions $AD$ and $BCD_2$) under $B$-rich and $C$-rich conditions. The figure on the left locates this pseudobinary on the $AD$-$BD$-$CD$ pseudoternary composition slice. The substitutional defect directions for each end-member of the pseudobinary end-members are shown by orange arrows. The defect direction vectors are drawn of varying lengths to indicate differences in their energetics. The dominant defect between each pair of substitutional defect is shown by a longer vector. The impurity phase directions for the end-members are shown by purple arrows. . . . . . . . . . . . . . . . . . . . . . . . . . . . . . 111

6.1 **Status of thermodynamic stability predictions prior to this work.** Number of half-Heusler compounds reported (blue circles, ICSD [5] and Ref. [6]) and predicted stable (red triangles, Ref. [6, 7] and OQMD [8, 9] ) using the defect-free $XYZ$ stoichiometry prior to this work as a function of nominal valence electron count (VEC) or (alternatively) net valence (NV). . . . . . . . 120

6.2 **Using defect-free structures with $XYZ$ composition predicts stability of 19-electron half-Heuslers poorly.** 19-electron $XYZ$ systems investigated in the present work for stability in the half-Heusler structure using only a defect-free $XYZ$ structure (any off-stoichiometry is ignored). Half-Heuslers predicted stable are represented by the plus (+) symbol. Previously reported nominal VEC = 19 half-Heuslers are represented by a circle. Compounds where the half-Heusler phase is predicted unstable are indicated by a minus (-) symbol. . . . . . . . . . . . . . . . . . . . . . . . . . . . . . . . . . 122

6.3 **X-ray diffraction pattern of NbCoSb composition contains a significant fraction of impurity phase.** Synchrotron diffraction pattern of the NbCoSb sample in a small angular range including the profile fit. The calculated Bragg diffractions show the quality of the fit with the two phases NbCoSb and $Nb_3Sb$. Experiments were performed by collaborators at Justus-Liebig-University Giessen and University of Houston. . . . . . . . . . . . . . . . . . . 123

6.4 **Cluster expansion results for the $Nb_{1-x}$CoSb system.** Formation enthalpy($\Delta$ $E_F$) of 173 different orderings (gray circles) of Nb-atom and vacancies in the Nb-sublattice of half-Heusler NbCoSb determined using DFT. The dotted line indicates the convex hull for these configurations of the NbCoSb (half-Heusler structure(half-Heusler))-CoSb (zinc Blende structure ($c$-ZnS)) binary system. The $Nb_{0.8}CoSb$ structure emerges as a stable ground state phase lying on the NbCoSb ternary convex hull (solid black line). The formation energies of this convex hull are determined from the three-phase region of $Nb_7Co_6$, $Nb_3Sb$, and $Nb_{0.8}CoSb$ at x = 0 (black square), the ordered $Nb_{0.8}CoSb$ ground state phase, and the hexagonal ground state phase of CoSb (red square). . . . . . . . . . . . . . . . . . . . . . . . . . . . . . . 124

6.5 **Valence balanced defective composition predict stability accurately.** 19-electron XYZ systems investigated in the present work for stability of the half-Heusler phase using the valence balanced (NV = 0) defective compositions. Systems with the half-Heusler phase predicted stable are represented by the plus (+) symbol. Among these, symbols of compounds previously reported as nominal VEC = 19 half-Heuslers are encircled. Compounds where the half-Heusler phase is predicted unstable are indicated by a minus (-) symbol and those which lie within chemical accuracy of DFT ($|E_{stability}| \leq$ 10 meV/ atom) are given by tilda ($\sim$) symbol. . . . . . . . . . . . . . . . . . . 128

6.6 **The defective valence balanced composition is always more stable than the 19-electron half-Heusler structure at the $XYZ$ composition.** $E_{stability}$ of the 108 half-Heusler structures studied here at the $X$-site-deficient valence-balanced (NV = 0) composition versus at the defect-free VEC = 19 composition. Negative values signify cases where half-Heusler structure is predicted stable. Cation deficiency increases the stability of nearly all half-Heusler structures. Stabilizing energies are larger for systems with larger band-gaps ($\mathrm{E}_g \geq$ 0.55 eV, filled circles) at the VEC = 18 composition. All stable nominal VEC = 19 half-Heuslers exhibit $\mathrm{E}_g \geq$ 0.55 eV. . . . . . . . . . . . . . . . . . . . 130

6.7 **Instability of the 19-electron half-Heusler structure at the $XYZ$ composition can be overcome by a correspondingly large electronic energy gap.** $\mathrm{E}_{stability}$ (in eV/formula unit) of the half-Heusler structures at VEC = 19 composition versus its band-gap ($\mathrm{E}_g$) at the off-stoichiometric valence balanced composition. The compounds predicted stable ($\mathrm{E}_{stability} \leq$ -10 meV/atom) in the off-stoichiometric valence balanced (NV = 0) structure are given by filled circles. . . . . . . . . . . . . . . . . . . . . . . . . . . . . . . 131

6.8 **Chemical trends in stability of half-Heusler compounds.** Calculated $E_{stability}$ values (cross symbols) for all of the 19-electron half-Heuslers at the $XYZ$ compositions investigated in this work. The $E_{stability}$ values are classified by the $Z$-site anion. Average $E_{stability}$ values for each case is shown as a big blue circle. The thick black lines are drawn as a guide to the eye to show the general trend in $E_{stability}$ values on going down a particular group in the periodic table. . . . . . . . . . . . . . . . . . . . . . . . . . . . . . . 133

6.9 **Trends in half-Heusler stability with with electronegativity of the $Z$-site atom.** Calculated values of average $E_{stability}$ (averaged for based on $Z$-site anion separately) for all the 19-electron half-Heuslers at the $XYZ$ compositions investigated in this work plotted as a function of the $Z$-site atom electronegativity. . . . . . . . . . . . . . . . . . . . . . . . . . . . 134

6.10 **Experimental verification of prediction of the Ti$_{0.75+x}$PtSb compound based on valence balanced rule.** XRD patterns of Ti$_{0.75+x}$PtSb (x = 0, 0.1) annealed at 1073 K. Experiments were performed by collaborators at Zhejiang University. . . . . . . . . . . . . . . . . . . . . . . . . . . . . . . . . . 137

7.1 **Strategy to identify synthesis conditions for preparation of high performing *nominally* 19-electron half-Heusler thermoelectric samples.** Schematic demonstrating the strategy adopted in the present work for recommending appropriate annealing temperature-composition synthesis conditions for the design of optimally doped *nominally* 19-electron half-Heusler thermoelectrics. . . . . . . . . . . . . . . . . . . . . . . . . . . . . . . 141

7.2 **Temperature-dependent evolution of single phase (light blue) half-Heusler in (a) V$_{0.8+x}$CoSb, (b) Nb$_{0.8+x}$CoSb and (c) Ti$_{0.75+x}$NiSb.** The solvus boundaries of the half-Heusler phase are given by the solid black lines. Compositions with single phase and multi-phase samples (from XRD) are represented by blue and unfilled black circles respectively. The dashed vertical line drawn at the $T$ = 0 K valence-balanced (NV = 0) composition separates the $n$-type and $p$-type region for the nominal composition of the sample. The top axis provides the nominal chemical carrier concentration ($n$) for each system. . . . . . . . . . . . . . . . . . . . . . . . . . . . . . . . . . . . . 142

7.3 **Explaining $X$-solubility in vacancies of the $X_yYZ$ ground state of *nominally* 19-electron half-Heuslers with DFT calculated $\Delta H_{def}$.** Fraction of vacancies ($f$) in the ground state structure ($x$ = 0) filled at $T_{anneal}$ = 1073 K (filled circles) or $T_{anneal}$ = 873 K (unfilled circle) versus the ratio $\Delta H_{def}/k_BT_{anneal}$. $\Delta H_{def}$ is the calculated defect energy for filling $X$-vacancies. The value of $f$ is obtained from systems studied in the present work (see Figure 7.2) and Ref. [10] ($Ti_{0.75+x}PtSb$). The dashed line is a guide to the eye describing correlation between experimentally observed $X$-solubility and $\Delta H_{def}$ (under $X$-rich conditions). Temperature-dependent solubility can be estimated from $\Delta H_{def}$. . . . . . . . . . . . . . . . . . . . . . . . . . . . . . . . . . . . . 146

7.4 **Defect energy of vacancy-filling defect scales with increasing electronic energy gap.** Defect energy ($\Delta H_{def}$) for filling $X$-vacancies in the ground state $X_yYZ$ structures versus band-gap ($E_g$) at the valence-balanced NV = 0 composition. Group-IV ($y$ = 0.75) and Group-V ($y$ = 0.8) cation based nominally NV = 1 (or VEC = 19) systems are shown by square and pentagon symbols respectively. The dashed line is a guide to the eye describing correlation between $\Delta H_{def}$ and $E_g$. . . . . . . . . . . . . . . . . . . . . . . . . . . . . . . 147

8.1 **Visual illustration of the concept of double half-Heuslers.** (a) Color scheme in the periodic table representing elements occupying various sites ($X$ (violet), $Y$ (red) and $Z$ (green)) of the cubic half-Heusler structure (in panel b). Quaternary half-Heusler compositions selected in the present work are based on elements given in bold font. (b) The *double* half-Heusler structure (disordered) with the general formula $X_2Y'Y''Z_2$ has equal occupancy on the $Y$-site (in half orange/ half magenta) such that the overall composition is valence balanced (net valence NV = 0). (c) Example pseudoternary $\mathrm{TiFe}_x\mathrm{Co}_y\mathrm{Ni}_{1-x-y}\mathrm{Sb}$ based on aliovalent substitution on the atomic $Y$-site. Double half-Heusler $\mathrm{Ti_2FeNiSb_2}$ (purple square) and the alloy compositions joining it to TiCoSb (blue square) are valence balanced (NV = 0). Adjacent compositions based on Fe (orange) and Ni (cyan) substitutions represent $p$ and $n$-type compositions respectively. Nominally NV $\neq$ 0 compositions (red/ white squares) are examples of *ternary defective* half-Heuslers which are unstable without defects ($\mathrm{TiFe_{1.5}Sb}$[11] and $\mathrm{Ti_{0.75+\delta}NiSb}$[12]). These NV $\neq$ 0 compositions will be referred to as the ternary components of the double half-Heusler composition. . . . . . . . . . . . . . . . . . . . . . . . . . . . . 152

8.2 **The quaternary half-Heusler composition space is almost completely unexplored.** Bar chart depicting the current status of exploration in possible ternary half-Heusler systems as opposed to quaternary systems. Compositions were obtained by imposing the valence balanced rule on the elemental combinations provided in figure 8.1 a. The dark blue color gives a conservative estimate of the fraction of explored compositions. The quaternary phase space is almost completely unexplored. . . . . . . . . . . . . . . . 156

8.3 **Predicted quaternary half-Heuslers and their stability ($E_{stability}$).** 351 quaternary half-Heusler compositions (divided between 5 sub-types) investigated in the present work for stability in the half-Heusler structure. Half-Heuslers predicted stable are represented by a plus (+) symbol. For compounds where the half-Heusler phase is predicted unstable, the space is left blank. The greyscale bar on the side gives the magnitude of predicted stability ($E_{stability}$, data provided in Ref. [13]) of the quaternary half-Heuslers. Predicted compounds for which only one of the ternary NV $\neq$ 0 component have a half-Heusler phase reported experimentally are denoted by thin circles. Predicted compounds for which both the ternary NV $\neq$ 0 components have a half-Heusler phase reported experimentally are denoted by thick circles. Previously reported quaternary half-Heuslers are denoted by boxes. . . 158

8.4 **Lattice thermal conductivity comparison of double half-Heusler and corresponding ternary half-Heusler.** (a) Calculated (line) and measured (scatter points) lattice thermal conductivity ($\kappa_L$) of TiCoSb (cyan) and $Ti_2FeNiSb_2$ (magenta) as a function of temperature. Experimental values of TiCoSb are taken from Sekimoto et al. [14]. Calculated phonon frequency dependence of (b) cumulative $\kappa_L$, (c) group velocities ($v_g$), and (d) phonon-phonon scattering rates in the two compounds at $T$ = 300 K. (e) Calculated $\kappa_L$ versus Gruniesen parameter ($\gamma$) for selected half-Heusler (triangle) and double half-Heusler (square) compounds based on commonly used elements. The regions are shaded based on a $\gamma^{-2}$ dependence of $\kappa_L$. . . . . . . . . . . . . . 161

8.5 **Experimental verification of double half-Heusler compound $Ti_2FeNiSb_2$.** Room temperature powder XRD pattern (cyan) of $Ti_2FeNiSb_2$ annealed at 1073 K. Theoretical XRD pattern for special quasi-random structure (SQS) of $Ti_2FeNiSb_2$ is given in black. Experiments were performed by Dr. Max Wood from the Snyder group at Northwestern. . . . . . . . . . . . . . . . . . 163

8.6 **Schematic distinguishing key differences between the temperature-dependent phase diagram of the half-Heusler and the double half-Heusler phases.** . . . . . . . . . . . . . . . . . . . . . . . . . . . . . . . . . . . . 165

9.1 **Schematic demonstrating difference between electronic structure of indirect semimetals and semiconductors.** . . . . . . . . . . . . . . . . . . . . 170

9.2 **Modelling valence and conduction band transport of VFe$_2$Al separately using single parabolic band modelling.** Variation of thermopower (|S|) in VFe$_2$Al with different type and concentration of doping[15, 16, 17, 18, 19, 20, 21, 22] at room temperature. (a,b) plot of log|S|-log|$\sigma$| which gives the weighted mobility ($\mu_w$) with $n$-type (a) and $p$-type (b) dopants. For both cases, the solid curves represent the prediction corresponding to constant values of $\mu_w$. (c,d) Themopower versus carrier concentration ($n$) plot to determine the effective mass ($m_s^*$) of $n$-type (c) and $p$-type (d) VFe$_2$Al samples (scatter points). The solid curves show the prediction for a constant $m^*$ which fit reasonably well across the entire range of $n$. . . . . . . . . . . . . . . . . . . . 171

9.3 **Estimating band-gap of VFe$_2$Al from high temperature resistivity data.** Arrhenius plot for resistivity measurements of three undoped VFe$_2$Al samples (filled circles) from previous reports[15, 18, 22]. At high temperatures, slope of the solid lines correspond to a small band-gap of $E_g$=0.03 eV. . . . . 172

9.4 **Band-gap estimates from temperature-dependent Seebeck and resistivity data for $VFe_2Al$ are consistent with each other.** Temperature dependence of Seebeck coefficient for $VFe_2Al$ sample (scatter points) doped with 10% Mo [20]. Solid lines represent predictions from two-band acoustic phonon scattering models with $E_g$ = 0.15 eV, 0.02 eV and -0.10 eV (semimetallic). The weighted mobility ($\mu_w$) values used in these models for majority and minority carriers were 440 $cm^2V^{-1}s^{-1}$ and 480 $cm^2V^{-1}s^{-1}$, respectively. Observed temperature dependence of Seebeck coefficients for $VFe_2Al$ can be best understood from a small gap semiconductor description of the compound. . . . . . . . . . . . . . . . . . . . . . . . . . . . . . . . . . . . . . . 174

9.5 **Seebeck coefficient is extremely sensitive to size of the electronic gap making it very useful for $E_g$ estimation.** Seebeck versus carrier concentration ($n$) plot of $n$- and $p$-type $VFe_2Al$ samples (scatter points) for the entire range of carrier concentration reported in the literature[15, 16, 17, 18, 19, 20, 21, 22]. The solid curves represent two-band acoustic phonon scattering model predictions for band-gap $E_g$=0.15 eV, 0.02 eV and -0.10 eV (semimetallic). In these models, weighted mobility values of 700 $cm^2V^{-1}s^{-1}$ and 300 $cm^2V^{-1}s^{-1}$ were chosen for conduction band and valence band transport respectively. Observed Seebeck values for $VFe_2Al$ can be best understood from a small gap semiconductor description of the compound. . . . . . . . . 175

9.6 **Atom resolved electronic band structure and density of states for $VFe_2Al$.** 177

9.7 **Crystal Orbital Hamiltonian Population (COHP) heat map for the first Γ point conduction band in the VFe$_2$Al electronic structure.** The *off-site* COHP terms which represent interation between orbitals on two different sites can be found outside the 4 large boxes (in thick black lines) drawn across the diagonal of the heat map. Negative and positive COHP values indicate bonding and anti-bonding interactions respectively. COHP value of zero indicates the absence of any interaction. Clearly, the Fe1-Fe2 $e_g$ interaction is the only relevant one for this state. . . . . . . . . . . . . . . . . . 179

9.8 **Crystal Orbital Hamiltonian Population (COHP) heat map for the seventh Γ point valence band in the VFe$_2$Al electronic structure.** The *off-site* COHP terms which represent interation between orbitals on two different sites can be found outside the 4 large boxes (in thick black lines) drawn across the diagonal of the heat map. Negative and positive COHP values indicate bonding and anti-bonding interactions respectively. COHP value of zero indicates the absence of any interaction. Since multiple interactions (between Fe-Al, Fe1-Fe2 and V-Al) appear to contribute in the formation of this state, selecting the most relevant interaction additionally requires analysing the orbital-projected partial density of states to identify the orbitals contributing the most. . . . . . . . . . . . . . . . . . . . . . . . . 180

9.9 **Partial density of states of orbitals involved in interactions with a large COHP value can be *negligibly* small.** Orbital projected partial density of states heat map for the seventh Γ-point valence band. . . . . . . . . . . . . . 181

9.10 **Molecular orbital diagram construction requires both COHP *and* pDOS calculations.** Orbital projected partial Density of States (pDOS) and $k$-resolved Crystal Orbital Hamiltonian Population (COHP) of $\Gamma$-point states of $VFe_2Al$. The x-axis indicates the band index of the $\Gamma$-point state. The indices of the valence (VB) and conduction bands (CB) are counted with respect to the Fermi-level ($E_f$). Degenerate bands are indexed together. The pDOS are determined by adding contributions from $s$ (blue bar), $t_{2g}$-type ($d_{xy}$, $d_{yz}$, $d_{zx}$ red bars) and $e_g$-type ($d_{x^2-y^2}$, $d_{z^2}$, red bars) orbitals separately regardless of the atom type. pDOS value of 1 mean complete contribution from a particular set. The COHP values were determined by averaging across all inter-atomic interactions between orbitals of the same type (for example averaging between Fe $d_{z^2}$ - V $d_{z^2}$ and Fe $d_{x^2-y^2}$ - V $d_{x^2-y^2}$ COHP to obtain Fe-V $e_g$ COHP). Negative and positive COHP values indicate bonding and anti-bonding interactions respectively. COHP value of zero indicates the absence of any interaction. In general, interaction strength increases as $t_{2g}$ < $e_g$ < $s$. . . . . . . . . . . . . . . . . . . . . . . . . . . . . . . . . . . . 182

9.11 **Molecular orbital diagram of $VFe_2Al$.** Schematic illustration of the molecular orbital diagram in $VFe_2Al$. The bonding (example $e_g$) and anti-bonding (example $e_g*$) interactions are concluded from partial density of states and $k$-resolved Crystal Orbital Hamilton Population (COHP) analysis of states at the $\Gamma$ point in the electronic structure (see example in Figure 9.9 and Figure 9.8). States close to the Fermi-level ($E_f$) predominantly show $e_g$ and $t_{2g}$ charater from V and Fe atoms. . . . . . . . . . . . . . . . . . . . . . . . . . . . 184

# List of Tables

7.1 Room temperature Hall carrier concentration ($n_H$) of phase pure (from XRD) $V_{0.8+x}$CoSb and $Nb_{0.8+x}$CoSb samples for different annealing temperatures ($T_{anneal}$). . . . . . . . . . . . . . . . . . . . . . . . . . . . . . . . . . . . . . . 144

# Chapter 1

# Introduction

## 1.1 Thermodynamics of off-stoichiometry in solids

### 1.1.1 Finite Temperature

At non-zero temperatures, thermal energy ($kT$) creates defects in the lattice of a compound and changes its composition. The off-stoichiometry observed with increasing temperature can be visualized in a temperature-composition phase diagram. Figure 1.1a sketches the composition-temperature phase diagram of a model binary ($A - B$) system for which the phases $A$, $B$, and $AB$, (depicted by shaded regions) all exhibit single phase width and are stable in the entire temperature range. In general, the maximum amount of off-stoichiometry in the stable single phase regions increases with temperature due to larger amounts of thermal energies available to form defects in the lattice. The white regions bordered by single phases represent two-phase equilibrium.

Solubility of different elements (at $T = T_o$, for example, see Figure 1.1a) within each phase can be simply understood using the Gibbs free energies of formation ($\Delta G_f$) of all stable phases (see Figure 1.1b). $\Delta G_f$ can be drawn as composition-dependent curves for each phase, where $\Delta G_f$ at a particular composition is determined with respect to the free

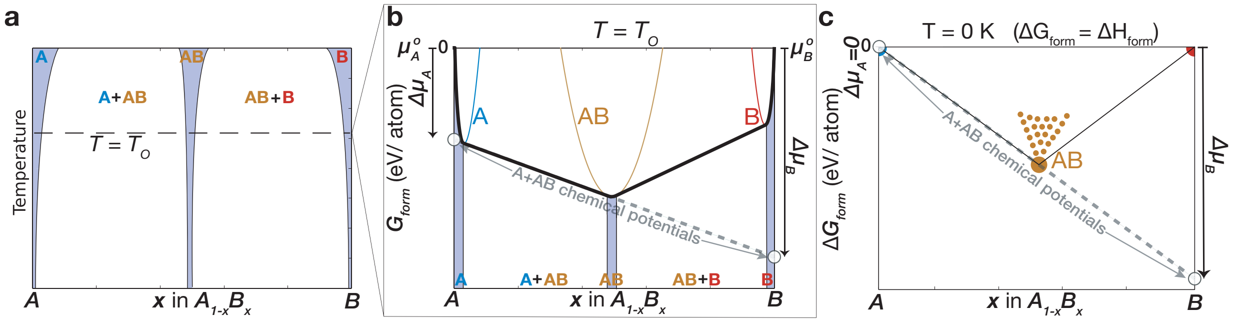

Figure 1.1: **Going from Experimental Phase diagrams to a $T$ = 0 K understanding of stability.** (a) Temperature-Composition phase diagram for a model binary system $A - B$ with three solid phases A, B and AB, and their adjoining two-phase regions. (b) Example free energy ($\Delta G_f$) models of the phases A (blue curve), B (red curve), AB (orange curve) at the temperature $T$ = $T_0$ in panel (a). Thick black lines drawn at the common tangents between the stable phases represent the lowest energy surface and determine compositional limits of the phase boundaries. (c) At 0 K, the Gibbs curves in (b) collapse and $\Delta G_f$ for each compound becomes a point ($\Delta H_f$). Common tangents drawn between stable phases form the 0 K low energy surface, or convex-hull.

energy of elemental phases $A$ ($G_A^0$) and $B$ ($G_B^0$). For example, the free energy of formation for the compound $AB_2$, for example, at the composition $x = 2/3$ is given by

$$\Delta G_f^{AB_2} = G_{AB_2} - 1/3 \times G_A^0 - 2/3 \times G_B^0 \tag{1.1}$$

where $G_{AB_2}$ is the free energy of the $AB_2$ compound in eV/ atom. It is important to note that when calculated on a per-atom basis (as in Figure 1.1 b) $G_A^0$ and $G_B^0$ are actually the *elemental* chemical potentials ($\mu_A^0$ and $\mu_B^0$) at constant pressure. Hence, the formation energy are all relative to the elemental chemical potentials and $\Delta G_f$ at the percentage composition $x = 0$ and $x = 1$ is zero (see Figure 1.1b).

The stability of a phase or combination of phases as seen in the phase diagram (see $T$ = $T_0$ in Figure 1.1a) is determined by the common tangent construction; a topic familiar from introductory texts on phase diagrams. In this technique, common tangents connecting the $\Delta G_f$ curves of all the phases involved are drawn and the lowest free energy surface (see thick lines in Figure 1.1b) is chosen in order to describe phase stability. This lowest energy surface, consisting of linear and non-linear (see thick black lines in Figure 1.1b) portions is known as the *convex-hull* of the $A - B$ system. The linear portions drawn from connecting common tangents between curves indicate compositions which undergo phase separation in order to lower the system's energy to that of the common tangent line. The non-linear portion of the convex-hull is created by a single low energy $\Delta G_f$ curve and indicates a single phase region. $\Delta G_f$ curves for metastable phases which cannot be seen in the phase diagram can also be represented by curves lying above the convex-hull.

In addition to demonstrating compositional stability, convex-hull constructions also contain complete information on how the chemical potentials of $A$ and $B$ atoms vary across the entire composition range. To obtain the chemical potentials of the elements $A$ and $B$ at a particular composition, one can simply draw a tangent to the convex-hull at that composition and extend it in either direction to find the intercepts on the $A$ ($x = 0$) and $B$-component ($x = 1$) y-axis. The intercept length along the $y$-axis (given in eV/atom) indicates change in chemical potentials with respect to that of the elemental species $\mu_A^0$ (for $A$) and $\mu_B^0$ (for $B$), respectively. So the chemical potentials for the $A$-$AB$ equilibrium in Figure 1.1b, for example, is $\mu_A^0$ + $\Delta\mu_A$ and $\mu_B^0$ + $\Delta\mu_B$ (see dashed grey line). The constant values of the chemical potential across the two phase composition range signifies the energy gain/loss associated with exchanging a single atom between phases in equilibrium (A and AB for example). We discuss plotting chemical potential diagrams using the convex-hull construction in the section 1.1.3 below.

### 1.1.2 T = 0 K

The curvature in the finite temperature $\Delta G_f$ arises from the entropic contribution ($-T\Delta S$) to the free energy, which typically varies non-linearly with composition. So at $T = 0K$, where $\Delta G_f = \Delta H_f$, the curvature associated with the entropic contribution vanishes for all phases, and the stable phases are represented by single points (see large circles in Figure 1.1c) lying on the convex-hull. These points indicate $\Delta H_f$ of the defect-free stoichiometric structure of the compound. The composition dependence of $\Delta H_f$ at $T = 0K$ for the stable phases is be depicted by including the energies of its defective structures in the convex-hull diagram. The composition of these defective structures deviate from the nominal stoichiometry of the compound in case of point defects such as vacancies, interstitials and anti-site defect. So structures with larger concentrations of point defects in the compound $AB$, for example, will lie further away from it in composition. The $\Delta H_f$ of these defective structures (see small orange points for $AB$ phase in Figure 1.1c) lie above the convex-hull signifying that they are metastable at $T = 0K$.

### 1.1.3 Chemical potential diagram construction from the convex-hull

The chemical potentials pertaining to various phase equilibria are needed for calculating point defect formation energies[2, 23, 24]. The range of such chemical potentials available for calculations can be directly visualized from a convex-hull construction (Figure 1.2). In the $A$-$B$ model system, the energies at the y-intercepts of a "common-tangent" line on the $A$ and $B$ energy axes are $\Delta\mu_A$ and $\Delta\mu_B$, respectively. As an example, for $AB$ in equilibrium with $A$ (Figure 1.2a), the $y$-intercepts of the line between the two compounds gives $\Delta\mu_A = 0$ and $\Delta\mu_B < 0$, as expected in equilibrium with elemental A. Similarly, $AB$ in equilibrium with $B$ (Figure 1.2c) gives $\Delta\mu_B = 0$ and $\Delta\mu_A < 0$. A compound $AB$ that is not in established equilibrium with either $A$ or $B$ (Figure 1.2b) will have both $\Delta\mu_A < 0, \Delta\mu_B < 0$.

Visualizing chemical potentials in the frequently used chemical potential space requires only the information from the convex-hull $y$-intercepts. In a typical binary chemical potential diagram, the $x$- and $y$-axes represent $\Delta\mu$ for each element (see right column of Figure 1.2). For the $A - B$ system with stable phases $AB$, $A$, and $B$, the two possible phase equilibria for $AB$ are with elemental $A$ ($\Delta\mu_A = 0$) or $B$ ($\Delta\mu_B = 0$). Applying the common-tangent approach to the convex-hull, as described above, allows one to plot

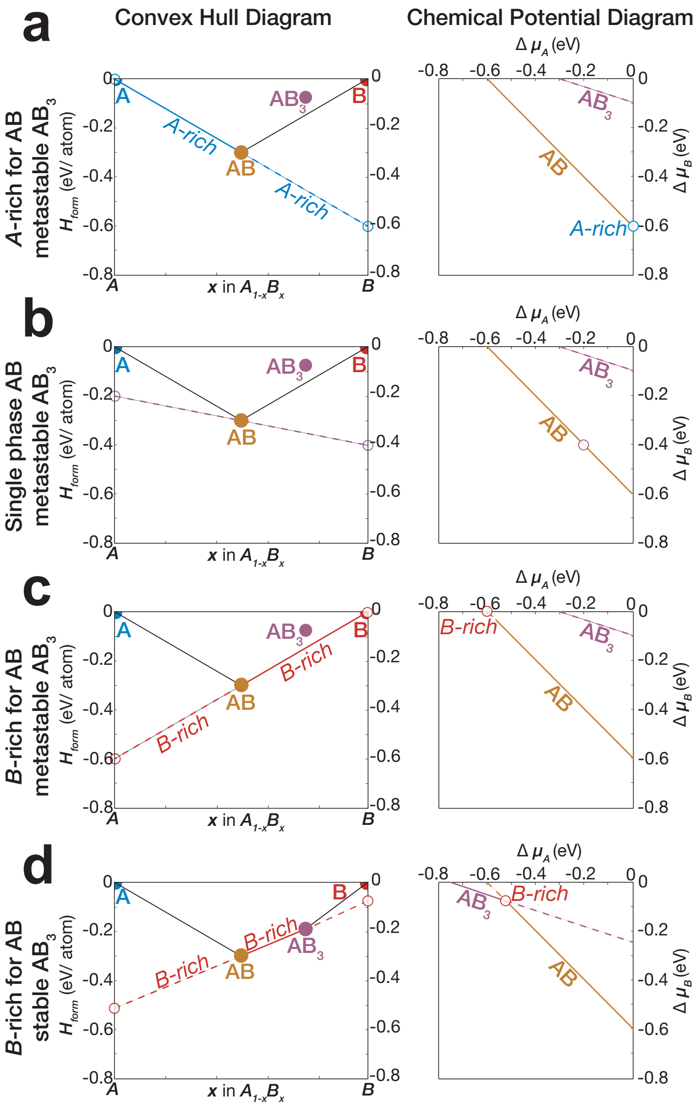

Figure 1.2: **Going from the convex-hull to chemical potential space representation of thermodynamic stability.** (a-c) A convex-hull construction for the hypothetical $A - B$ binary system (left column) with stable phases $A$, $B$, and $AB$ and metastable phase $AB_3$. (a) When phase $AB$ in in equilibrium with $A$ ($\Delta\mu_A = 0$), the change in elemental chemical potentials, $\Delta\mu_A$ and $\Delta\mu_B$, are directly read from the $y$ intercepts of the line connecting $AB$ and $B$ and plotted in chemical potential space (right column). (b) Shifting equilibrium from $AB$ and $A$ diverts $\Delta\mu_A$ and $\Delta\mu_B$ from their extrema until reaching equilibrium between $AB$ and $B$ (c), where $\Delta\mu_B = 0$. The line connecting every chemical potential between the two equilibria captures the entire range of accessible chemical potentials for $AB$. (d) When phase $AB_3$ become stable, the line representing its chemical potentials falls below that of phase $AB$ in chemical potential space. Phase equilibrium between $AB$ and $B$ is no longer possible, and is replaced by equilibrium between $AB$ and $AB_3$, reducing the range of $\Delta\mu_B$ accessible.

$\Delta\mu_A$ and $\Delta\mu_B$ for any composition constrained by available phase equilibria. In chemical potential space, a line drawn through the results encompasses all accessible chemical potentials for the $AB$ phase. A similar plot can be made for metastable $AB_3$. However, the magnitudes of $\Delta\mu_B$ and $\Delta\mu_A$ will be lower than those for compound $AB$ across the entire composition range, indicating less favorable energetics for formation (Figure 1.2(a-c)). Only phases with the lowest-lying lines in chemical potential space are stable. Additionally, the slope of a line drawn in chemical potential space represents stoichiometry. In the example provided, the slope for phases $AB$ and $AB_3$ are -1 and -1/4, respectively.

As additional phases "break" the convex-hull and become stable, they can reduce the range of accessible chemical potentials for other phases in the system. Following the example of Figure 1.2, when a phase $AB_3$ becomes stable (Figure 1.2 d), the $B$-rich equilibrium for phase $AB$ is no longer between $AB$ and $B$ - but rather between $AB$ and $AB_3$. Correspondingly, the line representing $AB_3$ in chemical potential space (right column of Figure 1.2 d) drops below that of $AB$, signifying that the $AB$ phase is no longer stable at certain compositions. As a result, the lowest magnitude of $\Delta\mu_B$ in $AB$ must be some finite value greater than 0.

### 1.1.4 Defect Energy

Consider, for example, the following defect reaction involving formation of an $A$-vacancy from the bulk of a model binary compound $AB$

$$AB \rightarrow A_{1-\delta}B + \delta\, A \tag{1.2}$$

the composition of the $AB$ phase changes slightly ($\delta$) and the atom removed from $AB$ gets placed in the elemental phase $A$. The molar enthalpy for such a defect reaction ($\Delta H_D$) is given by

$$\Delta H_D = H(A_{1-\delta}B) + \delta\, H(A) - H(AB) \tag{1.3}$$

where $H(A)$, $H(AB)$ and $H(A_{1-\delta}B)$ are the molar enthalpies of $A$, $AB$ and the defective structure. It is important to note that in addition to the enthalpy associated with the host structure [$H(AB)$] and defect structure [$H(A_{1-\delta}B)$], the defect formation enthalpy $\Delta H_D$ also depends on the enthalpy of the phase where the atom ends up [$H(A)$]. So $\Delta H_D$ in $AB$ could in principle be evaluated for any combination of phases ($AB$-$A$, $AB$-$AB_3$, etc.). However, $\Delta H_D$ is well-defined only if the phases are in thermodynamic equilibrium; i.e. the phases involved constantly exchange atoms with each other without spontaneously forming reaction product phases. The phase $AB$ can be in equilibrium with a relatively $A$-poor phase (i.e. $AB_3$, $B$) and a relatively $A$-rich phase (i.e. $A_3B$, $A$) in the $A - B$ binary system. So depending on which equilibrium $AB$ is participating in, $H(A)$ in equation 1.3 can be substituted by the enthalpy of another phase in the binary system. Consequently, $\Delta H_D$ can take different values based on the choice of chemical equilibrium conditions. The multiple values of $\Delta H_D$ is in stark contrast to intrinsic defects in elemental solids or even Schottkey and Frenkel defects in ionic solids (see Methods section). Even the simple binary compounds can participate in more than two equilibria if a multicomponent composition space (ternary (for example Na doping in PbTe), quaternary, pentenary etc.) is considered, making the problem significantly more complicated.

Since the defect formation enthalpy is defined on a per-defect basis in the dilute limit where lim $\delta \rightarrow 0$, we re-write the equation 1.3 for a single vacancy defect ($\Delta H_{def}$) by replacing $H(A)$ with the chemical potential of the atom $A$ ($\mu_A$) and write it as

$$\Delta H_{def} = E_{defect} - E_{pristine} + \mu_A \tag{1.4}$$

where the first term $E_{defect}$ - $E_{pristine}$ is the difference in energy between the defective and pristine (defect-free) structures. More generally, $\Delta H_{def}$ for all types of point defects (interstitials, vacancies and antisites) can be written as:

$$\Delta H_{def} = E_{defect} - E_{pristine} - \sum \Delta N_i \mu_i \tag{1.5}$$

where $\Delta N_i$ is the number of atoms of species $i$ added to or removed from the defective structure (+1 for interstitials, -1 for vacancies and for antisites +1 and -1 for the atomic species added and the atom species missing respectively) and $\mu_i$ is the chemical potential of the species $i$.

## 1.2 Thermoelectric Properties

Thermoelectric devices can directly convert waste heat into useful electricity, attracting considerable attention as a means to harvest the energy that is currently lost by dissipation. [25, 26] While the performance of a thermoelectric device — like any thermodynamic system — will be limited by its Carnot efficiency ($\Delta T/T$), this factor needs to be multiplied by an additional *irreversibility factor* determined by electrical and thermal materials properties. Since these properties are temperature dependent, the irreversibility factor can be expressed in terms of a well defined materials property $zT$, known as the thermoelectric figure of merit, only for a differential efficiency in the limit $\Delta T \rightarrow 0$. In terms of Seebeck coeffient $S$, electrical conductivity $\sigma$, lattice thermal conductivity $\kappa_{lat}$ and the electrical contribution $\kappa_{el}$ to the total thermal conductivity ($\kappa$), $zT$ can be expressed as

$$zT = \frac{S^2\ \sigma}{\kappa_{lat} + \kappa_{el}} T \tag{1.6}$$

Typical high performing thermoelectrics are degenerately doped semiconductors with the optimized material often requiring charge carrier concentrations ($n$) in excess of $10^{19}$ cm$^{-3}$. In principle, *all* materials properties in the expression for $zT$ depend on $n$. The dependency of $S$, $\sigma$, $L$ (Lorentz number) and $K_{el}$ are discussed in detail Ref. [25, 27, 28, 29]. The $\kappa_{lat}$ dependency on carrier concentrations, although not very well studied, arises from electron-scattering [30] and phonon renormalization effects [31] and become substantial at higher doping levels.

Following from equation 1.6, the strategies exercised to increase $zT$ chemically either target improving the electrical contribution — given by the electrical power factor in the numerator $S^2\ \sigma$ — or reducing the $K_L$. The main avenues to a achieve small $K_L$ include various scattering mechanisms for phonons [32, 33, 34] and more recently lattice softening strategies [35, 31]. Scattering of phonons due to changes in composition of a single phase material is understood using point-defect scattering models discussed at length in the Ref. [36, 37].

Electrical transport of a single-phase material with a single parabolic band (SPB) contributing to transport is often characterized by the weighted mobility $\mu_w$ [38] which can be expressed as

$$\mu_w = \mu_o\ \left(\frac{m_s^*}{m_e}\right)^{3/2} \tag{1.7}$$

where $\mu_o$ is the mobility parameter and $m_s^*$ is the Seebeck effective mass. While the mobility parameter $\mu_o$ — which is directly proportional to $\sigma$ — characterizes only the electrical conductivity, the weighted mobility $\mu_w$ (depending to the scattering mechanism for carriers considered) can be used to predict the magnitude of $\sigma$ for a given value of $S$. The $S$-$\sigma$ relation for materials with different $\mu_w$ values are calculated using acoustic-phonon-scattering SPB models in Figure 1.3. Larger $\mu_w$ values in the model offset the curves to higher $S$ and $\sigma$ values (see Figure 1.3). For the sake of comparison constant power factor lines have also been shown next to the curve. Although $\mu_w$ does not automatically mean

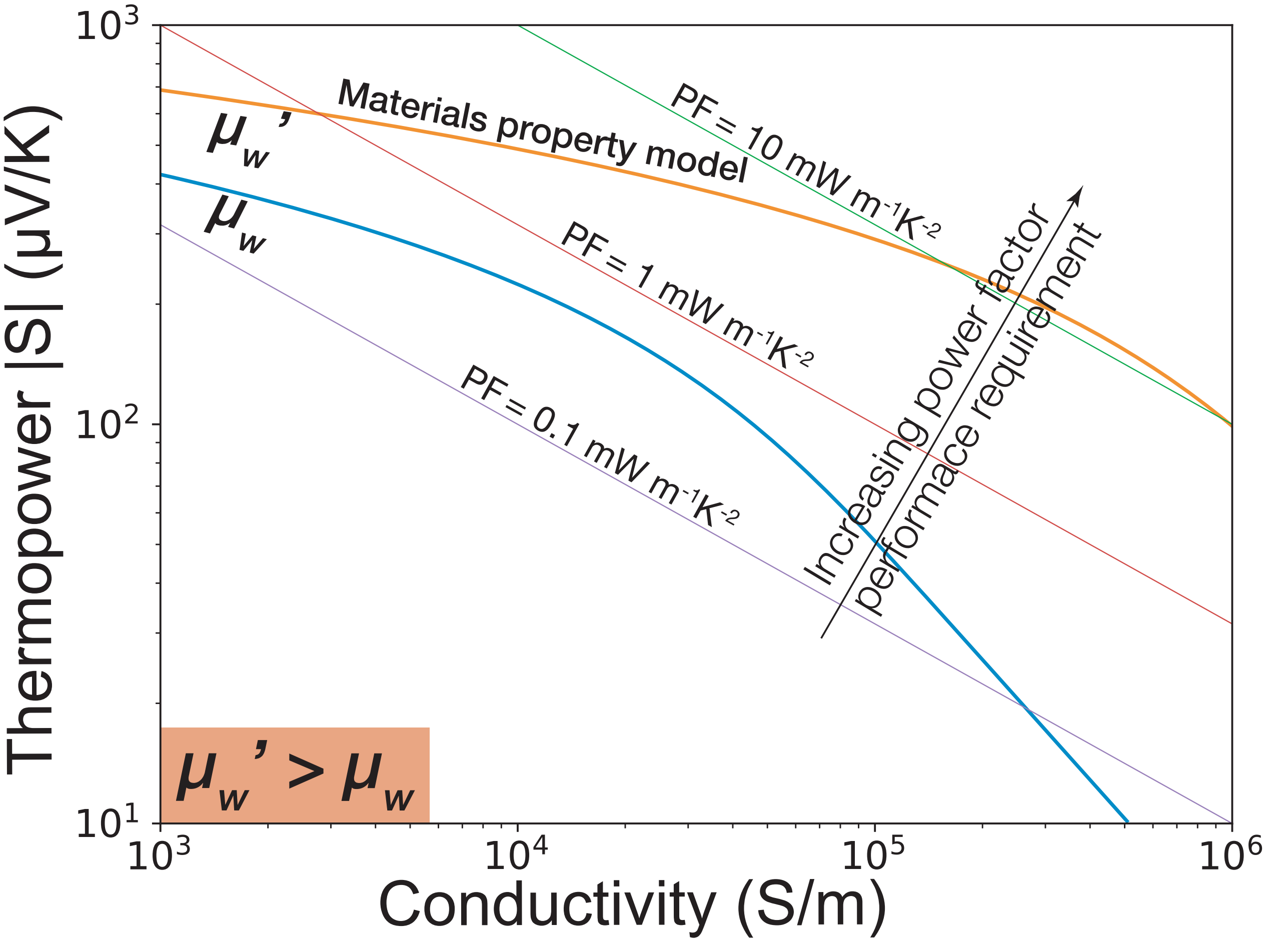

Figure 1.3: **Weighted Mobility for characterizing the electrical performace of thermoelectric materials.**Calculated Thermopower (|S|)-Conductivity ($\sigma$) relations (curves) using the single parabolic band (SPB) model with acoustic phonon scattering at two different values of weighted mobility ($\mu_w$). Multiple lines with constant power-factor values are plotted for a qualitative reference of device requirement for thermoelectric material.

a larger electrical power factor, it does mean a larger *optimized* power factor value. This optimized power factor value can be determined from the point at which the constant power factor line forms a tangent with the $S$-$\sigma$ curve. The plot connecting the optimized power-factor to $\mu_w$ in acoustic-phonon-scattering models is shown in the Figure 1.4. The optimized power factors within the single parabolic band model — with acoustic phonon scattering — occurs at $\sim$ 167 $\mu$V/ K. The Seebeck value only depends on the position of the Fermi-level with respect to the band-edge[29] and a value of $\sim$ 167 $\mu$V/ K corresponds to a Fermi-level position slightly inside the position (degenerately doped semiconductor). Another metric quite similar to the weighted mobility, known as the electronic quality factor, has been discussed recently in Ref. [39].

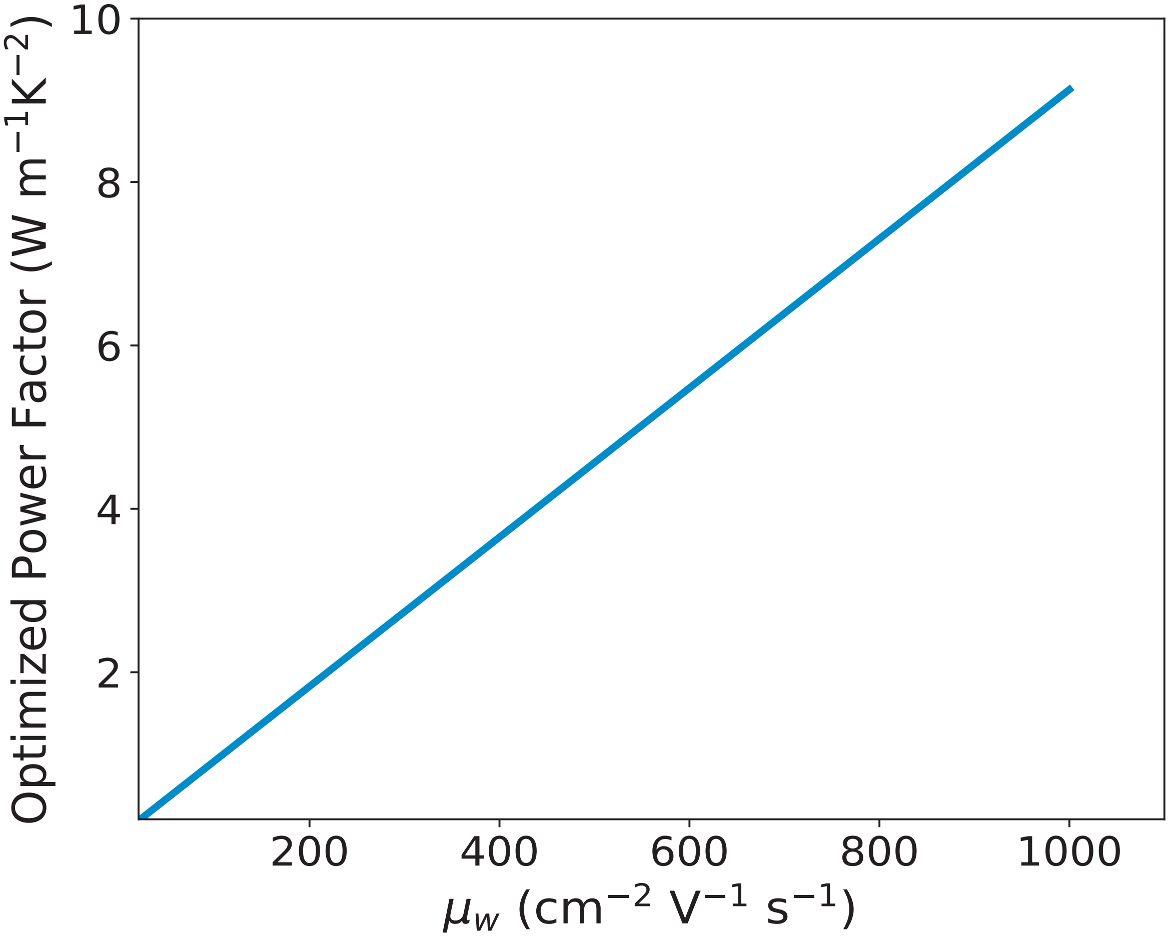

Figure 1.4: **Predicting maximum power factor with weighted mobility.** Optimized power factor value calculated using the single parabolic band (SPB) model under the acoustic phonon scattering assumption; plotted as a function of the weighted mobility value.

# Chapter 2

# Methodology

## 2.1 Density Functional Theory

Density functional theory (DFT) is based on two fundamental theorems by Hohenberg and Kohn. The first theorem states that 'the external potential V($\boldsymbol{r}$) is (to within a constant) a unique functional of $\rho(\boldsymbol{r})$; since, in turn V($\boldsymbol{r}$) fixes $\hat{\boldsymbol{H}}$ (the Hamiltonian operator) we see that the full many particle ground state is a unique functional of $\rho(\boldsymbol{r})$'. [40] Put differently, this means that the electron density uniquely determines the Hamilton operator and thus all properties of the system. The second theorem states that 'the functional that gives the ground state energy of the system, gives the lowest energy if and only if the input $\rho(\boldsymbol{r})$ is the true ground state density, $\rho_0$.' , reducing the $3N$-dimensional problem to $N$ dimensional. Kohn and Sham showed that a major part of the kinetic energy can be calculated to good accuracy (a problem with other methods using the direct density functional such as the Thomas-Fermi method [41]) by a set of non-interacting single-electron functions. These single electron 'orbitals' can replace the Schrodinger equation in systems of interacting nuclei and electrons that describes to find the ground state energy. [42] In the general form of the Kohn-Sham equations

$$\left[-\frac{\hbar^2}{2m_e}\nabla^2 + V(\boldsymbol{r}) + e^2\int\frac{n(\boldsymbol{r'})}{|\boldsymbol{r'}-\boldsymbol{r}|}d\boldsymbol{r'} + V_{xc}(\boldsymbol{r})\right]\psi_i(\boldsymbol{r}) = \epsilon_i\psi_i(\boldsymbol{r}) \tag{2.1}$$

where the first term is the kinetic energy term, the potential $V$ is the interaction between the electron and the atomic nuclei in the system, the third potential describes Coulombic interactions between the electron and electron density of all electrons in the system, and the fourth term $V_{xc}$ is the exchange-correlation potential.

The density functional theory (DFT) calculations [43] in this study were performed using Vienna ab-initio simulation package (VASP). [44, 45] We have used PerdewBurke Ernzerhof (PBE) formulation of the exchange correlation energy functional derived under a gradient-generalized approximation (GGA). [46] Generally, the plane-wave basis sets were truncated at a constant energy cutoff of > 1.3 $\times$ ENMAX were used, as were $\Gamma$-centered $k$-point meshes with a density of $\sim$ 8000 $k$-points per reciprocal atom (KPPRA). All structures were relaxed with respect to cell vectors and their internal degrees of freedom until forces on all atoms were less than 0.1 eV/nm. The lowest energy structures for defective structures in multiple systems were determined by comparing DFT energies of multiple structures at the valence balanced composition generated by the enumlib code [47, 48] was used to predict High-throughput predictions for thermodynamic stability were done using the Open Quantum Materials Database [9, 8].

The GGA+U calculations for $VFe_2Al$ in Chapter 9 were performed using U = 0.5 eV and U = 1.35 eV for $d$-states of V and Fe atoms respectively. These values were determined by proportionally scaling down the U values obtained by Do et al. [49] for $VFe_2Al$ using constrained DFT calculations ($U_{Fe}$ = 4 eV, $U_V$ = 1.5 eV). The $k$-resolved Crystal Orbital Hamilton Populations (COHPs) calculations were performed using the version 3.2.0 of the LOBSTER software.[50, 51, 52] The atom-projected electronic structure in Chapter 9 and **??** was plotted using PYMATGEN.[53] A separate code was written for plotting the orbital-projected electronic structure plotting in Chapter **??**.

## 2.2 Prediction of thermodynamic stability. Convex Hull Construction

The thermodynamic stability of a phase is determined by constructing the so-called convex hull of formation energies of all phases in the respective composition space. By definition, every phase that lies on the convex hull is thermodynamically stable, i.e., it has a formation energy lower than any other phase or linear combination of phases at its composition. By extension, all other phases that do not lie on the convex hull are metastable or unstable, i.e., there exists a phase or mixture of phases lower in energy at that composition.

Figure 1.2 depicts a the convex hull construction for a model binary system A-B. The formation enthalpies ($\Delta H_f$) of the compounds are calculated relative to the elemental chemical potentials of the components A ($\mu_A$) and B ($\mu_B$), which are simply the DFT-calculated total energies of the elements in their lowest energy bulk structures.

$$\Delta H_f = E_{compound} - \sum_{i=1}^{2} c_i \mu_i \tag{2.2}$$

where $E_{compound}$ is the DFT total energy of the compound of interest. Negative values of $DeltaH_f$ (Figure 1.2) for all the three structures considered ($A_3B$, $AB$ and $AB_3$) indicate their stability with respect to the elements $A$ and $B$. The convex hull connects phases that are lower in energy than any other phase or linear combination of phases at that overall composition. So, only the phase at AB is truly thermodynamically stable. Phases $A_3B$ and $AB_3$ are unstable with respect to $A - AB$ and $AB - B$ mixture of phases (by visual inspection, we see that the energy of $A_3B$ ($AB_3$) is higher than the phase mixture of $A - AB$ ($AB - B$) at the corresponding composition). For the phase stability analysis in Section 3, we consider all known and hypothetical phases in each composition space from the Open Quantum Materials Database (OQMD).[8, 9]

Further, the convex hull construction can be used to estimate the extent of thermodynamic stability (or instability) of a given phase. For this, we construct an additional convex hull in the composition space after *excluding the phase of interest* and determine the lowest-energy mixture of phases at that composition. So for the phase $AB$ (see Figure 2.1) for example, the convex hull excluding it is given by the dashed black lines in Figure 2.1. The lowest-energy decomposition products at the composition $AB$ is $A_3B - AB_3$. The difference between the $\Delta H_f$ of the phase ($AB$) and the lowest-energy mixture of phases from the second convex hull construction (see Figure 2.1) quantifies the extent to which the phase is stable (or unstable). In other words, the extent of stability ($E_{stability}$) of a phase is calculated using:

$$\Delta E_{stability} = \Delta H_f - \sum_{i=1}^{3} c_i \Delta\mu_i \qquad (2.3)$$

where $c_i$ is the composition and $\mu_i$ is the chemical potential of the constituent element i, determined by the 2- or 3-phase equilibria from the second convex hull construction excluding the phase of interest. Thus, a negative $E_{stability}$ for a phase implies its overall thermodynamic stability while a positive $E_{stability}$ indicates that other lower-energy mixture of phases exist at that composition.

We would like to emphasize on the subtle difference between $E_{stability}$ and the quantity called as the 'distance to convex-hull' $E_{CH}$ which is calculated only with respect to the convex-hull of lowest $\Delta H_f$ phases (solid line in Figure 2.1). So, by definition, unlike $E_{stability}$, $E_{CH} \geq 0$. When $E_{CH}$ > 0, $E_{stability}$ = $E_{CH}$ and when $E_{CH}$ = 0, $E_{stability} \neq E_{CH}$ (see Figure 2.1).

## 2.3 Cluster Expansion

The cluster expansion (CE) [54, 55, 56, 57, 58, 59, 60] method is a generalized Ising model in which the total energy of an arbitrary atomic configuration $S_i$ can be uniquely determined using a linear combination of basis Functions defined by the product of occupation variables for the lattice sites:

$$E(S_i) = J_0 + \sum_i J_i S_i + \frac{1}{2!}\sum_{i \neq j} J_{ij} S_i S_j + \frac{1}{3!}\sum_{i \neq j \neq k} J_{ijk} S_i S_j S_k + ..., \tag{2.4}$$

in which the coefficients $J_f$ are effective cluster interaction (ECIs) associated with a a cluster of lattice sites ($f$). For a binary alloy $A_x B_{1-x}$, the occupation of site i in this model is labeled by a spin variable $S_i$ = 1 or -1, where the sign depends on the type of atom. The ECI are obtained by fitting the form of Eq. to the energies determined from DFT for a set of ordered structures, each of which is characterized by the spin variables $S_i$. For a converged CE, ECIs tend to decrease rapidly with the number of lattice sites in the expansion; hence Eq. is generally truncated to include only a few smaller-sized clusters. The evaluation of the predictive power of a CE is evaluated using the cross-validation (CV) score, defined as:

$$(CV)^2 = \frac{1}{n}\sum_{i=1}^{n}(F_i^{direct} - F_i^{CE})^2 \tag{2.5}$$

where $F_i$ direct is directly calculated using DFT and $F_i^{CE}$ is predicted from a CE with ECIs obtained from a least-squares fit to energies of the ($n$-1) other structures. A converged set of effective cluster interactions (ECIs) thus obtained enable the prediction of the energies of structures across a wide range of composition. All CEs reported in this work were performed using the Alloy Theoretic Automated Toolkit (ATAT) [61, 62, 63].

## 2.4 Two-band Model for $VFe_2Al$ electrical transport

Utilizing experimental datasets from the literature, we parameterize an analytical band transport model to understand the electrical properties of $VFe_2Al$. Evidence of bipolar transport near room temperature and at carrier concentrations less than $\sim 10^{21}$cm$^{-3}$, suggests the necessity of a two-band model capturing majority and minority carrier transport. Here, we assume carrier lifetime to be limited by acoustic phonon scattering. We first build separate effective mass models for $T$ = 300K transport of the conduction and valence bands, using only samples in the single-band transport regime (entered by nominally doping the compound in excess of $\sim$$10^{21}$ cm$^{-3}$ carriers). Therefore, only samples in the regime of linearly increasing $|S|$ response to temperature were chosen

To build the transport models, data was collected from a variety of $n$-type (Co[15],Si [16, 17, 19], Ge[18], Sn[19], Mo[20], Pt[21], W[21]) and $p$-type (Ti[20], Zr[21], Re[22]) dopants used in previous thermoelectric studies. The weighted mobility— a carrier mobility parameter weighted by the density of states effective mass — is determined from thermopower (|S|)-conductivity ($\sigma$) relation. The weighted mobility is directly related to the thermoelectric power factor at a given doping level ($\eta = E_{\mathrm{f}}/k_{\mathrm{B}}T$) and temperature. Moreover, the influence of dopants on carrier mobility through effects such as alloy scattering is easy to assess via the weighted mobility. We also determine the Seebeck effective mass, $m_{\mathrm{s}}{}^*$, which relates to the density-of-states at the Fermi level, from the $|S|$ versus carrier concentration ($n$) relation. These $|S|$-$\sigma$-$n$ relations are detailed below through their mutual dependence on doping level $\eta$[29]. The Fermi integrals are denoted as: $F_j$, where

$j$ represents the order.

$$\begin{aligned}
\sigma &= \frac{8\pi e(2m_{\mathrm{e}}k_{\mathrm{B}}T)^{3/2}}{3h^3}\mu_{\mathrm{W}}\, F_0 \\
S &= \frac{k_{\mathrm{B}}}{e}(\frac{2F_1}{F_0} - \eta) \\
n &= 4\pi(\frac{2m_{\mathrm{s}}{}^{*}k_{\mathrm{B}}T}{h^2})^{3/2}F_{1/2}
\end{aligned} \tag{2.6}$$

Once the fitted band parameters $\mu_{\mathrm{W}}$ and $m_{\mathrm{S}}{}^{*}$ have been determined for the valence and conduction band, we then build a two-band model in order to fit the band offset ($E_{\mathrm{g}}$) that best describes the full data (i.e. including samples in the bipolar regime). The two band Seebeck and conductivity equations are shown below combining the electron and hole properties. Here, the relationship $\eta_{\mathrm{p}} = -(E_{\mathrm{g}}/(k_{\mathrm{B}}T) + \eta_{\mathrm{n}})$ has been fixed when determining $\sigma_{\mathrm{p}}$, $S_{\mathrm{p}}$, and hole carrier concentration $p$.

$$\sigma = \sigma_{\mathrm{p}} + \sigma_{\mathrm{n}} \qquad\qquad S = \frac{S_{\mathrm{p}}\sigma_{\mathrm{p}} + S_{\mathrm{n}}\sigma_{\mathrm{n}}}{\sigma_{\mathrm{p}} + \sigma_{\mathrm{n}}} \tag{2.7}$$

## 2.5 Double half-Heusler lattice thermal conductivity ($\kappa_L$) calculations

Lattice thermal conductivity ($\kappa_L$) calculations were performed within the framework of anharmonic lattice dynamics and Boltzmann transport equation, assuming that three-phonon interactions and isotope scattering dominate the total phonon scattering rates. To overcome the formidable computational cost in evaluating third-order interatomic force constants (IFCs), we employed the recently developed compressive sensing lattice dynamics (CSLD) method [64, 65] to efficiently extract both harmonic and anharmonic IFCs, the accuracy of which is further verified by comparing to the third-order IFCs obtained by finite displacement method.[66, 67] Afterwards, ShengBTE package[67] was employed to numerically solve the BTE under relaxation time approximation (RTA). The convergence of the calculated $\kappa_L$ was carefully examined with respect to the diameter cutoff of the third-order anharmonic IFCs and the grid of sampled phonon wavevector. We find that the diameter cutoffs of 5.0 Å and 4.5 Å for respectively half-Heusler and Double half-Heusler were sufficient to yield $\kappa_L$ with good convergence.

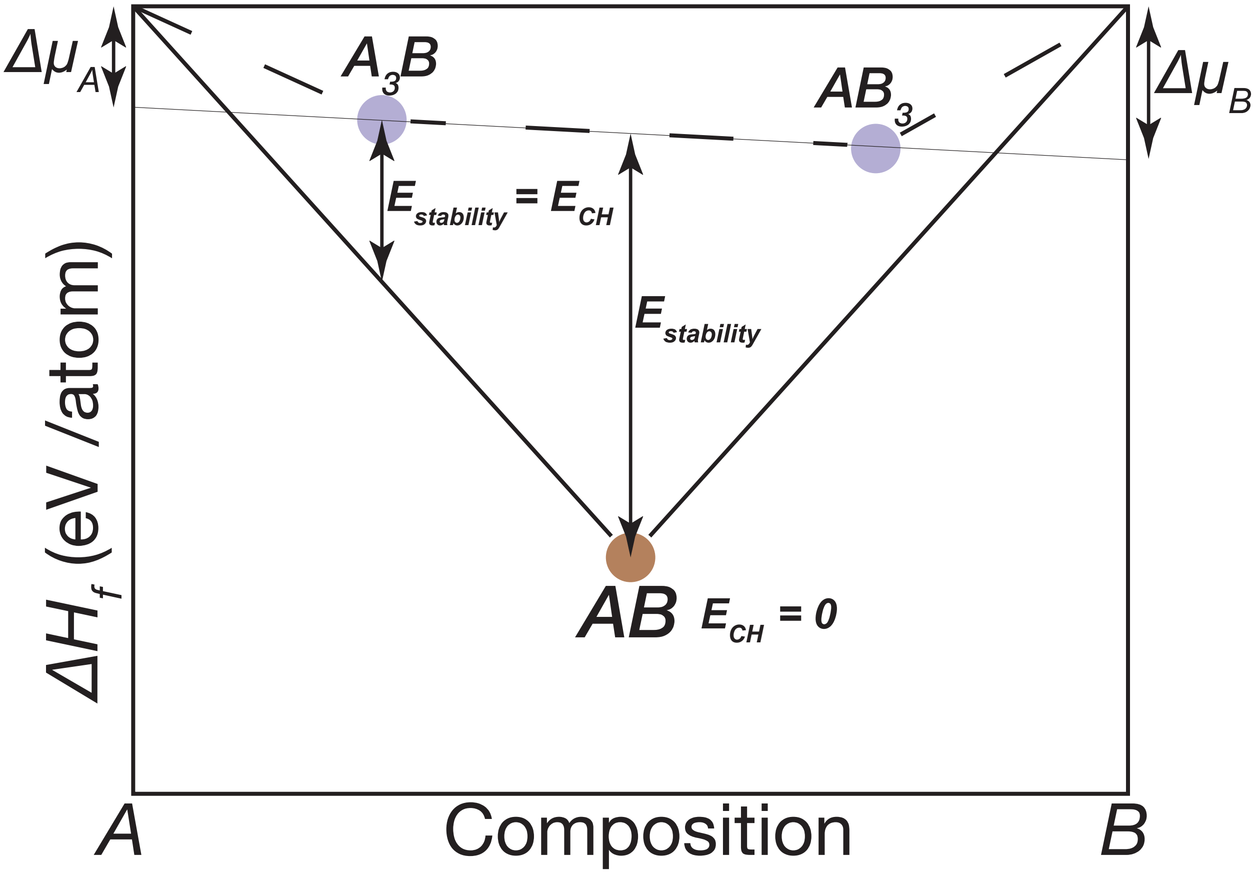
$\Delta\mu_A$
$A_3B$
$AB_3$
$\Delta\mu_B$
$E_{stability} = E_{CH}$
$E_{stability}$
$\Delta H_f$ (eV /atom)
AB
$E_{CH} = 0$
A
Composition
B

Figure 2.1: (a) **Differentiating $E_{stability}$ from $E_{CH}$ in a model binary convex hull.** Formation enthalpy ($\Delta H_f$) of the structures with the compositions $A_3B$, $AB$, $AB_3$ with respect to lowest energy elemental phases A ($\mu_A$) and B ($\mu_B$). The convex hull of the $A-B$ binary phase space is given by the solid line. $E_{stability}$ of $AB$ is calculated by constructing a convex hull of all other phases (dashed line), and using the constant elemental chemical potentials ($\mu_A$ + $\Delta\mu_A$ and $\mu_B$ + $\Delta\mu_B$) associated with the metastable equilibrium $A_3B$-$AB_3$. The convex-hull distance is the energy distance with respect to the lowest energy convex-hull (which contains only the thermodynamically stable phases). When $E_{CH}$ > 0, $E_{stability}$ = $E_{CH}$ and when $E_{CH}$ = 0, $E_{stability} \neq E_{CH}$.

# Chapter 3

# Visualizing Defect Energetics

## 3.1 Overview

The key to chemically controlling transport properties through defect engineering lies in understanding the stability of (a) the defect and (b) the compound itself relative to competing phases at other compositions in the system. The stability of a compound is already widely understood in the community using intuitive diagrams of formation enthalpy ($\Delta H_f$) vs. composition, in which the stable phases form the 'convex-hull'. In this work, we re-write the expression of defect formation enthalpy ($\Delta H_{def}$) in terms of the $\Delta H_f$ of the compound and its defective structure. We show that $\Delta H_{def}$ for a point defect can be simply visualized as intercepts in a two-dimensional convex-hull plot *regardless* of the number of components in the system and choice of chemical conditions. By plotting $\Delta H_f$ of the compound and its defects all together, this visualization scheme directly links defect energetics to the compositional phase stability of the compound.

## 3.2 Context and Motivation

Introductory textbooks in materials science often tabulate values of defect formation enthalpy ($\Delta H_{def}$) of intrinsic defects in crystalline solids. These tables typically compare $\Delta H_{def}$ for intrinsic defects in elemental metals, such as Ti, Co, Ni, W, etc. Other common examples involve comparisons of intrinsic Schottky and Frenkel defects in ionic compounds such as NaCl, KCl, AgCl, $CaF_2$, etc. In each of these cases, the defect does not alter the overall composition of the structure, and stability of the defect is determined with respect to the pristine host structure. Hence, $\Delta H_{def}$ for all such defect types takes a single value at given temperature and pressure allowing for a simple comparison and understanding of defects.

In contrast, the defect energetics of most other important point defects in crystalline compounds such as interstitials, vacancies and anti-sites is significantly more complicated. For compounds with two or more elements, even these simple defects will alter the overall composition. Hence, the stability of the defect must be assessed with respect to stable phases lying at other compositions in the system, instead of just the pristine host structure of the compound. For example, when NaCl is saturated with a Cl atmosphere, the stability of a Na-vacancy defect is determined with respect to NaCl and $Cl_2$ gas. When NaCl is saturated with elemental Na on the other hand, stability of the same defect is determined NaCl and metallic Na. As a result, unlike a Schottky defect in NaCl, the stability of the Na-vacancy defect can vary depending on the chemical equilibrium conditions. Hence, $\Delta H_{def}$ of simple point defects in crystalline compounds can take at least two values of defect energies which are ‘chemically controllable’.

The dependence of defect energetics on phase equilibrium allows for chemical control of any properties that are affected by point defects. In semiconductor compounds, for example, intrinsic charged defects set a thermodynamic limit on the number of charge carriers, or dopability, in the system. [68, 69] Changing chemical equilibrium conditions to tune

$\Delta H_{def}$ of intrinsic defects can offset this limit to allow more carriers in the semiconductor, thereby opening a wider range of electronic properties. For instance, in state-of-the-art $n$-type thermoelectrics PbTe and $Mg_3Sb_2$, electron dopability is barely possible unless the compounds are synthesized under cation-rich chemical conditions. [70, 2] Point defects also impact electrical, [71, 72] thermal, [13, 73] and ionic [74, 75, 76, 77, 78] transport significantly, making them important in studies for a variety of applications such as batteries, [79, 80, 81, 82] photovoltaics, [83, 84] thermoelectrics, [4, 85, 86, 87] thermochemical water splitting, [88, 89] solid oxide fuel cells, [90, 91] and transparent conducting oxides. [92] In view of the fact that practically all materials research focuses on properties impacted by simple defects in some way, understanding defect energetics within a thermodynamic framework which is widely used by the community will be very beneficial.

Formation enthalpies ($\Delta H_f$) are the most commonly used thermochemical quantity for composition dependent stability analysis. Given the $\Delta H_f$ for all possible phases in a system, plotting them in composition space is sufficient to distinguish the stable phases from the unstable ones. These plots, also known as convex-hulls, are commonly used to introduce the subject of thermodynamic stability through the common tangent construction. As a result, convex-hulls are widely used by the scientific community for reading stability prediction of compounds presented in high-throughput databases such as OQMD, [9, 8] Materials Project, [93] and the AFLOW library, [94] and for performing stability analysis using CALPHAD assessments. [95, 96]

In this work, we demonstrate that one can graphically solve for $\Delta H_{def}$ of simple point defects within the convex-hull construction itself. The $\Delta H_{def}$ of a defect involving the atom $A$ ($A$-vacancy and $A$-interstitial), for example, can be simply visualized as intercepts on the elemental $A$ axis of the convex-hull diagram. Since these elemental axes in the convex-hull diagrams represent the atomic chemical potential scale, one can visualize $\Delta H_{def}$ *regardless* of the chemical conditions considered. Hence, our visualization scheme takes into account the stability of both the defect and the compound in $\Delta H_{def}$ calculations. Furthermore, we also show that the graphical solution of $\Delta H_{def}$ for any complex multicomponent (ternaries, quaternaries etc.) compound can be visualized in simple two-dimensional plots without any loss of information. Since our approach simplifies application level defect thermodynamics using basic materials thermodynamics knowledge, we expect it to be a useful pedagogical tool for a wide community.

## 3.3 Results and Discussion

### 3.3.1 Graphical representation of point defect energies in convex-hulls

To visualize the defect formation energy, $\Delta H_{def}$, within the convex hull construction (see Figure 3.1), we re-write equation 1.5 in terms of the formation energies $\Delta H_f$ of the defective and pristine structures and simplify the expression (see Appendix A). In this new form of the expression, all $\Delta H_f$ terms necessary to determine $\Delta H_{def}$ can be read directly from the convex-hull diagram (Figure 3.1). Full derivations for each defect type in the general cases of a model binary compound $A_pB_q$ and a ternary compound $A_pB_qC_r$ are given in the Appendix A.

Figure 3.1 shows example sketches of various simple point defect types (interstitials, vacancies and antisites) in the compound $AB$. The $\Delta H_f$ of the defective structures are drawn such that they lie above the convex-hull, signifying metastability at $T = 0$ K. Note that, depending on how each defect type changes the stoichiometry of the compound, $\Delta H_f$ of the defective structures are either shown (Figure 3.1) at the percentage compositions $x <$ 0.5 ($A$-interstitials) or $x >$ 0.5 ($A$-vacancies, $B_A$ anti-sites). Structures with larger defect concentrations lie further away from the x = 0.5 composition. We draw two columns for each panel in Figure 3.1 indicating the chemical potentials (see unfilled circles) in $A$-rich and $B$-rich equilibrium conditions.

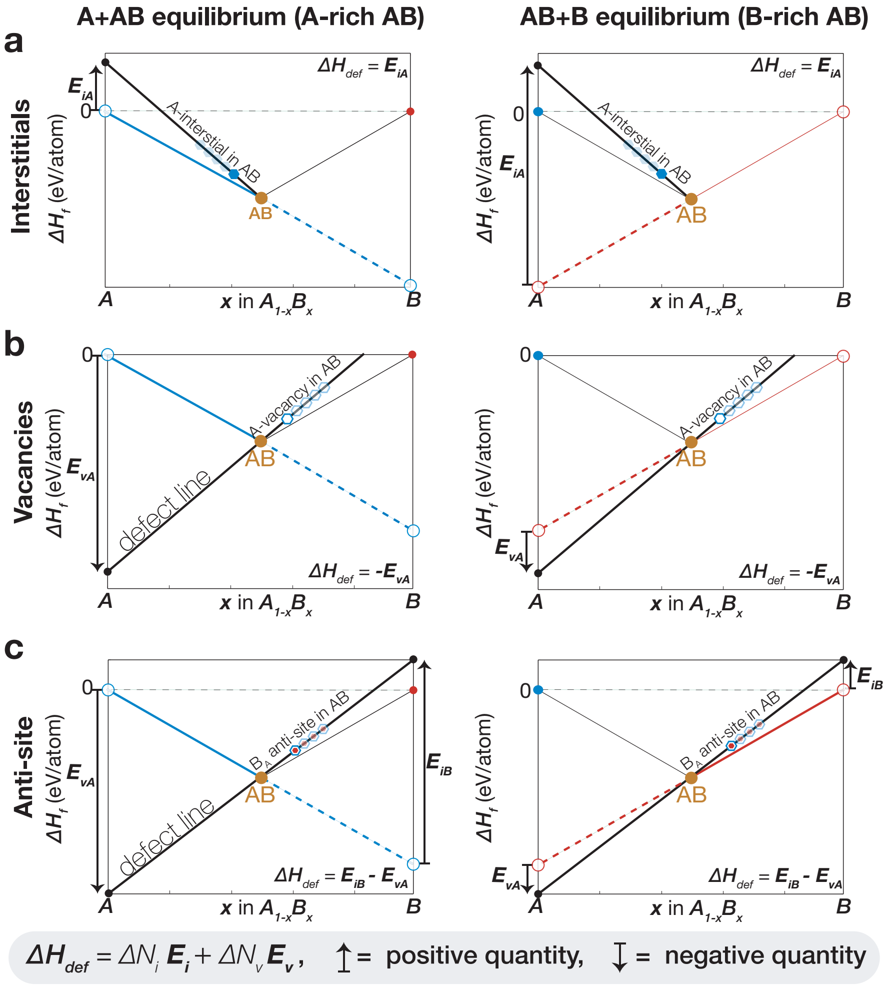
A+AB equilibrium (A-rich AB)
AB+B equilibrium (B-rich AB)
a
Interstitials
$\Delta H_f$ (eV/atom)
$\Delta H_{def} = E_{iA}$
$E_{iA}$
0
A-interstitial in AB
AB
A
x in $A_{1-x}B_x$
B
b
Vacancies
$E_{vA}$
A-vacancy in AB
defect line
$\Delta H_{def} = -E_{vA}$
c
Anti-site
$B_A$ anti-site in AB
$E_{iB}$
$\Delta H_{def} = E_{iB} - E_{vA}$
$\Delta H_{def} = \Delta N_i\, E_i + \Delta N_v\, E_v$, ↥ = positive quantity, ↧ = negative quantity

Figure 3.1: **Visualizing defect energetics on a convex-hull.** (a-c) Graphical solutions for defect energy $\Delta H_{def}$ of (a) A interstitial, (b) A vacancy, and (c) $B_A$ antisite defects in the binary compound $AB$. Formation energy ($\Delta H_f$) of the defect-free $AB$ structure is given by the orange circle. $\Delta H_f$ of defective $AB$ structures are shown as filled hexagons for interstitials (a), empty hexagons for vacancy defects (b), or a combination for anti-sites (c). Defective structures with the same value of $\Delta H_{def}$ are shown by translucent symbols and fall on the 'defect line' (solid black line). The left and right columns correspond to $A$-rich and $B$-rich equilibrium, respectively. The chemical potentials of $A$ and $B$ corresponding to these equilibrium conditions (large, empty circles) are determined from intercepts of the common tangent lines (blue and red lines in the left and right columns respectively). $\Delta H_{def}$ is determined using intercept (for example $E_i$) between the defect line and the common tangent line on the $A$ and $B$-component axis. The sign of these quantities are are given by the direction of the arrows next to them (see grey box). The expression to calculate $\Delta H_{def}$ is given in each panel. The general expression for calculating $\Delta H_{def}$ for all defect types in is given in the grey box at the bottom where $\Delta N_i$ = 0 or 1 and $\Delta N_v$ = 0 or -1 depending on whether the number of atoms of a particular species is added (1), removed (-1) or unchanged (0) in the defect.

To obtain $\Delta H_{def}$ graphically for the example of $A$-interstitials in Figure 3.1a, we simply join the $\Delta H_f$ of the pristine compound and the defective structure with a line. We will call this line as the “defect line" (see thick black line in Figure 3.1 a). We extend the defect line to find the energy where it meets the $A$-component axis (filled black circle at $x$ = 0). We determine $\Delta H_{def}$ by simply subtracting the chosen chemical potential of $A$ from this energy. Based on the geometry of the convex-Hull, we see that $\Delta H_{def}$ for $A$-rich equilibrium is smaller than in the case of $A$-poor equilibrium, as one might expect. In the case of $A$-vacancies, we extend the defect line in the same way to find the energy where it meets the $A$-component axis. To determine the $\Delta H_{def}$ we again subtract the chosen chemical potential of $A$, but this time we change the sign by multiplying by a factor of -1.

Based on the examples of the vacancy and interstitial defects, we learn a couple of rules:

(i) for defects involving the atomic species $i$, we extend the defect line towards the $i$-component axis to find the energy of intersection

(ii) after subtracting the chosen chemical potential of the species $i$, we either multiply by a factor of +1 or -1 depending on whether the atom was added to or removed from the structure to form the defect.

For the example of $B_A$ anti-site defects, which is associated with both $A$ and $B$ atoms, we extend the defect line on either sides to intersect with the $A$ and $B$-component axis. We determine the energy of intersection and subtract the corresponding choice of chemical potential. For the term on the $A$ side, we treat it as a vacancy and multiply by a factor of -1. For the term on the $B$ side, we treat it as an interstitial and multiply by a factor of 1. To obtain the $\Delta H_{def}$ we then add the two terms.

For the sake of our demonstration, we have drawn more defects at larger concentrations using translucent symbols in Figure 3.1. Since all these points fall on the same defect line they have the same value $\Delta H_{def}$, i.e same defect energy per-defect. In first-principles calculations, on the scale of most convex-hull diagrams, the $\Delta H_f$ of the defective structures and the compound often seem to fall on a line (see Figure 3.2). [97, 1] However, $\Delta H_{def}$ is defined in the dilute limit of defect concentration, and it is often shown that evaluation of accurate $\Delta H_{def}$ for point defects requires checking for convergence with respect to defect concentrations. [23, 98] So $\Delta H_{def}$ is obtained using defects closest in composition to the compound as shown by the opaque defect symbols in Figure 3.1.

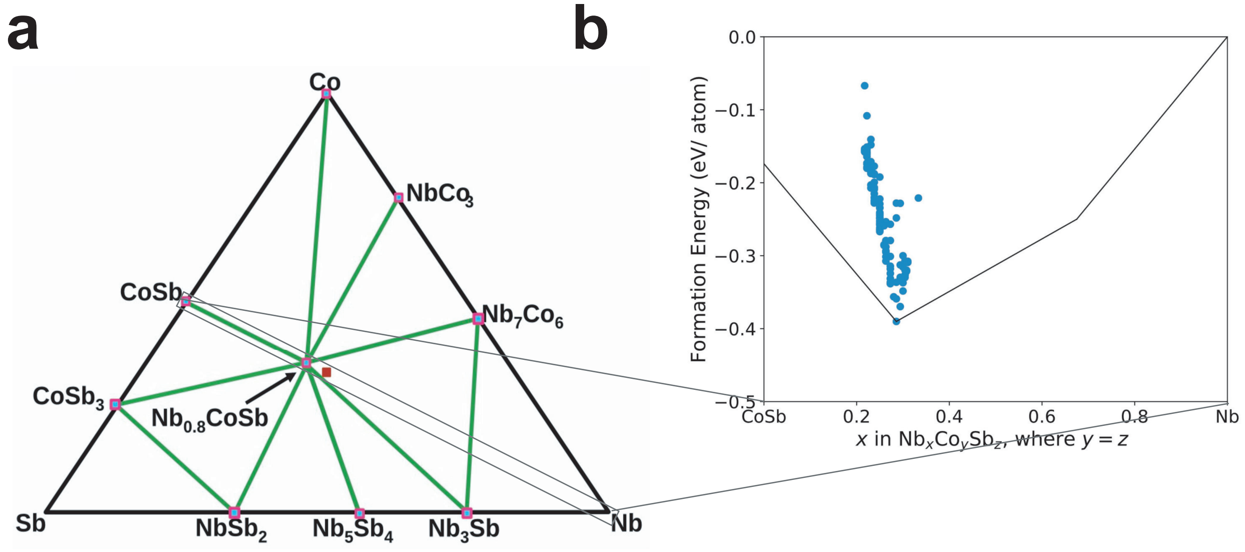

Figure 3.2: **Visualizing Formation Enthalpy ($\Delta H_f$) of defective structures in a ternary convex-hull.** Convex-hull of the Nb-Co-Sb system calculated using [1] DFT. The $\Delta H_f$ of $Nb_{0.8}CoSb$ phase and the defects in it along the 1-dimensional composition slice CoSb-Nb are shown using blue circles in the figure on the right.

Our graphical solution scheme to determine $\Delta H_{def}$ can be easily extended to multi-component systems (ternary, quaternary, etc.) for interstitials (see Figure 3.3 a,b) and vacancies using a pseudobinary construction. Plotting $\Delta H_f$ along the 1-dimensional composition line for these defects will naturally include the pure defect element enabling easy visualization of $\Delta H_{def}$ in the same way as described above. Although, visualization of $\Delta H_{def}$ for anti-site defects is not as straight-forward, it can still be done using a similar $\Delta H_f$ plot along a 1-D composition line joining the defect-free and the defective structures (see Figure 3.3 c,d). We note that even for the more complicated case of ternary compounds, the visualization scheme for all defect types are represented in sim-

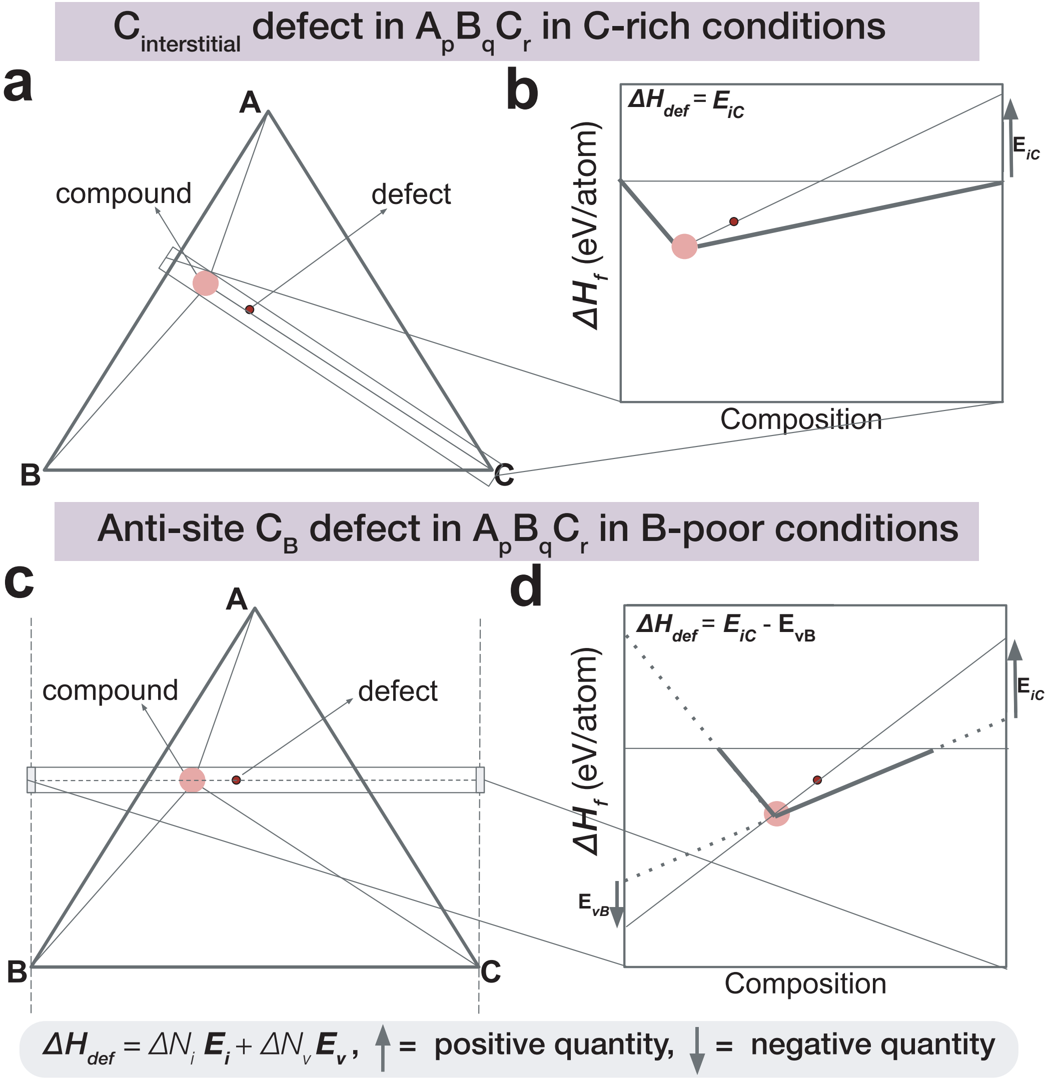
$C_{interstitial}$ defect in $A_pB_qC_r$ in C-rich conditions

Anti-site $C_B$ defect in $A_pB_qC_r$ in B-poor conditions

$\Delta H_{def} = \Delta N_i \boldsymbol{E_i} + \Delta N_v \boldsymbol{E_v}$, ↑ = positive quantity, ↓ = negative quantity

Figure 3.3: **Visualizing defect energetics of a ternary compound in a convex-hull.** Graphical solution for defect energy ($\Delta H_{def}$) of (a-b) C interstitial and (c-d) $C_B$ anti-site defects in the ternary compound $A_pB_qC_r$. The compound and the defective structures are represented by large orange and small red circles respectively. Panels a and c show the ternary convex-hulls in which the compound $A_pB_qC_r$ is in equilibrium with elements $A$, $B$ and $C$. Panels b and d show the $\Delta H_f$-composition convex-hull along the 1-D composition slice containing both the defect and the compound. The $\Delta H_{def}$ are shown for (a-b) C-rich ($A_pB_qC_r$-C two-phase region) and (c-d) B-poor ($A_pB_qC_r$-A-C three-phase region) conditions. Similar to the case of binary compounds (see Figure 3.1) $\Delta H_{def}$ is determined using intercept between the common tangent line and the defect line. The expression to calculate $\Delta H_{def}$ is given in each panel. The general expression for calculating $\Delta H_{def}$ for all defect types in is given in the grey box at the bottom where $\Delta N_i$ = 0 or 1 and $\Delta N_v$ = 0 or -1 depending on whether the number of atoms of a particular species is added (1), removed (-1) or unchanged (0) in the defect.

ple two-dimensional plots (see Figure 3.3 b,d). This feature is extendable to more complex multicomponent phase spaces as well.

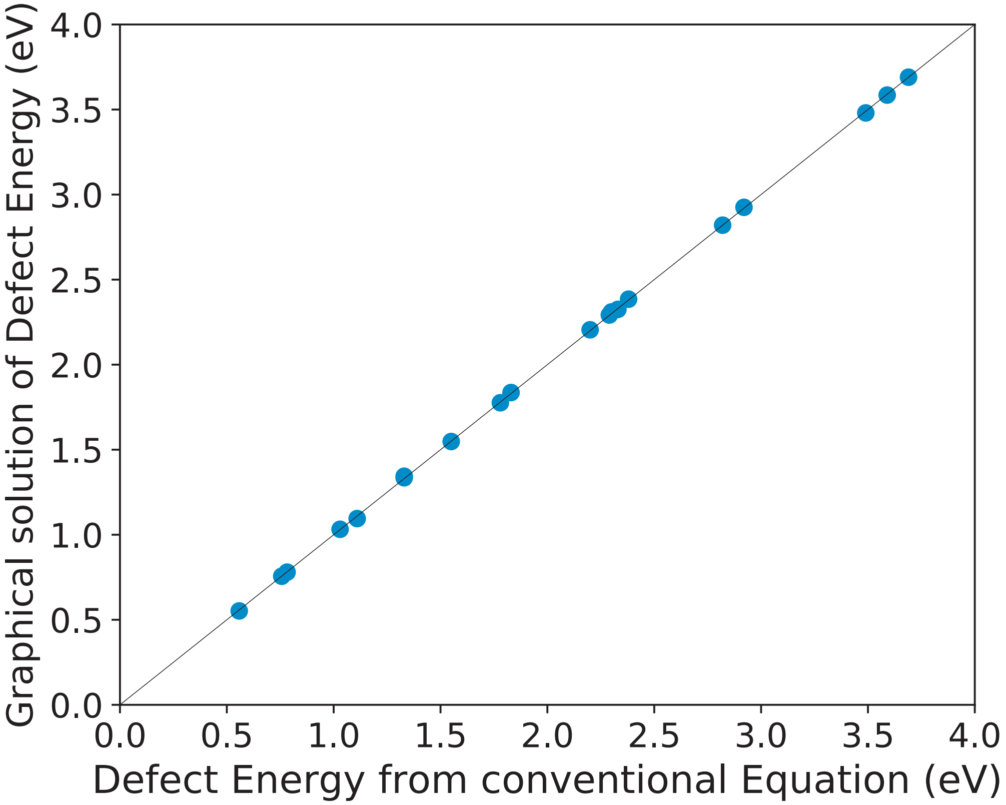

Figure 3.4: **Graphical solution of $\Delta H_{def}$ on convex-hulls are exact.** Comparision of defect energies for 20 half-Heusler systems calculated graphically to those determined using conventional defect energy expression

We compare $\Delta H_{def}$ calculated using our visualization scheme to those determined using equation 1.5 (see Figure 3.4) in our previous work [12] for interstitials in ternary half-Heusler systems ($Nb_{0.8}CoSb$, $Ta_{0.8}CoSb$ etc.). The equality in $\Delta H_{def}$ calculated using the two methods serves as numerical proof to our derivations in the present work.

### 3.3.2 Defining the "extended" convex-hull distance ($E_{eCH}$)

Within the context of the convex-hull construction, the defective structure of a stable compound is similar to a metastable compound in that both lie a finite energy distance above the convex-hull. In the case of metastable compounds, this convex-hull distance ($E_{CH}$) is useful for comparing the stability of structures at two different compositions. The Figure 3.5 shows a sketch of the model system $A-B$ with one stable compound $AB$ and two metastable structures $A_2B$ and $AB_2$ along with their $E_{CH}$ values. Between $A_2B$ and $AB_2$, $A_2B$ has a smaller $E_{CH}$ value and thereby is closer to thermodynamic stability.

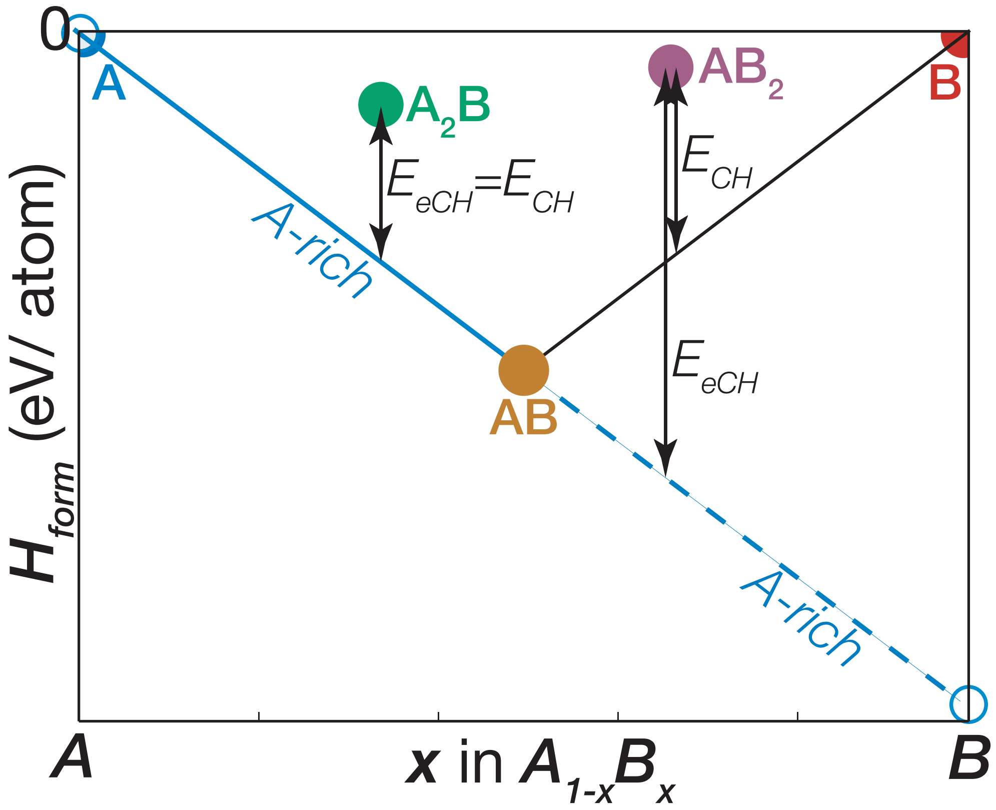

Figure 3.5: **Sketch differentiating the convex-Hull distance ($E_{CH}$) from the extended convex-hull distance ($E_{eCH}$) in a model binary convex-hull.**

While comparison of stability at different compositions is useful for metastable compounds, thermodynamic analysis of defects involves comparing stability of the same defect in different equilibria of the system. For such analysis, it is relevant to consider the energy distance of the structure with respect to the common tangent of the equilibria in question. We call this energy distance to the common tangent the *extended* convex-hull distance $E_{eCH}$. The Figure 3.5 shows the $E_{eCH}$ for $A_2B$ and $AB_2$ in the $A-rich$ conditions. The key differences between $E_{eCH}$ and $E_{CH}$ is that while $E_{CH}$ is not chemical potential dependent, but $E_{eCH}$ is. More importantly, $E_{CH}$ is the smallest value $E_{eCH}$ can take (i.e. $E_{eCH} \geq E_{CH}$). For $A_2B$, $E_{eCH} = E_{CH}$ under $A$-rich conditions and for $AB_2$, $E_{eCH} = E_{CH}$ under $B$-rich conditions.

The power of using $E_{eCH}$ for thermodynamic analysis of point defects lies in the fact that $\Delta H_{def}$ is directly proportional to the $E_{eCH}$ of the defect. Mathematically, $\Delta H_{def} \propto E_{eCH}$ is proven for various point defects in the Appendix A. Graphically, this proportionality can be seen quite straight-forwardly from Figure 3.1 and Figure 3.3 which shows that $\Delta H_{def}$ is simply a projection of $E_{eCH}$ on a compositional axis.

The visualization scheme presented in the current work is applicable for calculation of $\Delta H_{def}$ regardless of choice of chemical potential. The issue of multiple chemical potential values for calculating defect energetics of crystalline compounds is currently addressed using phase stability plots in chemical potential space. [99, 70] The construction of these plots using a model binary convex-hull is described in the introduction section (see Figure (1.2)). While these plots can in principle be used to derive $\Delta H_{def}$ corresponding to various equilibria, chemical potential space in general tends to be quite abstract for visualization considering that stoichiometry of each phase involved is depicted by the slope of the lines. As a result, plotting in the chemical potential space is often used in relatively advanced thermodynamic analysis and are often left out of introductory materials science textbooks. Owing to its simplicity, the convex-hull based approach discussed here could be a suitable pedagogical tool for teaching defect thermodynamics to a broader audience.

## 3.4 Conclusion

In conclusion, we show that one can graphically solve for the defect formation energies ($\Delta H_{def}$) of any multi-component compound within a two-dimensional convex-hull plot, including the effect of all possible chemical potentials. Using this visualization scheme, we integrate the thermodynamic analysis of phases and point defects within the same intuitive picture built in composition space. Considering that convex-hull diagrams are an introductory concept to a materials science audience and used widely today in predicting stability from high-throughput databases, our work can serve as a powerful tool to bring the understanding of defect thermodynamics to a larger audience.

# Chapter 4

# A Unified Understanding of Defects for Semiconductors and Insulators

## 4.1 Context and Motivation

Point defects can impact all transport and thermochemical properties of crystalline solids significantly. As a result, the study of point defects is important for a variety of device applications such as batteries,[79, 80, 81, 82] photovoltaics,[83, 84] thermoelectrics,[4, 85, 86, 87] thermochemical water splitting, [88, 100, 101] solid oxide fuel cells, [90, 91] and transparent conducting oxides [92]. Despite practically all applications requiring an in-depth understanding of point defects, the materials community studies defects in semiconductors and ceramic insulators using very distinct approaches.

In the field of solid state ionics for instance, defect concentrations in oxide compounds are studied by varying oxygen partial pressures in so-called Brouwer diagrams. This dependency of defect concentrations on chemical conditions is understood using principles of physical chemistry which define equilibrium reaction constants for all dominant defect reactions in the system. Example of a commonly studied defect reaction in oxide compounds is the reduction half-reaction which can be written in Kröger-Vink notation as

$$O_o^X \rightarrow 1/2\ O_2 + V_o^{\cdot\cdot} + 2e' \tag{4.1}$$

For this reaction describing the formation of an isolated oxygen vacancy defect, the concentration of the defects and charge carriers are related to the equilibrium constant $K_R$ for the reaction through the expression

$$K_R = pO_2^{1/2}[V_o^{\cdot\cdot}]n^2 \tag{4.2}$$

Other typical examples of dominant intrinsic defect reactions include formation of electronic ($K_e$), Schottky ($K_S$) and Frenkel ($K_F$) defects. Once all the relevant equilibrium constants are considered, the charge neutrality condition is imposed to model the partial pressure dependence of all defects.

In this approach for understanding defects, it is particularly noteworthy that the equilibrium reaction constants such as $K_R$, in principle, take a single value for each compound and is *independent* of the chemical conditions the compound was prepared in. Hence, the reduction reaction in a multi-component compound can be characterized using a single value for $K_R$ *regardless* of its complexity. By virtue of this simplification, the $K_R$ value across different compounds can be compared very easily, thereby allowing for a simple understanding of their reduction processes. Another strength of this approach is that the defect concentrations are plotted with respect to changing chemical conditions (such as the oxygen partial pressure) that are controllable directly in experiments.

This approach for studying defects in insulators has been used quite successfully in the field of Solid Oxide Fuel Cells (SOFC) since the study of defect concentrations is important for characterizing ionic conductivity in materials. In addition to simple modelling of defect concentrations, the study of thermodynamic quantities associated with the defect reaction such as solid state reduction entropy in this physical chemistry based approach is relevant for the field of Thermo-Chemical Water Splitting of materials.

Despite its success in modelling defect concentrations in mixed conductors, the Brouwer diagram approach has very little connection to changes in the electronic structure caused by formation of ionic defects. Point defects can affect charge carrier transport significantly through changes in electronic structure, thereby impacting most electronic material applications. For example, intrinsic point defects in semiconductors set a thermodynamic limit on the number of charge carriers, or dopability, thereby explaining asymmetry in electronic doping of most systems [69]. Defects also introduce mid-gap states which can affect carrier lifetimes, [83] Seebeck coefficient, [4] and coloration of materials [92]. These questions are answered typically using the theoretical construct of charged defects for which defect concentrations are Fermi-level-dependent.

Although this approach — rooted in the physics of defect energetics — is very useful for the study of electronic properties, it is studied almost exclusively using computational methods with no experimental techniques to verify theoretical predictions. This is quite unlike the physical chemistry based approach which uses experimental thermogravimetric methods to understand defect chemistry. [91] Furthermore, the data representation in the physics-based approach involves plotting defect energetics as a function of Fermi-level for different sets of chemical potentials. As a result, presenting this multi-dimensional data requires plotting on more than one panel and can become cumbersome in cases where multiple defects are calculated.

In this work, we build a unified understanding of defects in semiconductors and insulators which borrows from the strengths of both the approaches. We believe that our holistic approach to defects will help in establishing a common language of defects understandable by both the defect physics as well as the solid state ionics community. Such a language will be of great interest for research on mixed conductor materials since they can be approached by researchers in either communities. A very recent example of such multi-disciplinary interest in point defects research is that of battery materials which has seen interest from both the physical chemistry community [102, 103] as well as the defect physics community [104, 105, 106].

## 4.2 Results and Discussion

### 4.2.1 Mathematical Formulation for Building Brouwer Diagrams

Brouwer diagrams are usually discussed in the context of oxide materials and typically show the concentration of various defects depending on the oxygen partial pressure. For all off-stoichiometric compositions on which an impurity phase does not form (i.e, within the single phase region of the compound), defect concentrations can be modelled by considering all the important defects in the material simultaneously. Here, the formation of each defect is understood by expressing them in terms of defect formation reactions, and the concentration of the defects involved are related by the equilibrium constant ($K$) of the reaction.

Consider the oxide compound MO where the valence of the two elements involved is 2+ and 2- and vacancies are the dominant defect type. Construction of a typical Brouwer diagram (see Figure 4.1) for this oxide compound would first require considering the type of dominant complex defect (Frenkel or Schottky defect for example). For the sake of our demonstration (see Figure 4.1) we will work out the example for MO in which the Schottky defect is dominant. For this case, in addition to the reduction half-reaction above (see equation 4.1) which describes the formation of the oxygen vacancy, we will consider the *isolated* vacancy defect formation reaction

$$\Phi \rightarrow V_M'' + V_{\ddot{O}} \tag{4.3}$$

where the $V_M''$ and $V_{\ddot{O}}$ are charged vacancy defects which are isolated from each other and do not interact with each other. The equilibrium reaction constant $K_S^{isolated}$ for this reaction is related to defect concentrations through

$$K_S^{isolated} = [V_M''][V_{\ddot{O}}] \tag{4.4}$$

Additionally the hole and electron concentration is described using the reaction for electron-hole pair creation

$$\Phi \rightarrow e'' + h^{\cdot\cdot} \tag{4.5}$$

The equilibrium reaction constant $K_i$ for this reaction is expressed as

$$K_i = np \tag{4.6}$$

where $n$ and $p$ are the electron and hole carrier concentrations respectively. Furthermore, since all the defects considered are charged, we impose the charge neutrality condition on the system as follows

$$2[V_M''] + n \ = \ 2[V_o^{\cdot\cdot}] + p \tag{4.7}$$

Based on the charge neutrality equation semiconductor and insulator compounds, can be classified broadly, into two categories depending on whether the *stoichiometric composition* is dominated by electronic carriers ($n$ and $p$) or ionic defects ($V_M''$ and $V_o^{\cdot\cdot}$). The former case — in which the ionic defect concentrations [$V_M''$] and [$V_o^{\cdot\cdot}$] are negligible — occurs when the band-gap of the insulator is much smaller than the defect formation energies of the ionic defects and is characterized by $K_i >> K_S$. The Brouwer diagram for this case is shown in Figure 4.1. The three distinct regions in this figure can be understood by considering the different limiting chemical conditions (O-rich, O-poor, etc)

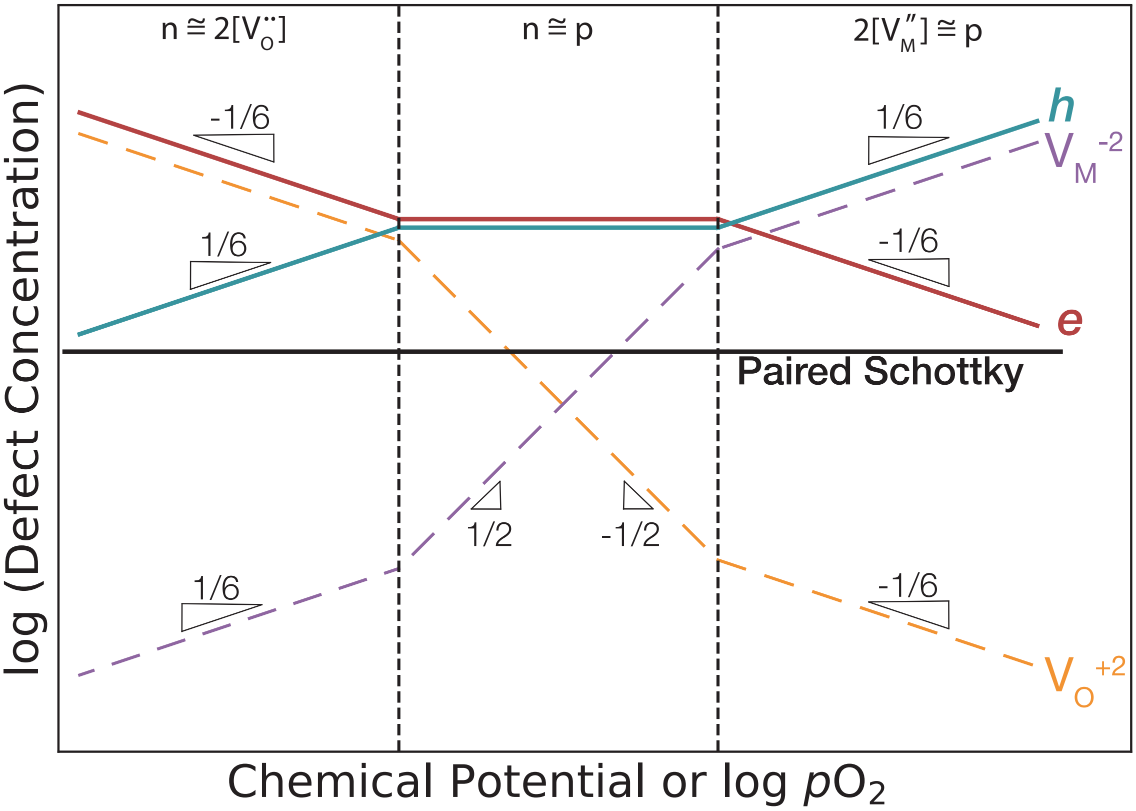

Figure 4.1: **Brouwer diagram example.** Typical Brouwer Diagram of a model oxide compound MO in which the vacancies $V_M''$ and $V_o^{\cdot\cdot}$ are the dominant point defect types. The $y$-axis gives log [], where [] represents concentration of the defect, and the $x$-axis gives log of the Oxygen partial pressure $pO_2$ (partial pressure). The Brouwer diagram can be broadly classified into three regions, separated by vertical dashed lines, with changing oxygen partial pressures. The slope of each defect and charge carrier concentrations in these regions are labelled next to them. In the extreme conditions (oxidizing and reducing), one of the point defects dominates ($V_M''$ and $V_o^{\cdot\cdot}$ respectively) causing a larger concentration of one of the carriers. In the intermediate conditions, neither of the vacancies clearly dominate and the charge carrier concentrations equal each other. The Brouwer approximations equating the dominant contributions to the charge neutrality condition in each region are mentioned above.

individually. Under reducing conditions with low oxygen partial pressures, Equation 4.7 can be approximated as

$$n \simeq 2[V_o^{\cdot\cdot}] \tag{4.8}$$

in which the relatively smaller values of $p$ and [$V_M''$] in comparison to n and [$V_O^{\cdot\cdot}$] are neglected. This approximation of the charge neutrality condition which depends on the chemical condition is called the Brouwer approximation.

After invoking the relevant Brouwer approximation for reducing conditions, one can solve Equations 4.3, 4.6, 4.1 and 4.8 to determine the partial pressure dependence of $[V_{\ddot{O}}]$, $[V_M]$, $n$ and $p$

$$[V_o^{\cdot\cdot}] \propto pO_2^{-1/6}, [V_M''] \propto pO_2^{1/6}, n \propto pO_2^{-1/6}, p \propto pO_2^{1/6} \tag{4.9}$$

For intermediate conditions of partial pressure, the Brouwer approximation for the charge neutrality Equation 4.7 becomes

$$n \ \simeq \ p \tag{4.10}$$

and the partial pressure dependence of the various defects becomes

$$[V_o^{\cdot\cdot}] \propto pO_2^{-1/2}, [V_M''] \propto pO_2^{1/2}, n = p = const \tag{4.11}$$

Under oxidizing conditions with high oxygen partial pressures the O-vacancy concentration and electron carrier concentrations are negligible and the the Brouwer approximation is expressed as

$$2[V_M''] \ \simeq \ p \tag{4.12}$$

such that the oxygen partial pressure dependence of the various defects becomes

$$[V_o^{\cdot\cdot}] \propto pO_2^{-1/6}, [V_M''] \propto pO_2^{1/6}, n \propto pO_2^{-1/6}, p \propto pO_2^{1/6} \tag{4.13}$$

The Brouwer diagram for MO in the $K_i$ » $K_S$ case has been constructed in Figure 4.1 using the partial pressure dependencies derived above. The oxidizing, reducing and intermediate conditions are separated in Figure 4.1 by vertical lines. We would like to note that for the qualitative models shown in Figure 4.1 the transition between the three regions is abrupt (discontinuous changes in slopes of the curves). In a real example, these transitions are expected to be more gradual.

### 4.2.2 Physics based approach to defects in semiconductors

The dependency of defect concentrations on chemical conditions is well-known and investigated in experimental reports on a regular basis. However, physics based defect theory additionally recognizes that defect formation energies ($\Delta H_{def}$), and thereby defect concentrations, in semiconductors can also have a Fermi-level dependence. Since Fermi-level ($E_f$) can change significantly with doping in semicondutors, especially in larger gap compounds with fewer electronic density of states to sample near $E_f$, $\Delta H_{def}$ can also vary significantly. We can understand the Fermi level dependence of charged defects using the simple example of the charged cation vacancy defect $V_{Na}^{-1}$ in NaCl. The process of Na-vacancy formation in excess Na conditions can be represented by the reaction

$$NaCl \rightarrow Na_{1-\delta}Cl + \delta\, Na \tag{4.14}$$

where the composition of the NaCl phase changes slightly ($\delta$) and the Na atom removed from NaCl gets placed in the elemental phase Na. In addition to the creation of an ionic point defect, the $V_{Na}^{-1}$ acceptor defect will also remove one carrier from the electron reservoir and place in Na metal (product phase). Energetically, this process is equivalent to removing an electron from the Fermi-level of NaCl and placing it at $< E_c^{product} >$, which represents the characteristic (average) energy of the electron in the product phase (Na metal) [69]. While this $< E_c^{product} >$ remains fixed, the equilibrium Fermi level in an insulator can take a range of values. Hence, the energy cost associated with creating $V_{Na}^{-1}$ will depend on the equilibrium $E_f$ value itself.

Quite similar to the concept of a work function, where the energy required to remove an electron depends on the $E_f$ value with respect to the vacuum level, the $V_{Na}^{-1}$ defect energy will also depend on the Fermi-level $E_f$ of NaCl relative to $< E_c^{product} >$. So, just like the value of the work function of NaCl increases with a lowering Fermi-level, so does the $V_{Na}^{-1}$ acceptor defect energy. As a result, under fixed temperature, pressure and chemical conditions (i.e. fixed Na chemical potential) the defect energy for $V_{Na}^{-1}$ in NaCl increases linearly with with lowering $E_f$. The slope of the line is equal to the charge state of the defect (in this case -1) because the energy required to create the defect is associated with the number of electrons removed from $E_f$ during its formation. So, for a two-electron acceptor such as $V_{Mg}^{-2}$ in MgO, the $E_f$ dependence of $\Delta H_{def}$ will have a slope of -2. In the case of donor defects, as one might expect, the defect energy increases with higher Fermi level. So for the donor defect $V_{Cl}^{+1}$ in NaCl, $\Delta H_{def}$ will have a slope of +1 when plotted against Fermi level.

Including chemical potential dependence discussed previously, the dependency on $E_f$ becomes the second parameter through which the defect concentrations can be controlled. The dependency of $\Delta H_{def}$ on chemical conditions for $V_{Na}^{-1}$ comes from the fact that the reservoir in which the Na atom ends up after removal from the host structure could have different chemical potentials. The Fermi level dependence comes from the fact that the energy of reservoir from which the the electron is removed or added during defect creation in NaCl can take a range of values. By putting together the chemical potential and $E_f$ dependencies of $\Delta H_{def}$, it can be expressed as

$$\Delta H_{def} = E_{defect} - E_{pristine} - \sum \Delta N_i \mu_i + qE_F \tag{4.15}$$

where $\Delta N_i$ is the number of atoms of species $i$ added to or removed from the defective structure (+1 and -1 for the atomic species added and removed respectively), $\mu_i$ is the atomic chemical potential of the species $i$, $q$ is the charge state of the defect and $E_F$ is the Fermi level.

The sketch of a typical defect energy diagram plotting $\Delta H_{def}$ versus $E_f$ for vacancy defects in a model oxide compound MO is shown in Figure 4.2a. As in the case of $V_{Na}^{-1}$ in NaCl and $V_{Mg}^{-2}$ in MgO, the likely charge states of the defects drawn are related to the valence of the atoms involved (+2 and -2 for M and O respectively). Hence, the charge states of the vacancy defects $V_M^{-2}$ and $V_O^{+2}$ are -2 and +2 respectively. Accordingly the slope of $\Delta H_{def}$ are also -2 and +2 respectively. It is important to note that the $\Delta H_{def}$ lines drawn in Figure 4.2a hold under fixed temperature, pressure, and chemical conditions. Changes in chemical conditions will shift the $\Delta H_{def}$ lines (see Figure 4.2 b) by changes in relevant atomic chemical potentials according to equation 4.15.

Using the information provided in Figure 4.2a regarding charged defects as well as the electronic density-of-states, one can determine the equilibrium position of the Fermi-level ($E_f^{eq}$) by solving for charge neutrality conditions by listing all the charged components as in the equation 4.7. Typically, for intrinsic semiconductors, $E_f^{eq}$ (see Figure 4.2a and b) tends to lie close to the $E_f$ where the $\Delta H_{def}$ of the dominant intrinsic defects (namely $V_M^{-2}$ and $V_O^{+2}$) cross each other in energy. In addition to the $E_f^{eq}$, $\Delta H_{def}$ in Figure 4.2a also provides a thermodynamic limit to extrinsic electronic dopability of the semiconductor under given conditions of $T$, $P$ and chemical conditions. The $n$-type dopability of MO according to Figure 4.2a is given by the Fermi level where $\Delta H_{def}$ of the acceptor defect $V_M^{-2}$ crosses 0 eV. When the $E_f$ reaches this position due to extrinsic doping, ionic $V_M^{-2}$ defects form almost spontaneously to compensate for any additional donor defects in the system. Because the compensation is almost entirely through ionic defect formation with no electrons being added to the system, the $E_f$ cannot be moved any further towards the conduction bands. Similarly, the extent of $p$-type dopability is given by the Fermi level where $\Delta H_{def}$ of the donor intrinsic defect $V_O^{+2}$ crosses 0 eV. Since the $\Delta H_{def}$ of these intrinsic defects depend on the chemical conditions, the equilibrium $E_f$ and the extent of electronic dopability are both also chemical-condition-dependent (see Figure 4.2b).

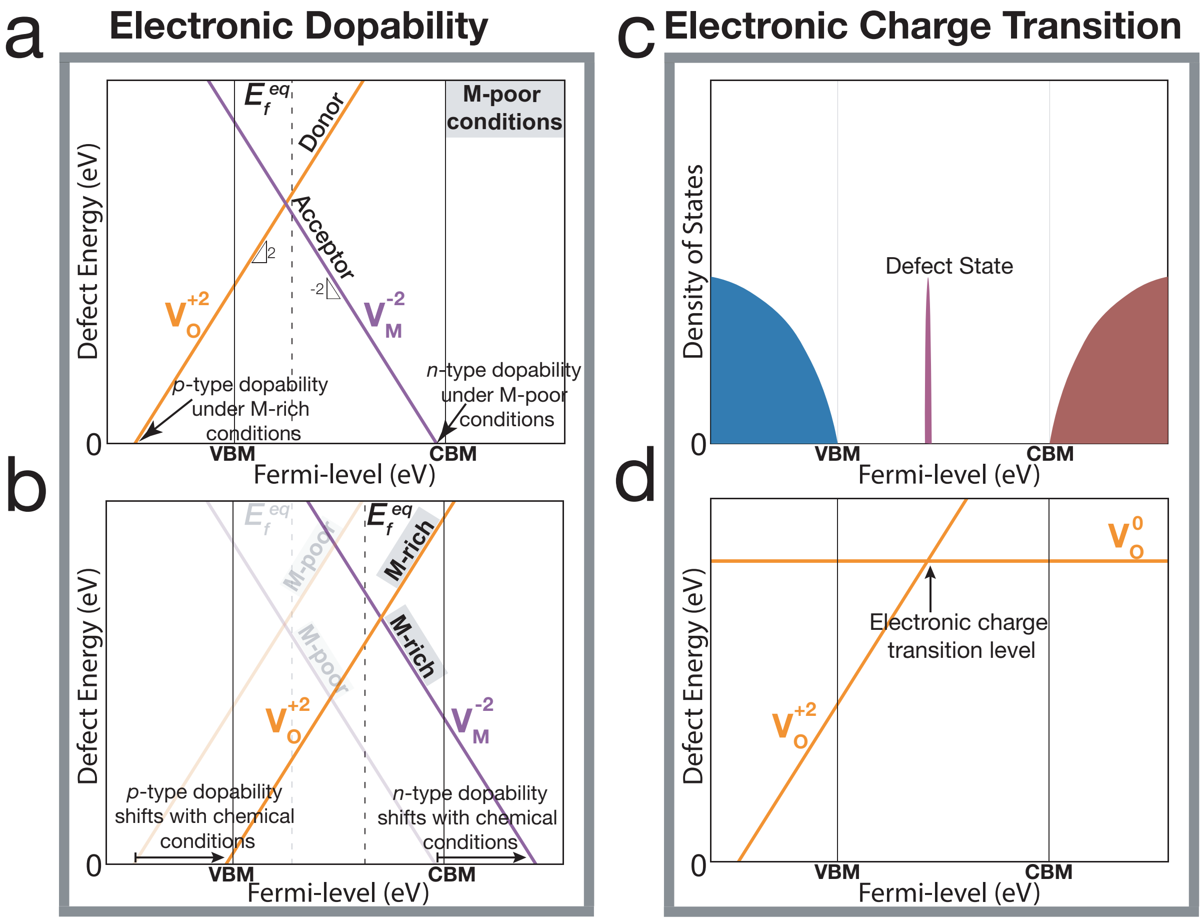

Figure 4.2: **Relating electronic properties and electronic structure to defect thermodynamics.** ((a) and (b)) Thermodynamics of the dominant intrinsic vacancy defects in the model insulator system MO determining its electronic dopability. The defect formation energeies ($\Delta H_{def}$) of the acceptor ($V_M^{-2}$) and donor ($V_O^{+2}$) defects depend on the Fermi-level ($E_f$) with a slope equal to their valence. The thermodynamic limit to the $E_f$ (dopability) under given temperature, pressure and chemical conditions is determined by the points where $\Delta H_{def}$ = 0 (a). This limit is shifted with changing chemical conditions (b). (c) The electronic density of states for the example of oxygen vacancy deep defect (defect level lies far from either band-edges) in MO. The defect level containing 2 states appears in a very narrow energy window indicating the localized nature of the states. At $E_f$ above the defect level, electronic charge equal to 2e localizes around the defect and the defect transitions from charge +2 to 0. The transition is observed as a change in slope of the $\Delta H_{def}$ versus $E_f$ plot for the defect.

Another important aspect of this theory is that defect energetics can be related to changes in the electronic structure associated with the formation of point defects (see Figure 4.2c and d). Oxygen vacancy in the large-gap oxides for example, are well-known to typically introduce mid-gap deep defect states [107] such as the one shown in Figure 4.2c. The defect states exist in a very small range of Fermi-level, indicating a near-dispersionless band localized in real space around the defect site. Since the equilibrium Fermi-level is not determined by the $V_O^{+2}$ defect alone, it can in principle lie on either sides of the defect state. To understand the thermodynamics of deep defects better, we will consider the case of $E_f$ lying above and below the defect states separately.

When the $E_f$ lies below the defect level in Figure 4.2c, the electronic charge created during defect formation will not occupy the defect state. For this case, the defect has a +2 charge state since (see Figure 4.2d) the two electrons associated with the O-vacancy formation will spatially delocalize from the defect site and join the electron reservoir like a charged defect. As a result, the $\Delta H_{def}$ versus $E_f$ line for this case will have a slope of +2 (see Figure 4.2d). When the $E_f$ lies above the defect level, the two electrons associated with the defect formation effectively occupy the two states resulting from the defect formation. Hence, for this case there will be no additional energy cost for defect formation irrespective of the position of the Fermi-level and the $\Delta H_{def}$ versus $E_f$ line will have a slope of 0 (see Figure 4.2d).

From a defect chemistry standpoint a key difference between the two cases is that when $E_f$ lies above the defect level, a localization of charge (due to the defect state filling up) should occur around the defect site. This charge localization can distort the ionic positions around the defect so significantly that the position of the defect level in Figure 4.2c itself could change.[107] In such a case, the defect level of the charged ($V_O^{+2}$) and the charge neutral defect ($V_O^0$) will not coincide. Furthermore, the position of the thermodynamic charge transition level in Figure 4.2d should also not necessarily coincide with with either of two defect levels ($V_O^0$ and $V_O^{+2}$). Figures 4.2c and 4.2d are drawn for pedagogical purposes under the assumption that charge localization has no effect on the position of the defect level and therefore the charge transition level $\Delta H_{def}$.

### 4.2.3 Experimental Demonstration of Fermi-level Dependence of [$V_{Pb}$] in PbTe

The $E_f$ dependence of $\Delta H_{def}$ in semiconductors as a theoretical concept is quite well-known and has been discussed at length in many previous works. However, to the best of our knowledge, there are no previous works which investigate the $E_f$-dependent thermodynamics of charged defects experimentally. The experimental evidence for the $E_f$ dependence of $\Delta H_{def}$ can be observed in semiconductors with partial electronic doping efficiencies of extrinsic dopants. In well-known examples of oxide compounds like Ceria ($CeO_{2-x}$), the excess charge introduced through extrinsic doping using elements such as $Gd^{3+}$ is expected to be compensated completely by formation of $V_{\ddot{O}}$ defects. The completely opposite limit for charge compensation in the extrinsic defect reactions is through the formation of free charge carriers in well-known semicondutors such as P-doped Si. While these compensation behaviors are well appreciated among researchers studying ionic and electronic materials respectively, semiconductors are not thermodynamically constrained to either of these limits. Hence it is possible that extrinsic doping could lead to a measurable change in both the charge carrier concentration *and* off-stoichiometry due to formation of charge compensating ionic defects. This behaviour of partial charge compensation on extrinsic doping can be observed in $n$-type $Mg_2Si$ (compensating $V_{Mg}^{-2}$),[108] $n$-type InSb (compensating $V_{In}^{-3}$),[86] $n$-type $Mg_3Sb_2$ (compensating $V_{Mg}^{-2}$),[2] $n$-type PbTe (compensating $V_{Pb}^{-2}$)[70] and $n$-type SnTe (compensating $V_{Sn}^{-2}$) [109]. Formally, this behaviour in I-doped PbTe can be expressed through the reaction

$$Te_{Te}^{X} + x\ Pb_{Pb}^{X} + I \rightarrow I_{\dot{T}e} + x\ V_{Pb}^{''} + (1 - 2\ x)\ e' + x\ Pb + Te$$

where 0 < x < 1 signifies a partial ionic compensation behaviour through the formation of Pb-vacancies.

To demonstrate the $E_f$ dependence of $\Delta H_{def}$ from experimental data, we choose I-doped PbTe from Ref. [70] because the samples were knowingly prepared under Te-rich and Pb-rich conditions in this work. In our model, the Pb-vacancy defect concentrations ($[V_{Pb}^{-2}]$) were estimated using experimentally measured Hall carrier concentration data as discussed in Ref. [70]. The $[V_{Pb}^{-2}]$ data used here were all estimated from samples prepared under Te-rich conditions with varying I-doping levels and annealed at T = 973 K in Ref. [70]. Using data from samples prepared under the same saturating chemical conditions fixes the Pb chemical potentials. Hence any variation in $V_{Pb}^{-2}$ concentration between samples are due to changes in $E_f$ due to I-doping. The $V_{Pb}^{-2}$ concentrations increase monotonically with increasing I-doping.

Since the samples were annealed and quenched subsequently, [70] the high temperature ($T$ = 973 K) thermodynamic state is assumed to be frozen for the Hall-measurements performed at room temperature. Therefore, the measured carrier concentrations and thereby the estimated defect concentrations are assumed to be frozen from the $T$ = 973 K state. These defect concentrations ($n_{def}$) for the defect $def$ is connected to $\Delta H_{def}$ through the general expression

$$n_{def} = s_{def} \;\; exp\left( -\frac{\Delta H_{def} - T\Delta S_{def}^{non-conf}}{kT} \right) \tag{4.16}$$

where $\Delta S_{def}^{non-conf}$ is the non-configurational entropy associated with the formation of defects, $s_{def}$ is the concentration of the symmetrically distinct Wyckoff sites on which the defect would form, $k$ is the Boltzman's constant and $T$ is the annealing temperature. The expression in equation 4.16 can in principle be used to solve for $\Delta H_{def}$ if the $T\Delta S_{def}^{non-conf}$ is negligible. However, at the high temperature of $T$ = 973 K this term could play a significant role in determining off-stoichiometry in the compound. For this reason, we will present the calculated $\Delta H_{def} - TS_{def}^{non-conf}$ versus $E_f$ in our analysis (see Figure 4.4) instead of $\Delta H_{def}$. These enthalpic and entropic contributions can presumably be separated

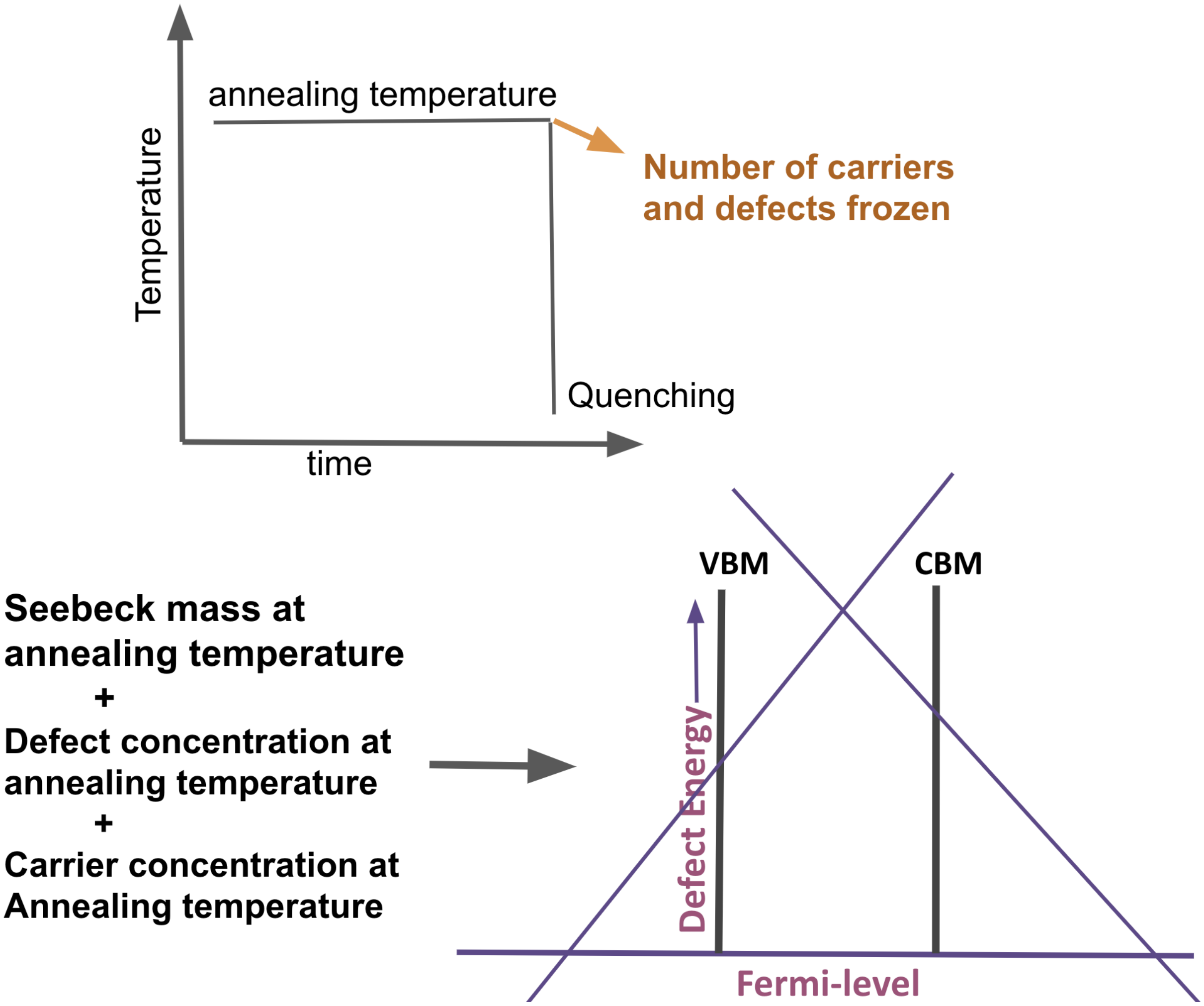
annealing temperature
Number of carriers and defects frozen
Temperature
Quenching
time
Seebeck mass at annealing temperature
+
Defect concentration at annealing temperature
+
Carrier concentration at Annealing temperature
VBM
CBM
Defect Energy
Fermi-level

Figure 4.3: **Schematic showing the procedure to obtain the defect diagram using experimental data.** In order to estimate the defect energetics accurately within a thermodynamic framework, the samples need to be annealed (and quenched subsequently) at the temperature of interest. The number of defects and number of carriers are presumed to be frozen from this annealing temperature. The $E_f$ dependence of $\Delta H_{Def}$ is calculated for the annealing temperature. Determining the equilibrium $E_f$ for each sample at the annealing temperature will also require the Seebeck effective mass from this temperature.

if data for more than one annealing temperature is available. Examples of common types of non-configurational entropy are vibrational, electronic and magnetic entropy. We note that the $\Delta S_{def}^{non-conf}$ can depend significantly on the extent of off-stoichiometry in the compound.

In addition to carrier and defect concentrations data, the model also requires band-gap

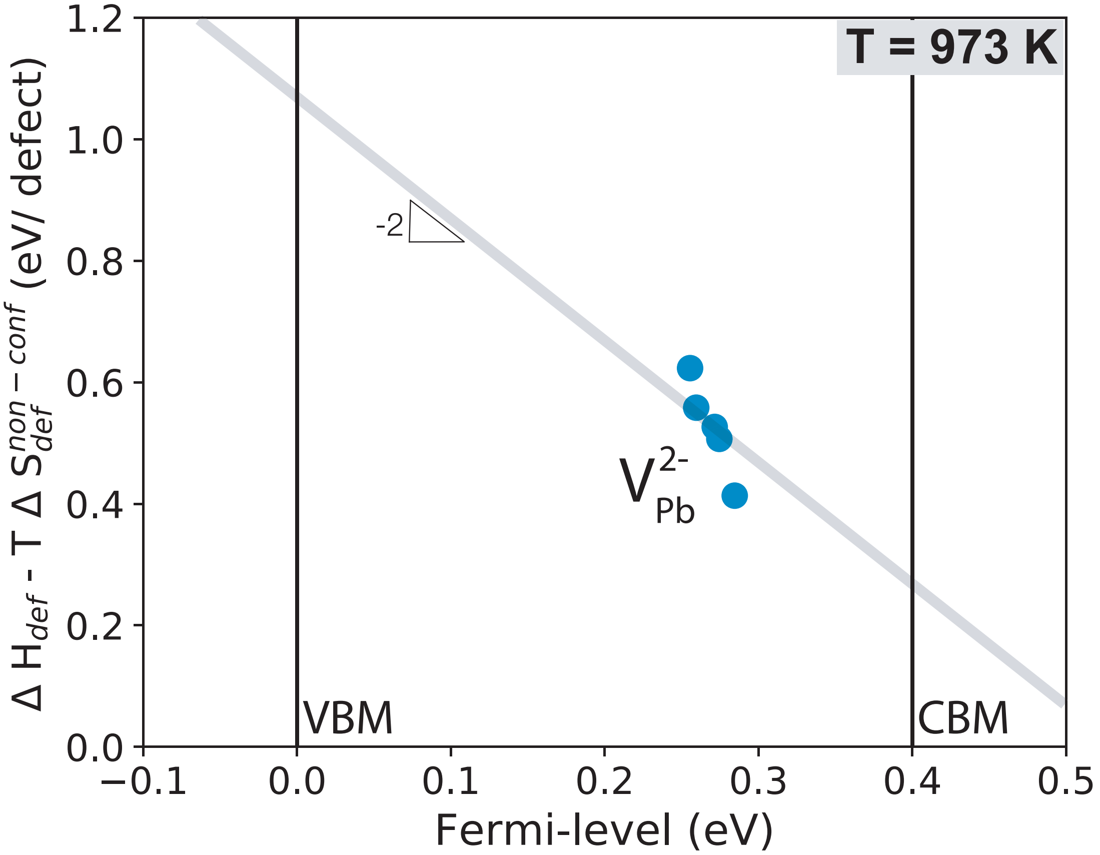

Figure 4.4: **The Fermi-level ($E_f$) dependence of $\Delta H_{def} - TS_{def}^{non-conf}$ (T = 973 K) for the $V_{Pb}^{-2}$ in PbTe determined from experimental data.** A solid line with a slope of -2 is shown for reference.

and density-of-states masses for the conduction and valence bands as inputs in order to determine the Fermi-level. Since the carrier and defect concentrations are attributed to $T = 973K$ in the model, we also use the band-gap ($E_g = 0.4eV$ [110]) and density-of-states mass values ($m_n*$ = 0.46 $m_e$,[111] $m_p*$ = 2.3 $m_e$ obtained by extrapolating the high temperature $p$-type Seebeck masses data from Ref. [112]) corresponding to this temperature.

Results from the model (see Figure 4.4) show that the thermochemistry of the Pb-vacancy formation process in PbTe is significantly $E_F$-dependent. In fact, the slope of the $\Delta H_{def} - TS_{def}^{non-conf}$ versus $E_f$ data might be greater than -2 presumably due to greater contributions from $S_{def}^{non-conf}$ at higher $E_f$ due to larger deviations from the site-balanced stoichiometry. While the results of Figure 4.4 suggest that changes in defect energetics with $E_f$ should not be ignored, the model used here could serve as possible way for experimental validation of calculated $\Delta H_{def}$ of charged defects in future works.

### 4.2.4 Understanding the Brouwer Diagram with Fermi-level dependence

After demonstrating the $E_f$ dependence of $\Delta H_{def}$ we take a closer look at its implication for the construction of Brouwer diagrams. We remind the reader here that the Brouwer diagram for the model system MO constructed in Figure 4.1 assumed no explicit dependence on $E_f$. Now, we consider the same model system MO as above in which the Schottky defect is the dominant defect. For the sake of simplicity we will assume the two vacancy defects involved ($V_M^{-2}$ and $V_O^{+2}$) are shallow defects i.e. their charge transition levels do not lie in the gap.

Before moving ahead we simplify Equation 4.15 a little bit further. We note that since $E_{defect}$ and $E_{pristine}$ are intrinsic to the material and are unaffected by changes in the chemical and/or electron reservoirs, the two terms can be replaced with a constant $C_i$

$$\Delta H_{def} = C_i - \sum \Delta N_i \mu_i + q_i E_F \tag{4.17}$$

Next, we investigate whether the equilibrium reaction constants $K^{isolated}$, $K_i$ and $K_O$ given in Equations 4.4, 4.6, and 4.2 have any $E_f$ dependency, since the mathematical formulation of Brouwer diagrams assumes that they are constants of a semiconductor (unless there are impurity phases). In the case of the isolated vacancy reaction constant, we can rewrite $K^{isolated}$ as

$$K_S^{isolated} = s_{V_M''}\ s_{V_{\ddot{O}}}\ exp\left(\frac{-(\Delta H_{V_M''} + \Delta H_{V_{\ddot{O}}})}{kT}\right) \tag{4.18}$$

Considering the charge states -2 and +2 for the cation and anion defects respectively, the numerator in the exponent can be rewritten as

$$\Delta H_{V''_M} + \Delta H_{V_{\ddot{O}}} = C_{V''_M} + C_{V_{o}^{\cdot\cdot}} + \mu_M + \mu_o - 2\ E_F + 2\ E_F$$

As expected, the chemical potentials add up to give a constant value related to the formation enthalpy of the compound MO ($2 \times \Delta H_{MO}$), which is a constant value independent of chemical conditions. Moreover, we find that the Fermi level dependency also vanishes. Hence, the expression for $\Delta H_{V''_M} + \Delta H_{V_{\ddot{O}}}$ and thereby $K_S$ will simplify to a constant value *regardless* of atomic chemical potential and Fermi-level.

$$\Delta H_{V''_M}\ +\ \Delta H_{V_{\ddot{O}}}\ =\ C_{V''_M} + C_{V_{o}^{\cdot\cdot}} + 2\ \Delta H_{MO} \tag{4.19}$$

One can similarly work out that the equilibrium reaction constants $K_i$ and $K_R$ should remain independent of $E_f$. These results suggest that any semiconductor system in which the dominant acceptor and donor defects are (i) shallow defects and (ii) form a stoichiometric and charge balanced pair, must yield a dependency on oxygen partial pressure (and more generally, the chemical potential for any compound) of defect concentrations similar to that observed in a typical Brouwer diagram (see Figure 4.1).

We note here that this conclusion is directly transferable to non-oxide semiconductors as well, only in that case, the oxygen partial pressure in the x-axis of the Brouwer diagram will be replaced by the chemical potential of the element of interest. To confirm the results regarding the effect of $E_f$ dependence of charged defects on Brouwer diagrams, we consider the example of $Mg_3Sb_2$ in which the dominant donor and acceptor defects are $Mg_i^{+2}$ and $V_{Mg}^{-2}$ respectively. [2]. We note that both of these defects are shown to be shallow defects and form a stoichiometric, charge balanced pair.

In Figure 4.5 we plot the Mg chemical potential dependence of the ionic defect and carrier

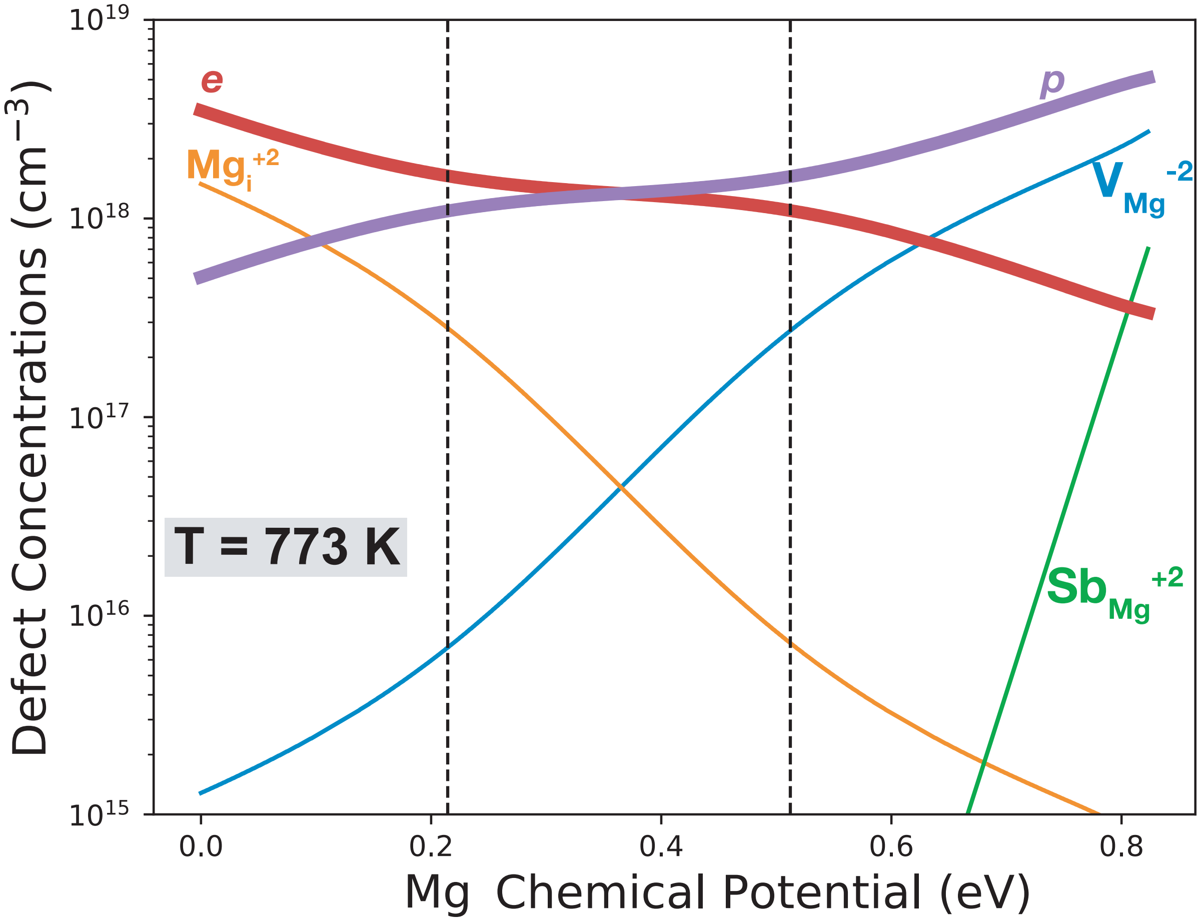

Figure 4.5: **Brouwer diagram for $Mg_3Sb_2$ with Fermi-level dependence of point defect energetics accounted for.** Concentration of important intrinsic charged defects and charge carriers in $Mg_3Sb_2$ calculated as a function of Mg-chemical potential. The defect energies (which implicitly also have a fermi-level dependence) and density of states masses are taken from Ref. [2]. The dominant defect types $Mg_i^{+2}$ and $V_{Mg}^{-2}$ are both shallow defects. Despite the Fermi-level dependence, the plot resembles the one shown in Figure 4.1 with three distinct regions of Mg chemical potential dependencies separated by vertical lines which are drawn as guides to the eye.

concentrations in $Mg_3Sb_2$. Indeed we find that similar to the typical Brouwer diagram of the model system MO (see Figure 4.1), the chemical potential dependencies of log[] are not linear in the range of the Mg-chemical potential shown. Instead, just like in Figure 4.1, the x-axis range could be divided broadly into three regions of low, intermediate and high Mg-chemical potential where the dependency of log [] on chemical potential seems linear. These results suggest that even the log[] versus Mg-chemical potential plot for

$Mg_3Sb_2$ can be modeled using equilibrium reaction constants $K_f$ (for Frenkel reaction), $K_i$ and $K_R$ ($Mg_i$ formation reaction). In this model, $K_f$ would be related to the sum $\Delta H_{V''_{Mg}} + \Delta H_{Mg_i^{\cdot\cdot}}$, $K_i$ would be related to the band-gap of $Mg_3Sb_2$ and $K_R$ would be related to $\Delta H_{Mg_i^{\cdot\cdot}}$ and the Mg-chemical potential.

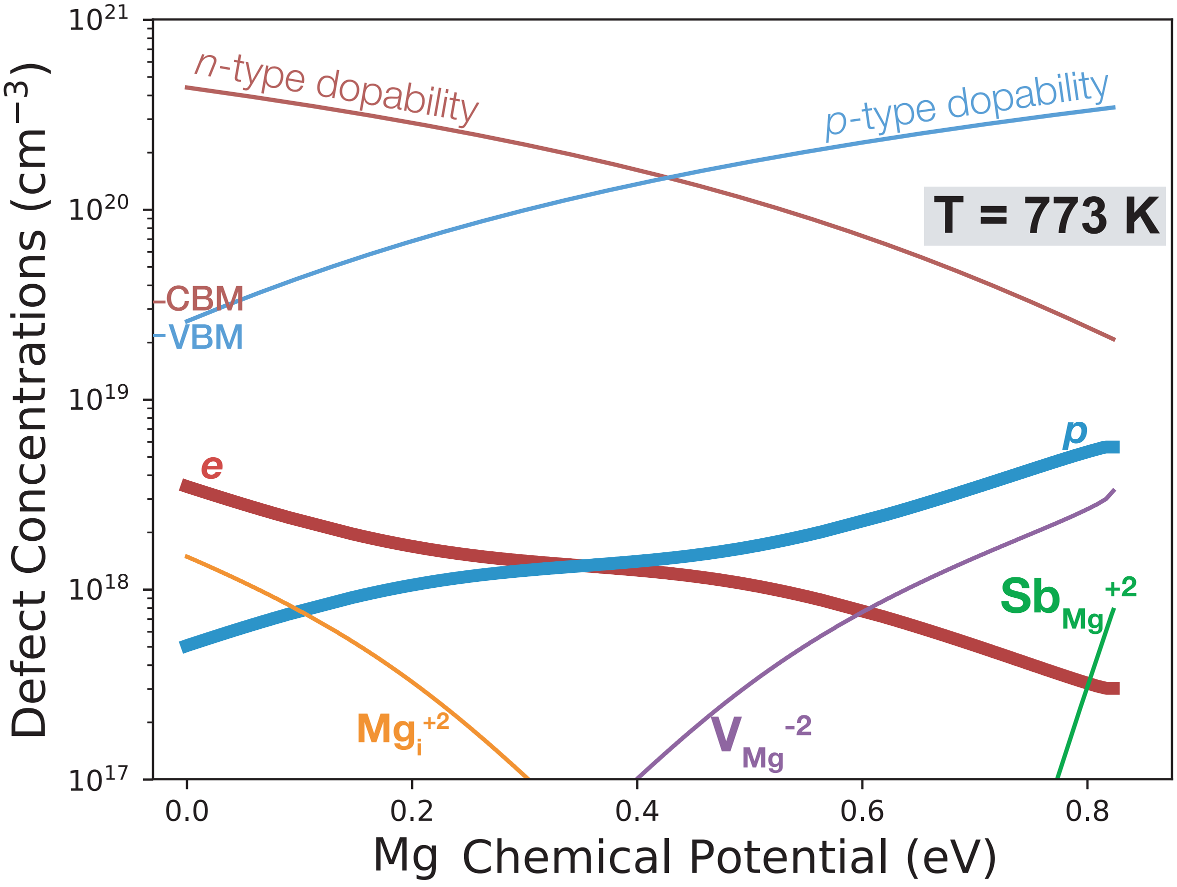

Figure 4.6: **Presenting electronic dopability information on a Brouwer diagram.** Concentration of important intrinsic charged defects and charge carriers in $Mg_3Sb_2$ calculated as a function of Mg-chemical potential. The defect energies (which implicitly also have a fermi-level dependence) and density of states masses are taken from Ref. [2]. The $n$ and $p$-type dopabilities (red and blue lines) and are determined by the carrier concentrations from the $E_f$ at which $\Delta H_{def}$ of the $V_{Mg}^{-2}$ and $Mg_i^{+2}$ defects becomes 0 eV. The VBM and CBM markers are determined by the carrier concentrations at the valence and conduction band edges.

Although the Brouwer diagram representation such as the one shown in Figure 4.5 are often not used in computational works discussing the $E_f$ dependence of $\Delta H_{def}$, they could be quite helpful in conveying the main results in a direct and condensed fashion (see

Figure 4.6). The $E_f$ dependence of $\Delta H_{def}$ is often calculated to understand how the electronic dopability depends on changing chemical conditions. $Mg_3Sb_2$ for example exhibits a measurable $n$-type dopability only in Mg-rich conditions for which the $\Delta H_{V''_{Mg}}$ values of the compensating acceptor defect is higher. Traditionally, the shifts in electronic dopability with changing chemical conditions are shown by plotting multiple $\Delta H_{def}$ versus $E_f$ diagrams corresponding to different chemical conditions. The most relevant information to take-away from these panels plotted for differing chemical potentials is (i) the equilibrium $E_f$, (ii) the $\Delta H_{def}$ values of various defects at the equilibrium $E_f$ and (iii) the $E_f$ at which $\Delta H_{def}$ of the dominant compensating defect crosses 0 eV relative to the valence and conduction band edges (see Figure 4.2 a and b). The $\Delta H_{def}$ versus $E_f$ description requires communicating to the reader in terms of Fermi-level, which is not a commonly measured property and not as physically intuitive as carrier or defect concentrations. Furthermore, plotting $\Delta H_{def}$ for an entire range of $E_f$ values understates the importance of the actual defect energies which can be found at the equilibrium Fermi-level only for a given set of chemical potentials. A data visualization scheme in which (i), (ii) and (iii) are plotted together in a single panel as a function of changing chemical conditions could be more direct (see Figure 4.6).

We note that (i) and (ii) for $Mg_3Sb_2$ are already plotted as a function of Mg chemical potential in 4.5. In Figure 4.6 the $n$ and $p$-type dopability of $Mg_3Sb_2$ are given by the carrier concentrations at the $E_f$ where the $\Delta H_{def}$ of the dominant compensating defect crosses 0 eV. Similarly the valence and conduction band edges are represented by the carrier concentrations at those Fermi-level values. The position of the band-edges on the y-axis depends on the density of states mass of the conduction and valence bands. The defect concentrations are calculated from defect energy values at the equilibrium $E_f$.

The representation in Figure 4.6 reduces the dimensionality of the data without losing any relevant information on electronic dopability, important electronic structure features (band gap, density of states and position of the band-edges with respect to dopability limits), defect and carrier concentration. In the case of the binary compound $Mg_3Sb_2$ for example, the 3-dimensional data $\Delta H_{defect}$ (versus Mg chemical potential and $E_f$) is condensed to a easy-to-read 2-dimensional plot (only versus Mg chemical potential). One can easily extend this visualization scheme for more compositionally complex multi-component systems, by plotting along chemical potential points of interest (generally corresponding to multi-phase equilibria).

### 4.2.5 Isolated and Paired defect formation

The isolated vacancy defect reaction plays a crucial role in the mathematical formulation of the Brouwer diagram. Depending on the material in question however, one might have to additionally consider the reaction involving the formation of Schottky pairs

$$\Phi \rightarrow (V''_M V_{\ddot{O}})^X \tag{4.20}$$

where $(V''_M V_{\ddot{O}})$ is a paired Schottky defect complex. The reaction constant for this paired defect reaction is given by the expression

$$K_S^{Paired} = [(V''_M V_{\ddot{O}})] \tag{4.21}$$

The biggest difference between a Schottky pair and isolated vacancies is that the Schottky pair defect does not have any oxygen partial pressure dependency because it is a stoichiometric defect (which does not change the overall composition of the compound). As a result, concentration of the paired Schottky defect in the model system MO in Figure 4.1 should show as a flat line for all values of oxygen partial pressures. This thermodynamic behaviour is in stark contrast to the unpaired *non-stoichiometric* point defects (vacancies, interstitials and anti-site defects) which are not stoichiometric defects and their concentrations can vary with chemical potential.

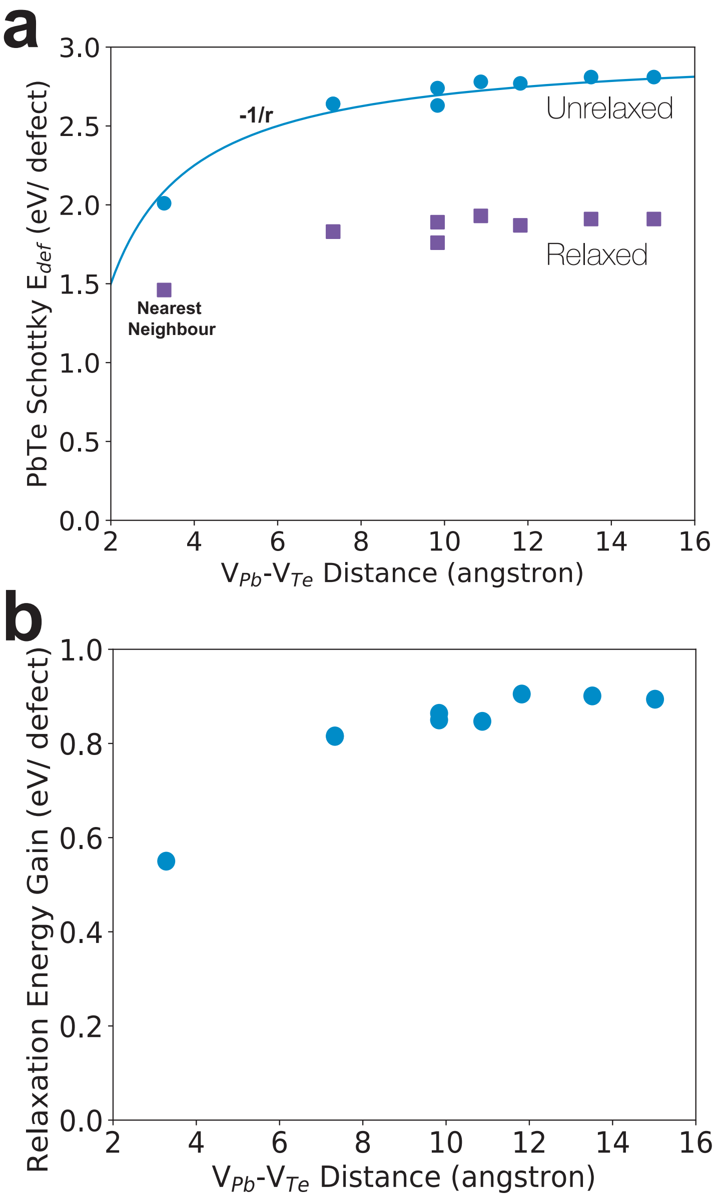

Figure 4.7: **Electrostatic and strain contributions to binding energy in the Schottky defect pair of PbTe.** (a) Defect energy (in eV/defect) of a Schottky defect in PbTe as a function of the distance between the vacancy pair in a 128 atom supercell. To estimate the electrostatic contributions to binding between the vacancy pair, we calculate the relaxed (blue circles) and unrelaxed (purple squares) separately. The electrostatic contribution from the unrelaxed calculations can be modelled with a 1/r dependence (solid blue line). (b) The energy gained from relaxing all degrees of freedom in the supercell as a function of the distance between the vacancy pair. This energy contribution is calculated by subtracting the relaxed energies from the unrelaxed energies shown in (a).

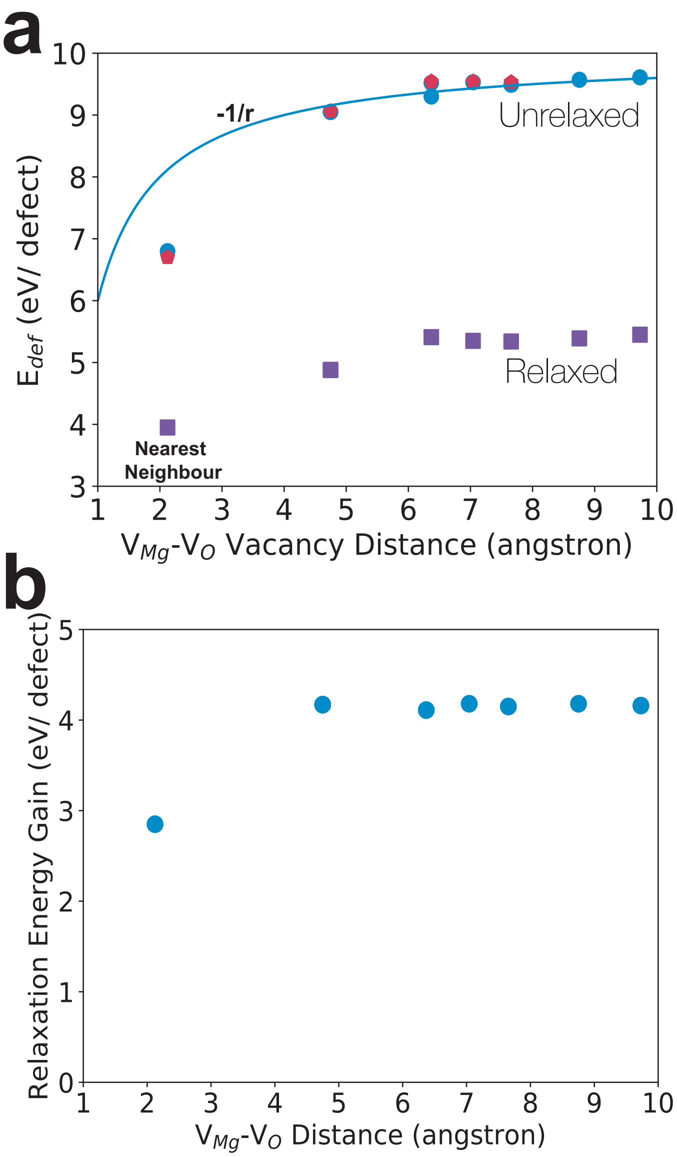

Figure 4.8: **Electrostatic and strain contributions to binding energy in the Schottky defect pair of MgO.** (a) Defect energy (in eV/defect) of a Schottky defect in MgO as a function of the distance between the vacancy pair in a 128 atom supercell. To estimate the electrostatic contributions to binding between the vacancy pair, we calculate the relaxed (blue circles) and unrelaxed (purple squares) separately. For the sake of verifying convergence in this low dielectric constant material we also calculate the unrelaxed energies in a 432 atom supercell (pink). The electrostatic contribution from the unrelaxed calculations can be modelled with a 1/r dependence (solid blue line). (b) The energy gained from relaxing all degrees of freedom in the supercell as a function of the distance between the vacancy pair. This energy contribution is calculated by subtracting the relaxed energies from the unrelaxed energies shown in (a).

The equilibrium reaction constant $K_S^{Paired}$ will presumably take a larger value than $K_S^{isolated}$ — which is related to the sum of the isolated vacancies $\Delta H_{def}^{V_M''} + \Delta H_{def}^{V_{\ddot{O}}}$ — due to a binding energy for pairing to occur between the vacancy defects. To estimate the likelihood of pairing to occur between dominant vacancy pairs, we calculate the $\Delta H_{def}$ between them as a function of distance. Since the binding energy of a defect pair is expected to arise almost entirely by electrostatic attraction between the oppositely charged cation and anion vacancies, screening of the interaction can play an important role in determining the binding energy. Hence, we choose MgO and PbTe for our analysis because they crystallize in the same rock-salt structure but have very different values of dielectric constants ($<$ 10 and $\sim$ 400, respectively).

To distinguish the electrostatic contributions from contributions arising from strain field interactions we perform our $\Delta H_{Def}$ calculations in two steps (see Figure 4.7 a and Figure 4.8). In the first step, we calculate $\Delta H_{Def}$ by simply creating a vacancy but not allowing for any relaxation in the structure. Due to electrostatic interactions, the $\Delta H_{Def}$ in this step is expected to decrease as the vacancies start coming closer (see Figure 4.7 a and Figure 4.8). Subsequently, we allow for a complete relaxation of ionic positions and cell vectors. In this step, a further decrease in energy due to relaxation of atoms around the vacancy is expected. However, as the vacancies come closer together the energy gained due to ionic relaxation decreases presumably due to larger interactions between the strain fields associated with the two vacancies (see Figure 4.7 a). In both materials, the nearest neighbour configuration is the most favorable for pairing between the cation and anion vacancies.

As expected, the binding energy in the paired vacancy defect essentially arises from an electrostatic attraction which is negated to a certain extent at smaller distances by strain energy contributions. The electrostatic energy gain in both materials follows a -1/r trend for the most part presumably due to Coulombic attraction between the defects. The electrostatic contribution to the binding energy in MgO is $\sim$ 4 times that of PbTe which can be attributed to its smaller dielectric constant.

To estimate the relative defect concentrations of the paired Schottky defect with the unpaired vacancy defects, we simply compare their $\Delta H_{def}$ on a per-atom basis under stoichiometric conditions. The $\Delta H_{SchottkyPair} \sim$ 0.75 eV for paired defect in PbTe which is smaller than the $\Delta H_{def} \sim$ 1 eV for the isolated defects under stoichiometric conditions (i.e. for the fermi-level at which the $\Delta H_{def}^{V''_M} = \Delta H_{def}^{V_{\ddot{O}}}$) Ref. [113] for vacancy defects individually. Similarly $\Delta H_{def} \sim$ 1.95 eV for a Schottky defect in MgO which is smaller than $\Delta H_{def}$ $\sim$ 2.8 eV.[69] Hence, the concentration of the paired defect are expected to exceed isolated vacancy concentrations by a much larger factor for MgO compared to PbTe. Similar to Schottky defects, one can also expect stoichiometric Frenkel pairs to also have a similar binding behavior. However, in the case of a Frenkel pair there is an additional possibility of the intersitial defect moving into the vacancy site of the pair upon ionic relaxation if the interstial-vacancy pair is placed too close. This behaviour of the Frenkel pairs has been demonstrated for $Mg_3Sb_2$ recently. [114, 115]

# Chapter 5

# Predicting Solubility in Complex Materials with Pen-and-Paper Drawings.

## 5.1 Context and Motivation

Determining the maximal solubility in solids is of great interest for many materials applications ranging from metals design, to thermoelectrics [3] and battery materials [116, 117]. Experimental reports often conclude that the solubility limit is reached upon observation of impurity phases. However, this limit to solubility is not necessarily the *maximal* limit because solubility, besides temperature and pressure, will also depend on chemical conditions. In simple terms, this means that the observed limit to solubility also depends on the type of impurity phase observed with it. As a result, a complex multi-component compound which could have multiple candidates as impurity phases will also have multiple limits to solubility. In such a case, identifying the maximal solubility limit from experiments can become tricky; requiring preparation and analysis of many compositions using a 'phase boundary mapping' approach [118, 119, 3, 120, 4, 2, 121, 122, 70, 123, 124, 125, 126, 127] before arriving at a reproducible conclusion.

The two main lessons from phase boundary mapping exercises of various supposedly well-known thermoelectric materials is that previous works on these compounds had either (a) ignored the possibility for multiple limits to solubility, thereby missing out on compositions with higher performance or (b) were unable to explain the origin of multiple discrepancies in reported values of solubility. An example of the first case is that of Ce-doped $CoSb_3$, [3] in which samples containing the $CeCoSb_3$ impurity phase was shown to have a much higher Ce-solubilities than previous attempts [128]. The second case is exemplified by the $Mg_2Si$-$Mg_2Sn$ pseudobinary system for which there have been widely varied reports of solid-solubility limits between the two end-members. Phase boundary mapping of this system in the Mg-Si-Sn ternary later revealed that any equilibria containing both $Mg_2Si$ and $Mg_2Sn$ should have the same Sn and Si solubilities respectively in these end-member compounds. [127]

In the present work, we build an intuitive visual framework in composition space rooted in defect thermodynamics which can qualitatively identify trends in the various solubility limits with type of impurity phase (or alternatively chemical conditions). Using just the chemical intuition of dominant defects and previously available phase diagrams, our visualization scheme can identify the impurity phases yielded when the *maximal* solubility limit is reached and the special chemical conditions in which the limits to solubility will be equal (see Figure 5.1). Typically, defect thermodynamics in complex materials is understood either mathematically or by plotting in the relatively abstract chemical potential space. [121] Our visualization scheme provides the solution to the problem directly in composition space itself; which can help in chalking out solubility design strategies in simple pen-and-paper drawings before embarking on the complicated exercise of phase boundary mapping exercises.

We explain the framework using a few examples from past five years of phase boundary mapping research. In the process, we show how better choices for composition and chemical conditions could have been made prior to beginning experiments for increasing solubility. After this, we demonstrate the predictive power of our solubility guidelines introduced in the present work. We use our visualization scheme to identify complex quaternary thermoelectric systems with unusual solubility behavior that have been ignored until now due to seemingly innocuous assumptions.

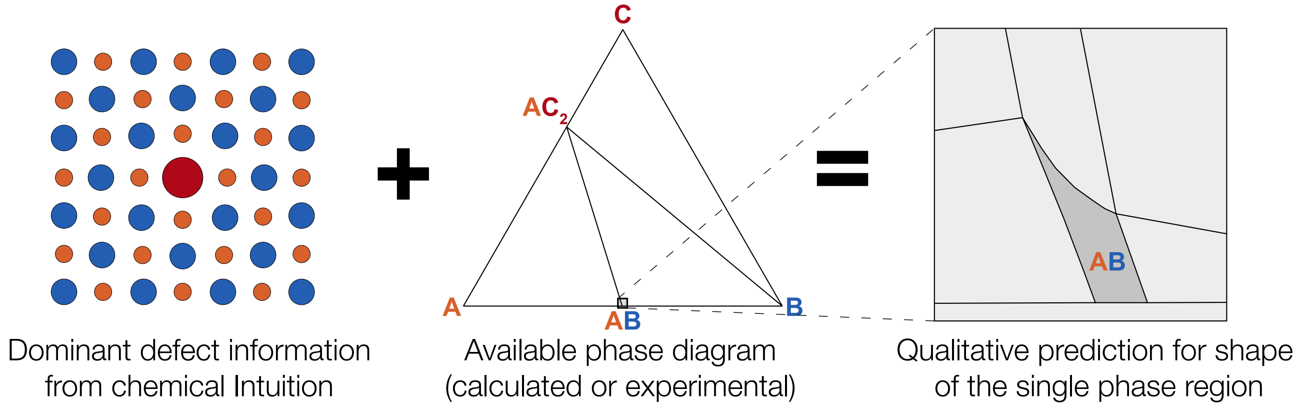
C
AC$_2$
A
AB
B
AB
Dominant defect information from chemical Intuition
Available phase diagram (calculated or experimental)
Qualitative prediction for shape of the single phase region

Figure 5.1: **Sketch summarizing the problem statement for this chapter.** Can we use available phase diagram information (experimental or computational) and combine it with our chemical intuition regarding the dominant defect to qualitatively predict the shape of the single phase region (and thereby the various limits to defect solubility)? As we deal with more complex materials, the answer to this question will come in handy.

## 5.2 Results and Discussion

### 5.2.1 Thermodynamic Solubility Guidelines for Multi-component Systems

To develop thermodynamics-based solubility guidelines we revisit the convex-hull framework for $\Delta H_{def}$ visualization developed in Section 3. We begin by considering the example of the $B_i$ defect in the ternary compound $A_pB_qC_r$ (see Figure 5.2 a and b). The three dimensional representation of the convex-Hull is shown in Figure 5.2 a. The compound $A_pB_qC_r$ is the only stable compound in the three component system, forming tie lines with the elemental phases in the convex-hull. The common tangent planes for the 3 three phase equilibria in which $A_pB_qC_r$ participates are numbered. The $B$-interstitial defect in the compound lies above the convex-hull at an off-stoichiometric composition along $B$. The top view of the convex-hull is shown in Figure 5.2 b. The $B_i$ defect structure lies on tie line connecting $A_pB_qC_r$ and $B$. Generally, the defect formation energy ($\Delta H_{def}$) from Section 3.3.2

$$\Delta H_{def} = cE_{eCH} \tag{5.1}$$

where $E_{eCH}$ is the extended convex-hull distance of the defect and $c$ is a constant related to the compositions of the defect and the parent compound. From the properties of $E_{eCH}$ we know that $E_{eCH} \geq E_{CH}$. From this inequality we learn that $\Delta H_{def}$ will take its smallest value when $E_{eCH}$ = $E_{CH}$. As shown in Figure 3.5, for any metastable structure, $E_{eCH}$ = $E_{CH}$ when chemical potentials of the *equilibrium region containing* the structure is considered. Since all point defects change the composition of the parent compound along different directions (see Figure 5.2 c), the smallest $\Delta H_{def}$ value for each defect will also lie in different equilibria. So, in the case of the $B_i$ defect for example, $\Delta H_{def}$ will be smallest in the $A_pB_qC_r$-$B$ equilibrium because it contains the composition of the $B_i$ defect (see Figure 5.2 c).

We further investigate the $E_{eCH}$ of $B_i$ for the equilibria 1 and 2 (see Figure 5.2 a and b). In these cases the $E_{eCH}$ value in these cases will be determined with respect to the common tangent planes 1 and 2 respectively, as shown in the Figure 5.2 a. The 3-dimensional visualization of the convex-hull (see Figure 5.2 a) shows that both these planes will intersect in the composition line connecting the phases $A_pB_qC_r$ and $B$ which contains the $B_i$ defect composition. As a result, the $E_{eCH}$ for both equilbria 1 and 2 will also be determined by the $A_pB_qC_r$-$B$ tie line in the convex-hull and thereby must be equal.

From the $B_i$ defect thought experiment we learn two guidelines regarding chemical conditions for maximum solubility and special cases where defects have equal solubility. To generalize these guidelines succinctly we define the the concept of *defect direction* and *impurity phase direction*. On a multi-component phase diagram, the defect direction is

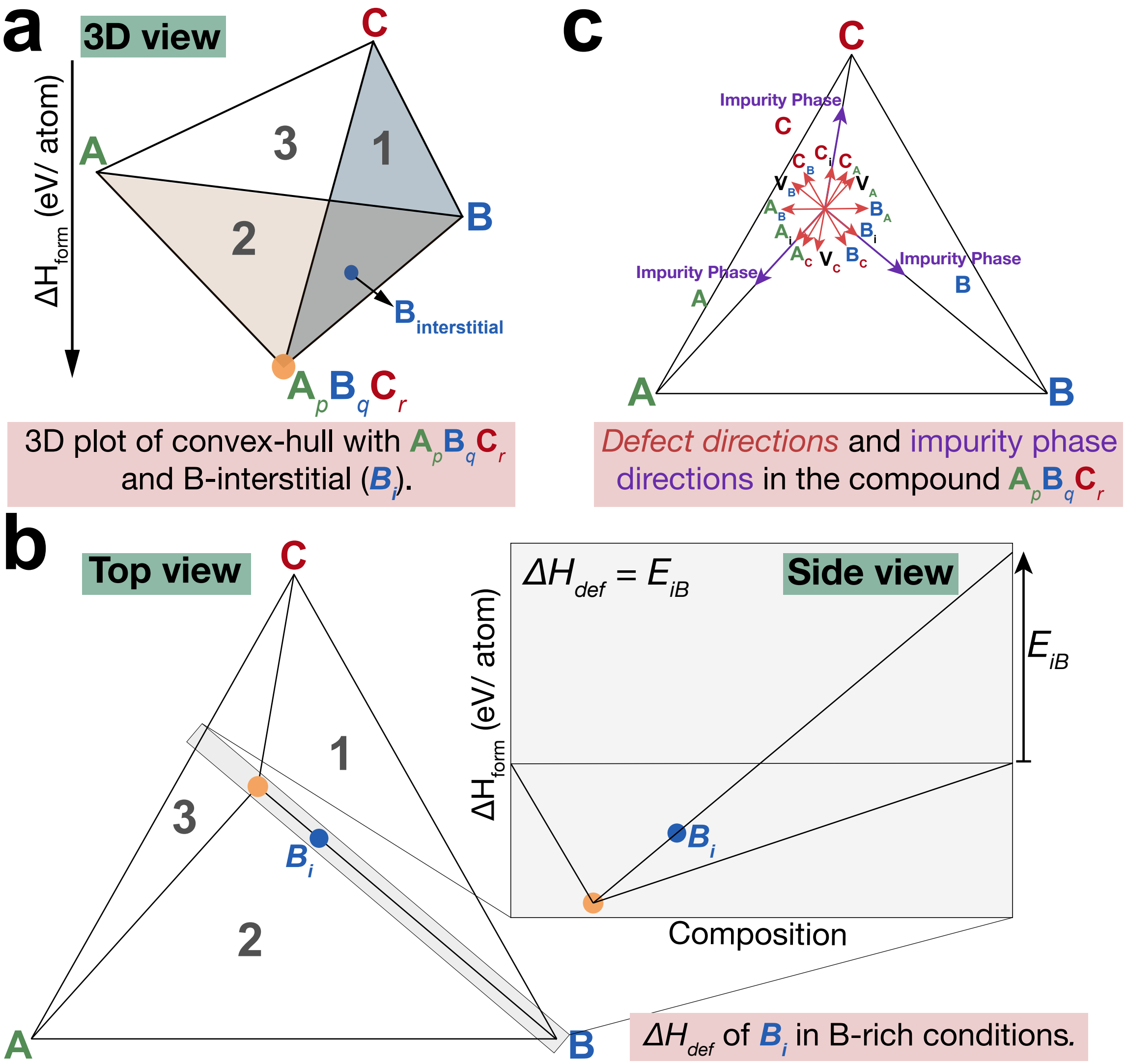
a
3D view
C
A
B
3
1
2
ΔH_form (eV/ atom)
B_interstitial
A_p B_q C_r
3D plot of convex-hull with A_p B_q C_r and B-interstitial (B_i).
c
C
Impurity Phase C
C_B C_i C_A
V_B V_A
A_B B_A
A_i B_i
A_C V_C B_C
Impurity Phase A
Impurity Phase B
A
B
Defect directions and impurity phase directions in the compound A_p B_q C_r
b
Top view
C
1
3
2
B_i
A
B
ΔH_def = E_iB
Side view
ΔH_form (eV/ atom)
E_iB
B_i
Composition
ΔH_def of B_i in B-rich conditions.

Figure 5.2: **Building a visualization tool for predicting maximal solubility limit with simple pen-and-paper drawings.** (a) Ternary convex-hull of the model system $A$-$B$-$C$ containing a single stable compound $A_pB_qC_r$. The formation energy ($\Delta H_f$) of the compound $A_pB_qC_r$ and the $B$-interstitial defect ($B_i$) in it are shown by orange and blue filled circles respectively. The three common tangent planes representing compositions in which the $A_pB_qC_r$ phase will yield two impurity phases are numbered 1, 2 and 3. (b) Left: Ternary phase diagram of the model system $A$-$B$-$C$. Can also be visualized as the top view of (a). Right: side-view of (a) along the one-dimensional composition slice indicated in the left panel. (c) Sketch showing the directions along which the composition of the compound $A_pB_qC_r$ will change due to various point defects (or *defect directions*) or shown with orange arrows. The direction of the impurity phases with respect to $A_pB_qC_r$ (or *impurity phase directions*) are shown with purple arrows. The dominant defect direction and the impurity phase direction information is sufficient to qualitatively predict the region of maximal solubility.

the compositional direction along which the defect shifts the stoichiometry of the parent phase. Hence defect directions can essentially be thought of as vectors which originate at the composition of the parent compound (see Figure 5.2 c). The impurity phase direction is simply given by the compositional direction joining the parent compound and impurity phases. Similar to the defect direction, the impurity phase directions also originate at the composition of the parent compound. Defect directions of all possible point defects in $A_pB_qC_r$ and the impurity phase directions of this compound are shown in the Figure 5.2 c. For the model compound $A_pB_qC_r$, there are 12 defect directions (complex defects have not been considered) and 3 impurity phase directions. In principle however, for a n-component compound (n > 2) in an n-component phase space, the number of defect directions will scale as n(n+1) and there should be no limit on the number of impurity phase directions.

The two solubility guidelines emerging from the thermodynamic analysis above can be stated as follows:

(i) Solubility of a defect is maximum in the thermodynamic equilibrium containing the defect direction. Solubility of the defect will be lowest in the equilibrium containing the direction opposite to the defect direction. The number of phases participating in these equilibria will not change this conclusion.

(ii) In cases where the defect direction overlaps with or lies opposite to the impurity phase direction, solubility of the defect will be equal in all multi-phase equilibria containing the parent compound and the impurity phase in question. Following from (i), this solubility value which is equal in multiple equilibria will also be an extreme value (maximum or minimum). The structure of the impurity phase will not change this conclusion.

We will first apply these guidelines to make predictions regarding the solubility of various defects in the model system $A_pB_qC_r$. By applying guideline (i) we learn that the equilibrium 1 should have maximum solubility of $C_A$, $V_A$ and $B_A$. Equilibrium 2 should have a maximum solubility of $A_C$, $V_C$ and $B_C$. Equilibrium 3 should have maximum solubility of $A_B$, $V_B$ and $C_B$. In the case of the defects $A_i$, $B_i$ and $C_i$, where the defect direction overlaps with the impurity phase direction, the guideline (ii) (which subsumes guideline (i)) is also invoked. The solubility of these defects is equal and maximum in equilibria 2 and 3, equilibria 1 and 2 and equilibria 1 and 3 respectively.

Next we will investigate the chemical conditions for minimum solubility of each of these point defects. For this, the guidelines (i) and (ii) require considering the equilibrium containing the direction opposite to the defect direction. Since each defect in the set of 12 point defects for $A_pB_qC_r$ have a directionally opposite conjugates ($V_C$ and $C_i$, $A_C$ and $C_A$ etc.) which are $180^o$ apart, the conjugates will exchange directions. By applying guideline (i) we learn that the equilibrium 1 will have a minimum solubility for $A_C$, $A_i$ and $A_B$. Equilibrium 2 will have a minimum solubility for the defects $C_B$, $C_i$ and $C_A$. Equilibrium 3 will have minimum solubility for the defects $B_A$, $B_i$ and $B_C$. In the case of the defects $V_A$, $V_B$ and $V_C$, where the defect directions are opposite to the impurity phase direction, the guideline (ii) (which subsumes guideline (i)) is also invoked. The solubility of these defects is equal and minimum in equilibria 2 and 3, equilibria 1 and 2 and equilibria 1 and 3 respectively.

We will now verify the solubility guidelines by applying them to the real life thermoelectric semiconductor examples of Ce-doped $\mathrm{CoSb_3}$, Ni-interstitials in TiNiSn and Te-doped $\mathrm{Mg_3Sb_2}$.

### 5.2.2 Applying the Guidelines to previous examples

#### Ce-doped $\mathrm{CoSb_3}$

Since adding the filler $n$-type dopant (common examples are Yb, K, Ce) in $\mathrm{CoSb_3}$ makes it a three component system, understanding solubility trends of the extrinsic dopant requires a ternary phase diagram analysis. Figure 5.3 a shows the zoomed-in version of the Ce-Co-Sb ternary phase diagram at $T$ = 973 K taken from Ref. [3]. The compositions of Ce-doped $CoSb_3$ which will yield no impurity phases are shown by a thin solid orange line which begins at the undoped $CoSb_3$ point. Although the the amount of Ce in this line can vary up to 1 %, moving the compositions away from the 1-3 stoichiometry of the undoped compound, we will call it the $CoSb_3$ phase. Compositions made outside the orange line will yield impurity phases. On the Co-Sb binary, excess Co compositions in $CoSb_3$ will yield the $CoSb_2$ impurity phase and liquid Sb impurity phase should separate out with excess Sb. At ternary compositions containing Ce, two other impurity phases, namely $CeCoSb_3$ and $CeSb_2$, can separate out in addition to $CoSb_2$ and liquid Sb. Depending on the composition, the ternary samples can yield either one or two impurity phases. Regions yielding two impurity phases are numbered 1 (liquid Sb and $CeSb_2$ impurity), 2 ($CeSb_2$ and $CeCoSb_3$ impurity) and 3 ($CeCoSb_3$ and $CoSb_2$). The relatively smaller boundaries separating these regions from each other represent compositions which will contain only a single impurity phase.

In mixtures with impurity phases, the composition of the $CoSb_3$ phase itself (point on the orange line) will depend on the number of impurity phases. In the larger regions containing two impurity phases (1, 2 and 3 in Figure 5.3 a), the $CoSb_3$ phase is constrained by the Gibb's phase rule to take only a single value in composition space. The composition of Ce-doped $CoSb_3$ in the region 1 (liquid Sb and $CeSb_2$ impurity) is given by the blue point on the orange line. In the regions 2 and 3, $CoSb_3$ has a higher Ce content but these points are indistinguishable from each other as they essentially overlap in composition space (orange point on the solid orange line).

To understand the relative position of the $CoSb_3$ phase compositions in the regions 1, 2 and 3 using the solubility guidelines we first draw the defect direction as well as the competing phase directions (see arrows in 5.3 b). Thermodynamically, the filler Ce-dopant in the Skutterudite structure is the same as an interstitial defect in that only the number of Ce atoms in the structure will change in either case. Hence, the dominant filler defect will

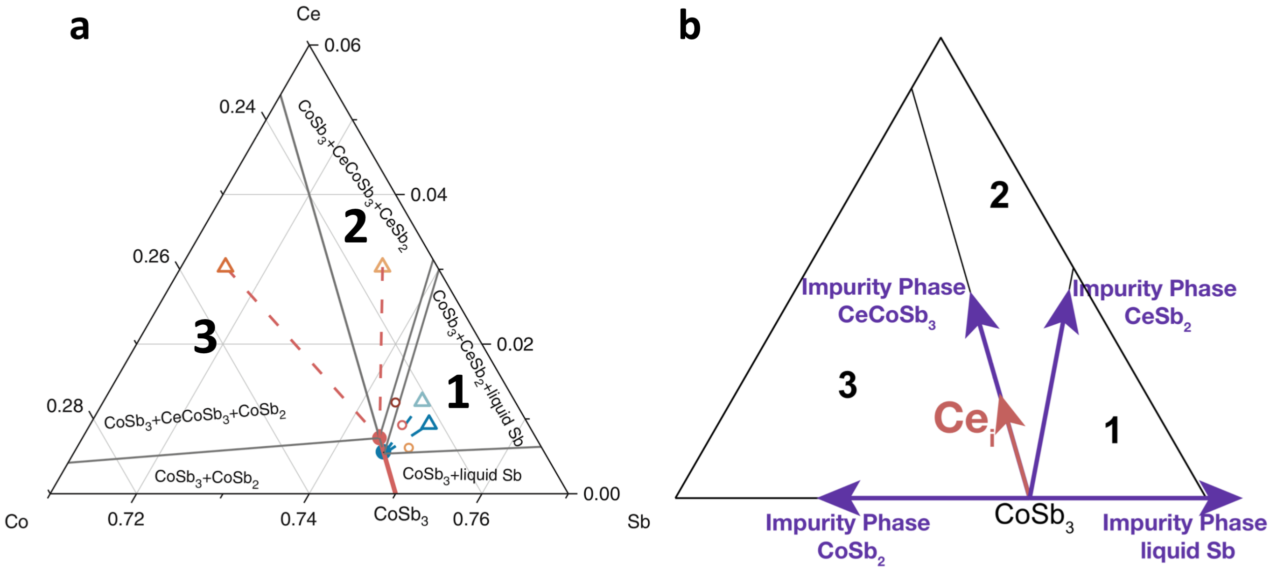
a
Ce
0.06
0.24
0.04
0.26
0.02
0.28
0.00
Co
0.72
0.74
CoSb$_3$
0.76
Sb
CoSb$_3$+CeCoSb$_3$+CeSb$_2$
CoSb$_3$+CeSb$_2$+liquid Sb
CoSb$_3$+CeCoSb$_3$+CoSb$_2$
CoSb$_3$+CoSb$_2$
CoSb$_3$+liquid Sb
1
2
3
b
Impurity Phase CeCoSb$_3$
Impurity Phase CeSb$_2$
Impurity Phase CoSb$_2$
Impurity Phase liquid Sb
Ce$_i$
CoSb$_3$
1
2
3

Figure 5.3: **Rationalizing Ce$_i$ solubility in CoSb$_3$ prepared in varied chemical conditions.** (a) Ternary Co-Sb-Ce phase diagram zoomed in close to the ternary CoSb$_3$ phase (orange line) taken from Ref. [3]. The compositional regions which yield two impurity phases in CoSb$_3$ samples are numbered 1, 2 and 3. The relatively smaller regions which yield just one impurity phase lie in between these numbered regions. The impurity phases for the larger regions are labelled. (b) Sketch showing the dominant defect (Ce$_i$) direction and the impurity phase directions for CoSb$_3$.

have the same defect direction as the Ce-interstitial. Since the defect direction overlaps with the CeCoSb$_3$ impurity phase direction we use the guideline (ii) (which subsumes the guideline (i)) first to understand the Ce-solubility trends. As expected, Ce-solubility is highest and equal in regions 2 and 3. More generally in agreement with guideline (i), the solubility is highest in the equilibrium containing the CeCoSb$_3$ impurity phase. Following from guideline (ii), we further note that, because the impurity phase direction CeSb$_2$ is neither overlapping nor opposite to the defect direction, the Ce-solubility in regions 1 and 2 (which involve CoSb$_3$ and CeSb$_2$ phases) will be unequal.

### Te-doping in Mg$_3$Sb$_2$

Similar to the case of Ce-doped CoSb$_3$, Te-doped Mg$_3$Sb$_2$ is also a three-component system and understanding Te-solubility will require a ternary phase diagram analysis. Unlike the

Skutterudite example however, the $Mg_3Sb_2$ example is more complex on two counts. First, the dominant extrinsic defect is a substitutional defect ($Te_{Sb}$) instead of an interstitial defect and its energetics is affected by the chemical potential of both Te as well as Sb. Hence, it is not straightforward whether the maximum Te-solubility will occur in Te-rich (region 2 in Figure 5.4) or Sb-poor conditions (region 1 in Figure 5.4). Second, concentrations of the intrinsic compensating charged defect $V_{Mg}^{-2}$ are comparable to that of the extrinsic defect.

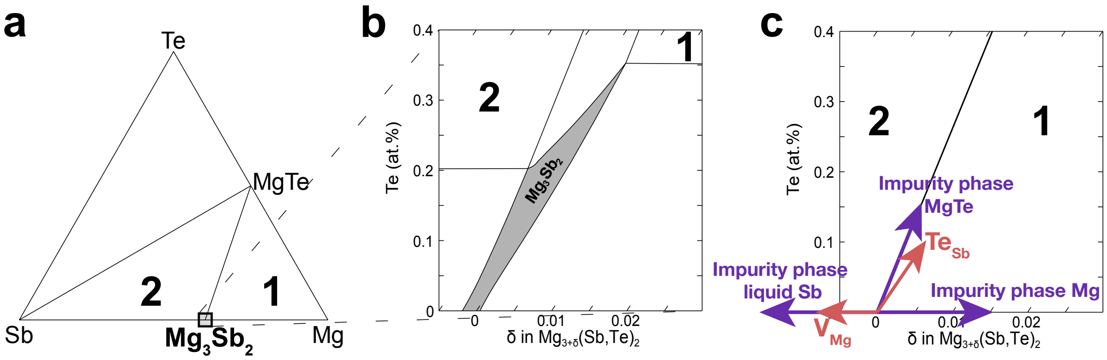

Figure 5.4: **Rationalizing chemical conditions of maximal $Te_{Sb}$ solubility in $Mg_3Sb_2$.** (a) $T$ = 0 K Mg-Sb-Te ternary phase diagram. The compositional regions which yield two impurity phases in $Mg_3Sb_2$ are numbered 1 and 2. (b) $T$ = 900 K Mg-Sb-Te ternary phase diagram zoomed-in close to the $Mg_3Sb_2$ phase [2]. The compositional region which yields no impurity phase in $Mg_3Sb_2$ phase is shown in grey. The unnumbered compositional regions yield one impurity phase (c) Schematic showing the dominant defect ($Te_{Sb}$) direction and the impurity phase directions for $Mg_3Sb_2$.

The Figure 5.4 a shows the Mg-Sb-Te ternary phase diagram and the inset shows a version zoomed-in close to the $Mg_2Sb_2$ single phase region calculated in Ref. [2]. The compositions which will yield no impurity phases are shown with the grey region (see Figure 5.4 b). Unlike the case of Ce-doped $CoSb_3$, the single phase region has a noteworthy width due to large changes in the concentration of the $V_{Mg}^{-2}$ defect. Although there is a large amount of $Te_{Sb}$ and $V_{Mg}^{-2}$ defects moving the composition of the single phase region away from the binary 3-2 stoichiometry of the undoped compound, we will reference the entire grey region in Figure 5.4 as just the $Mg_3Sb_2$ phase. Compositional regions of the phase diagram (see Figure 5.4 a) which will yield two impurity phases are numbered 1

(Mg and MgTe) and 2 (MgTe and Sb). These regions are separated by relatively smaller region which yield only MgTe as a single impurity phase (see Figure 5.4 b). The Mg and Sb impurity phases will phase separate under Mg-excess and Sb-excess compositions respectively.

To understand the Te-solubility in $Mg_3Sb_2$ in view of the thermodynamic guidelines, we explicitly draw the defect direction and impurity phase directions. Based on guideline (i), we notice straightaway that region 1 contains the $Te_{Sb}$ defect direction and should therefore show the highest Te-solubility. Indeed, the maximum solubility of Te in $Mg_3Sb_2$ is observed in the region 1. The guideline (ii) is not applicable here since the $Te_{Sb}$ defect direction does not overlap with any impurity phase direction.

### Ni-interstitials in TiNiSn

Since TiNiSn is a three component system, understanding Ni-solubility in TiNiSn requires a ternary phase diagram analysis. The zoomed-in version of the Ti-Ni-Sn phase diagram at T = 1273 K taken from Ref. [4] is shown in Figure 5.5 a. The single phase region of TiNiSn is shown by the solid green line. Although the the amount of Ni in this line can vary, moving the composition away from the 1-1-1 stoichiometry of the undoped compound significantly, we will call it the TiNiSn phase. All compositions lying outside the solid green line will yield either one or two impurity phases. Regions containing two impurity phases are numbered 1 ($Ti_5NiSn_3$ and $Ti_6Sn_5$), 2 ($Ti_6Sn_5$ and liquid Sn impurity), 3 (liquid Sn and $TiNi_2Sn$ impurity) and 4 ($TiNi_2Sn$ and $Ti_5NiSn_3$). Compositional regions lying between these portions of the diagram will contain only one impurity phase. In regions 1, 2, 3 and 4 which contain two impurity phases, the TiNiSn phase is constrained by the Gibb's phase rule to have a single composition which is represented by the blue and green circles at the end of the green line. So, in addition to yielding the $Ti_5NiSn_3$ and $Ti_6Sn_5$ impurity phases, the composition of the TiNiSn phase for *any* sample prepared in region 1 will be given by the blue point.

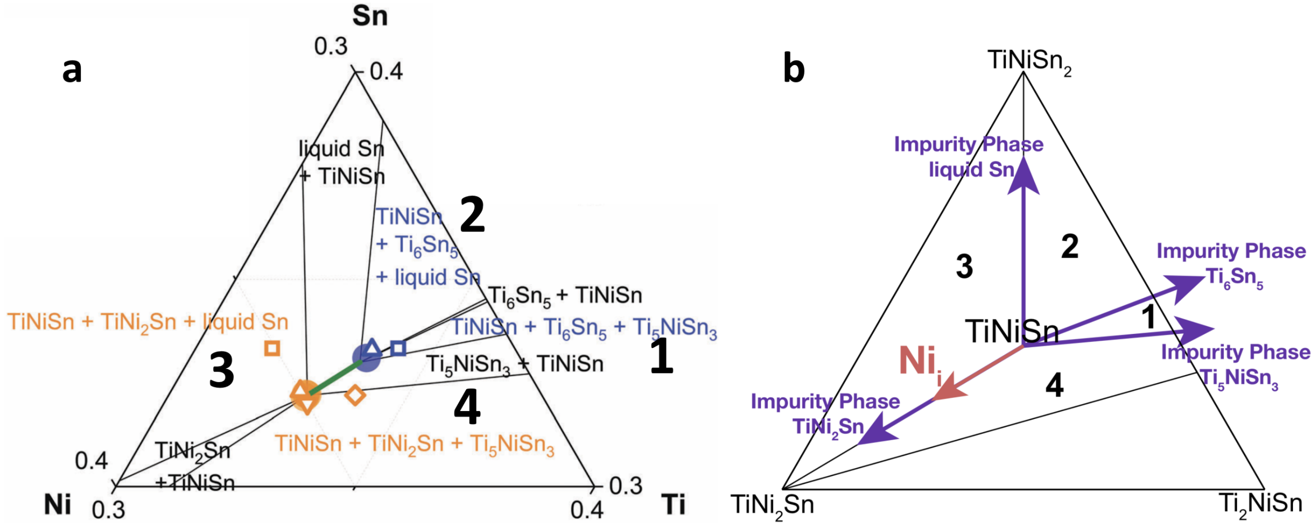
a
Sn
0.3
0.4
liquid Sn
+ TiNiSn
TiNiSn
+ $Ti_6Sn_5$
+ liquid Sn
2
$Ti_6Sn_5$ + TiNiSn
TiNiSn + $Ti_6Sn_5$ + $Ti_5NiSn_3$
1
TiNiSn + $TiNi_2Sn$ + liquid Sn
3
$Ti_5NiSn_3$ + TiNiSn
4
TiNiSn + $TiNi_2Sn$ + $Ti_5NiSn_3$
0.4
$TiNi_2Sn$
+TiNiSn
Ni
0.3
0.3
0.4
Ti
b
$TiNiSn_2$
Impurity Phase
liquid Sn
3
2
Impurity Phase
$Ti_6Sn_5$
1
TiNiSn
$Ni_i$
Impurity Phase
$Ti_5NiSn_3$
4
Impurity Phase
$TiNi_2Sn$
$TiNi_2Sn$
$Ti_2NiSn$

Figure 5.5: **Rationalizing $Ni_i$ solubility in TiNiSn prepared in varied chemical conditions.** (a) Ternary Ti-Ni-Sn phase diagram zoomed in close to the ternary TiNiSn phase (green line) taken from Ref [4]. The compositional regions which yield two impurity phases in half-Heusler TiNiSn samples are numbered 1, 2, 3 and 4. The compositions which yield just one impurity phase lie in between these numbered regions. The impurity phases are labelled in each case. (b) Sketch showing the dominant defect ($Ni_i$) direction and the impurity phase directions for TiNiSn.

Technically the TiNiSn phase should have four distinct compositions corresponding to the regions 1, 2, 3 and 4 in the Figure 5.5 a. However, even on the scale of this zoomed-in phase diagram, it is hard to distinguish the two points at the end of the single phase region. To understand this dependence of Ni-solubility on chemical conditions we apply the solubility guidelines. We notice that the defect direction overlaps with the full-Heusler $TiNi_2Sn$ impurity phase (Figure 5.5 b). As a result, the Ni solubility is highest in all equilibria containing TiNiSn and the impurity phase $TiNi_2Sn$, which are both regions 3 and 4. Hence solubility is equal and maximum in regions 3 and 4. The direction opposite to the $Ni_i$ defect direction is contained by the region 2, which following from guideline (i) should have the smallest Ni solubility. Although the Ni solubility in regions 1 and 2 is hard to distinguish in Figure 5.5 a, EPMA-WDS data provided in Ref. [4] indeed confirms a smaller Ni content for the case of region 2 ($Ti_{33.5}Ni_{33.2}Sn_{33.3}$) when compared to region 1

($Ti_{33.4}Ni_{33.4}Sn_{33.2}$). Nevertheless, the extremely close Ni percentage composition for region 1 and 2 still needs an explanation. To this end, we will note that the direction opposite to the $Ni_i$ defect direction is quite close to the impurity phase direction of $Ti_6Sn_5$. Following from guideline (ii) then, Ni solubilities in regions 1 and 2 should be similar.

The TiNiSn-$TiNi_2Sn$ system is a typical pseudobinary system where mixing occurs at the vacant sublattice of the TiNiSn half-Heusler structure. As a result, the Ni-solubility in the TiNiSn half-Heusler can often be understood just like other simpler pseudobinaries between elements or binary compounds such as W-Cr or PbS-PbTe, respectively. In this understanding, the solubility of PbS in PbTe will remain the same regardless of whether the conditions are Pb-rich or Pb-poor. This is because, just as in the case of TiNiSn-$TiNi_2Sn$, the dominant defect direction ($S_{Te}$) overlaps with the impurity phase (PbS) direction. As a result, drawing the solvus curves in the typical pseudobinary system such as PbTe-PbS using a single line on a one-dimensional composition slice is actually even representative of Pb-rich and Te-rich chemical conditions. This equal solubility is a thermodynamic requirement and has recently been shown to even hold in cases such as $Mg_2Si$-$Mg_2Sn$ (Ref. [127]) for which the previous works had multiple discrepancies in the reported solvus. TiNiSn-$TiNi_2Sn$ is a slightly different system in that it is a pseudobinary between ternary compositions. But just like the simpler PbTe-PbS system, TiNiSn-$TiNi_2Sn$ is also constrained by guideline (ii) for equal Ni-solubility in regions 3 and 4, which are both Ni-rich conditions (see Figure 5.5)). However, the similarity of Ni-solubility on the Ni-poor side (see region 1 (Ti-rich) and region 2 (Sn-rich) in Figure 5.5), for which there is no equivalent in the simpler PbTe-PbS system, is merely a coincidence of the fact that the impurity phase $Ti_6Sb_5$ lies so close to the 1-1 TiSn stoichiometry. To this extent, ternary compound based pseudobinaries can be more complex than those based in binary compounds. In the following section, we discuss pseudobinaries in the more complex quaternary composition space in which our thermodynamic guidelines predict even the solvus curve separating the two-phase region and the solid-solution to be chemical-condition-dependent.

### 5.2.3 Predicting Unusual Pseudobinary Phase Diagrams

Phase diagrams of pseudobinary solid-solution systems are perhaps the most commonly studied for materials design. In the case of thermoelectrics, psudobinary phase diagrams of chalcogenide systems such as PbTe-PbS, [129] PbTe-SrTe [130] and PbTe-$AgSbTe_2$ [131] are often studied to predict accurate synthesis conditions for designing two-phase nanostructured materials. The solubility of the two phases into each other in a typical pseudobinary is usually drawn along a 1-dimensional compositional line joining the end-members. As discussed above using the guideline (ii) for the cases of TiNiSn-$TiNi_2Sn$ and $Mg_2Si$-$Mg_2Sn$, the assumption in drawing a single solvus curves for pseudobinaries along a 1-dimensional composition line is that they should be independent of chemical conditions associated with elements other than $Ni_i$ or $Sn_Si$ defect. This result however, does not necessarily hold for all pseudo binary examples.

Consider the model pseudobinary system $AD - BCD_2$ (see Figure 5.6) which is a prototype composition for systems in the Chalcogenide (PbTe-$AgSbTe_2$), Skutterudite ($CoSb_3$-$Co_2Sn_3Te_3$) [121] and Heusler (TiCoSb-$Ti_2FeNiSb_2$) [13] families of compounds. Among these, the chalcogenide based pseudobinaries [132, 133, 134, 135, 73, 136, 137, 138, 139] in particular have attracted a lot of attention for their thermoelectric properties in the past two decades owing to early reports of $zT > 2$ in PbTe-$AgSbTe_2$ [132]. Beside being set in a more complex quaternary composition space, this system is also different from the examples discussed above in that one of its end-members is a mixed cation system. The conclusions we make in this section however, should also in principle apply for the simpler pseudobinary examples such as Si-ZnS as well.

To understand how the solvus boundaries might depend on chemical conditions using our thermodynamic guidelines, we draw the defect directions and the impurity phase directions for the end members $AD$ and $BCD_2$ on a pseudoternary composition slice $AD$-$BD$-$CD$ (see Figure 5.6). We consider the substitutional defects $B_A$ and $C_A$ in $AD$ and $A_B$

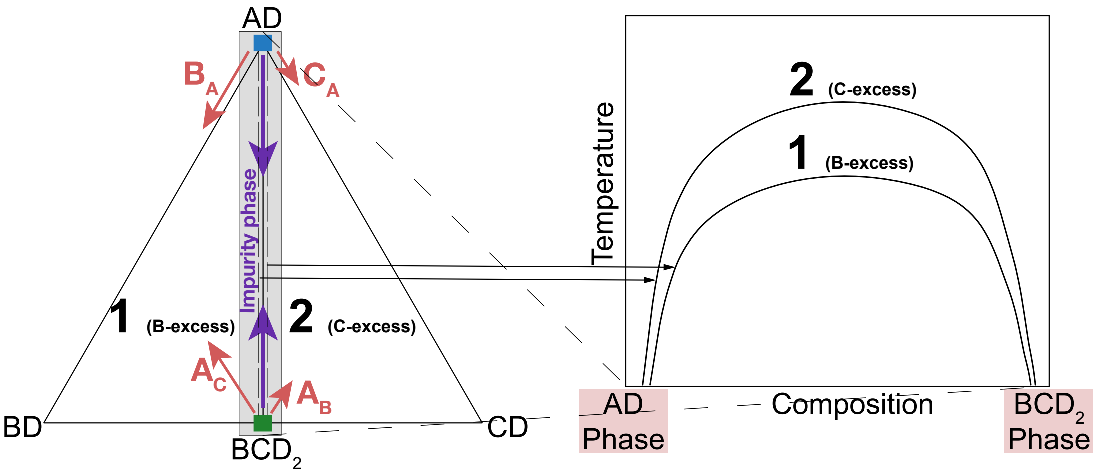

Figure 5.6: **Prediction of unusual pseudobinary solid-solution phase diagram.** Sketch for a possible Temperature-Composition phase diagram (right) for the model pseudobinary system $AD - BCD_2$. The $x$-axis represents the composition between the $AD$ and $BCD_2$ *phases* (instead of the exact compositions $AD$ and $BCD_2$) under $B$-rich and $C$-rich conditions. The figure on the left locates this pseudobinary on the $AD$-$BD$-$CD$ pseudoternary composition slice. The substitutional defect directions for each end-member of the pseudobinary end-members are shown by orange arrows. The defect direction vectors are drawn of varying lengths to indicate differences in their energetics. The dominant defect between each pair of substitutional defect is shown by a longer vector. The impurity phase directions for the end-members are shown by purple arrows.

and $A_C$ in $BCD_2$. The length of the defect direction vectors are unequal, indicating that the tendency to form one kind of substitutional defect is much larger than the other. A good example of such defect behaviour is observed in the PbTe-AgSbTe$_2$ case where Pb substitutes almost exclusively on the Sb-site [140]. The key difference between the system drawn in Figure 5.6 and the typical pseudobinary examples such as TiNiSn-TiNi$_2$Sn and Mg$_2$Si-Mg$_2$Sn is that the substitutional defect directions do not overlap with the impurity phase directions. Hence, following from guideline (ii) the solubility of the substitutional defects in $B$-rich and $C$-rich conditions will be unequal. This expected difference in solubility between chemical conditions should clearly show in a temperature-composition phase diagram (see Figure 5.6). Although, we choose a complex quaternary system, our conclusions based on thermodynamic theory should in principle also apply to similar systems (possibly Si-ZnS) in ternary composition space.

### 5.2.4 Solubility of defect complexes

Although we do not discuss here any examples of complex defects, the solubility guidelines (i) and (ii) can be extended to them without any loss of information. Obviously, defect directions in the case of these complex defects will be different from the compositional directions of the point defects (examples in Figure 5.2)

### 5.2.5 What if I do not know the phase diagram beforehand?

Both guidelines (i) and and (ii) suggest that the defect solubility should be highest along the defect direction. So in principle, if the goal of the study is to achieve maximum solubility, even the knowledge of the phase diagram (see Figure 5.1) is not required. Synthesizing the samples simply along the compositional the direction recommended by the thermodynamic guidelines should by sufficient to achieve maximum solubility from the. We will note however that this might not be very straightforward exercise experimentally since the intended *nominal* composition of the samples can often be quite different from the *actual* composition which gets made. An example of such compositional differences have been clearly described in a phase diagram by Ohno et al in Ref. [120]. These differences in composition occur possibly due to large inequalities in the vapour pressure of the elements used in synthesis. Although such a shift in the intended composition of the samples are expected to be systematic to a large extent, its magnitude can be large enough to impact solubility significantly by changing chemical conditions. As a result, to check if the samples were prepared along the intended compositions chosen by applying the thermodynamic guidelines, we also recommend checking the impurity phases formed in the process. If the multi-phase equilibria involving the impurity phase contains the defect direction expected from the above guidelines, the unintended shift in composition should have no bearing on the resulting solubility.

### 5.2.6 Effects of Fermi-level dependency of defect energetic dependence of $\Delta H_{def}$ in semiconductors

All the three examples, namely $CoSb_3$, $Mg_3Sb_2$ and TiNiSn, discussed above are semiconductor materials. The fact that solubility guidelines predict defect solubility trends correctly in all three cases speaks for its value in semiconductor design strategies. However, the thermodynamic theory used to develop the solubility guidelines is exact only for metallic systems and it is possible that their conclusions do not hold in the case of all insulator examples. As discussed in Chapter 4, solubility of charged defects in semiconductors is determined by evaluating its $\Delta H_{def}$ value at the equilibrium position of the Fermi-level ($E_f^{eq}$). In cases where (a) the position of $E_f^{eq}$ was determined entirely by a single charged defect or (b) the dominant defect was charge neutral with the position of $E_f^{eq}$ having no bearing on its solubility, the guidelines developed in Section 5.2.1 would still hold. However, the position of $E_f^{eq}$ can sometimes be quite sensitive to the energetics of more than one (two in most cases) charged defects. This other defect(s), is the compensating defect with a charge opposite in sign to the defect whose solubility we are interested in. Since the thermodynamic guidelines developed in section 5.2.1 only accounts for cases with a single defect they can not make a direct conclusions regarding the position of $E_f^{eq}$.

Nevertheless, these more complicated cases of solubility, can still be treated by going one step further. For this, we remember that the overall (occurring simultaneously *regardless* of $E_f$ values) changes in charged defect energetics with varying chemical conditions (chemical potential changes) will qualitatively still be consistent with the guideline (i). So, we can use the thermodynamic guideline (i) for both the charged defects (defect of interest and compensating defect) individually for predicting the extent to which the $E_f^{eq}$ shifts. These $E_f^{eq}$ shifts can subsequently used to estimate if the solubility for the defect of interest increases or decreases.

After considering energetics of both defects, we expect the conclusions from solubility guideline (i) to still be quite robust except possibly when the compensating defect is much more sensitive to chemical conditions than the defect of interest itself. The example of Te-solubility in $Mg_3Sb_2$ ($E_g$ = 0.6 ev) shown in Figure 5.4 accounts for both $Te_{Sb}^{+1}$ and $V_{Mg}^{-2}$ defects and their $E_f$ dependencies. As discussed above, the example of Te-solubility in $Mg_3Sb_2$ is in agreement with the guideline (i) despite the Mg-chemical potential (relevant to the compensating $V_{Mg}^{-2}$ defect) changing between its extreme values. The conclusion of guideline (ii), discussing the chemical conditions in which solubility of the defect is equal, can be sensitive to the magnitude of the band-gap if we are interested in charged defects. In larger band-gap systems, the Fermi-level can be quite sensitive to the number of carriers which in turn depend on the chemical conditions. As a result, if the defect of interest is charged the solubilities could become unequal. We would like to point out however, that in larger gap systems with smaller dielectric constants the binding energy to form charge neutral defect complexes is also higher. As a result, most reports discussing point defects in larger gap systems automatically assume that the dominant defects form charge neutral complexes Ref. [116, 117]. Conclusions of guideline (ii) will remain unchanged if the dominant defect is charge neutral.

# Chapter 6

# A Valence Balanced Rule for Discovery of Defective half-Heulsers

## 6.1 Overview

The stability of the semiconductor transition metal based half-Heusler compounds, with the general formula $XYZ$, is often understood using the well-known 18-electron rule. This rule for stability has been used extensively in previous computational works for understanding stability of experimentally reported 18-electron compounds and predict new ones almost exhaustively. However, there are also reports of non-18-electron compounds as well, the thermodynamic stability of which — in addition to seemingly disobeying the widely accepted 18-electron rule — cannot be reproduced using computational approaches. This inability to computationally corroborate the thermodynamic stability of these compounds diminishes the predictive power required for an efficient high-throughput search.

Using first-principles DFT we systematically investigate the thermodynamic stability and off-stoichiometry in 108 nominal 19-electron half-Heusler (hH) compounds. We demonstrate unambiguously that considering a cation deficiency towards the off-stoichiometric valence balanced, VEC=18 composition is necessary for explaining the stability of all previously reported nominal VEC=19 compounds. This is understandable in terms of an energy benefit from a Zintl valence balance that offsets the energy penalty of forming defects in nearly all cases. Thus, we propose a valence balanced rule to understand the ground state stability of half-Heuslers *regardless* of stoichiometry and nominal electron count (8, 18, 19, 27 etc.). Using this generalized rule we (a) predict 16 previously unreported nominal 19-electron XYZ half-Heuslers and (b) rationalize the reports of giant off-stoichiometries in compounds such as $Ti_{1-x}NiSb$, which has been known for over 50 years. Of the 16 new compounds predicted here, $Ti_{1-x}PtSb$ was synthesized and the half-Heusler phase confirmed through X-ray studies.

## 6.2 Introduction to Chemistry of Heusler Thermoelectrics

Heusler compounds, with the general formula $XYY'Z$, are an extensively studied class of functional materials based in an intermetallic chemistry which spans a significant fraction of the periodic table. [141] Each element in this cubic structure forms an interpenetrating FCC lattice. When $Y$ an $Y'$ are same element in these compounds — as in the example of $VFe_2Al$ — the resulting structure is known as the full-Heusler structure. A vacant $Y'$ site in the structure instead would lead the so-called half-Heusler structure type, which is another compound in Heusler family.

Typical stable half-Heusler compounds are semiconducting and have attracted attention as potentially high-performing thermoelectrics [142, 143]. These materials exhibit extraordinary electrical properties [144] and thermal properties which can be engineered substantially through control of defects [4, 13, 85]. The thermoelectric figure of merit ($zT$) of both $n$-[145, 146] and $p$-type [147, 148, 149] half-Heusler materials are comparable to that of state-of-the-art thermoelectrics. Additionally, these materials have superior mechanical properties [150, 151] in comparison to well-known chalcogenide-based thermoelectrics, making them more advantageous for device applications.

### 6.2.1 Zintl Chemistry perspective of half-Heuslers. A Valence Balanced Rule

Valence electron counting (VEC) in half-Heusler compounds is widely used for a straightforward understanding of their electrical and magnetic properties. [141] All transition metal based semiconducting half-Heulsers, such as TiNiSn, stabilize at a VEC = 18 configuration (VEC = 0 ($\mathrm{Ti}^{4+}s^0d^0$) + 10 ($\mathrm{Ni}^0d^{10}$) + 8 ($\mathrm{Sn}^{4-}$ $s^2p^6$) = 18). The semiconducting properties of VEC = 18 half-Heuslers allows for an understanding analogous to that of ionic compounds within the Zintl chemistry framework.[152] Within this framework, one can rationalize the VEC = 18 half-Heuslers as a subset of all valence balanced (net valence (NV) = 0) semiconductors *regardless* of their VEC value.

The half-Heusler $XYZ$ structure (space group F-43m) consists of three atomic sites located at the Wyckoff positions $X$ = 4a (0, 0, 0), $Y$ = 4c ($\frac{1}{4}$, $\frac{1}{4}$, $\frac{1}{4}$) and $Z$ = 4b ($\frac{1}{2}$, $\frac{1}{2}$, $\frac{1}{2}$). Typically $X$-site atoms are early transition metal elements, $Y$-site atoms are late transition metal elements and the $Z$-site is occupied by $p$-block metals (Sb, Sn, Bi for example). The electronegativities of the $X$-site atom lies in the range 1.2-1.7, whereas that of the $Y$ and $Z$-site atoms are quite similar and lie in much higher ranges 1.8-2.4 and 1.7-2.2 respectively.[141] Hence, among the three elements, the $X$-site atoms form an electropositive sub-lattice of the structure. Due to the significant electronegativity differences between $X$ and the other sub-lattices, the conduction band states have a predominantly $X$-type character making it the cationic sub-lattice which donates its valence electrons and becomes $s^0d^0$. The more electronegative $Y$- and $Z$-site atoms on the other hand, form an $sp^3$ covalently-bonded tetrahedrally-coordinated anionic substructure due to their similar electronegativities. In addition to the electronegativity differences, the band-gap in typical VEC = 18 half-Heuslers arises from a strong coupling between the

$d$-states from the nearest neighbor $X$- and $Y$-site atoms which are both tetrahedrally coordinated sub-lattices.[152, 6]

The electron count of 18 in half-Heuslers corresponds to empty and filled valence shells ($Xs^0d^0$ + $Yd^{10}s^0p^0$ + $Zs^2p^6$) of the cation and anions respectively – where the filled $d^{10}$ states of the $Z$-atoms are not considered valence electrons and ignored for the counting. Hence the historic '18-electron rule' is simply a special condition of the valence balanced configuration (e.g. Net valence (NV) = 4 ($Ti^{4+}s^0d^0$) + 0 ($Ni^0d^{10}$) - 4 ($Sn^{4-}$ $s^2p^6$) = 0) in structures with $XYZ$ composition where the electron count refers to one filled $s^2p^6$-bonding configuration (attributed to anion $Z$) and one filled $d^{10}$-bonding configuration (attributed to late transition metal $Y$). For the same structure this special condition of 18 electrons will equal to 8 electrons if the compound has $Y$-atom which is a $p$-block element (for example:- LiSiAl [153], $Mg_2Si$ etc). Similarly, in the case the $X$-site atom is replaced by a rare-earth element, such as the half-Heusler semiconductor DyNiSb, the valence balanced configuration is attained at 27-electron (e.g. Net Valence (NV) = 3 ($Dy^{3+}s^0f^9$) + 0 ($Ni^0d^{10}$) - 3 ($Sb^{3-}$ $s^2p^6$) = 0). Depending on the choice of the rare-earth element like Gd (25-electron), Tb (26-electron), Ce (19-electron) and Nd (21-electron) the number of valence electrons will be different. In all these cases, valence balancing (Net Valence (NV) = 0) ensures a completely filled bonding states and completely empty anti-bonding states. Deviating from this closed shell configuration leads to a weakening of bonding interactions, thereby destabilizing the material. Thus, we conclude that having a valence-balanced configuration, regardless of its electron count, is a necessary condition for stabilizing the ground state of stoichiometric half-Heusler semiconductors.

As can be expected from their structural similarities with half-Heuslers, well-known Zintl compounds are also commonly known to stabilize with valence balancing. For instance, binary skutterudite compounds such as $CoSb_3$ consist of a covalently bonded polyanionic unit $(Sb_4)^{4-}$ and a cationic sub-lattice $Co^{3+}$ in the $d^6$ configuration. The structure of $CoSb_3$ can be understood as NV = 12 (4 $Co^{+3}$ $d^6$) - 12 (3 $Sb_4^{4-}$ $s^2p^6$) = 0 valence balanced compound. Similarly, more complex Zintl compounds such as $Ca_{14}AlSb_{11}$ is found in a semiconducting valence balanced (NV = 28 (14 $Ca^{2+}$) - 9 ($AlSb_4^{9-}$)- 7 ($Sb_3^{7-}$) - 12 (4 $Sb^{3-}$) = 0) configuration. It is important to note that while the electron count per formula unit between these compounds differ from each other, the valence balanced NV = 0 feature is common. This powerful valence balanced rule has been used in design of complex multi-component Zintls for thermoelectric and magnetic applications.[154, 155, 156, 157]

## 6.3 Context and Motivation

While 18-valence electron half-Heuslers are typically semi-conducting due to complete filling of bonding orbitals, non-18-electron systems are expected to exhibit a metallic behavior. Reports of half-Heuslers predominantly consist of compounds with a VEC = 18 (e.g. TiNiSn, TiCoSb etc). On the other hand, reports of non-18-electron half-Heuslers (VEC =17 (e.g. ScPtSn, TiCoSn), VEC = 19 (e.g. TiNiSb, VCoSb)) are more rare (see Figure 6.1). The large number of VEC = 18 compounds is attributed to the strong bonding interaction associated with the filled bonding and unfilled anti-bonding states that occurs when the Zintl valences are balanced. [152]

Transition metal based VEC = 18 half-Heuslers have already been investigated extensively with 63 compounds (see Figure 6.1) synthesized previously (from the Inorganic Crystal Structure Database [5], Ref. [6] and Ref. [7]). Additionally, if stability predictions from high-throughput computational approaches [6, 7] are counted, the number of VEC = 18 half-Heuslers adds to a total of 82 (see Figure 6.1). The number of experimentally reported non-18-electron half-Heuslers (VEC = 17 (e.g. ScPtSn, TiCoSn), VEC = 19 (e.g. TiNiSb, VCoSb)) in ICSD however, are typically an order of magnitude smaller in number (see Figure 6.1). Unlike the case of VEC = 18 compounds in which computational approaches are able to predict novel stable compositions in addition to verifying the ones already reported, high-throughput computations for VEC = 19 half-Heuslers

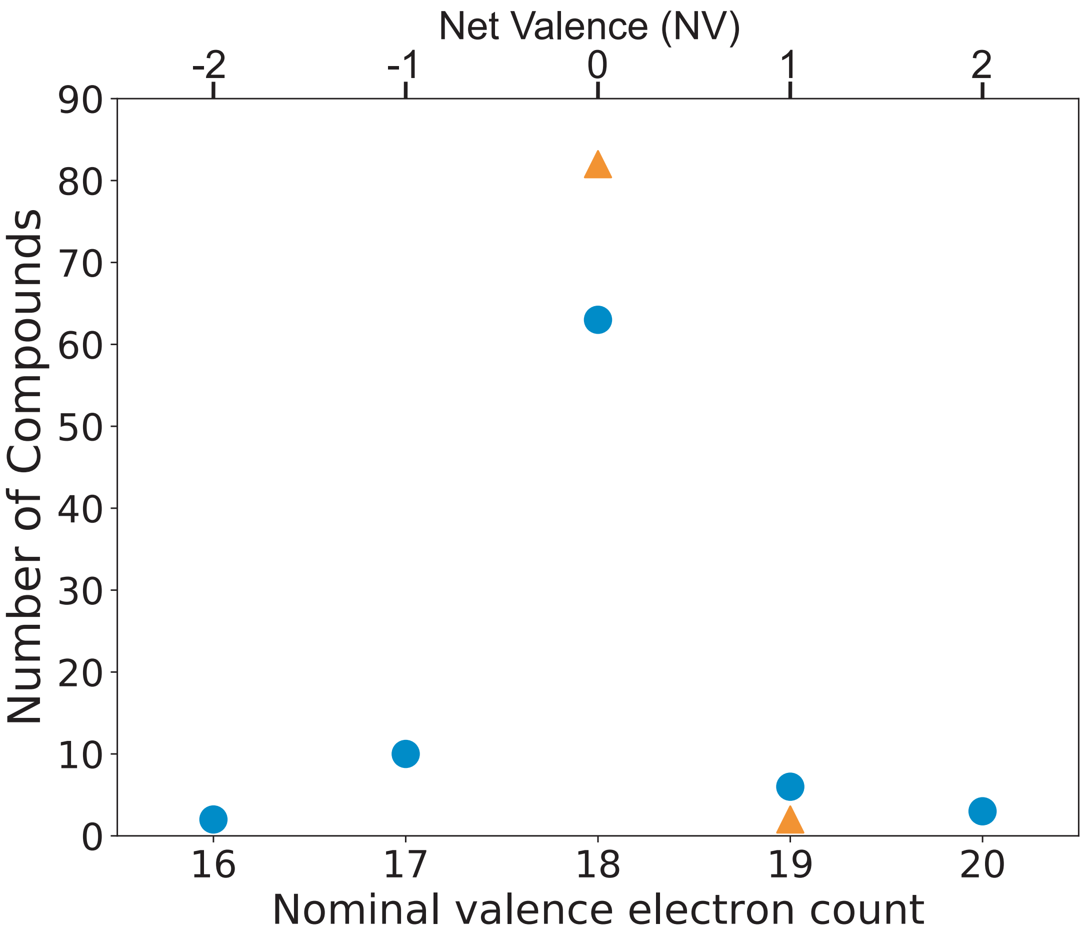

Figure 6.1: **Status of thermodynamic stability predictions prior to this work.** Number of half-Heusler compounds reported (blue circles, ICSD [5] and Ref. [6]) and predicted stable (red triangles, Ref. [6, 7] and OQMD [8, 9] ) using the defect-free $XYZ$ stoichiometry prior to this work as a function of nominal valence electron count (VEC) or (alternatively) net valence (NV).

using the $XYZ$ stoichiometry underpredicts the number of 19-electron compounds (see Figure 6.1). The poor predictive power of first-principles thermodynamics in 19-electron half-Heuslers suggests that the origin of its stability is not well understood. Due to their much smaller numbers, non-18-electron compounds are often thought to be stable *despite* the weak bonding interactions associated with their partially occupied bonding or anti-bonding states, making them outliers or exceptions to the '18-electron rule'.

The electrical properties of the few known VEC = 19 half-Heuslers have long been discussed in the light of their metallic electronic structure. However, contrary to expectations, these compounds are also emerging as potential thermoelectric materials. [158, 159, 160, 161, 87] Recently, the NbCoSb system exhibit a $zT \sim 0.9$ at 1100 K, [87] which is comparable to state of the art VEC = 18 half-Heusler thermoelectrics such as (Ti,Zr,Hf)NiSn compounds [162, 145]. The good thermoelectric properties of these materials suggest that we should consider them as heavily doped n-type semiconductors instead of simply classifying them as metals.

Owing to their interesting thermoelectric properties, it is important to explore the phase space of VEC = 19 half-Heuslers further. Since half-Heuslers occur in a very large number of chemically reasonable combinations of elements, checking for the thermodynamic stability of each compound experimentally is laborious. Laboratory discovery can be significantly expedited by first narrowing down the likely compositions using first-principles based thermodynamic predictions. [6]

## 6.4 Results and Discussion

### 6.4.1 Phase stability prediction *ignoring* any off-stoichiometry in $XYZ$

In this study, we study 108 compounds from VEC = 19 family belonging to the IV-X-V, IV-XI-IV, V-IX-V, V-X-IV sub-groups (see Figure 6.2) using first-principles density functional theory calculations. The seven VEC = 19 half-Heuslers reported in ICSD [5] (namely VCoSb, TiNiSb, NbCoSb, NbRhSb, NbIrSb, TaCoSb and ZrNiBi, see circles in Figure 6.2) also constitute a subset of these half-Heusler structures. To understand the influence defects could have on the stability of these compounds, we first we check for thermodynamic stability of these structures by ignoring any kind of off-stoichiometry. We find that only one (TiNiSb) of the experimentally reported seven is predicted to be stable (see Figure 6.2). Unlike the VEC = 18 half-Heusler systems, prediction of VEC = 19 half-Heuslers using the defect-free structure under-predicts the number of stable compounds (see Figure 6.1) with respect to the few known compounds. Clearly, stability of VEC = 19 half-Heuslers is not understood well enough to reliably distinguish stable compounds from the unstable ones, and stability predictions based on the $XYZ$ stoichiometry alone cannot be trusted.

### 6.4.2 Nb-deficiency in NbCoSb structure

To understand the stability of 19-electron half-Heuslers, we first take a closer look at the VEC =19 example of NbCoSb to resolve the discrepancies between DFT prediction and experimental findings (see Figure 6.2). The synchrotron diffraction data collected for the NbCoSb composition (Figures  6.3) [1] show a multiphase material with the majority phase of “NbCoSb” (90.1(3) wt%) and a minor impurity phase of $Nb_3Sb$ (9.9(1) wt%), suggesting that the half-Heusler single phase region might lie at a slightly different composition. Refining isothermal displacement parameters of all atoms as well as the Nb-occupancy, a site occupancy factor of 84.3(2) % is obtained for Nb indicating a

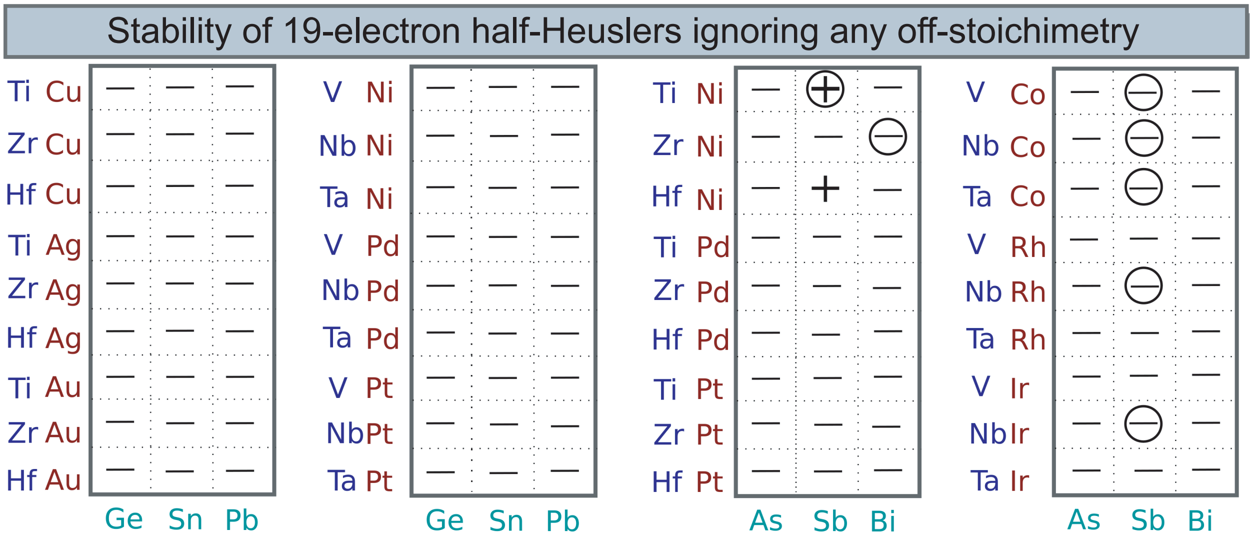
Stability of 19-electron half-Heuslers ignoring any off-stoichiometry

| | Ge | Sn | Pb |
|---|---|---|---|
| Ti Cu | − | − | − |
| Zr Cu | − | − | − |
| Hf Cu | − | − | − |
| Ti Ag | − | − | − |
| Zr Ag | − | − | − |
| Hf Ag | − | − | − |
| Ti Au | − | − | − |
| Zr Au | − | − | − |
| Hf Au | − | − | − |

| | Ge | Sn | Pb |
|---|---|---|---|
| V Ni | − | − | − |
| Nb Ni | − | − | − |
| Ta Ni | − | − | − |
| V Pd | − | − | − |
| Nb Pd | − | − | − |
| Ta Pd | − | − | − |
| V Pt | − | − | − |
| Nb Pt | − | − | − |
| Ta Pt | − | − | − |

| | As | Sb | Bi |
|---|---|---|---|
| Ti Ni | − | ⊕ | − |
| Zr Ni | − | − | ⊖ |
| Hf Ni | − | + | − |
| Ti Pd | − | − | − |
| Zr Pd | − | − | − |
| Hf Pd | − | − | − |
| Ti Pt | − | − | − |
| Zr Pt | − | − | − |
| Hf Pt | − | − | − |

| | As | Sb | Bi |
|---|---|---|---|
| V Co | − | ⊖ | − |
| Nb Co | − | ⊖ | − |
| Ta Co | − | ⊖ | − |
| V Rh | − | − | − |
| Nb Rh | − | ⊖ | − |
| Ta Rh | − | − | − |
| V Ir | − | − | − |
| Nb Ir | − | ⊖ | − |
| Ta Ir | − | − | − |

Figure 6.2: **Using defect-free structures with $XYZ$ composition predicts stability of 19-electron half-Heuslers poorly.** 19-electron $XYZ$ systems investigated in the present work for stability in the half-Heusler structure using only a defect-free $XYZ$ structure (any off-stoichiometry is ignored). Half-Heuslers predicted stable are represented by the plus (+) symbol. Previously reported nominal VEC = 19 half-Heuslers are represented by a circle. Compounds where the half-Heusler phase is predicted unstable are indicated by a minus (-) symbol.

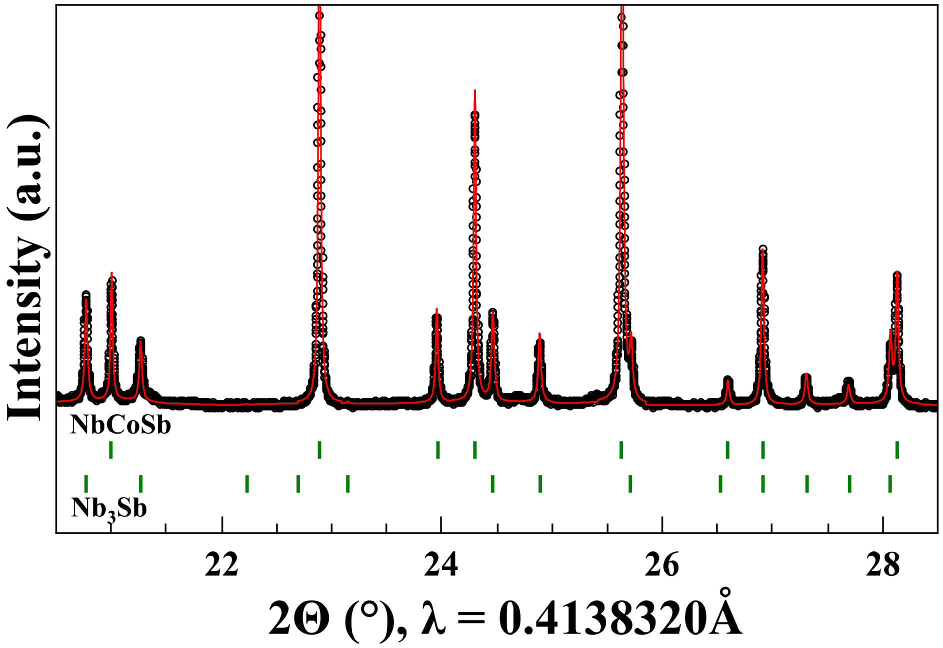

Figure 6.3: **X-ray diffraction pattern of NbCoSb composition contains a significant fraction of impurity phase.** Synchrotron diffraction pattern of the NbCoSb sample in a small angular range including the profile fit. The calculated Bragg diffractions show the quality of the fit with the two phases NbCoSb and $Nb_3Sb$. Experiments were performed by collaborators at Justus-Liebig-University Giessen and University of Houston.

Nb-deficient phase with a composition of $Nb_{0.84}CoSb$. The obtained phase fractions (in wt %) from the Rietveld refinement of the two phases correspond to a molar composition of $Nb_{0.84}CoSb$ + 0.067 $Nb_3Sb$. [1]

We note that ignoring any off-stoichiometry, DFT predicts that the 19-electron NbCoSb structure is predicted to be unstable (see Figure 6.2). In order to understand the large concentration of vacancies observed in the Nb-sublattice (hereafter, a vacancy will be referred to as $\dot{o}$) of the half-Heusler phase, we investigate off-stoichiometry in the system by performing a pseudo-binary cluster expansion (CE) for $Nb_{1-x}\dot{o}_xCoSb$ system (see Figure 6.4). Both the cubic end-members of this example, namely NbCoSb and CoSb, lie above the Nb-Co-Sb ternary convex-hull (see the solid line in Figure 6.4). The formation energies of structures lying at intermediate compositions are calculated with respect to the total energy of the end-members and is provided in eV/mixing-atom. Clearly, the formation enthalpy for the half-Heusler structure decreases on approaching the valence electron count (VEC) = 18 composition ($Nb_{0.8}CoSb$) from either sides. These results, suggesting approximately 20% vacancies on the Nb sub-lattice are in agreement with the Rietveld refinement of the X-ray data. After considering off-stoichiometry in the DFT calculations, we find that the NbCoSb composition must phase separate into the Nb-deficient half-Heusler phase $Nb_{0.8}CoSb$ and the impurity phases $Nb_3Sb$ and $Nb_7Co_6$ (trace amounts). Unless Nb-vacancies are considered, these impurity phases — which are also observed in

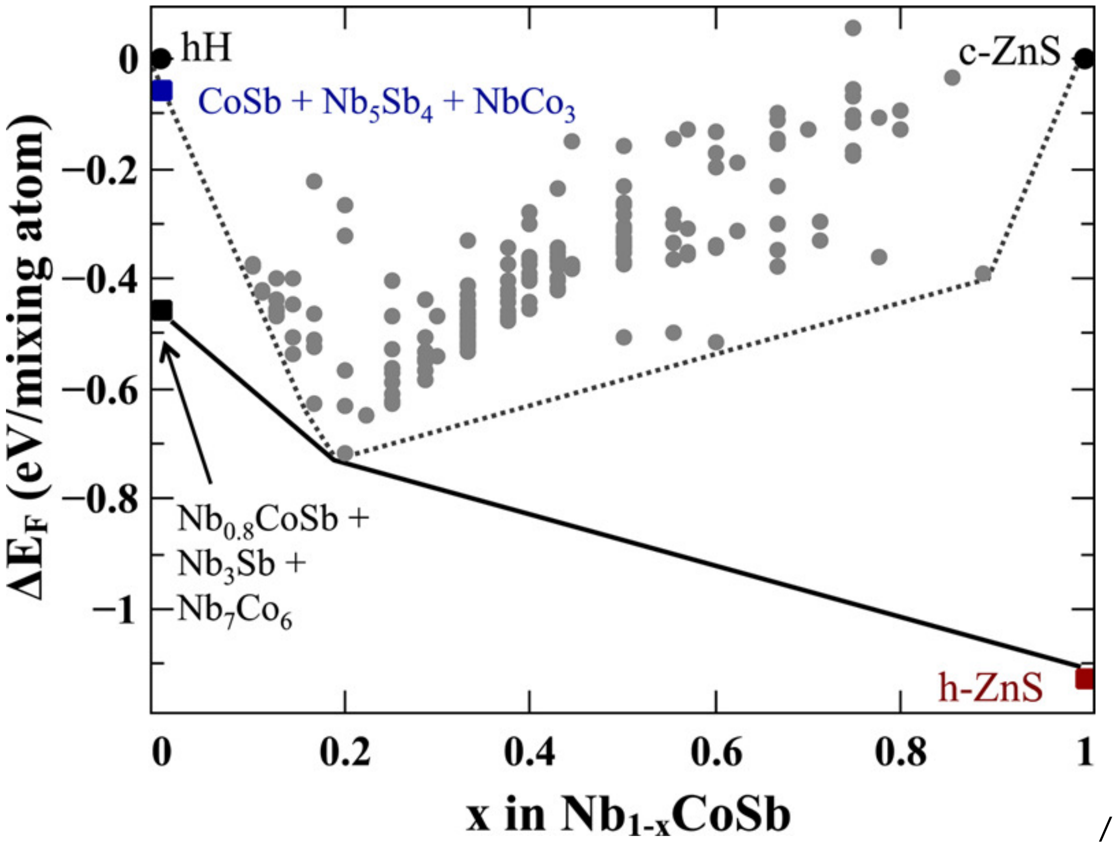

Figure 6.4: **Cluster expansion results for the $Nb_{1-x}$CoSb system.** Formation enthalpy(Δ $E_F$) of 173 different orderings (gray circles) of Nb-atom and vacancies in the Nb-sublattice of half-Heusler NbCoSb determined using DFT. The dotted line indicates the convex hull for these configurations of the NbCoSb (half-Heusler structure(half-Heusler))-CoSb (zinc Blende structure ($c$-ZnS)) binary system. The $Nb_{0.8}CoSb$ structure emerges as a stable ground state phase lying on the NbCoSb ternary convex hull (solid black line). The formation energies of this convex hull are determined from the three-phase region of $Nb_7Co_6$, $Nb_3Sb$, and $Nb_{0.8}CoSb$ at x = 0 (black square), the ordered $Nb_{0.8}CoSb$ ground state phase, and the hexagonal ground state phase of CoSb (red square).

the X-ray data — would have been predicted incorrectly ($Nb_5Sb_4$, CoSb (hexagonal phase) and $NbCo_3$ phases). Among the lowest energy configurations of Nb/$\dot{o}$ ordered phases only the half-Heusler $Nb_{0.8}CoSb$ breaks the Nb-Co-Sb ternary convex hull (Figure 6.4) and emerges as a stable ground state phase, thereby resolving the apparent discrepancy in DFT results with experimental findings. The complete Nb-Co-Sb ternary phase diagram calculation which includes the stable $Nb_{0.8}CoSb$ phase is presented in Figure 3.2.

### 6.4.3 Why Nb-vacancies? Extending the Valence Balanced rule to accommodate defects

One can understand the compositional stability of the ground state 18-electron $Nb_{0.8}CoSb$ half-Heusler using its valence balanced configuration.[1] While the 18-electron electron count in this system can be achieved at infinitely many compositions by creating vacancies at the $Y$- and/or $Z$-site of the stoichiometric structure, its stable $X$-site deficient composition can be uniquely identified by its valence balanced configuration (NV = 4 (0.8 $Nb^{5+}$ $s^0d^0$) - 1 ($Co^{1-}$ $d^{10}$) -3 ($Sb^{3-}$ $s^2p^6$) = 0). For example, when compared to the stoichiometric structure (NV = 5 ($Nb^{5+}$ $s^0d^0$) - 1 ($Co^{1-}$ $d^{10}$) - 3 ($Sb^{-3}$ $s^2p^6$) = 1), the Y-site deficient 18-electron composition $NbCo_{8/9}Sb$ (NV = 5 ($Nb^{5+}$ $s^0d^0$) - $\frac{8}{9}$ ($\frac{8}{9}$ $Co^{1-}$ $d^{10}$) - 3 ($Sb^{3-}$ $s^2p^6$) = 1.12) deviates away from the valence balanced configuration. Similarly, the Z-site deficient 18-electron composition $NbCoSb_{0.8}$ also deviates away from the valence balanced configuration (NV = 5 ($Nb^{5+}$ $s^0d^0$) - 1 ($Co^{-1}$ $d^{10}$) - 2.4 (0.8 $Sb^{3-}$ $s^2p^6$) = 1.6). While the 18-electron count imposes a constraint only on the (i) combination of atoms chosen and (ii) type of defect in stoichiometric VEC = 19 NbCoSb, the valence balanced configuration (NV = 0) imposes additional constraints on the site of the defect to uniquely determine its composition. While this valence balanced rule can be applied consistently across all stoichiometric half-Heuslers with VEC = 8 and 18, it can be generalized even further to include defects in half-Heuslers if all nominally 19-electron compounds show a similar trend in compositional stability. In the following sections we establish the generality of this valence balanced rule by (a) explaining all previous reports of stable nominal VEC = 19 half-Heuslers and (b) using it to reliably predict nominal VEC = 19 TiPtSb, which was not possible under the framework of the previously known 18-electron rule for stoichiometric 1-1-1 half-Heuslers.

### 6.4.4 Predicted stability of $XYZ$ composition after considering cation vacancies

For all the 108 VEC = 19 half-Heusler compositions considered here, once cation vacancies are considered, the stoichiometric half-Heusler composition $XYZ$ is predicted to be unstable in all cases (Figure 6.6). Even the TiNiSb and HfNiSb VEC = 19 compositions, which were predicted stable when any kind of off-stoichiometry is ignored, (see Figure 6.2) are now predicted to be unstable. The extent of instability ($E_{stability}$, for unstable compounds $E_{stability}$ = $E_{CH}$ > 0) of the VEC = 19 composition varied largely across families, ranging from 30 meV/atom for ZrNiSb to 558 meV/atom for HfAgGe. Even among the compounds reported previously, the instabilities are rather large (ranging up to 195 meV/atom for TaCoSb) and cannot be simply attributed to DFT error or the entropy associated with the temperatures at which the materials were synthesized. This is in contrast to the case of typical stoichiometric VEC = 18 half-Heuslers such as TiNiSn where Open Quantum Materials Database (OQMD)[8, 9] correctly predicts the thermodynamic phase stability of 60 of the 63 previously known compounds.

### 6.4.5 Confirming the valence balanced rule from previously reported *nominally* VEC = 19 half-Heuslers

For each of the previously reported nominal VEC = 19 half-Heuslers, the valence balanced (NV = 0, VEC = 18) structures (example $Ti_{0.75}NiSb$, $Ta_{0.8}CoSb$) is predicted stable (Figure 6.5), thereby resolving the multiple discrepancies pointed out in Figure 6.2 between DFT and experimental[163, 164, 165, 159] reports via the valence balanced rule. In contrast to a methodology which considers only defect-free structures, the valence balanced rule can be used to reliably distinguish stable *nominally* VEC = 19 compounds from the unstable ones. This reliability in predictive power is crucial for the accelerated discovery of new compounds. The prediction and confirmation of previously unreported VEC = 19 half-Heuslers is discussed in the sections below.

In addition to the large instabilities, we find that the $XYZ$ compositions lie in multiphase regions suggesting a driving force for phase separation at the VEC = 19 composition. Based on this result one would expect to observe impurity phases in previously reported compounds. Indeed, studies reporting synthesis of the nominally VEC = 19 half-Heuslers (NbCoSb [158], NbIrSb [165], VCoSb [159], TiNiSb [164]) often contain reports of impurity phases. NbCoSb is often synthesized with $Nb_5Sb_4$ [87] or $Nb_3Sb$ [1] impurities. Half-Heusler NbIrSb samples were prepared with persistent impurity phases despite several efforts (grinding, higher reaction temperature) to make the material single phase. [165] Large amounts of ferromagnetic impurity phases have been reported for the VCoSb composition.[163] The amount and type of impurity phases however, were often not analyzed and in a few cases [159] small amounts of impurity phases might also have been missed.

Our-prediction of a cation deficient off-stoichiometry in these compounds also agrees well with experiments. The single phase region of nominally 19-electron half-Heusler $Nb_{1-x}CoSb$ was found to lie in the off-stoichiometric range $x$ = 0.16-0.2. [1, 87] Multiphase $Ti_{30}Ni_{36}Sb_{34}$ samples annealed at 873 K indicate up to 20% cation vacancies in the half-Heusler phase. [166] We suggest here that the impurity phases in the $XYZ$ composition of nominally 19-electron half-Heuslers occur due to the formation of (18+$\delta$)-electron based half-Heusler phase.

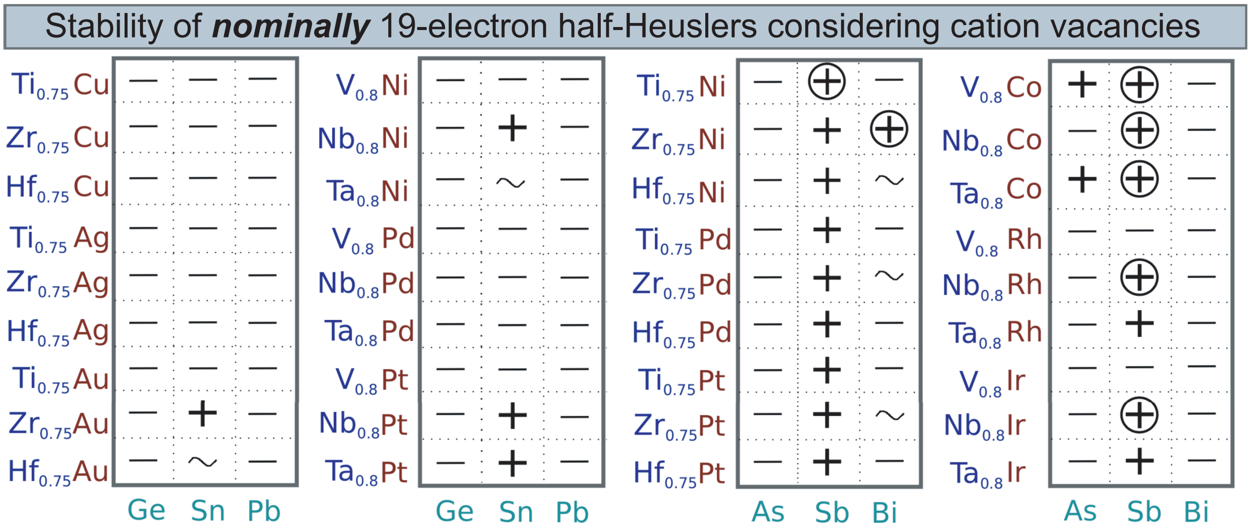

Stability of ***nominally*** 19-electron half-Heuslers considering cation vacancies

| | Ge | Sn | Pb |
|---|---|---|---|
| $Ti_{0.75}Cu$ | − | − | − |
| $Zr_{0.75}Cu$ | − | − | − |
| $Hf_{0.75}Cu$ | − | − | − |
| $Ti_{0.75}Ag$ | − | − | − |
| $Zr_{0.75}Ag$ | − | − | − |
| $Hf_{0.75}Ag$ | − | − | − |
| $Ti_{0.75}Au$ | − | − | − |
| $Zr_{0.75}Au$ | − | + | − |
| $Hf_{0.75}Au$ | − | ~ | − |

| | Ge | Sn | Pb |
|---|---|---|---|
| $V_{0.8}Ni$ | − | − | − |
| $Nb_{0.8}Ni$ | − | + | − |
| $Ta_{0.8}Ni$ | − | ~ | − |
| $V_{0.8}Pd$ | − | − | − |
| $Nb_{0.8}Pd$ | − | − | − |
| $Ta_{0.8}Pd$ | − | − | − |
| $V_{0.8}Pt$ | − | − | − |
| $Nb_{0.8}Pt$ | − | + | − |
| $Ta_{0.8}Pt$ | − | + | − |

| | As | Sb | Bi |
|---|---|---|---|
| $Ti_{0.75}Ni$ | − | ⊕ | − |
| $Zr_{0.75}Ni$ | − | + | ⊕ |
| $Hf_{0.75}Ni$ | − | + | ~ |
| $Ti_{0.75}Pd$ | − | + | − |
| $Zr_{0.75}Pd$ | − | + | ~ |
| $Hf_{0.75}Pd$ | − | + | − |
| $Ti_{0.75}Pt$ | − | + | − |
| $Zr_{0.75}Pt$ | − | + | ~ |
| $Hf_{0.75}Pt$ | − | + | − |

| | As | Sb | Bi |
|---|---|---|---|
| $V_{0.8}Co$ | + | ⊕ | − |
| $Nb_{0.8}Co$ | − | ⊕ | − |
| $Ta_{0.8}Co$ | + | ⊕ | − |
| $V_{0.8}Rh$ | − | − | − |
| $Nb_{0.8}Rh$ | − | ⊕ | − |
| $Ta_{0.8}Rh$ | − | + | − |
| $V_{0.8}Ir$ | − | − | − |
| $Nb_{0.8}Ir$ | − | ⊕ | − |
| $Ta_{0.8}Ir$ | − | + | − |

Figure 6.5: **Valence balanced defective composition predict stability accurately.** 19-electron XYZ systems investigated in the present work for stability of the half-Heusler phase using the valence balanced (NV = 0) defective compositions. Systems with the half-Heusler phase predicted stable are represented by the plus (+) symbol. Among these, symbols of compounds previously reported as nominal VEC = 19 half-Heuslers are encircled. Compounds where the half-Heusler phase is predicted unstable are indicated by a minus (-) symbol and those which lie within chemical accuracy of DFT ($|E_{stability}| \leq 10$ meV/ atom) are given by tilda (~) symbol.

### 6.4.6 Previously unknown compounds predicted stable using the valence balanced rule

Out of the 108 compounds studied here, we find a total of 23 nominally VEC = 19 half-Heuslers stable in their valence balanced (NV = 0, VEC = 18) cation poor structures (Figure 6.5), 16 of which are previously unreported. We predict new half-Heusler phases in 10 Sb-based, 2 As-based and 4 Sn-based ternary systems (Figure 6.5). We also find 4 cases which are too close to call as their $E_{stability}$ falls within the range [-10 meV/atom, 10 meV/atom] and could be attributed to a DFT error. Nominally VEC = 19 half-Heuslers have only been reported for Sb and Bi-based compounds. We propose Sn and As-based compounds as new additions to the nominally VEC = 19 half-Heusler family. These compounds are significantly stable ($E_{stability}$ < -20 meV/atom) and comparable to the already reported example of half-Heusler $Zr_{0.75}NiBi$ ($E_{stability}$ = -11 meV/atom). Some compounds such as $Nb_{0.8}$NiSn (Figure 6.5) contain only relatively inexpensive and abundant elements and could be explored as inexpensive alternatives for thermoelectric applications.

The nominally VEC = 19 compounds are a large family consisting of $\sim$300 combination of elemental groups for the X, Y and Z-site atoms [141] (namely the sub-groups III-XI-V, III-X-IV, IV-IX-III, IV-X-V, IV-XI-IV, V-IX-V, V-X-IV, V-XI-III, VI-VIII-V, VI-IX-IV, VI-X-III). The fact that stability of these compounds is almost never limited by the large defect concentrations (see Figure 6.5) suggests that valence balanced rule is robust and can be used in further discoveries with reasonable confidence. Similar to the previously unreported Sn- and As-based compounds predicted here one might expect to find more nominally VEC = 19 compounds from the large phase space of possible ternary systems, opening up a new dimension for potential materials research and discovery. While other nominally VEC = 19 compounds can be explored, the current prediction of 23 compounds is already more than one-third of the 61 predicted exhaustively for VEC = 18 half-Heuslers. Just like stoichiometric VEC = 18 half-Heuslers, the pseudo 18-electron nature of new nominally VEC = 19 compounds could be suitable for thermoelectric applications.

### 6.4.7 Semiconducting electronic structure driven stability

Most of the cation-deficient, valence-balanced (NV = 0, VEC = 18) structures studied here are found to be semiconducting ($E_g \geq 0$). Generally, the compounds with larger band-gaps ($E_g \geq 0.55$ eV) are stabilized to a greater extent relative to the small band-gap ($E_g \leq 0.55$ eV) cases (Figure 6.6). The stabilizing effect of the band-gap may be associated with the electronic energy gained after losing 1 electron/formula-unit from the ‘conduction band’ of the stoichiometric VEC = 19 half-Heusler as the structure becomes cation-deficient. This gain in electronic energy may overcome the $E_{stability}$ at the VEC = 19 composition, giving rise to thermodynamic stability in the 23 compounds predicted here. It seems that, for a particular value of $E_{stability}$ at the VEC = 19 composition a correspondingly

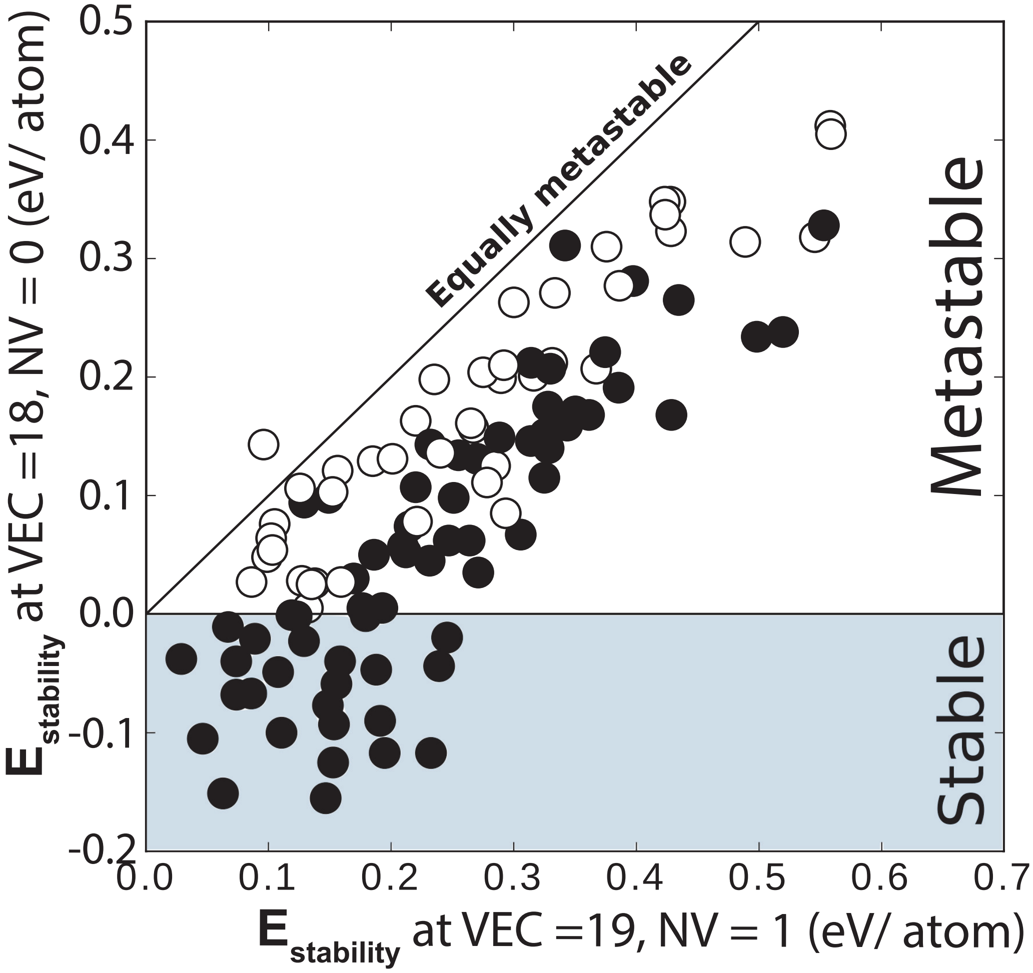

Figure 6.6: **The defective valence balanced composition is always more stable than the 19-electron half-Heusler structure at the $XYZ$ composition.** $E_{stability}$ of the 108 half-Heusler structures studied here at the $X$-site-deficient valence-balanced (NV = 0) composition versus at the defect-free VEC = 19 composition. Negative values signify cases where half-Heusler structure is predicted stable. Cation deficiency increases the stability of nearly all half-Heusler structures. Stabilizing energies are larger for systems with larger band-gaps ($E_g \geq 0.55$ eV, filled circles) at the VEC = 18 composition. All stable nominal VEC = 19 half-Heuslers exhibit $E_g \geq 0.55$ eV.

large band-gap at the valence balanced composition is required to stabilize the nominal VEC = 19 half-Heusler phase (see dotted line in Figure 6.7). Most compounds predicted stable however, exhibit both (i) a small $E_{stability}$ for the defect-free structure and (ii) a large stabilizing band-gap (see solid line in Figure 6.7). It is interesting to note that all the compounds predicted stable lie in the larger band-gap range with $E_g \geq 0.55$ eV (see Figure

6.6).

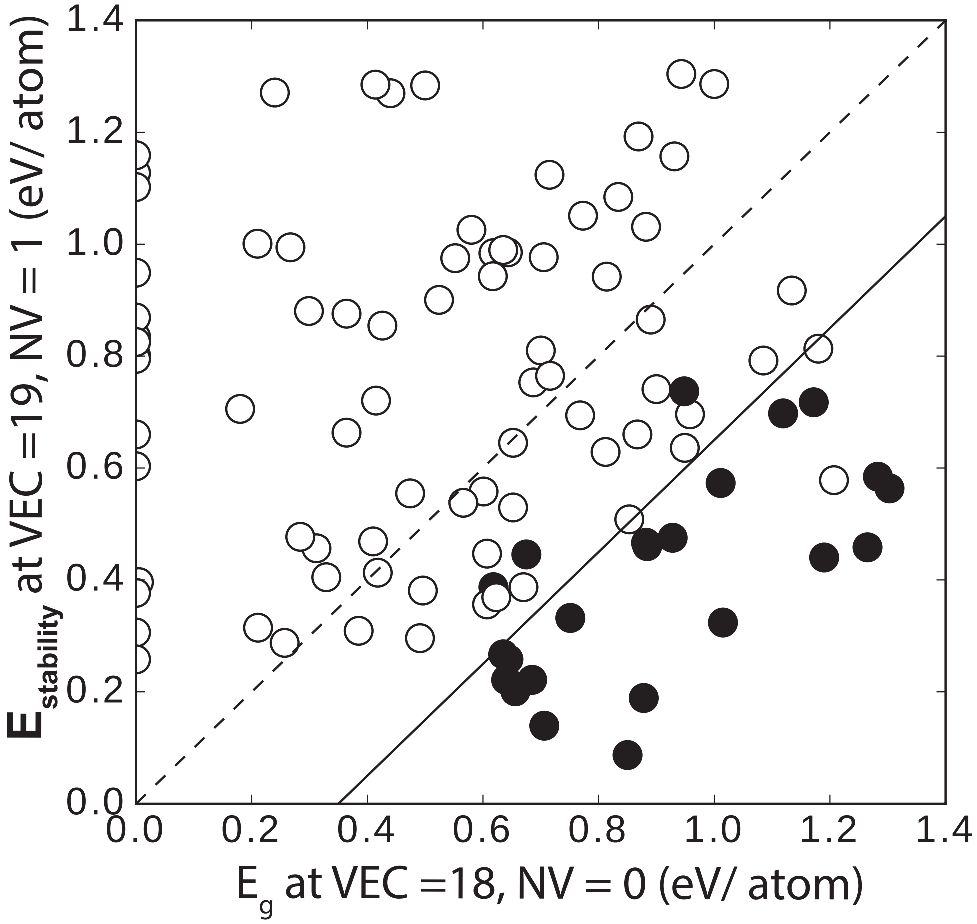

Figure 6.7: **Instability of the 19-electron half-Heusler structure at the $XYZ$ composition can be overcome by a correspondingly large electronic energy gap.** $E_{stability}$ (in eV/formula unit) of the half-Heusler structures at VEC = 19 composition versus its band-gap ($E_g$) at the off-stoichiometric valence balanced composition. The compounds predicted stable ($E_{stability} \leq$ -10 meV/atom) in the off-stoichiometric valence balanced (NV = 0) structure are given by filled circles.

For off-stoichiometries of the magnitude discussed here (20-25 % vacancies), one would expect an energy penalty for formation of vacancies to be quite significant. This energy penalty should compete with stabilizing effect of $E_g$, possibly even overcoming it in a few cases. Contrary to this expectation, we find that off-stoichiometric half-Heusler structures are nearly always (107 out of 108 cases) more stable with respect to the defect-free structure (see Figure 6.6) even for systems with small $E_g$ ($\sim$ 0 ev) (see Figure 6.7). This suggests that the structure readily accommodates the large vacancy concentrations to attain the valence balanced configuration. The spontaneous formation of large concentration of vacancies might seem counterintuitive. However, complete vacancies on the cationic $X$-site leads to the stable zinc blende structure with the same $sp$-bonding as in the half-Heuslers. This suggest half-Heuslers have some chemical similarities to intercalation compounds where the $X$ cation add flexibly to tune the electron count towards the thermodynamically stable valence-balanced composition.

### 6.4.8 Chemical Trends in stability of the *nominally* VEC = 19 half-Heusler family

Since calculations were performed for over 100 compounds in the present work spanning across different anion chemistries (see Figure 6.5), we investigate the trends in stability with electronegativity and size of the anion. We note that Sb- and Sn-based compounds are predicted to have most number of stable nominally 19-electron half-Heusler compounds (see Figure 6.5). To understand this trend, we explicitly plot the $E_{stability}$ values of the $XYZ$ composition for all the systems belonging to different anion chemistries (see Figure 6.8). For a straightforward comparison of the 6 anions, we also average the $E_{stability}$ value in each case. The positive value of all the 108 systems indicate — as discussed above — that the 19-electron $XYZ$ compositions are unstable. As concluded from Figure 6.7, a small $E_{stability}$ value at the $XYZ$ composition is necessary for the defective cation-deficient structure to become stable. In line with this expectation, we find that the average $E_{stability}$ values (in ascending order: Sb, Sn, As, Bi, Ge, Pb) are inversely correlated to the number of compounds predicted stable for each anion (see Figure 6.5). On going down a group of anionic elements, we find that the $E_{stability}$ values first decrease and then increase (for both groups).

We attribute this non-monotonic behaviour of $E_{stability}$ to the competing effects of size and electronegativity on going down the group. On going down a group, the size of the anion increases, but its electronegativity decreases. Structural parameters which are correlated to size of the anion, such as the sum of ionic radii and average atomic masses, have been identified in previous works [167, 6] as important metrics to distinguish half-Heusler structure types from other phases (primarily orthorhombic, space group Pnma) which crystallize at the $XYZ$ composition. These studies for 18-electron compounds have shown, in line with our results (see Figure 6.5 and Figure 6.8), that the Ge- and

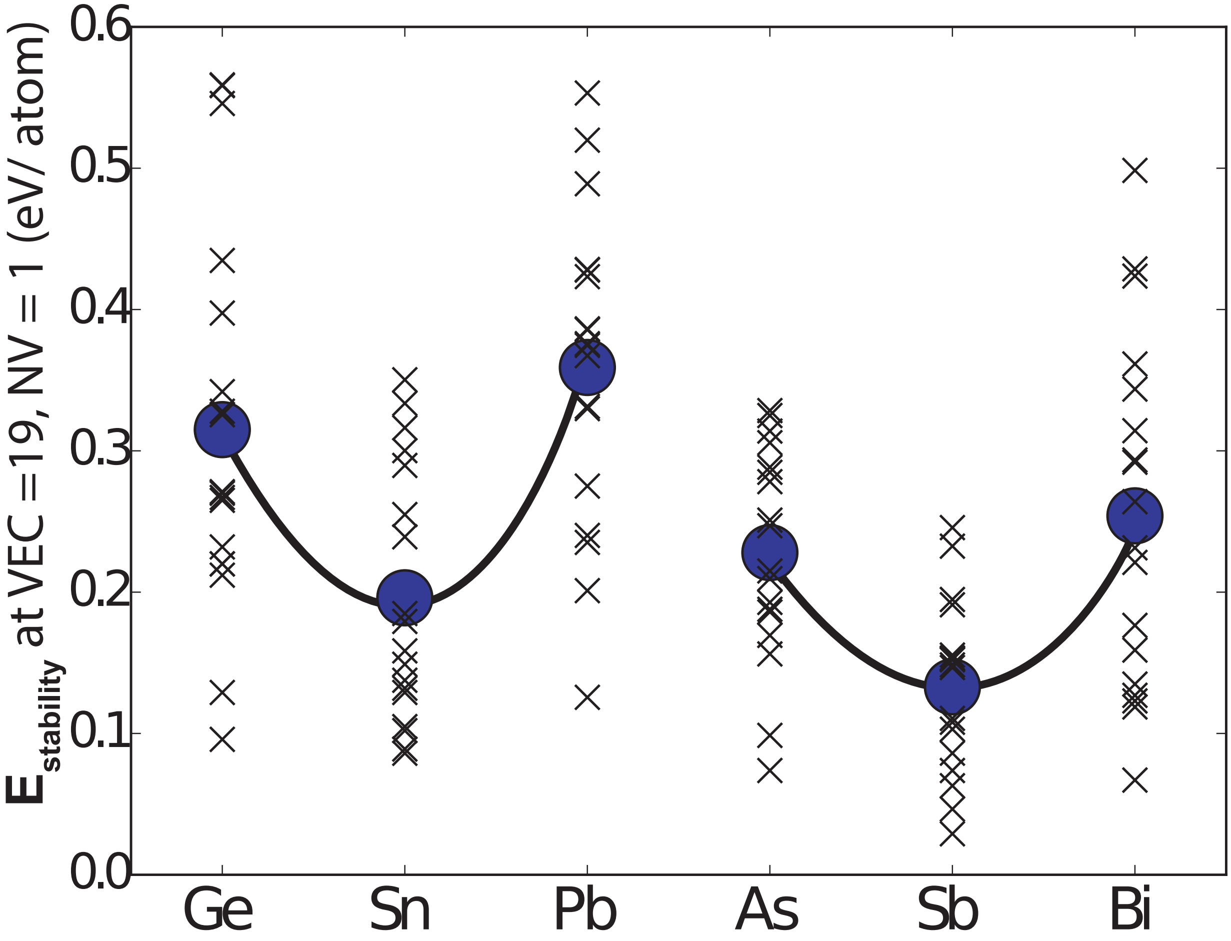

Figure 6.8: **Chemical trends in stability of half-Heusler compounds.** Calculated $E_{stability}$ values (cross symbols) for all of the 19-electron half-Heuslers at the $XYZ$ compositions investigated in this work. The $E_{stability}$ values are classified by the $Z$-site anion. Average $E_{stability}$ values for each case is shown as a big blue circle. The thick black lines are drawn as a guide to the eye to show the general trend in $E_{stability}$ values on going down a particular group in the periodic table.

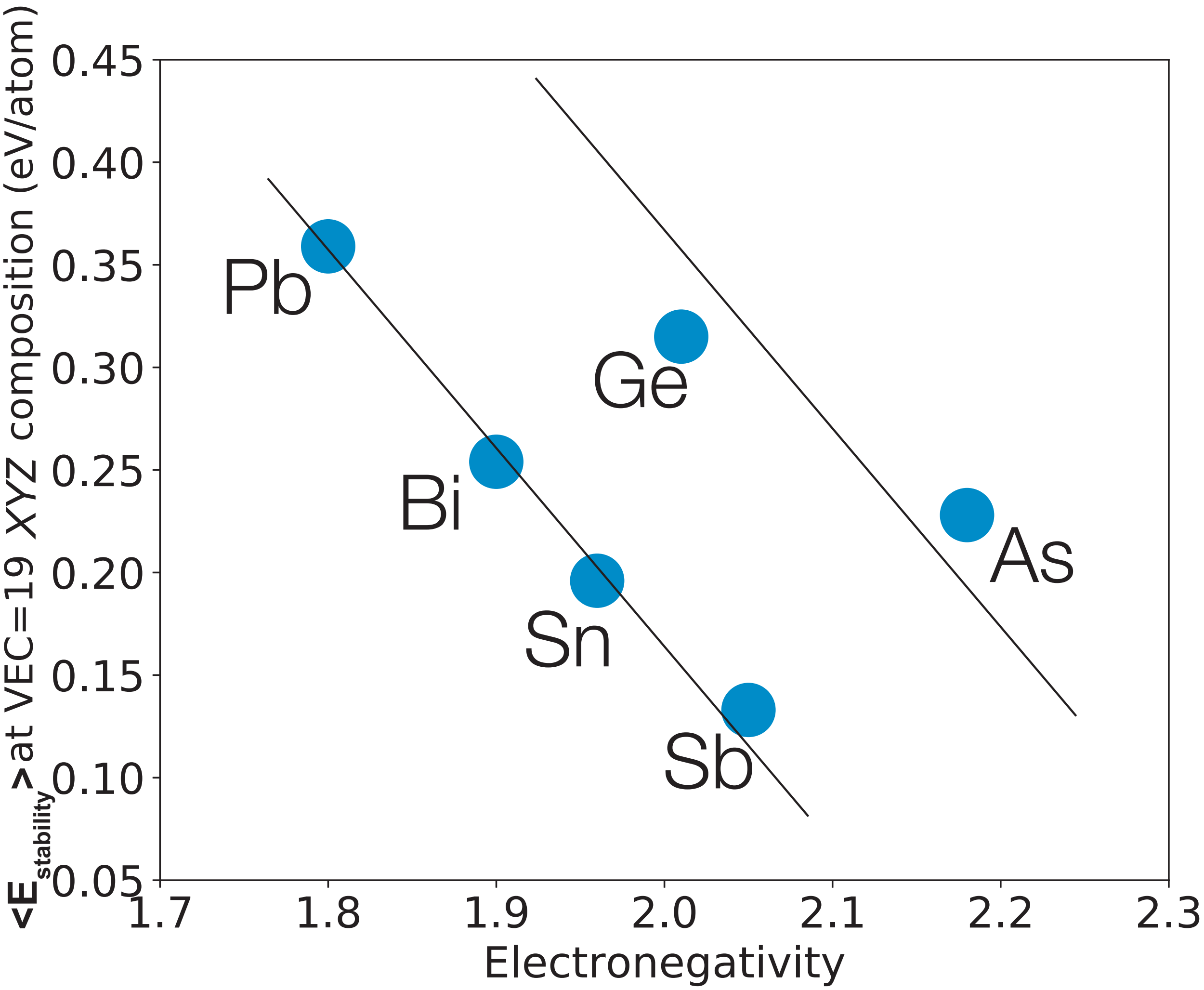

Figure 6.9: **Trends in half-Heusler stability with with electronegativity of the $Z$-site atom.** Calculated values of average $E_{stability}$ (averaged for based on $Z$-site anion separately) for all the 19-electron half-Heuslers at the $XYZ$ compositions investigated in this work plotted as a function of the $Z$-site atom electronegativity.

As-based compounds rarely form the half-Heusler phase due to their smaller size or mass. The larger anions Bi and Pb, on the other hand, are not as stable as their Sb and Sn, presumably because of their electronegativities. From the Zintl understanding of half-Heusler semiconductors, we know that the $Z$-site element constitutes a part of the electronegative anionic framework. Hence, a $Z$-site element with a smaller electronegativity must be conflicting with stability of the half-Heusler semiconductor within the Zintl

Picture. We plot average $E_{stability}$ as a function of the anionic electronegativity in Figure 6.9. As expected, $E_{stability}$ for Pb-, Bi-, Sn-, Sb-based compounds decreases almost linearly with increasing electronegativity thereby explaining the relatively smaller number of Bi- and Pb-based compounds. The $E_{stability}$ versus electronegativity trend in Ge and As is off-set due to their much smaller sizes. Although the chemical trends of thermodynamic stability are discussed for only a few nominally VEC = 19 half-Heusler compounds, the analysis is applicable for half-Heusler families with other electron-counts, too.

### 6.4.9 Experimental Verification

To verify our predictions of new 19-electron compounds, the previously unknown nominally VEC = 19 compound $\mathrm{Ti}_{1-x}\mathrm{PtSb}$ ($T_{anneal}$ = 1073 K) was synthesized at $x$ = 0 and 0.1. The powder XRD pattern of $\mathrm{Ti}_{0.75}\mathrm{PtSb}$ indicates that the main phase of the samples are the half-Heusler phase (see Figure 6.10) and some impurity peaks of the $\mathrm{PtSb}_2$ phase. The impurity peaks almost vanish for the $\mathrm{Ti}_{0.85}\mathrm{PtSb}$ sample, indicating it is nearly phase pure. The discovery of a cation-deficient half-Heusler $\mathrm{Ti}_{0.75+x}\mathrm{PtSb}$ in the nominally 19-electron system provides a strong experimental validation of our prediction strategy based on the valence balanced rule.

## 6.5 Conclusion

In conclusion, we demonstrate that the stability of half-Heuslers at multiple nominal electron counts, 8, 18 and 19, are best understood using a valence balanced rule. We establish that while the nominal electron counts for these half-Heusler systems might be different, their ground state structures always have a common net valence (NV) of 0 when described within a Zintl framework. This rule allows the nominally 19-electron half-Heuslers to flexibly tune its stoichiometry by accommodating large concentrations of cation vacancies to attain the ground state valence-balanced configuration. This understanding of compositional stability in the emerging thermoelectric nominal VEC = 19 half-Heuslers, previously not available from the '18-electron rule' for stoichiometric half-Heuslers, was used to predict 16 new compounds. The newly predicted off-stoichiometric half-Heusler phase $\mathrm{Ti}_{0.75+x}\mathrm{PtSb}$ was synthesized and confirmed using x-ray studies. The valence balanced rule adds multiple dimensions to the phase space for discovery of possible half-Heuslers by including different intrinsic and extrinsic defects in the structure to attain a valence-balanced configuration.

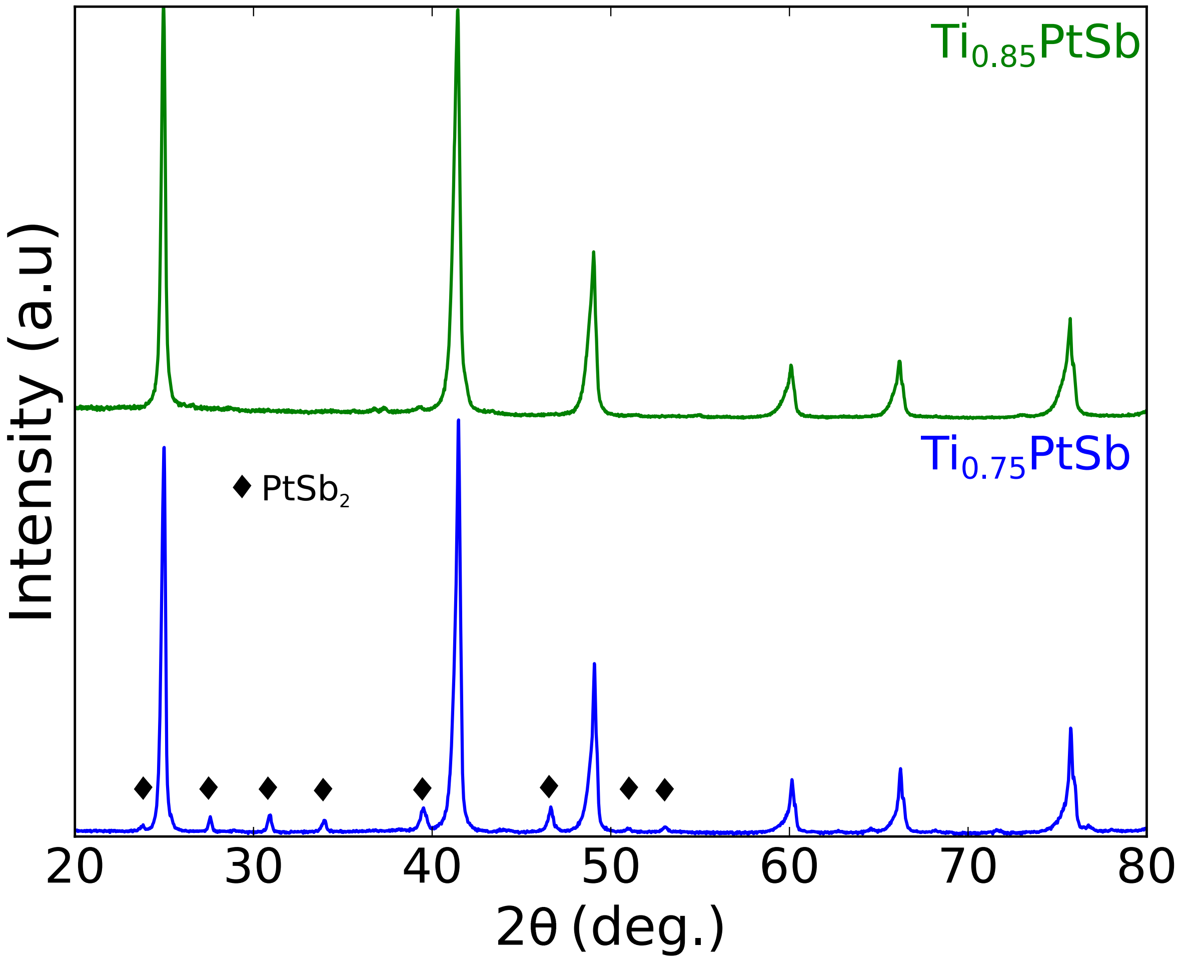

Figure 6.10: **Experimental verification of prediction of the Ti$_{0.75+x}$PtSb compound based on valence balanced rule.** XRD patterns of Ti$_{0.75+x}$PtSb (x = 0, 0.1) annealed at 1073 K. Experiments were performed by collaborators at Zhejiang University.

# Chapter 7

# Temperature-dependent $n$-type self-doping in *nominally* 19-electron half-Heusler thermoelectrics

## 7.1 Overview

The origin of stability of the relatively rare 19-electron half-Heusler compounds — known in the literature for over two decades — had been unclear for a long time. As a result, previous experimental studies have often interpreted these metal-like compounds as outliers to the 18-electron rule with the same well-known $XYZ$ stoichiometry. However, the recent discovery of a semiconducting ground state $X_yYZ$ ($y$ = 0.8 or 0.75) in these compounds warrants a closer look at their apparently metallic properties that often make them good thermoelectric (TE) materials. By systematically investigating the temperature dependence of off-stoichiometry ($x$) in $V_{0.8+x}CoSb$, $Nb_{0.8+x}CoSb$, and $Ti_{0.75+x}NiSb$ we find that $x$ invariably increases with increasing temperature, leading to an n-type self-doping behavior. In addition, there is also a large phase width (range of $x$) associated with each phase that is temperature-dependent. Thus, unlike in typical 18-electron half-Heuslers (eg: TiNiSn), the temperature dependence of vacancy and carrier concentration ($n$) in nominally 19-electron half-Heuslers links its transport properties to synthesis conditions. The temperature dependence of $x$ and $n$ are understood using density functional theory (DFT) based defect energies ($\Delta H_{def}$) and phase diagrams. $\Delta H_{def}$ (in cation-rich conditions) are calculated for 21 systems which can be used in predicting cation solubility in this family of compounds. Using this simple strategy, suitable composition and temperature synthesis conditions are devised for obtaining an optimized $n$ to engineer TE properties in phase-pure $V_{0.8+x}CoSb$, and the previously unexplored $Ta_{0.8+x}CoSb$. The small $\Delta H_{def}$ values for well-known compounds such as $V_{0.8+x}CoSb$ reveals why these compounds can lie close to the VCoSb composition, explaining why the defective nature of these compounds have remained hidden from the community for so long.

## 7.2 Context and Motivation

The thermoelectric properties of defective nominally 19-electron half-Heusler systems with the general formula $X_yYZ$ ($y$ = 0.75 and 0.8) are very sensitive to chemical composition. [87] Unlike the well-known $XYZ$ half-Heuslers, the charge-carrier concentration ($n$) of which is usually tuned through extrinsic doping, $X$-site vacancies in $X_yYZ$ can be easily filled to dope them degenerately $n$-type. [1, 87] In addition to $n$, the large tunable vacancy concentration can lend itself favorably to thermal conductivity reduction via phonon scattering and lattice softening mechanisms. [73] The nominally 19-electron $Nb_{0.8+x}CoSb$ ($x$ = 0.02) was found to exhibit a $zT \sim$ 0.9 at 1100 K, [87] which is comparable to the well known multi-component half-Heusler thermoelectrics such as (Ti,Zr,Hf)NiSn compounds with a $zT$ = 1.2-1.5. [145, 162, 146]

Apart from impacting the intrinsic properties of the half-Heusler phase directly, choosing chemical compositions that yield metallic impurity phases could also have a detrimental effect on the overall thermoelectric performance of the sample. In the case of nominally 19-electron half-Heusler systems, synthesis of the standard $XYZ$ compositions in most systems (NbCoSb [158], NbIrSb [165], VCoSb [163, 159], TiNiSb [164]) often contains reports of impurity phases. The optimized high $zT$ $Nb_{0.82}CoSb$ composition is free of the metallic impurity phases, such as $Nb_5Sb_4$ [87] or $Nb_3Sb$ [1] which are often reported at the NbCoSb composition.[1, 87, 158] In addition to the impacting thermoelectric performance negatively, the metallic impurities can also make it hard to distinguish the intrinsic properties of the pure phase half-Heusler from the properties of the impurity phase.

Although knowledge of compositional phase stability is central to engineering desirable thermometric properties, a clear understanding of the phase-pure stoichiometry in nominally NV = 1 (or VEC = 19) half-Heuslers is still lacking. While the $Nb_{0.8+x}CoSb$ — in agreement with the DFT predicted ground state [10, 1, 87] — has been reported as a phase-pure half-Heusler at the $x$ = 0 composition, experimental observations in other systems differ significantly from $T$ = 0 K DFT predictions. For example, the reported composition for half-Heusler $Ti_{0.75+x}NiSb$ has $x$ = 0.05 instead of the valence-balanced $x$ = 0. [166] Similarly, $Ti_{0.75+x}PtSb$ is found to be nearly phase pure at the $x$ = 0.10 composition. [10] $V_{0.8+x}CoSb$ is an extreme example, which is reported to be a nearly phase-pure half-Heusler at the NV = 1 VCoSb composition (i.e., $x$ = 0.2).

In view of the fact that thermoelectric properties of nominally 19-electron half-Heuslers are very closely linked their compositional phase stability, (see Figure 7.1) we build a defect-energetics-based predictive framework for solubility in all the newly discovered systems (see Figure 6.5). For this, we take the same approach as we did in Chapter 6. We first understand the $X$-atom solubility in experimentally reported compounds ($V_{0.8+x}CoSb$, $Nb_{0.8+x}CoSb$, and $Ti_{0.75+x}NiSb$) using DFT calculated defect energies ($\Delta H_{def}$). Using this analysis the $\Delta H_{def}$ calculations for previously unreported compounds can be used to estimate a temperature-dependent solubility on the $X$-site.

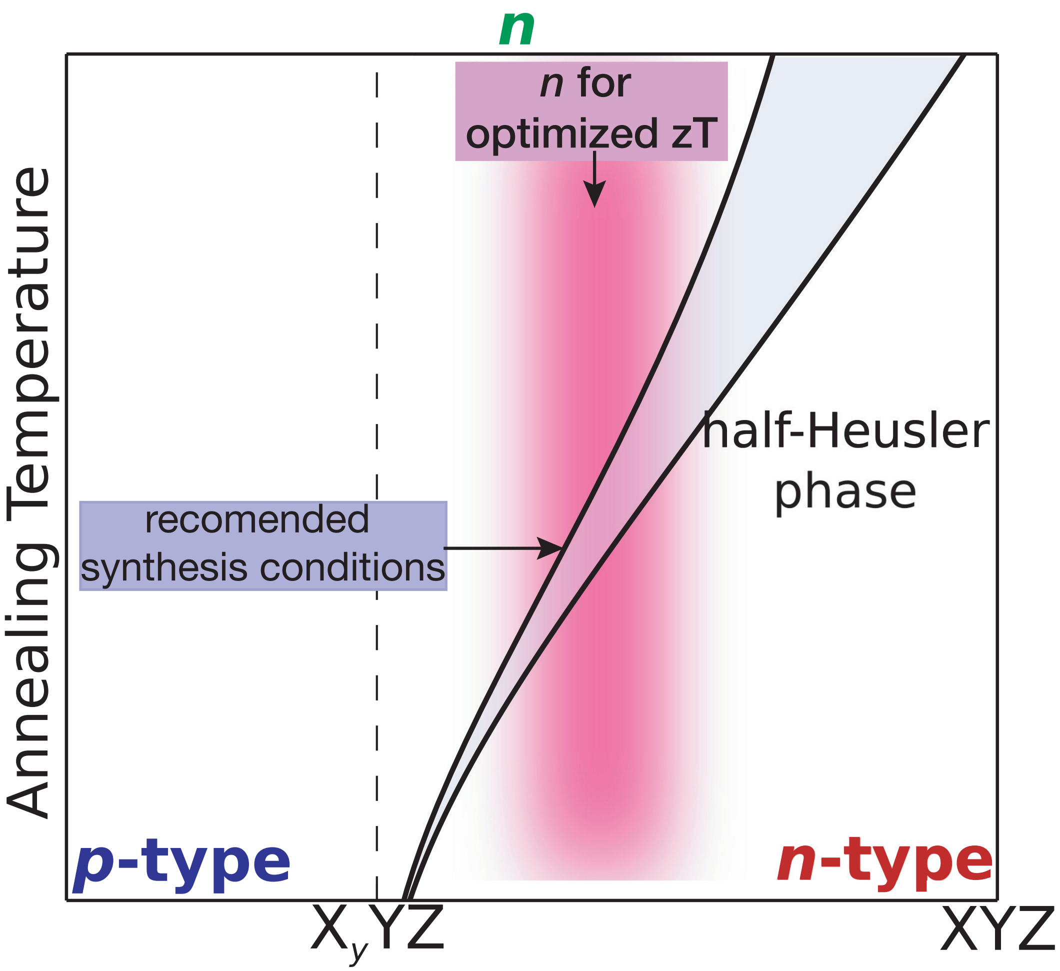
n
n for
optimized zT
half-Heusler
phase
recomended
synthesis conditions
Annealing Temperature
p-type
n-type
$X_yYZ$
XYZ

Figure 7.1: **Strategy to identify synthesis conditions for preparation of high performing *nominally* 19-electron half-Heusler thermoelectric samples.** Schematic demonstrating the strategy adopted in the present work for recommending appropriate annealing temperature-composition synthesis conditions for the design of optimally doped *nominally* 19-electron half-Heusler thermoelectrics.

## 7.3 Results and discussion

Using the experimental reports of high temperature phase stability in half-Heusler $V_{0.8+x}CoSb$, $Nb_{0.8+x}CoSb$ and $Ti_{0.75+x}NiSb$ from Ref. [12] and their predicted $T$ = 0 K defective stoichiometries (Chapter 6) we construct a composition-temperature phase diagram for each compound (see Figure 7.2). An exponential functional form is chosen to sketch the temperature dependence of the phase boundaries (see Methods section). The curvature of

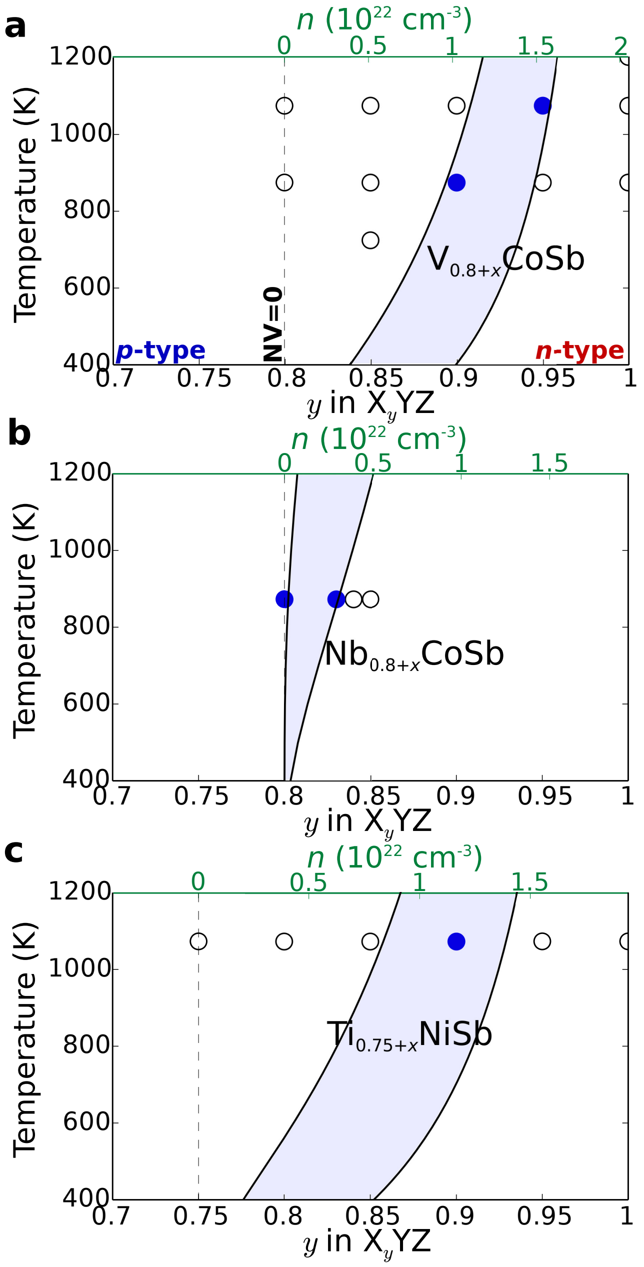

Figure 7.2: **Temperature-dependent evolution of single phase (light blue) half-Heusler in (a) $V_{0.8+x}$CoSb, (b) $Nb_{0.8+x}$CoSb and (c) $Ti_{0.75+x}$NiSb.** The solvus boundaries of the half-Heusler phase are given by the solid black lines. Compositions with single phase and multi-phase samples (from XRD) are represented by blue and unfilled black circles respectively. The dashed vertical line drawn at the $T$ = 0 K valence-balanced (NV = 0) composition separates the $n$-type and $p$-type region for the nominal composition of the sample. The top axis provides the nominal chemical carrier concentration ($n$) for each system.

the phase boundaries (see Figure 7.2) depends on the fraction of vacancies ($f$ = $x$ / (1-$y$)) filled in the $X_yYZ$ structure. In the expression for $f$, $y$ = 0.8 and 0.75 for group-V (V and Nb) and group-IV (Ti) cation based systems respectively. As the temperature-dependent shift in stoichiometry of the phase is limited by the number of vacancies available for filling (1-$y$, per formula unit) the phase boundaries straighten up as $f$ approaches 1.

The data points representing samples with phase pure half-Heusler XRD patterns (see blue symbols in 7.2), either lie in the single phase region (light blue in Figure 2) or close to it ($Nb_{0.8}CoSb$) within the instruments limit to detect impurity phases ($\sim$ 2 atomic %). The $Nb_{0.8}CoSb$ composition is drawn in the multi-phase regions despite its phase-pure XRD pattern (see Ref. [12, 87]). The presence of small amounts of undetected metallic CoSb impurity phases in $Nb_{0.8}CoSb$ are concluded based on its large Hall carrier concentration ($n_H$) (see Table 1). Such a large $n_H$ cannot be expected from the half-Heusler phase alone, as at this NV = 0 composition $Nb_{0.8}CoSb$ should have properties of an intrinsic semiconductor with small $n$. The temperature dependence of Seebeck coefficient ($S$) in $Nb_{0.8}CoSb$ samples are in fact consistent with a smaller $n$ because $S$ peaks at 800 K, [87] typical of bipolar transport in intrinsic semiconductors. The large value of the measured $n_H$ is therefore presumably due to a metallic impurity phase.

The half-Heusler single phase in all three examples shifts quite significantly towards larger $X$-compositions with increasing temperature (see Figure 7.2). Both the cation-rich and cation-poor phase boundaries, shift towards the $XYZ$ compositions (see Figure 7.2). This is particularly clear from the $V_{0.8}CoSb$ example for which experimental phase stability data is available at multiple temperatures. The temperature-dependent shift of the single phase region suggests that the low-temperature compositions lie closer to $x$ = 0 and not the equiatomic $XYZ$ composition. This is consistent with prediction of a $T$ = 0 K composition at $x$ = 0 in these systems. [10]

The temperature-dependent stoichiometry in these compounds can be understood in terms of the solubility of additional $X$-atoms in its semiconducting ground state $X_yYZ$ ($y$

= 0.75 or 0.8) structure. As $X$-atoms donate free carriers to the half-Heusler structure doping them $n$-type, differences in phase composition between two annealing temperatures is reflected in their room temperature $n_H$ measurements. $n_H$ of the phase pure $V_{0.8+x}CoSb$ sample annealed at $T_{anneal}$ = 1073 K ($x$ = 0.15) is greater than phase pure sample annealed at $T_{anneal}$ = 873 K ($x$ = 0.1) by a factor of $\sim$ 2.5 (see Table 7.1). Hence, temperature emerges as a sensitive degree-of-freedom to control electrical transport properties in nominally 19-electron half-Heuslers.

Table 7.1: Room temperature Hall carrier concentration ($n_H$) of phase pure (from XRD) $V_{0.8+x}CoSb$ and $Nb_{0.8+x}CoSb$ samples for different annealing temperatures ($T_{anneal}$).

| Composition | Annealing Temperature ($T_{anneal}$) | Carrier Concentration ($10^{21}$ cm$^{-3}$) |
|---|---|---|
| $V_{0.95}CoSb$ | 1073 K | 21 |
| $V_{0.9}CoSb$ | 873 K | 8.6 |
| $Nb_{0.83}CoSb$ | 873 K | 2.48 |
| $Nb_{0.8}CoSb$ | 873 K | 0.82 |

To exploit annealing temperature as a design parameter in thermoelectric $V_{0.8+x}CoSb$, we use our phase diagram analysis (see Figure 7.2 a). Using the isoelectronic $Nb_{0.8+x}CoSb$ as a model system [87] we apply the following design requirements: (a) phase pure half-Heusler material, and (b) an optimized n $\sim 1 \times 10^{21}$ cm$^{-3}$ for high zT at the operational temperature $T$ = 773 K. We find that $n_H \sim 8.6 \times 10^{21}$ cm$^{-3}$ for $x$ = 0.1, $T_{anneal}$ = 823 K (see Table 7.1) is already lower than previous reports on carrier concentration in the $V_{0.8+x}CoSb$ system [159] by over a factor of 2. $n_H$ can be decreased further via extrinsic doping options (such as Sn on Sb site), which have been explored successfully for the $Nb_{0.8+x}CoSb$ compound. [161] Thus, we recommend $V_{0.9}CoSb$ ($T_{anneal}$ = 823 K) as a better starting point for extrinsic doping instead of the commonly investigated 1-1-1 composition.

In addition to its impact on thermoelectric properties, $X$-site composition could also affect the exciting magnetic properties of these systems. The equiatomic composition VCoSb has been predicted to be a half-metallic ferromagnet with potential applications in spintronic devices.[168] The large magnetic moment in VCoSb is expected to arise from the 'metallic' electron in the conduction band of the nominally NV = 1 $XYZ$ structure. Despite the metal-like $n_H$ ($\sim 2 \times 10^{22}$ cm-3) of the VCoSb composition,[159] it is reported experimentally as a weak itinerant ferromagnet. [169, 170] We show for the first time that typically NV < 1 in pure phase half-Heusler $V_{0.8+x}$CoSb, even up to very high temperatures. Our results suggest that investigating magnetic properties of half-Heusler $V_{0.8+x}$CoSb at the phase-pure compositions (instead of the equiatomic composition) could resolve the discrepancies between theory and experiments.

Due to differences in $X$-atom solubility between the systems (see Figure 7.2), $n$ can be very system dependent. The $n_H$ of single phase $V_{0.8+x}$CoSb ($x$ = 0.1, $T_{anneal}$ = 873 K) is greater than that of phase-pure $Nb_{0.8+x}$CoSb (see Table 7.1) prepared at the same temperature by over a factor of $\sim$ 3. To understand the contrasting solubilities of nominally NV = 1 (or VEC = 19) half-Heuslers, we calculate the defect formation enthalpies ($\Delta H_{def}$) for adding an $X$-atom in the vacancy position of the ground state $X_yYZ$ structure. Since the temperature-dependent shift in the single phase compositions are bound by the $X$-rich phase boundary in all the examples (see Figure 7.2), we calculate the $\Delta H_{def}$ for the $X$-rich chemical conditions.

We compare the calculated $\Delta H_{def}$ with the experimentally observed solubility at the $X$-rich phase boundary composition of various nominally 19-electron half-Heusler systems (see Figure 7.3). In addition to the three systems studied here (see Figure 7.2), we also consider the stoichiometry of $Ti_{0.75+x}$PtSb at $T_{anneal}$ = 1073 K which is investigated in Ref. [10]. The solubility is expressed as the fraction of vacancies ($f = x/(1-y)$, see Figure 7.3) filled in the $X_yYZ$ structure. The phase boundary compositions are chosen to lie between the observed phase pure composition and the two-phase composition (see Figure 7.2). The error bar in the value of $f$ (see Figure 7.3) is due to the difference between these two compositions. In the case of $Ti_{0.75+x}$PtSb (see Ref. [10]), $Ti_{0.84}$PtSb is chosen as the Ti-rich half-Heusler composition as the XRD pattern of $Ti_{0.85}$PtSb shows very small

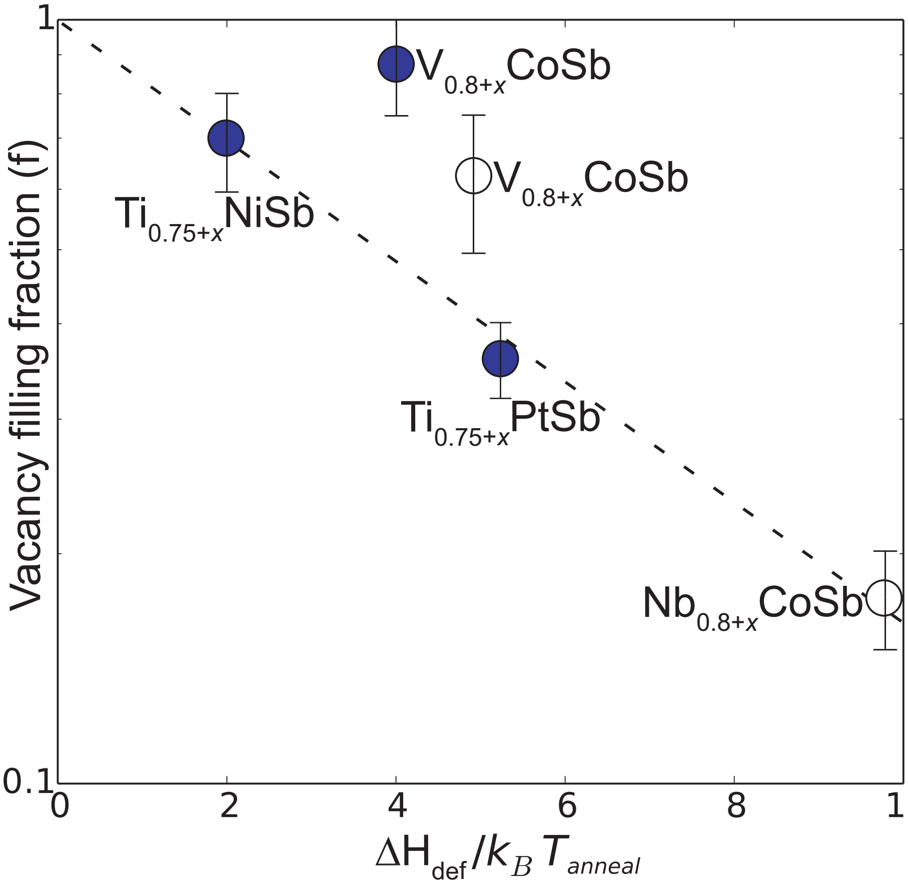

Figure 7.3: **Explaining $X$-solubility in vacancies of the $X_yYZ$ ground state of *nominally* 19-electron half-Heuslers with DFT calculated $\Delta H_{def}$.** Fraction of vacancies ($f$) in the ground state structure ($x$ = 0) filled at $T_{anneal}$ = 1073 K (filled circles) or $T_{anneal}$ = 873 K (unfilled circle) versus the ratio $\Delta H_{def}/k_BT_{anneal}$. $\Delta H_{def}$ is the calculated defect energy for filling $X$-vacancies. The value of $f$ is obtained from systems studied in the present work (see Figure 7.2) and Ref. [10] ($Ti_{0.75+x}PtSb$). The dashed line is a guide to the eye describing correlation between experimentally observed $X$-solubility and $\Delta H_{def}$ (under $X$-rich conditions). Temperature-dependent solubility can be estimated from $\Delta H_{def}$.

impurity phase peaks which cannot be identified as the Ti-poor impurity phase $PtSb_2$. The error bars in the value of $f$ (see Figure 7.3) for $Ti_{0.75+x}PtSb$ are due to the limit of the instrument for detecting secondary phases. In general, the experimentally observed vacancy filling fraction ($f = x/(1-y)$) increases for smaller $\Delta H_{def}$. The observed $f$ in $Nb_{0.8+x}CoSb$, $Ti_{0.75+x}NiSb$ and $Ti_{0.75+x}PtSb$ are strongly correlated to the $\Delta H_{def}$ regardless of annealing temperature (see Figure 7.3). While $V_{0.8+x}CoSb$ might seem like an outlier to the trend with the other systems (see Figure 7.3), $\Delta H_{def}$ qualitatively captures its difference in solubility with the isoelectronic $\mathrm{Nb}_{0.8+x}$CoSb. Hence, we sort the calculated $\Delta H_{def}$ by elemental groups of the $X$-atom (see Figure 7.4).

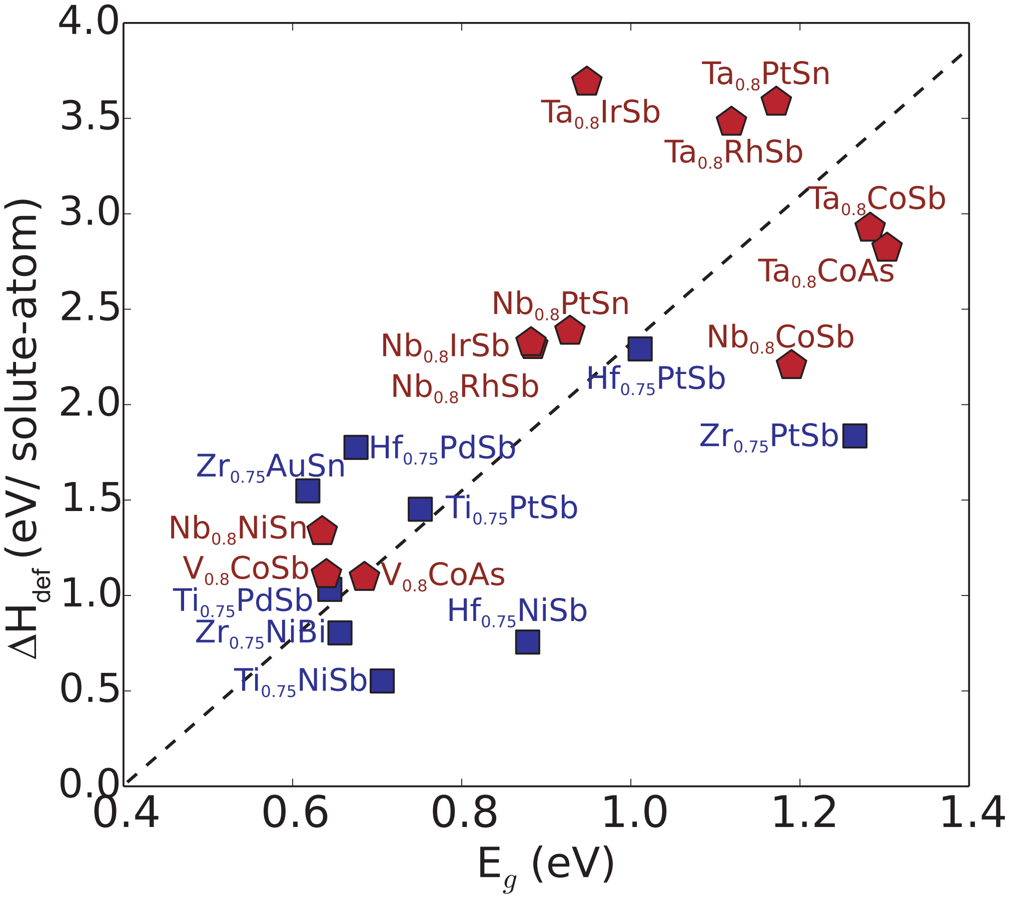

Figure 7.4: **Defect energy of vacancy-filling defect scales with increasing electronic energy gap.** Defect energy ($\Delta H_{def}$) for filling $X$-vacancies in the ground state $X_yYZ$ structures versus band-gap ($E_g$) at the valence-balanced NV = 0 composition. Group-IV ($y$ = 0.75) and Group-V ($y$ = 0.8) cation based nominally NV = 1 (or VEC = 19) systems are shown by square and pentagon symbols respectively. The dashed line is a guide to the eye describing correlation between $\Delta H_{def}$ and $E_g$.

The $\Delta H_{def}$ are calculated for the 21 nominally 19-electron systems (see Figure 7.4) which are either previously reported or predicted to be thermodynamically stable in the half-Heusler phase [10]. The $\Delta H_{def}$ for compounds with larger cations (specially group-V based compounds) is greater than those with smaller cations ($\Delta H_{def}^{Ta} > \Delta H_{def}^{Nb} > \Delta H_{def}^{V}$), presumably due to a larger penalty for adding atoms to the ground state $X_yYZ$ structure. Furthermore, we find that $\Delta H_{def}$ scales roughly with the band-gap ($E_g$) at the 18-electron NV = 0 $X_yYZ$ composition, suggesting a smaller solubility for large $E_g$ systems in general (see Figure 7.4). The trend in $\Delta H_{def}$ with $E_g$ occurs due to the electronic energy gain which stabilizes the $X_yYZ$ structure with respect to the $XYZ$ composition. [10]

The calculated $\Delta H_{def}$ can be used to estimate the temperature-dependent deviations (see Figure 7.3 and 7.4) from the $T$ = 0 K $X_yYZ$ structure for future experimental studies. A qualitative way of using the calculated $\Delta H_{def}$ (see Figure 7.4) is to understand that compounds with a smaller $\Delta H_{def}$ would show larger deviations from the semiconducting NV = 0 composition. Thus the large $\Delta H_{def}$ system $\mathrm{Ta}_{0.8+x}$IrSb can be expected to show very small deviations from this composition even at high temperatures. On the other hand, $\mathrm{Ti}_{0.75+x}$NiSb and $\mathrm{V}_{0.8+x}$CoSb — both phase diagrams already known experimentally (see Figure 7.2) — show the smallest $\Delta H_{def}$ among group-IV or group-V cation based systems respectively; suggesting that they should exhibit the largest temperature dependence in stoichiometry. Since the time these results were published back in 2018, [12] researchers have investigated $X$-solubility in more systems. The trend we predicted for $X$-atom solubility based on $\Delta H^{Ta}_{def}$ > $\Delta H^{Nb}_{def}$ > $\Delta H^{V}_{def}$ was recently confirmed in Ref. [171].

It is desirable to predict relatively inexpensive systems such as $\mathrm{Nb}_{0.8+x}$CoSb, which can exhibit reproducible high temperature thermoelectric properties without exhibiting hysteresis during heating and cooling cycles. For such robust performance one needs to identify systems with an optimized $n$ and a weak temperature dependence in stoichiometry (as in $\mathrm{Nb}_{0.8+x}$CoSb, see Figure 7.2) across the entire range of operational temperatures. We recommend $\mathrm{Ta}_{0.8+x}$CoSb as a potential candidate for such applications. Based on the observed trend in $X$-rich solubility with $\delta H_{def}$ (see Figure 7.3), we estimate $n \sim 3 \times 10^{21}$ cm$^{-3}$ at $x$ = 0.03 for phase-pure $\mathrm{Ta}_{0.8+x}$CoSb synthesized with a $\mathrm{T}_{anneal}$ = 1300 K.

## 7.4 Conclusion

In conclusion, we show that the stable composition of nominally 19-electron half-Heuslers shifts from $X_yYZ$ ($y$ = 0.8 or 0.75) at $T$ = 0 K towards the well-known $XYZ$ stoichiometry, effectively doping itself $n$-type. Hence, unlike in typical half-Heuslers with an equiatomic stoichiometry (eg: TiNiSn), intrinsic electronic and thermal transport properties of these systems can be engineered through a judicious choice of annealing temperature to control defects. The phase diagram analysis and defect calculations presented can guide future experimental efforts in choosing the right composition and temperature synthesis conditions to engineer desirable thermoelectric properties.

# Chapter 8

# Double half-Heulsers

## 8.1 Overview

Since their discovery around a century ago, the structure and chemistry of the multi-functional half-Heusler semiconductors have been studied extensively as three component systems. The elemental groups constituting these ternary compounds with the nominal formula *XYZ* are well established where most stable compositions follow a valence balanced rule (a generalization of the 18 electron rule). From the very *same* set of well-known elements and stability guidelines we explore a much larger phase space of possible *quaternary double* ($X'X''Y_2Z_2$, $X_2Y'Y''Z_2$, and $X_2Y_2Z'Z''$), *triple* ($X'_2X''Y_3Z_3$) and *quadruple* ($X'_3X''Y_4Z_4$) half-Heusler compounds. Using a reliable, first-principles thermodynamics methodology on a selection of 365 novel compositions, we predict 131 novel quaternary compounds to be stable which is already larger in number than those reported extensively for ternary systems (82). Thermoelectric performance of the state-of-the-art ternary half-Heusler compounds are limited by their intrinsically high lattice thermal conductivity ($\kappa_L$). In comparison to ternary half-Heuslers, thermal transport in double half-Heuslers is dominated by low frequency phonon modes with smaller group velocities and limited by disorder scattering. The double half-Heusler composition $Ti_2FeNiSb_2$ was synthesized and confirmed to have a significantly lower lattice thermal conductivity (factor of 3 at room temperature) than TiCoSb, thereby providing a better starting point for thermoelectric efficiency optimization. We demonstrate a dependable strategy to assist the search for low thermal conductivity half-Heuslers and point towards a huge composition space for implementing it. Our findings can be extended for systematic discovery of other large families of multi-component intermetallic semiconductors.

## 8.2 Context and Motivation

Half-Heusler compounds have attracted significant research attention for their thermoelectric properties [152, 172, 173] in the past decade. Due to its diverse chemical space to tune properties, multiple instances of high performance thermoelectrics (NbFeSb[147], TaFeSb[7] and ZrCoBi[148] for $p$-type and TiNiSn [145, 146] for $n$-type transport) are found within this family of compounds. The high performance in half-Heusler compounds is primarily associated with their exceptional electrical transport properties.[144] However, in comparison to some of the best themoelectric materials based on IV-VI compounds [174, 175], ternary half-Heusler compounds are at a disadvantage due to their intrinsically large lattice thermal conductivity ($\kappa_L$). ZrCoBi, for example,[148] has one of the lowest reported $\kappa_L$ = 10 W/m-K among the high performing half-Heusler compounds (T = 300 K), whereas the state-of-the-art thermeoelectric material PbTe has intrinsic lattice thermal conductivity of 2 W/m-K[176]. Thus, it is desirable to find a strategy for discovering new semiconductors with the electronic properties of half-Heusler compounds but with inherently lower $\kappa_L$.

In addition to the well-known dependence of $\kappa_L$ on chemical composition through phonon scattering [177, 73] and lattice softening mechanisms [148, 73], lattice thermal conductivity also depends on the primitive unit cell size.[178] For two materials with comparable bulk properties, such as Debye temperature, average mass per unit cell, specific heat ca-

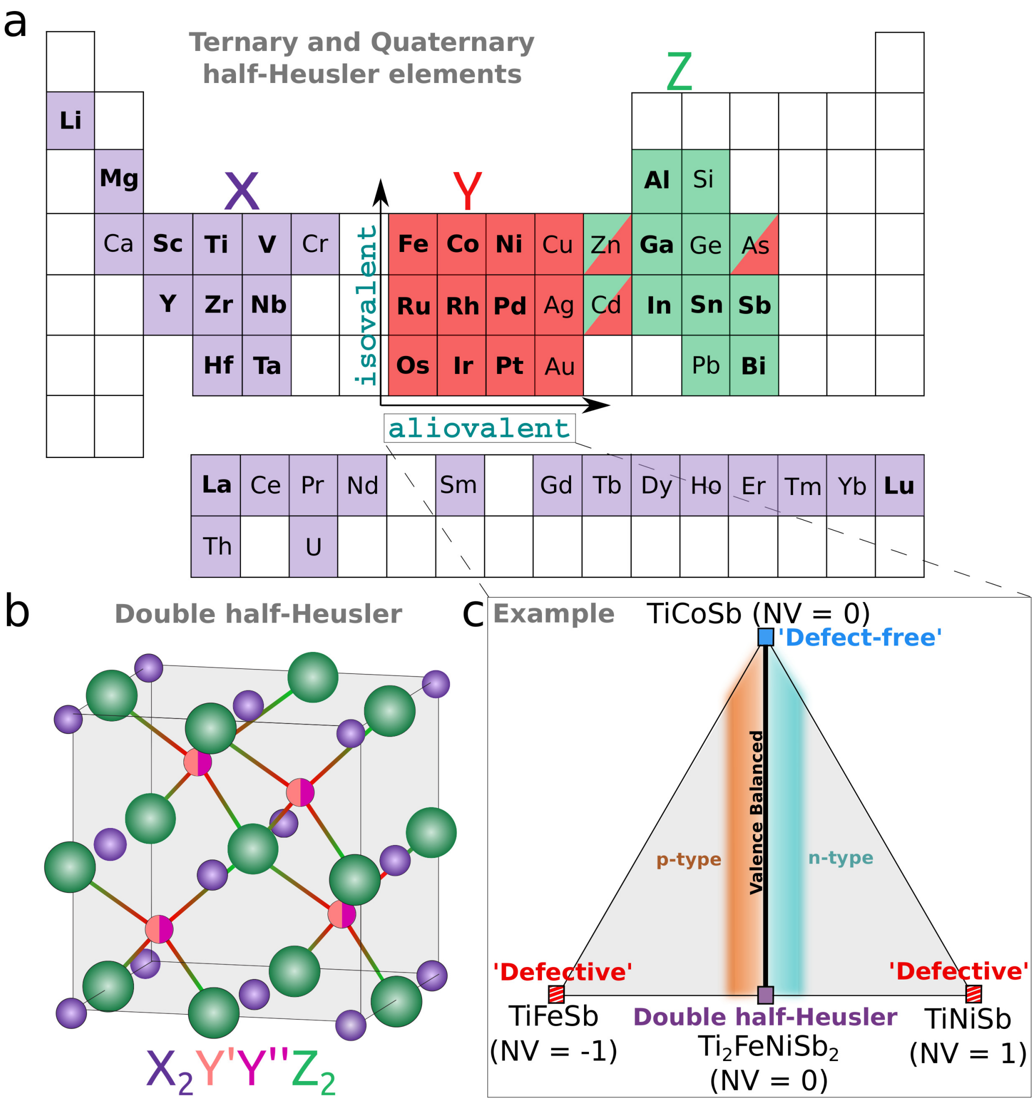
a
Ternary and Quaternary half-Heusler elements
X
Y
Z
Li
Mg
Ca Sc Ti V Cr
Y Zr Nb
Hf Ta
Fe Co Ni Cu Zn
Ru Rh Pd Ag Cd
Os Ir Pt Au
Al Si
Ga Ge As
In Sn Sb
Pb Bi
isovalent
aliovalent
La Ce Pr Nd Sm Gd Tb Dy Ho Er Tm Yb Lu
Th U
b
Double half-Heusler
X2Y'Y''Z2
c
Example
TiCoSb (NV = 0)
'Defect-free'
Valence Balanced
p-type
n-type
'Defective'
'Defective'
TiFeSb (NV = -1)
Double half-Heusler
Ti2FeNiSb2 (NV = 0)
TiNiSb (NV = 1)

Figure 8.1: **Visual illustration of the concept of double half-Heuslers.** (a) Color scheme in the periodic table representing elements occupying various sites ($X$ (violet), $Y$ (red) and $Z$ (green)) of the cubic half-Heusler structure (in panel b). Quaternary half-Heusler compositions selected in the present work are based on elements given in bold font. (b) The *double* half-Heusler structure (disordered) with the general formula $X_2Y'Y''Z_2$ has equal occupancy on the $Y$-site (in half orange/ half magenta) such that the overall composition is valence balanced (net valence NV = 0). (c) Example pseudoternary $TiFe_xCo_yNi_{1-x-y}Sb$ based on aliovalent substitution on the atomic $Y$-site. Double half-Heusler $Ti_2FeNiSb_2$ (purple square) and the alloy compositions joining it to TiCoSb (blue square) are valence balanced (NV = 0). Adjacent compositions based on Fe (orange) and Ni (cyan) substitutions represent $p$ and $n$-type compositions respectively. Nominally NV $\neq$ 0 compositions (red/ white squares) are examples of *ternary defective* half-Heuslers which are unstable without defects ($TiFe_{1.5}Sb$[11] and $Ti_{0.75+\delta}NiSb$[12]). These NV $\neq$ 0 compositions will be referred to as the ternary components of the double half-Heusler composition.

pacity and Gruniesen parameter, the magnitude of lattice thermal conductivities ($\kappa_L$) depends primarily on the number of atoms in the primitive unit cell ($N$). [178] Complex materials with larger $N$ have smaller $\kappa_L$ due to a relatively small fraction of high group velocity ($v_g$) acoustic modes compared to lower $v_g$ optical modes. Well-known examples of low $\kappa_L$ materials with a large $N$ are $La_2Mo_2O_9$ ($N$ = 624, $\kappa_L$ = 0.7 W/ m-K)[179] and $Yb_{14}AlSb_{11}$ ($N$ = 104, $\kappa_L$ = 0.6 W/ m-K)[180].[178] For ternary half-Heuslers however, $N$ = 3 indicates the huge potential for low thermal conductivity materials discovery if the effective $N$ of the could be increased systematically.

A well-known family of compounds with varying cell-sizes comprises those based on the Pervoskite structure.[181] The high symmetry structures of the ternary Perovskites ($ABO_3$, example cubic $BaTiO_3$) have $N$ = 5 while quaternary double Perovskites ($A_2B'B''O_6$, example cubic $Sr_2FeMoO_6$ ($N$ = 10), monoclinic $La_2CuSnO_6$[182] ($N$ = 40)) have $N \geq 10$ when ordered. Double Perovskites have a number of advantages over simple Perovskites in tuning their functionalities for solar cell applications, magnetoresistive properties, etc.[181, 183, 184, 185] With the additional possibilities of a new element, the number of double Perovskites is also several times larger than simple Perovskite compounds.[181, 183]

Like Perovskites, half-Heuslers can be made from a variety of elements with each site occupied by elements in different regions of the periodic table (see Figure 8.1 a). The possible ternary half-Heusler compositions (nominally $XYZ$) based on these elements can be chosen by assigning a valence to each element in the compound and imposing the valence balanced rule (a generalization of the well-known 18 electron rule for half-Heuslers),[10] according to which the net valence (NV) of the three components add up to 0 for most stable compounds (e.g. NV of TiCoSb = 4 ($Ti^{+4}$ $s^0d^0$) - 1 ($Co^{-1}$ $d^{10}$) - 3 ($Sb^{-3}$ $s^2p^6$) = 0). While quaternary compositions of the half-Heusler phases are studied routinely, these are almost always based on isovalent substitution between ternary systems with no unique valence balanced composition (example $Ti_{0.5}Zr_{0.5}NiSn$ and $Ti_{0.2}Zr_{0.8}NiSn$) and hence do not favor the formation of ordered compounds like the double perovskites.[186] As a result, these alloy compositions often form disordered solutions which are stabilized by temperature. Aliovalent substitution, however, can give rise to a unique valence balanced composition (for example Fe and Ni substitution on the atomic $Y$-site in $Ti_2FeNiSb_2$, see Figure 8.1 c) which is also characteristic of the compound forming 18-electron ternary half-Heuslers.[10] Hence, just like ternary half-Heuslers,[6] one can expect ordered ground states at these unique compositions to form stable compounds. Inspired by double Perovskites, in which the 'double' could refer to doubling of the Perovskite formula unit ($A_2B'B''O_6$ versus $ABO_3$), we define double half-Heuslers (see Figure 8.1 c) as stable quaternary compounds based on aliovalent substitution ($X_2Y'Y''Z_2$ versus $XYZ$ where $Y'$ and $Y''$ are not isovalent). To distinguish these compounds from the other isovalently alloyed quaternary compositions (example $Ti_{0.5}Zr_{0.5}NiSn$), we call these aliovalently substituted compounds (example $Ti_2FeNiSb_2$) as double half-Heuslers *regardless* of whether they undergo an order-disorder transition at a higher temperature. Although the disordered phase may have a distinct and possibly stronger scattering mechanism for phonons, the double half-Heusler composition ensures that for $\kappa_L$, the *effective* $N > 3$.

The quaternary compositions of the double half-Heusler systems could present a much larger phase space for materials discovery in comparison to the ternary compositions. As we demonstrate here, there are a very large number of predicted stable double half-Heuslers awaiting experimental discovery. In addition to their applications as thermoelectrics, double half-Heuslers could also find use in transparent conducting thin-films (e.g. TaIrGe [187]), topological semi-metals (e.g. HfIrAs [6]), and spintronics (e.g. $V_{0.8+\delta}CoSb$ [168, 12]) for which the ternary half-Heuslers are already being studied.[141]

## 8.3 Results and Discussion

### 8.3.1 Locating double half-Heuslers in a pseudoternary phase space

Consider the example of the pseudoternary $TiFe_xCo_yNi_{1-x-y}Sb$ (see Figure 8.1 c), which allows for the aliovalent substitution of Fe, Co, and Ni atoms on the atomic $Y-$site (see Figure 8.1 a). The end-members, namely TiFeSb, TiCoSb, and TiNiSb all have different net valence (NV = -1, 0 and 1). In such a compositional phase space the valence balanced end-members (like TiCoSb in Figure 8.1 c) are candidates to form half-Heusler phases and have been studied rigorously (see Figure 8.2) either as experimental reports [6, 167, 173, 7] or as first-principles thermodynamic predictions [6, 188, 167, 173, 7]. Systems of the non-valence balanced end-members (TiFeSb and TiNiSb in Figure 8.1 c) on the other hand, were not expected to form in the Heusler phase due to a perceived electronic configuration unfavorable for strong bonding interactions.[141] However, the two NV $\neq$ 0 systems shown (Ti-Fe-Sb and Ti-Ni-Sb) were recently reported to form half-Heusler phases at alternate defective stoichiometries ($TiFe_{1.5}Sb$ and $Ti_{0.75+\delta}NiSb$ respectively) to attain a more stable electronic configuration.[11, 10, 12] Since these discoveries nominally NV $\neq$ 0 compounds have attracted some attention as *ternary defective* half-Heuslers (see Figure 8.1 c and Figure 8.2). [1, 87, 10, 12, 85] Possibly due to only one 'likely' (NV = 0) half-Heusler candidate among the three end-members of such pseudoternaries, a large compositional space in the middle has seldom been investigated previously. However, the 'double' half-Heusler composition such as $Ti_2FeNiSb_2$ (4 ($Ti^{+4}$ $s^0d^0$) - 1 (0.5 $Fe^{-2}$ $d^{10}$) - 0 (0.5 $Ni^0$ $d^{10}$) - 3 ($Sb^{-3}$ $s^2p^6$) = 0), and the alloy compositions connecting it to TiCoSb are also valence balanced with semiconducting $p$- and $n$-type transport achievable at adjacent compositions (see Figure 8.1 c and transport properties in [13]). In the present work, we will refer to the nominally NV $\neq$ 0 systems such as TiNiSb and TiFeSb as the two ternary components of the quaternary double half-Heusler compound, $Ti_2FeNiSb_2$.

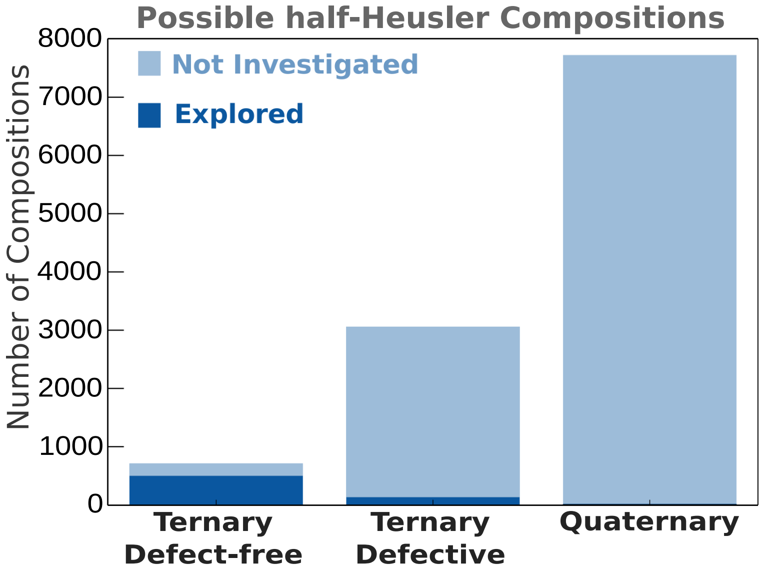

Figure 8.2: **The quaternary half-Heusler composition space is almost completely unexplored.** Bar chart depicting the current status of exploration in possible ternary half-Heusler systems as opposed to quaternary systems. Compositions were obtained by imposing the valence balanced rule on the elemental combinations provided in figure 8.1 a. The dark blue color gives a conservative estimate of the fraction of explored compositions. The quaternary phase space is almost completely unexplored.

### 8.3.2 Enormous compositional phase space of quaternary *double*, *triple* and *quadruple* half-Heuslers.

Similar to $Ti_2FeNiSb_2$, possible double half-Heusler compositions based on equal occupancies on the $X-$ (e.g. $ScVCo_2Sb_2$) and $Z-$site (e.g. $Ti_2Ni_2InSb$) are also possible. Furthermore, there are additional 'triple' (e.g. $Nb_2MgCo_3Sb_3$) and 'quadruple' (e.g. $Nb_3LiCo_4Sb_4$) half-Heusler compositions, as well, which obey the valence balanced rule (NV = 0). We applied the valence balanced rule to elemental combinations from Figure 8.1 a to estimate the number of possible defect free ternary half-Heuslers, defective ternary half-Heuslers and quaternary half-Heuslers (see Figure 8.2). We use a valence of +1 for Li, +2 for group-II elements, +3 for group-III elements and rare-earth Lanthanides, +4 for group-IV elements, Cr and Actinides, -2 for group-VIII elements, -1 for group-IX elements, 0 for group-X elements, +1 for group-XI elements, +2 for group-XII elements,

-5 for Al, Ga, In, -4 for Si, Ge, Sn, Pb, -3 for As, Sb, Bi. The number of ternary defective compositions are counted by the nominally NV $\neq 0$ combinations based on the elements in the Figure 8.1 a.

Furthermore, we also estimate the number of compositions explored previously in these categories (see Figure 8.2). For this, we consider all compositions which either (i) have been reported in experimental studies to form a stable phase (not necessarily in half-Heusler half-Heusler structure) or (ii) accessed computationally for thermodynamic stability (including compositions predicted to phase separate or crystallize in structures other than half-Heusler). We count all the cases contained in the inorganic crystal structure database (ICSD) [5] and those examined through rigorous high-throughput computations [6, 167, 7, 173]. We note that experimental studies reporting phase separating compositions are hard to find in the literature and are not contained in any databases such as the ICSD. Hence, our count of explored ternary and quaternary compositions can be considered as a conservative estimate of the explored composition space given in 8.2.

We find a huge phase space of 7719 possible quaternary half-Heusler compositions (see Figure 8.2). This number is over 10 times larger than that of the defect-free ternary systems (715 possible composition) based on the same set of elements. We estimate the fraction of explored compositions (see Experimental Procedure section) for defect-free ternary systems is $\sim$ 64% (see Figure 8.2). In stark contrast, only 0.07 % of the possible quaternary half-Heusler compositions have been explored with 4 reports ($Ti_2FeNiSb_2$[189], $ScNbNi_2Sn_2$, $Zr_2Ni_2InSb$, and $Hf_2Ni_2InSb$[190]) of the half-Heusler phase in past experiments. There are no past reports — measurements or calculations — of thermal conductivity on such quaternary compositions in the literature.

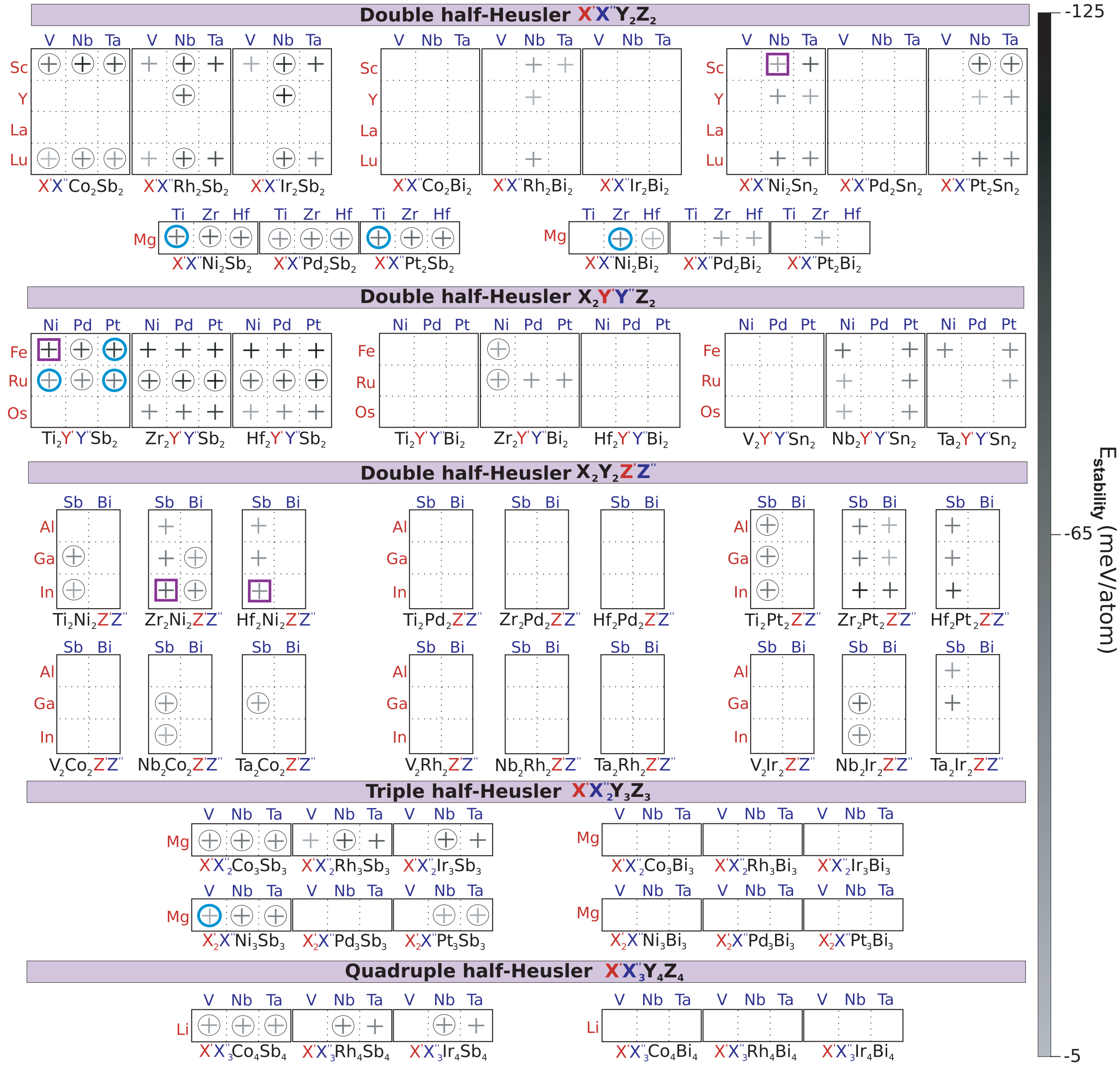

Figure 8.3: **Predicted quaternary half-Heuslers and their stability ($E_{stability}$).** 351 quaternary half-Heusler compositions (divided between 5 sub-types) investigated in the present work for stability in the half-Heusler structure. Half-Heuslers predicted stable are represented by a plus (+) symbol. For compounds where the half-Heusler phase is predicted unstable, the space is left blank. The greyscale bar on the side gives the magnitude of predicted stability ($E_{stability}$, data provided in Ref. [13]) of the quaternary half-Heuslers. Predicted compounds for which only one of the ternary NV $\neq$ 0 component have a half-Heusler phase reported experimentally are denoted by thin circles. Predicted compounds for which both the ternary NV $\neq$ 0 components have a half-Heusler phase reported experimentally are denoted by thick circles. Previously reported quaternary half-Heuslers are denoted by boxes.

### 8.3.3 Stability prediction for selected double, triple and quadruple half-Heuslers.

We select 369 quaternary half-Heusler (315 double half-Heusler, 36 triple half-Heusler and 18 quadruple half-Heusler) compositions to perform high-throughput calculation for examining the thermodynamic stability using convex-hull analysis (see Figure 8.3) within the Open Quantum Materials Database (OQMD).[8, 9] In the present work we avoid Ge, As, Pb and Si based compounds which have relatively fewer reports of ternary half-Heuslers [6, 167]. The chosen compositions (given in Figure 8.3) are based on a subset of elements (given in bold font in Figure 8.1 a) well-known to form ternary half-Heusler compounds.

The 315 double half-Heusler compositions studied here are divided into three classes (126 $X'X''Y_2Z_2$, 81 $X_2Y'Y''Z_2$ and 108 $X_2Y_2Z'Z''$ compositions) based on the site of substitution in the $XYZ$ structure (see Figure 8.1 a). Our calculations are in agreement with past experimental reports of the half-Heusler phase in $Ti_2FeNiSb_2$,[189] $ScNbNi_2Sn_2$, $Zr_2Ni_2InSb$, and $Hf_2Ni_2InSb$ [190]. We predict 48 $X'X''Y_2Z_2$, 36 $X_2Y'Y''Z_2$ and 27 $X_2Y_2Z'Z''$ new double half-Heusler compounds (see plus symbols in Figure 8.3), suggesting that substitution on either of the three atomic sites are quite favorable. Out of the 36 possible triple half-Heusler ($X'_2X''Y_3Z_3$) and quadruple half-Heusler ($X'_3X''Y_4Z_4$) compositions combined, we predict 13 and 7 new compounds, respectively of each sub-type (see Figure 8.3). Similar to ternary half-Heusler compounds, Sb-based compositions have the largest fraction of predicted stable compounds, followed by Sn- and then Bi-based compounds. This trend in stability of the semiconducting half-Heusler phases can be associated with the requirement of large size[167] and large electronegativity for the $Z$-site atom. Although we do not calculate As and Ge-based double half-Heuslers here, based on stability calculations (see Figure 6.8 and Figure 6.9) and their relatively lesser previous reports (list provided in Ref. [13]) of ternary half-Heuslers, we expect them to be relatively rarer.

### 8.3.4 Guidelines for laboratory discovery

Going through the list of 132 predicted new compounds using experimental synthesis can be quite daunting. To guide experimental efforts in initial choice of more likely compositions for laboratory discovery, we arrange (see color bar in Figure 8.3) the compounds according to their predicted stability ($E_{stability}$). Compounds represented with darker plus symbols in Figure 8.3 are predicted to be more stable relative to decomposition into competing phases. The $E_{stability}$, formation energy ($\Delta H_f$) and band-gap of the compounds predicted to be stable are provided in Ref. [13] in descending order of predicted stability ($E_{stabilit}$).

We also use past experimental reports of the half-Heusler phase in ternary systems to categorize the predicted quaternary half-Heuslers by their likelihood to form compounds. The predicted quaternary half-Heuslers are based on aliovalent substitution in two nominally NV $\neq 0$ ternary XYZ structures (for example TiFeSb and TiNiSb for $Ti_2FeNiSb_2$, see Figure 8.1 c). As a result, the stability of quaternary half-Heuslers must be correlated to the stability of its ternary NV $\neq 0$ components which are investigated to a relatively larger extent (see ternary defective bar in Figure 8.2). Based on this rationale, the likelihood of predicted quaternary half-Heusler phase to stabilize increases depending on whether one (see thin circles in Figure 8.3, for example $Ti_2Ni_2InSb$) or both (see thick circles in Figure 8.3, for example $MgTiNi_2Sb_2$) of its ternary NV $\neq 0$ components have a half-Heusler phase previously reported for them. We caution that this classification based on past experimental reports may not be complete simply because a large fraction of ternary nominally NV $\neq 0$ systems are still unexplored (see Figure 8.2).

### 8.3.5 Discovery of low $\kappa_L$ quaternary half-Heuslers

We compare measured $\kappa_L$ of double half-Heusler $Ti_2FeNiSb_2$ to that of its corresponding ternary system TiCoSb with the same average atomic mass. At room temperature, $\kappa_L$ of

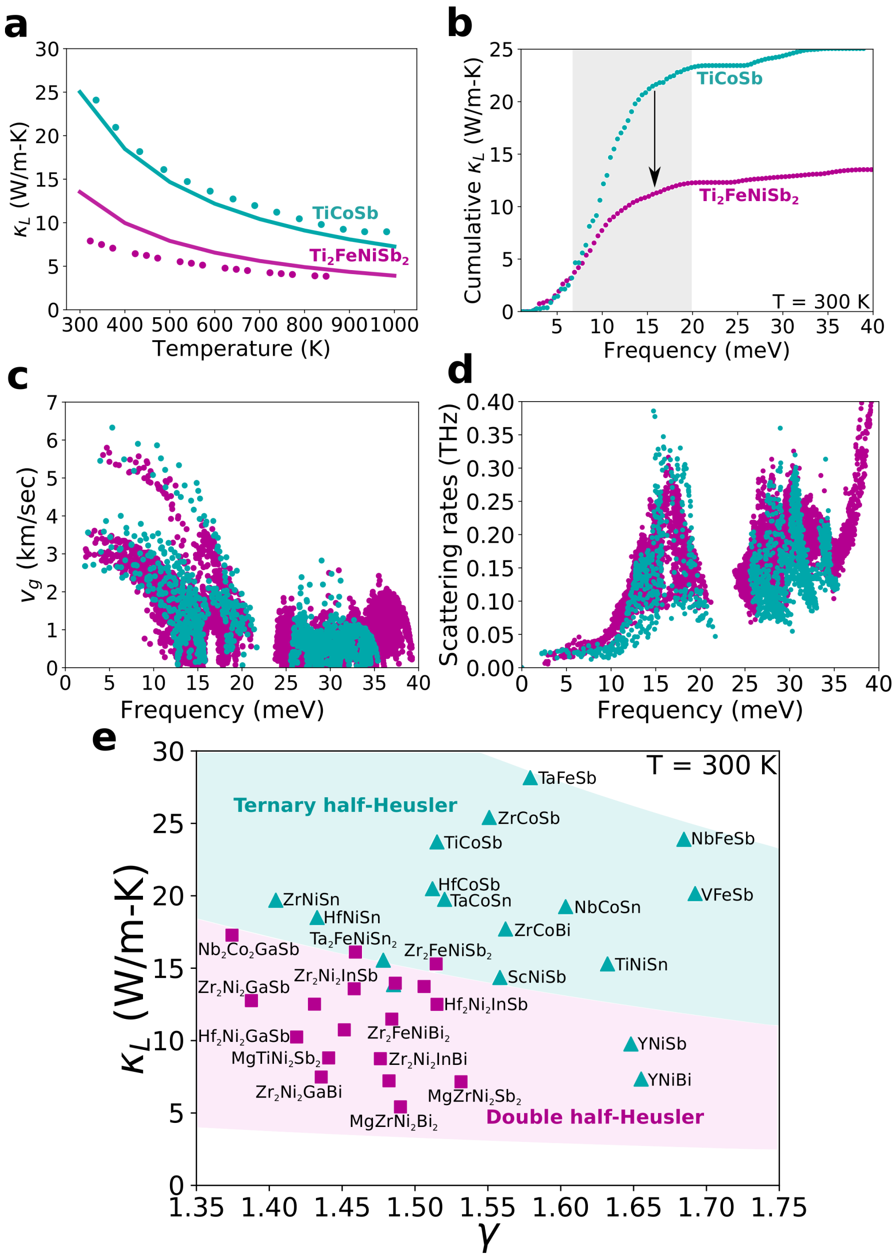

Figure 8.4: **Lattice thermal conductivity comparison of double half-Heusler and corresponding ternary half-Heusler.** (a) Calculated (line) and measured (scatter points) lattice thermal conductivity ($\kappa_L$) of TiCoSb (cyan) and $Ti_2FeNiSb_2$ (magenta) as a function of temperature. Experimental values of TiCoSb are taken from Sekimoto et al. [14]. Calculated phonon frequency dependence of (b) cumulative $\kappa_L$, (c) group velocities ($v_g$), and (d) phonon-phonon scattering rates in the two compounds at $T$ = 300 K. (e) Calculated $\kappa_L$ versus Gruniesen parameter ($\gamma$) for selected half-Heusler (triangle) and double half-Heusler (square) compounds based on commonly used elements. The regions are shaded based on a $\gamma^{-2}$ dependence of $\kappa_L$.

$Ti_2FeNiSb_2$ is smaller than TiCoSb by a factor of 3 (see Figure 8.4 a). To examine the origin of the smaller $\kappa_L$ in $Ti_2FeNiSb_2$ we calculate the lattice thermal conductivity of its ordered ground state from first-principles considering only three-phonon processes (see Figure 8.4 a). The calculated $\kappa_L$ is very similar to the measured values, especially at higher temperatures.

Calculated cumulative $\kappa_L$ in TiCoSb and $Ti_2FeNiSb_2$ as a function of frequency (see Figure 8.4 b) suggests that over 90 % of the thermal transport in both compounds occurs in phonon modes corresponding to the acoustic modes of the ternary structure. The difference in the $\kappa_L$ between the two compounds occurs primarily in the high energy range (7-20 meV, see shaded grey region in Figure 8.4 b) corresponding to the acoustic modes of TiCoSb. Both compounds largely show a similar dependence of group velocity ($v_g$) as well as scattering rates on phonon frequencies (see Figure 8.4). However, the group velocity ($v_g$) of phonons in $Ti_2FeNiSb_2$ is in general much lower than that of the corresponding longitudinal and transverse acoustic modes of TiCoSb (see Figure 8.4 c). As can been understood from simple ball-spring models for cell-doubling,[178] the difference in $v_g$ becomes more prominent in the higher frequency range (10-20 meV) of the acoustic modes in TiCoSb (see Figure 8.4 c). The phonon scattering rates of the double half-Heusler $Ti_2FeNiSb_2$ structure are also slightly larger in the 7-12 meV frequency range (see Figure 8.4 d). The trend of lower $\kappa_L$ for double half-Heuslers compared to ternary half-Heuslers is reproduced in a survey of 35 compounds (see Figure 8.4 e) calculated in a similar way. This confirms our expectation that double half-Heusler with the more complex crystal chemistry would in general have lower lattice thermal conductivities than traditional ternary half-Heusler.

The weaker temperature dependence in the measured $\kappa_L$ of $Ti_2FeNiSb_2$ in comparison to the calculated values (see Figure 8.4 a) can possibly be attributed to the presence of alloy scattering mechanism associated with disorder in the Fe/Ni sub-lattice. The disorder in the system was confirmed by the powder XRD pattern of $Ti_2FeNiSb_2$ (see Figure 8.5) as no superlattice peaks associated with Fe/Ni ordering were observed. The alloy scattering mechanism is not captured in our $\kappa_L$ calculations which were performed on the ordered $Ti_2FeNiSb_2$ structure assuming only Umpklapp scattering which has a relatively stronger ($T^{-1}$) temperature dependence when compared to the alloy scattering mechanism.

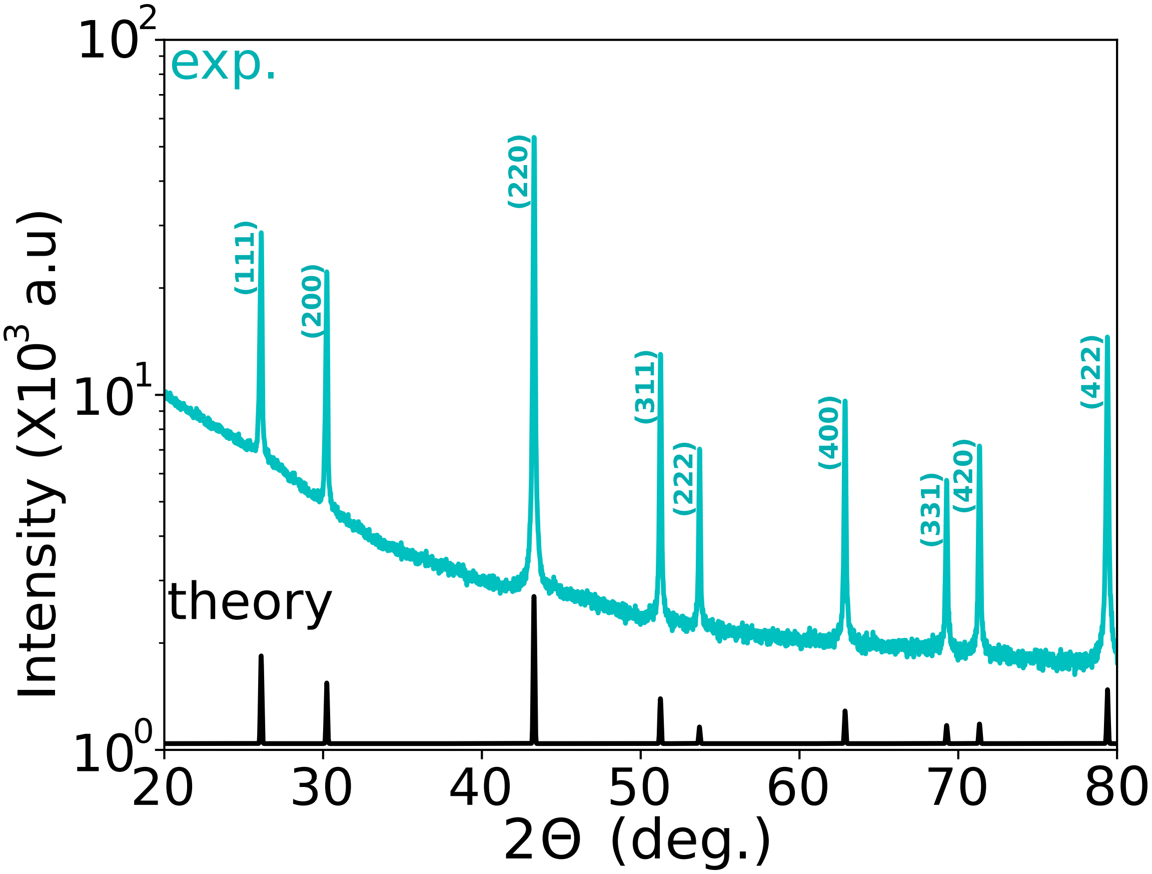

Figure 8.5: **Experimental verification of double half-Heusler compound $Ti_2FeNiSb_2$.** Room temperature powder XRD pattern (cyan) of $Ti_2FeNiSb_2$ annealed at 1073 K. Theoretical XRD pattern for special quasi-random structure (SQS) of $Ti_2FeNiSb_2$ is given in black. Experiments were performed by Dr. Max Wood from the Snyder group at Northwestern.

To understand the observed global cubic symmetry of the half-Heusler phase, we estimate the energy difference between the ordered and disordered phase by calculating the energy of the special quasi-random structure of $Ti_2FeNiSb_2$. The disordered phase of $Ti_2FeNiSb_2$ is only 23.6 meV/mixing-atom higher in energy than the ordered phase. This difference in energy can be overcome by thermal energy alone at 275 K, thereby explaining the observed disordered $Ti_2FeNiSb_2$ phase. Recent reports of short range ordering observed in electron diffraction pattern of ternary defective half-Heuslers suggests that short range ordering[85] could also exist in double-Half-Heusler compounds and its impact on thermal conductivity should also be considered. It is important to note that double half-Heuslers could be alloyed with the defective half-Heusler phases ($Ti_{0.75+\delta}NiSb$[12, 10] and $TiFe_{1.5}Sb$[11]) of its ternary components to introduce vacancies and interstitial defects which can be expected to decrease the thermal conductivity further. While the alloy scattering mechanism of phonons are good for thermoelectric applications by reducing thermal conductivity, the same scattering mechanisms are also likely to reduce charge carrier mobility and electrical conductivity possibly depending on site of substitution.[191] The net benefit in thermoelectric performance would be characterized by the ratio of lattice thermal conductivity to charge carrier mobility.[192]

### 8.3.6 Subtle differences distinguishing Double half-Heuslers from half-Heusler compounds

In this work, we call the quaternary half-Heusler compound $Ti_2FeNiSb_2$ a double half-Heusler compound *despite* the observed on the $Y$-site at the temperatures of interest. Although one might choose to see it as an alloy 'solid solution' due to the disordering, the double half-Heusler nomenclature here is deliberate due to subtle differences with respect to commonly studied half-Heusler solid-solutions resulting from isovalent alloying. The stability in the $Ti_2FeNiSb_2$ composition, unlike the isovalently alloyed $Ti_{0.5}Zr_{0.5}NiSn$ composition, lies in the ordering tendency on the Fe/Ni sub-lattice. This leads to a phase diagram for the double half-Heusler phase which is fundamentally different from that of the isovalently alloyed solid solution (see Figure 8.6). While the single phase region of the latter evolves in the pseudobinary phase diagram evolves from the end-member compositions, the double half-Heusler single phase evolves from the middle composition (see Figure 8.6). Due to these differences, we choose think of high temperature $Ti_2FeNiSb_2$

as a ‘disordered compound’ instead of an alloy between two end-members. Given that the double half-Heusler composition space is almost entirely unexplored (see Figure 8.2), we believe that differentiating these compositions from isovalently alloyed half-Heusler solid-solutions through use of appropriate nomenclature is very important.

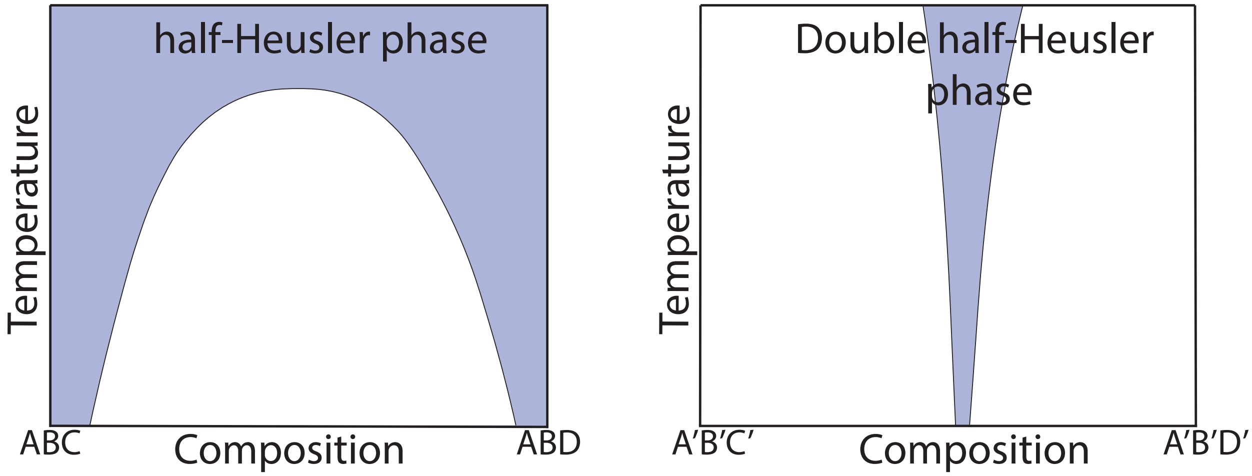

Figure 8.6: **Schematic distinguishing key differences between the temperature-dependent phase diagram of the half-Heusler and the double half-Heusler phases.**

### 8.3.7 Potential for exploration of low cost thermoelectrics in quaternary half-Heusler phase space

While other quaternary compounds can be investigated for thermodynamic stability, the current prediction of 131 new compounds is already greater than the 82[6, 167, 173, 7, 5] (lists provided in Ref. [13]) extensively predicted /reported transition metal based ternary defect-free half-Heusler phases. This result suggests that, despite a hundred years of Heusler history, only a small fraction of half-Heuslers have been investigated previously. Among the new compounds predicted here, 32 are based on relatively abundant or inexpensive elements (namely Li, Mg, Y, Ti, Zr, Hf, V, Nb, Ta, Fe, Ni, Co, Al, Ga, In, Sn, Sb and Bi, list provided in Ref. [13]) commonly used for synthesis of half-Heusler compounds, and serve as an immediate prediction for experimental synthesis. Given the intrinsically smaller $\kappa_L$ of quaternary half-Heusler compounds (see Figure 8.4 e) due to its complex crystal chemistry, they present a new avenue for thermoelectric materials discovery. The present work only deals with quaternary equivalents of transition metal based half-Heusler compounds with 18-valence electrons. The concepts discussed here are easily applicable to other multi-component Heusler based structures[193] such as 8-electron Nowotnye-Juza phases (for example LiAlSi)[153, 194], $f$-block element based half-Heuslers (for example DyNiBi) [195], 24-electron full-Heuslers (for example $VFe_2Al$)[141, 196, 197], and Li-based 18-electron Heuslers [198] opening up the possibility for an even larger phase space of materials with versatile properties.

## 8.4 Conclusion

We demonstrate that the number of known half-Heusler based semiconductors, despite its hundred years of history, may only be a fraction of the actual number of stable compounds. The previously unexplored semiconductor compositions can be conceived by choosing aliovalently substituted combinations which are valence balanced and predicted systematically using first-principles thermodynamics of stability. From this strategy we discover quaternary (double, triple and quadruple) half-Heusler compounds with thermal conductivities intrinsically lower than traditional ternary half-Heuslers owing to their complex crystal chemistry. As a result, we significantly advance the decade long search for low thermal conductivity half-Heuslers without tampering with its underlying transition metal chemistry which forms the basis of their exciting properties suitable for thermoelectrics, spintronics, topological band structures and transparent conducting thin-films.

# Chapter 9

# 24-electron Full-Heulser $VFe_2Al$, Semi-metal or Semiconductor?

## 9.1 Overview

There is renewed interest in the full-Heusler $VFe_2Al$ composition for its exceptional thermoelectric power factors in bulk and thin film phase. Despite the technological importance of its electrical properties, the electronic structure of bulk $VFe_2Al$ is poorly understood, with conflicting experimental as well as computational reports of band-gap ($E_g$) in over two decades of literature. Hence, there is no general consensus on the $E_g$ of $VFe_2Al$ and the observed properties are sometimes erroneously ascribed to exotic phenomena due to poor understanding of the electronic structure. In this study, using the $VFe_2Al$ example, we show that thermoelectric transport properties — electrical resistivity and Seebeck coefficients — can be used to determine $E_g$ *self-consistently*. Our two-band model, which explains the compilation of data from a variety of $n$ and $p$-type $VFe_2Al$ compositions, demonstrates that its electronic properties can be explained as a valence balanced semiconductor with a very small band-gap ($E_g$ = 0.03 +/- 0.01 eV). In this small $E_g$ semiconductor understanding, the model suggests that nominally undoped $VFe_2Al$ samples appear metallic because of intrinsic defect concnetrations on the order of $\sim 10^{20}$

defects/cm$^{-3}$.

Commonly used experimental techniques to investigate $E_g$ can be sensitive to the size of the band-gap, electronic structure features (direct versus indirect gap) and also the number of intrinsic charge carriers, which can frequently depend on synthesis conditions. Since $E_g$ obtained from transport property modelling is essentially independent of all such factors, it can be used as a more robust approach for band-gap estimation. This conceptual insight highlights the importance of using transport property analysis directly for understanding electronic structure when conventional methods for measuring $E_g$ yield results which are conflicting with the observed properties.

The electrical transport analysis reveals that the electronic mobility in the compound is dependent on the doping site. To understand these trends in the observed electrical transport and the electronic structure in the context of its local bonding, we construct a molecular orbital (MO) picture of $VFe_2Al$. For this, we perform a $k$-resolved Crystal Orbital Hamiltonian Population (COHP) analysis in which the most relevant interactions are selected based on orbital projected partial density of states contributions. The resulting MO diagram, rooted in this rigorous quantitative analysis, is notably different than the previous ones presented for a valence balanced interpretation of $VFe_2Al$.

## 9.2 Context and Motivation

The thermoelectric properties of the full-Heusler alloy composition of $VFe_2Al$ have been studied extensively [21]. The compound is based on non-toxic, inexpensive and earth abundant elements, making it ideal for mass-produced, consumer products for waste heat recovery or refrigeration if sufficient thermoelectric efficiency can be achieved. The thermoelectric power factor of $n$-type bulk $VFe_2Al$[21, 18] exceeds that of commercially available $n$-type $Bi_2Te_3$ [199] at room temperature. Recently, remarkable thermoelectric properties were reported in films having the full-Heusler alloy composition of $VFe_2Al$, but with a metastable body centered cubic structure.[200] The high thermoelectric power factor and low thermal conductivity reported in the films [200] warrant a closer look at the transport properties of the bulk full-Heusler material, which has already been studied extensively, for a better understanding of the unique chemistry of this composition.

Many full-Heusler compounds such as $VFe_2Al$ appear to be stable with 24 valence electrons[141] per formula-unit, which suggests a possible molecular orbital explanation for the electronic structure and stability near a semiconducting composition as commonly found in Zintl phases [178] and half-Heusler thermoelectrics [152]. Nevertheless, in a majority of studies bulk $VFe_2Al$ has been interpreted as an indirect semimetal (see Figure 9.1) with a pseudogap,[201, 202, 141, 21] due to early photoemission[203], NMR[204] and computational[205, 206, 207] studies describing it as a semimetal.

However, some properties of bulk $VFe_2Al$ are more consistent with a semiconductor (see Figure 9.1) rather than a semimetal description [208]. For example, the nominally stoichiometric compound shows a decreasing electrical resistivity with increasing temperature, which is consistent with a semiconductor description[203]. The discrepancy between observed transport and semimetallic understanding of $VFe_2Al$ has occasionally been rationalized using possible exotic phenomena such as $3d$ heavy fermion behavior[203, 207]. However, subsequent heat capacity measurements do not appear to corroborate this behavior[209]. As a result, there is no general consensus on the band-gap and the observed transport properties in bulk $VFe_2Al$ is poorly understood.

Here we review the thermoelectric properties of a variety of $n$ and $p$-type $VFe_2Al$ samples presented in the literature. We show that the experimental Seebeck coefficient, electrical resistivity and thermal conductivity as a function of temperature and doping is consistent with an interpretation of $VFe_2Al$ as a small band-gap semiconductor with $E_g \approx 0.03 \pm 0.01$ eV rather than a semimetal. We attribute the past semimetalic interpretation of experimental data to the large concentration of intrinsic defects in the material which are present even in undoped $VFe_2Al$. This interpretation enables a modeling of the

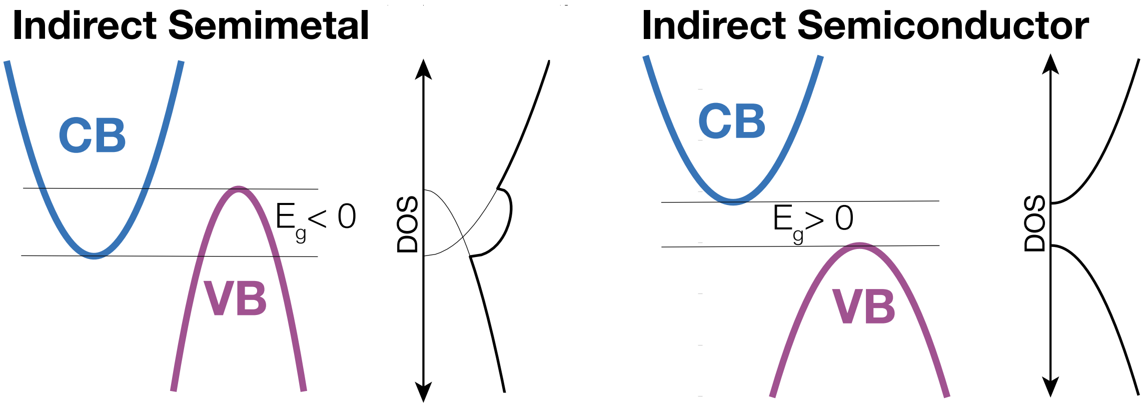

Figure 9.1: **Schematic demonstrating difference between electronic structure of indirect semimetals and semiconductors.**

thermoelectric performance, including a prediction of maximum $zT$ as well as engineering strategies for improving the thermoelectric properties that should be applicable to both bulk and thin film materials.

## 9.3 Band-gap Estimation

### 9.3.1 Weighted Mobility and Seebeck Mass

The trends in Seebeck coefficient $S$ and electrical conductivity $\sigma$ for $VFe_2Al$ with temperature and doping are generally that expected from a small band gap semiconductor. With sufficient doping, the electrical properties are determined by one band, either the conduction or valence band. The weighted mobility ($\mu_w$) of charge carriers in the dominant band can be determined from the variation of $|S|$ with $\sigma$ [210, 28] (see Section 2.4). Figure 9.2a,b shows that $\mu_w$ for both electrons and holes is in the range from 250-700 $cm^2V^{-1}s^{-1}$, which is comparable to the best thermoelectric materials, $Bi_2Te_3$ based alloys [199].

The Seebeck mass ($m_s^*$), is determined from the dependence of Seebeck on carrier concentration ( Figure 9.2c,d, Section2.4). Since Hall carrier concentration can be affected by

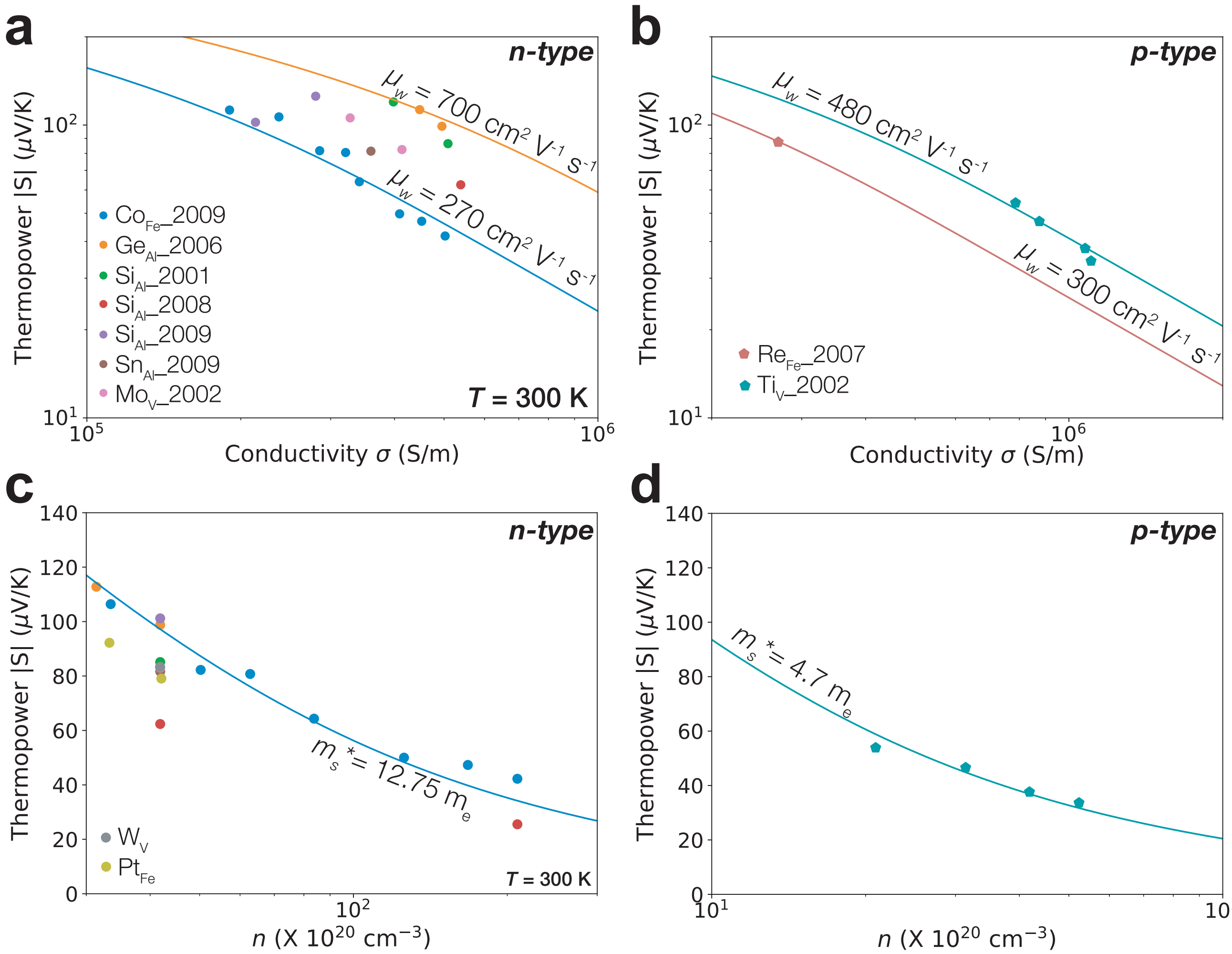

Figure 9.2: **Modelling valence and conduction band transport of VFe$_2$Al separately using single parabolic band modelling.** Variation of thermopower (|S|) in VFe$_2$Al with different type and concentration of doping[15, 16, 17, 18, 19, 20, 21, 22] at room temperature. (a,b) plot of log|S|-log|$\sigma$| which gives the weighted mobility ($\mu_w$) with $n$-type (a) and $p$-type (b) dopants. For both cases, the solid curves represent the prediction corresponding to constant values of $\mu_w$. (c,d) Themopower versus carrier concentration ($n$) plot to determine the effective mass ($m_s^*$) of $n$-type (c) and $p$-type (d) VFe$_2$Al samples (scatter points). The solid curves show the prediction for a constant $m^*$ which fit reasonably well across the entire range of $n$.

magnetic impurities and is often not reported, we used the chemical carrier concentration ($n$) calculated from the nominal valence electron concentration that includes dopants in the samples.

The conduction band appears to be heavier with values of $m_s^* = 13m_e$ than the valence bands $m_s^* = 5m_e$, where $m_e$ is the mass of an electron (see Figure 9.2c,d). Such large Seebeck mass values are typical of half-Heusler compounds[152, 147], and could indicate multiple band effects particularly at higher carrier concentrations [211].

### 9.3.2 Temperature-Dependent Electrical Transport Analysis

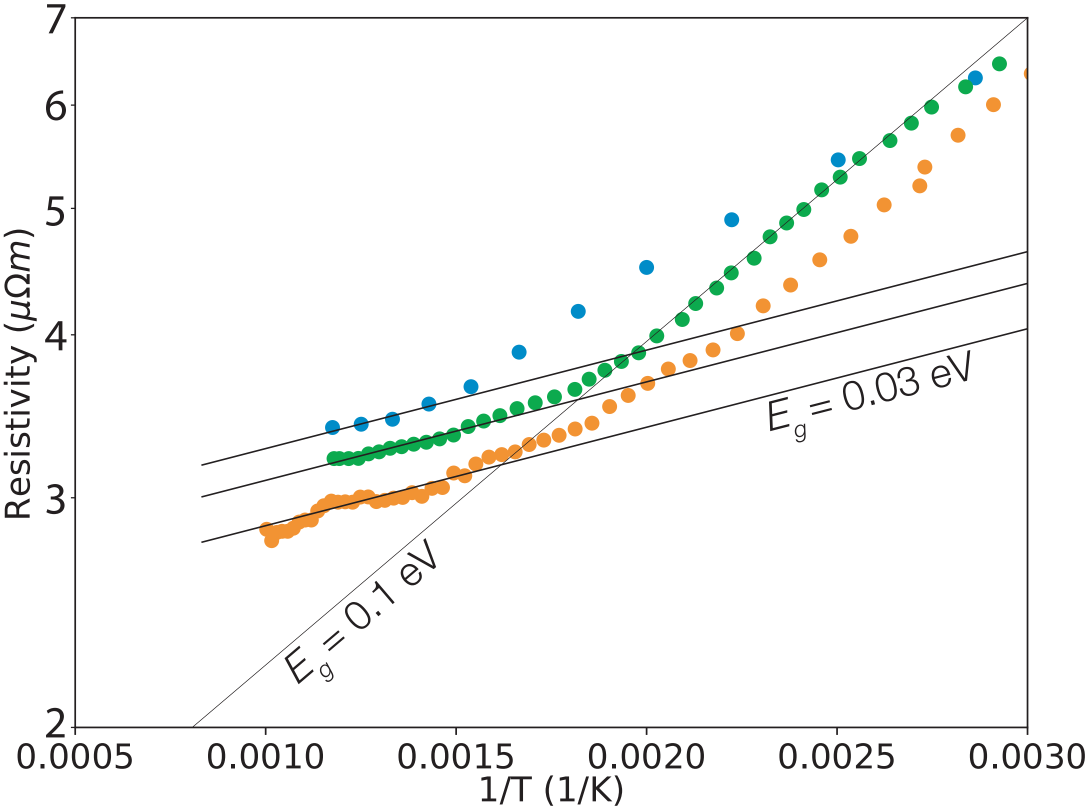

Figure 9.3: **Estimating band-gap of VFe$_2$Al from high temperature resistivity data.** Arrhenius plot for resistivity measurements of three undoped VFe$_2$Al samples (filled circles) from previous reports[15, 18, 22]. At high temperatures, slope of the solid lines correspond to a small band-gap of $E_g$=0.03 eV.

The effect on transport properties (electrical resistivity, Seebeck, Hall effect, electronic portion of thermal conductivity, etc.) due to having both electrons and holes (bipolar effect) can be used to estimate the band gap (or negative band gap for a semimetal). Although there is substantial variability in the reported samples and techniques to estimate band gap, the data, using three methods, are generally consistent with a positive band gap in the range of 0.02eV to 0.04eV.

A classic method to estimate band gap of a semiconductor is to examine the temperature-dependent resistivity in the intrinsic regime. An Arrhenius plot of the high temperature resistivity data from three, previous reports on undoped $VFe_2Al$ samples follows $\rho \propto \exp\left(\frac{Eg}{2kBT}\right)$ suggesting $E_g$ = 0.03 eV (see Figure 9.3). Fitting the data at lower temperatures would give larger values for $E_g$, possibly explaining the value of 0.1 eV reported in a previous temperature-dependent resistivity analysis.[203]

Another common method to estimate band gaps in thermoelectric materials is to use the Goldsmid-Sharp method [212] which examines the peak in thermopower |S| as a function of temperature (Figure 9.4) in a moderately doped semiconductor using $E_g \approx 2e|S_{max}|T_{max}$. For an accurate estimate, the ratio of the weighted mobility of the conduction and valence band is needed [212], which have been estimated from the section above. Once again, we see that a small positive band gap with $E_g$ = 0.03 eV fits much better than a large gap such as $E_g$ = 0.15 eV or negative $E_g$ = -0.1 eV (semimetal, see Figure 9.4).

### 9.3.3 Modelling Room Temperature Bipolar Transport

The bipolar effect is also noticeable at room temperature Seebeck data of lightly doped VFeAl (see Figure 9.5). Using the $\mu_{\mathrm{W}}$ and $m_{\mathrm{s}}{}^*$ values attained for electron and hole conduction in the previous sections the Seebeck coefficient at *any* dopant concentration can be modelled by constructing a two-band model. This two-band model will have 4 parameters: $m_{\mathrm{s}}{}^*$ for valence band, $m_{\mathrm{s}}{}^*$ for conduction band, the ratio of weighted mobility of the two bands $\mu_{\mathrm{W}}$ and the electronic band gap. The peaks in thermopower (|S|) values observed on the p-type and n-type side (see Figure 9.5) depends on the band-gap and the weighted mobility ratio. The band-gap determine the absolute magnitude of the peak heights and the weighted mobility ratio determines the relative heights of the two peaks.

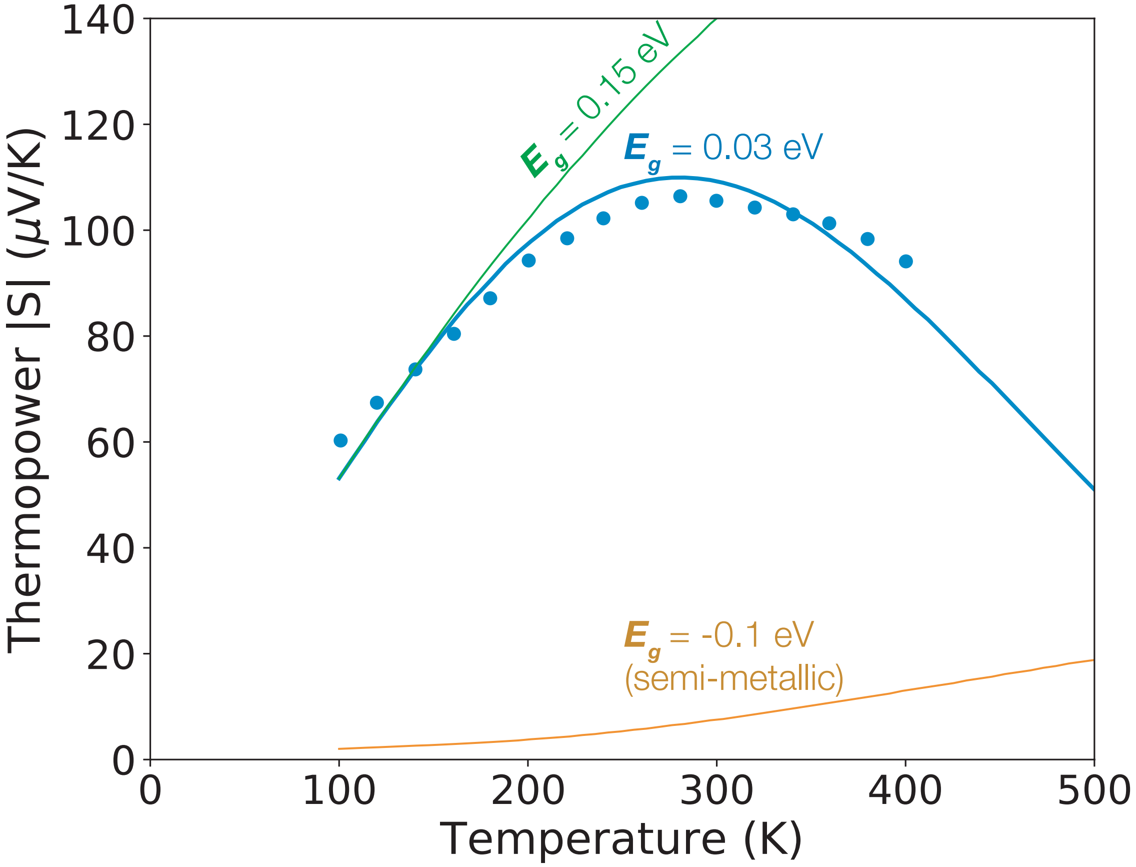

Figure 9.4: **Band-gap estimates from temperature-dependent Seebeck and resistivity data for $VFe_2Al$ are consistent with each other.** Temperature dependence of Seebeck coefficient for $VFe_2Al$ sample (scatter points) doped with 10% Mo [20]. Solid lines represent predictions from two-band acoustic phonon scattering models with $E_g$ = 0.15 eV, 0.02 eV and -0.10 eV (semimetallic). The weighted mobility ($\mu_w$) values used in these models for majority and minority carriers were 440 cm$^2$V$^{-1}$s$^{-1}$ and 480 cm$^2$V$^{-1}$s$^{-1}$, respectively. Observed temperature dependence of Seebeck coefficients for $VFe_2Al$ can be best understood from a small gap semiconductor description of the compound.

The room temperature Seebeck data from a variety of compositions reported in the literature appears to peak around $\sim$ -140 $\mu$ V K$^{-1}$ for n-type and $\sim$ +70 $\mu$ V K$^{-1}$ for p-type, which fits $E_g$=0.02 eV in the two-band model well (see Figure 9.5). Increasing $E_g$ above $\sim$0.1 eV gives a very poor fit (see Figure 9.5). For example, a band-gap of 0.15 eV predicts maximum Seebeck values exceeding 200 $\mu V/K$, which is much larger than any observed

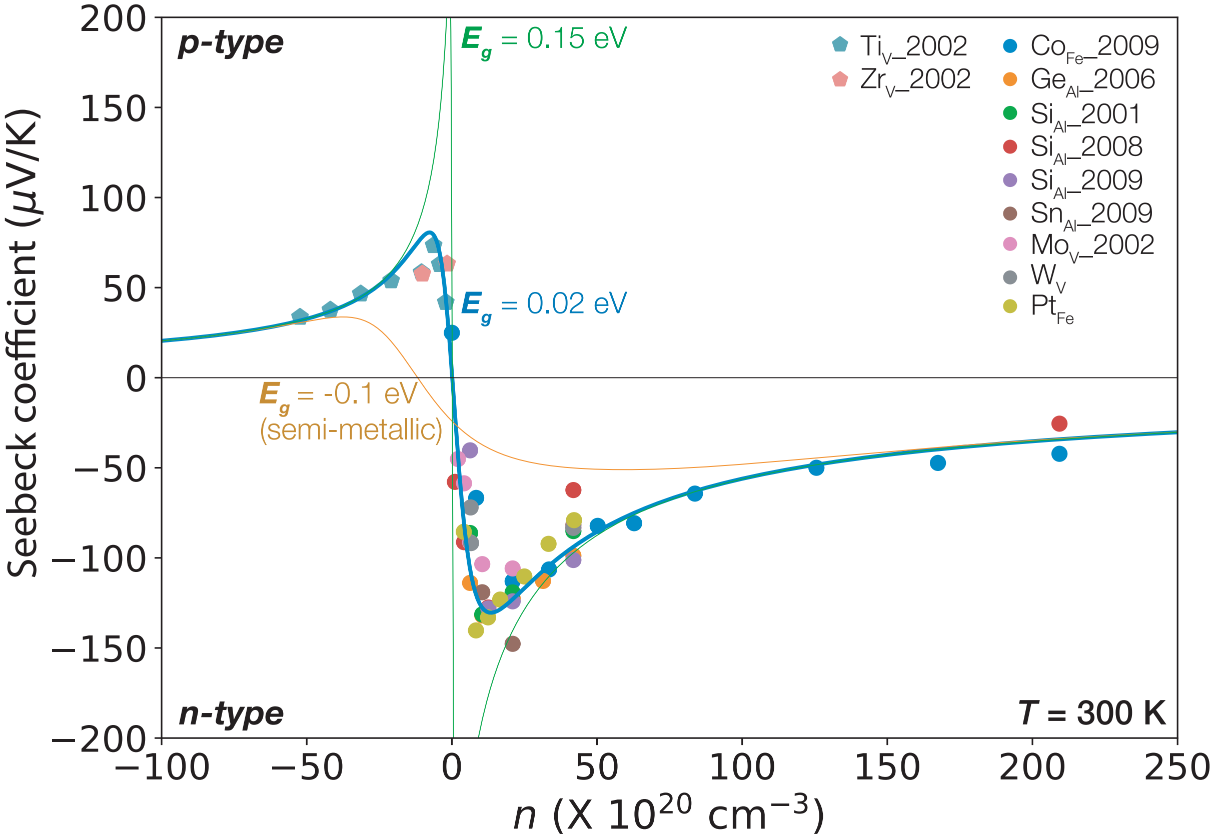

Figure 9.5: **Seebeck coefficient is extremely sensitive to size of the electronic gap making it very useful for $E_g$ estimation.** Seebeck versus carrier concentration ($n$) plot of $n$- and $p$-type $VFe_2Al$ samples (scatter points) for the entire range of carrier concentration reported in the literature[15, 16, 17, 18, 19, 20, 21, 22]. The solid curves represent two-band acoustic phonon scattering model predictions for band-gap $E_g$=0.15 eV, 0.02 eV and -0.10 eV (semimetallic). In these models, weighted mobility values of 700 cm$^2$V$^{-1}$s$^{-1}$ and 300 cm$^2$V$^{-1}$s$^{-1}$ were chosen for conduction band and valence band transport respectively. Observed Seebeck values for $VFe_2Al$ can be best understood from a small gap semiconductor description of the compound.

value. Similarly, modelling the material as a semimetal with $E_g$= -0.1 eV predicts Seebeck values smaller than 50 $\mu V/K$ over the entire doping range. The two-band model uses $\mu_w$ values of 700 cm$^2$ V$^{-1}$ s$^{-1}$ for electrons and 300 cm$^2$ V$^{-1}$ s$^{-1}$ for holes based on the analysis of heavily doped materials above. The large ratio of $\mu_w$ values (> 2) leads to the asymmetry in peak Seebeck values observed.

In early experimental reports, $VFe_2Al$ has often been described as semimetal based on the observation of a measurable density of states at the Fermi-level.[203] Undoped $VFe_2Al$

typically shows a low, metal-like Seebeck coefficient of $\geq$25 $\mu V/K$[21, 202, 15, 19, 17, 20, 18, 16, 213, 22] and carrier concentrations of the order of $\sim$$10^{20}$ cm$^{-3}$.[201] These findings are actually also consistent with the small gap semiconductor understanding if large intrinsic defect concentrations are considered. Half-Heusler compounds are well-known to accommodate large amounts of intrinsic defects in the cubic structure,[13, 85, 4, 10, 12, 87, 1] so a defect concentration of $\sim$$10^{20}$ cm$^{-3}$ in $VFe_2Al$ is quite plausible especially considering V and Fe have similar chemistry but different number of valence electrons. Using a $p$-type carrier concentration of $10^{20}$ cm$^{-3}$, and the valence band parameters derived above would correspond to a Fermi-level which lies $\sim$0.02 eV inside the valence band indicating that nominally stoichiometric $VFe_2Al$ is degenerately doped due to presence of intrinsic defects. Although the small Seebeck coefficient of undoped $VFe_2Al$ at room temperature might appear metal-like, we note that it is caused instead by a bipolar transport regime (see Figure 9.5) due to a very small band-gap. Some works suggest that the small $E_g$, which is consistent with transport properties of the material, could also result from presence of defects at elevated temperatures.[71]

## 9.4 Electronic Structure and Molecular Orbital Picture

Depending on the level of theory used in the first-principles calculations, both semimetallic and semiconducting electronic structures have been reported[205, 206, 207, 214, 215, 211, 216, 217, 49, 218] for $VFe_2Al$ in the full-Heusler structure. In calculations showing the semimetallic bandstructure of $VFe_2Al$ the hole and electron pockets lie in separate high symmetry points (namely $\Gamma$ and $X$ respectively). The valence bands at $\Gamma$ and the conduction band at $X$ do not overlap in $k$-space but have the same energy over a 0.1 eV energy range so that the electronic structure can be described as a simple semimetal with negative band gap, $E_g \sim -0.1$eV. In the case of semiconductor band structure reports, the bands look essentially the same with true valence bands at $\Gamma$ and a conduction band

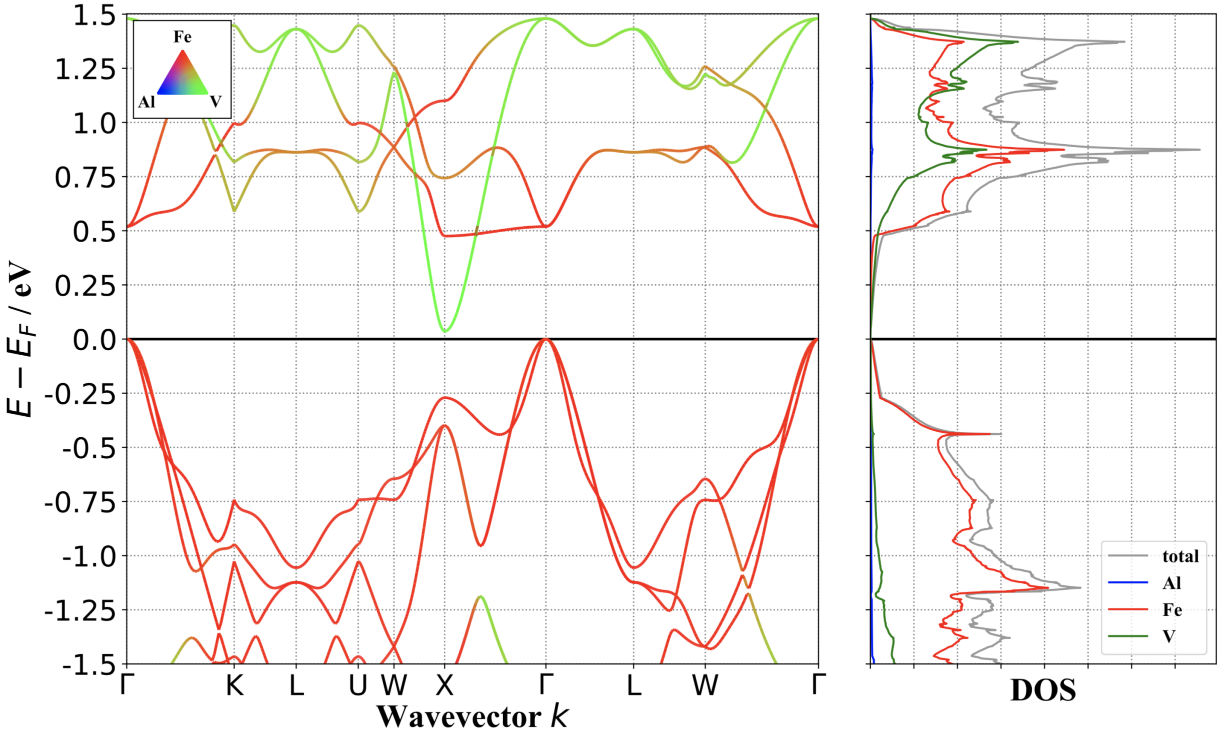

Figure 9.6: **Atom resolved electronic band structure and density of states for $VFe_2Al$.**

at $X$ but with predicted indirect band-gap ($E_g$) values $> 0.2$ eV. Occasionally, the $E_g$ values have been rationalized [214] using experimentally reported 'pseudogap' [201, 204] in the electronic structure. However, in these experimental works a semimetallic electronic structure was still expected for $VFe_2Al$ and the 'pseudogaps' were not representative of the indirect gap between X and $\Gamma$ pockets.[201, 204]

We calculate the electronic band structure of $VFe_2Al$ using GGA+U calculations where the Hubbard U is selected to give a small band-gap $E_g$ = 0.03 eV (see Figure 9.6) since it is most consistent with our transport property analysis above. The valence band maximum (VBM) is triply degenerate at the $\Gamma$ point with a significant Fe character. The conduction band minimum (CBM), on the other hand, consists of a single band with V character at $X$ due to highly dispersive V states. The valence and conduction bands have the same valley degeneracy of $N_v$ = 3, since the single $X$-point pocket consists of 6 half-pockets in the Brillouin zone of this cubic structure.

The nature of the electronic bands can be rationalized using molecular orbital (MO) diagrams, which enables insight into the local bonding [152] and its effect on the valence and conduction bands in $VFe_2Al$. To construct the MO diagram (see Figure 9.11), we first determine the orbital character of all states at the $\Gamma$ point using orbital projected partial density of states (pDOS) (see Figure 9.10). Subsequently, we perform and a $k$-resolved Crystal Orbital Hamiltonian Population (COHP) analysis to investigate the nature[219] (bonding versus anti-bonding) and strength of interaction between these orbitals. The $k$-resolved COHP analysis will be performed on the $\Gamma$-point state of the electronic structure. In our analysis, we consider 4 conduction band states and 12 valence band states each with an occupancy of 2. The valence bands chosen in our analysis contain all the 24 valence electron of the compound ($8 \times 2$ from Fe, 5 from V and 3 from Al).

Since $VFe_2Al$ has 4 atoms in the primitive unit cell the COHP matrices are quite complicated, with over 900 elements. The COHP matrix for each $\Gamma$-point state in the electronic structure were plotted separately to simplify our analysis. The example $\Gamma$-point heat maps for the first conduction band and the seventh valence bands are provided in the Figures 9.7 and 9.8 respectively. We note that, these matrices symmetric and so we are only interested in unique elements in the lower triangle of the matrix (see Figures 9.7 and 9.8). Furthermore, for the sake of the MO diagram construction which requires analysis of bonding interactions, we are only interested in *off-site* COHP terms. To easily locate these terms we draw boxes across the diagonal of the heat map (see Figures 9.7 and 9.8). The *off-site* COHP terms can be found outside these boxes.

The COHP analysis of the first $\Gamma$-point conduction band (see Figure 9.7) clearly reveals that the Fe1-Fe2 $d_{z^2}$ and $d_{x^2-y^2}$ interaction is the only non-zero interaction. Since the the first and second conduction bands are degenerate, this indicates that they are formed by an $e_g$-type interaction. Furthermore, the positive COHP value of this interaction indicates that it is anti-bonding in nature. Unlike the example of the first conduction band, the COHP analysis of the seventh $\Gamma$-point valence band (see Figure 9.7), suggests that

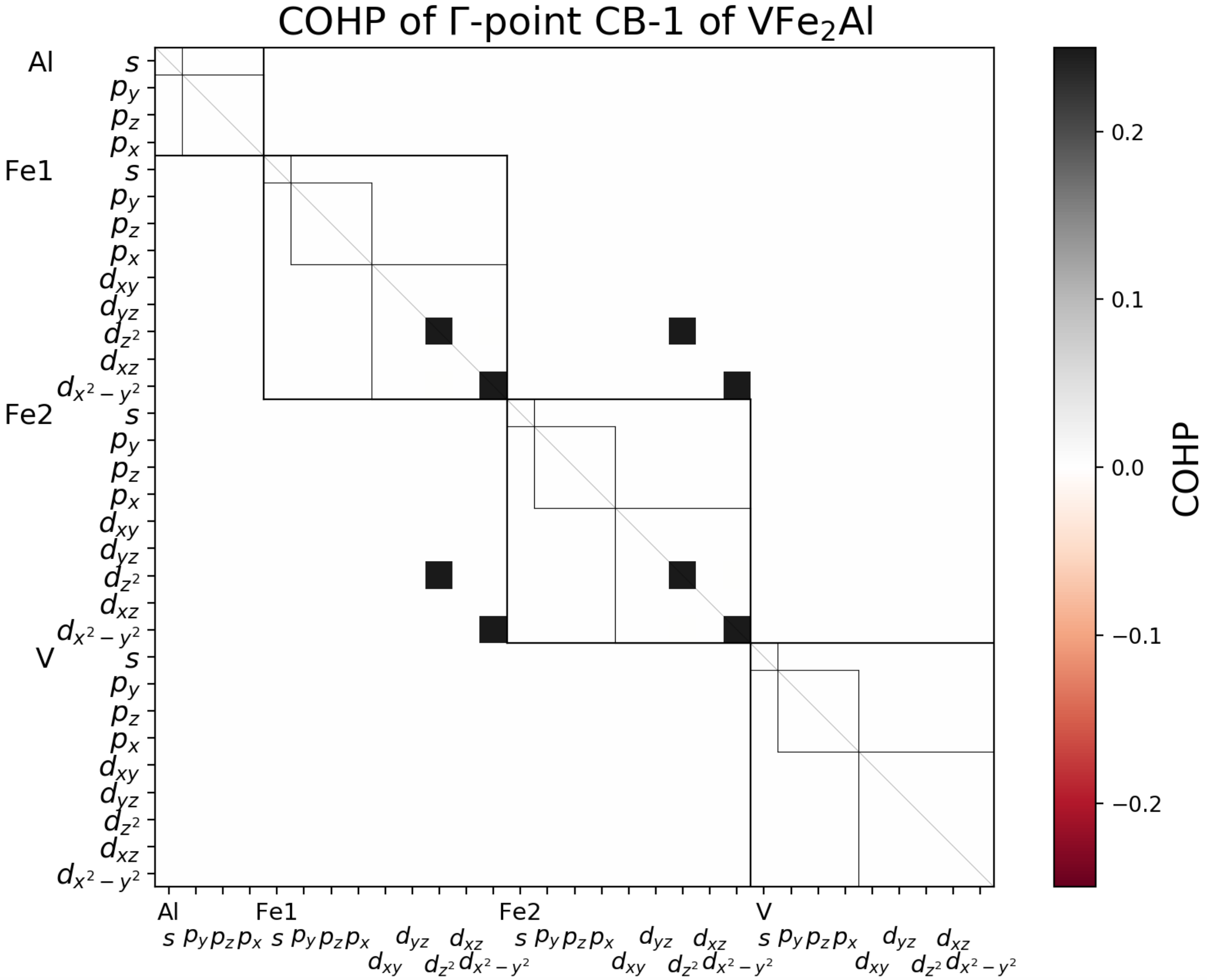

Figure 9.7: **Crystal Orbital Hamiltonian Population (COHP) heat map for the first Γ point conduction band in the $VFe_2Al$ electronic structure.** The *off-site* COHP terms which represent interation between orbitals on two different sites can be found outside the 4 large boxes (in thick black lines) drawn across the diagonal of the heat map. Negative and positive COHP values indicate bonding and anti-bonding interactions respectively. COHP value of zero indicates the absence of any interaction. Clearly, the Fe1-Fe2 $e_g$ interaction is the only relevant one for this state.

multiple interactions (between Fe-Al, Fe1-Fe2 and V-Al) contribute to the formation of the state. While all these interactions can in-principle be included in our molecular orbital analysis, we investigate the orbital-projected partial density-of-states of this state (see Figure 9.9) to further simplify the resulting MO picture. We find that this triply de-

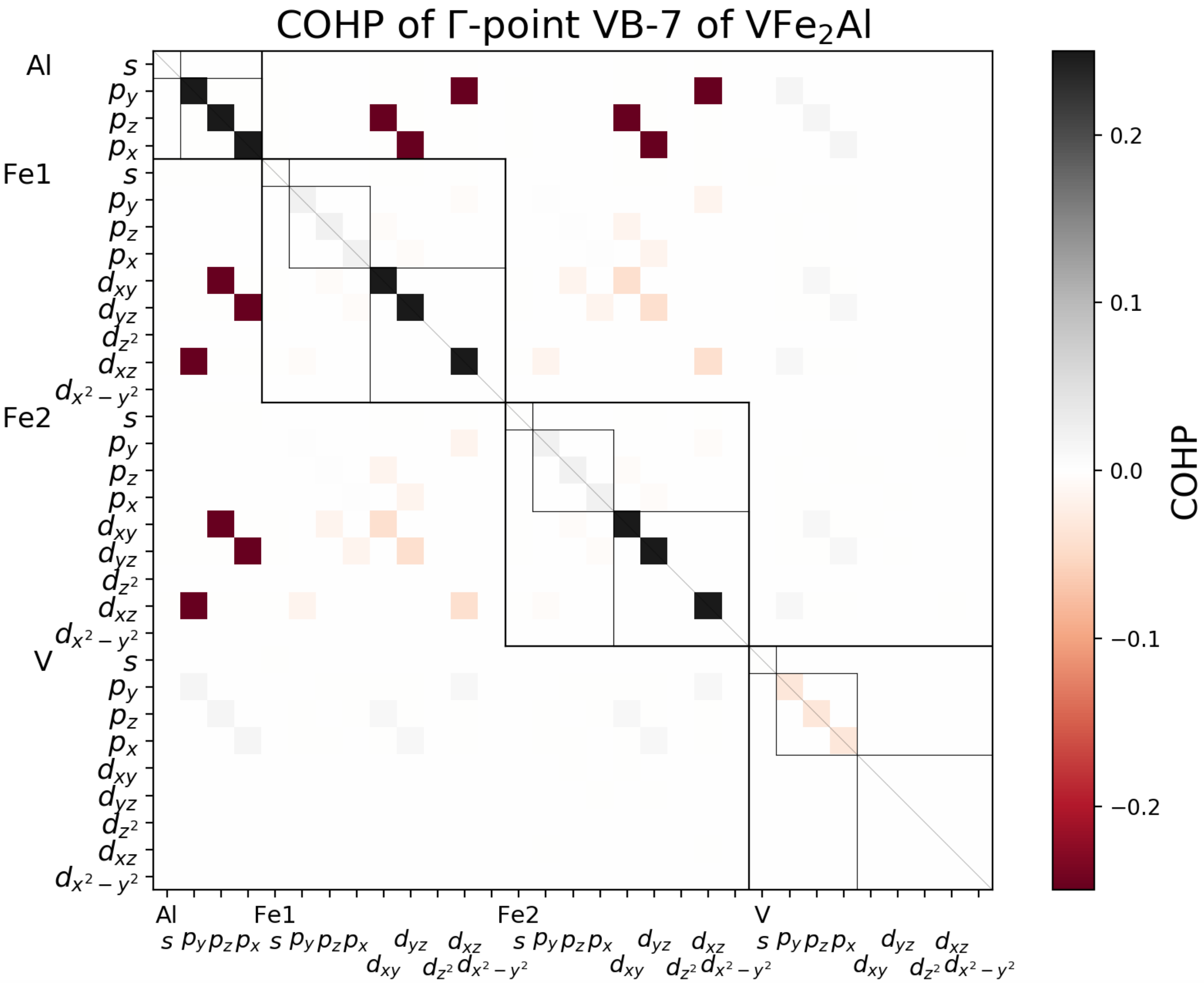

Figure 9.8: **Crystal Orbital Hamiltonian Population (COHP) heat map for the seventh Γ point valence band in the VFe$_2$Al electronic structure.** The *off-site* COHP terms which represent interation between orbitals on two different sites can be found outside the 4 large boxes (in thick black lines) drawn across the diagonal of the heat map. Negative and positive COHP values indicate bonding and anti-bonding interactions respectively. COHP value of zero indicates the absence of any interaction. Since multiple interactions (between Fe-Al, Fe1-Fe2 and V-Al) appear to contribute in the formation of this state, selecting the most relevant interaction additionally requires analysing the orbital-projected partial density of states to identify the orbitals contributing the most.

generate state is contributed predominantly by Fe $t_{2g}$ type orbitals. Hence we conclude that the Fe1-Fe2 $t_{2g}$ interaction (which is a bonding interaction with a negative COHP value) is the most relevant among all the interactions shown in Figure 9.8. We note here

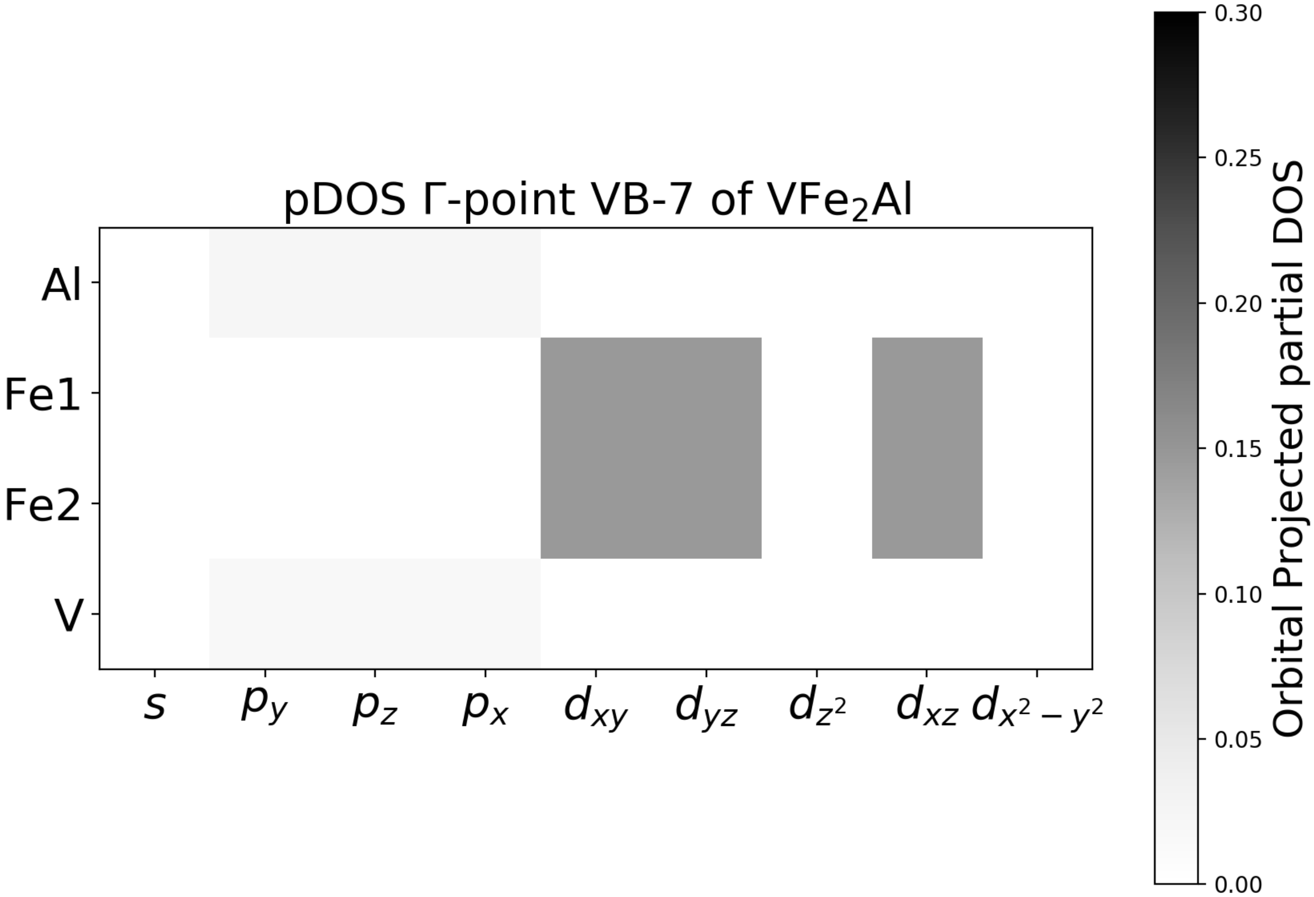

Figure 9.9: **Partial density of states of orbitals involved in interactions with a large COHP value can be *negligibly* small.** Orbital projected partial density of states heat map for the seventh Γ-point valence band.

that among all the interactions shown in Figure 9.8, Fe1-Fe2 $t_{2g}$ interaction is not the strongest in magnitude. Instead the Al-Fe interactions have the largest magnitude of COHP values and making conclusions regarding the most relevant interactions entirely on the basis of the COHP magnitudes would have erroneously yielded Al $p$ -Fe $d$ as the answer. This analysis suggests that studying bonding solely on the basis of COHP values can be misleading.

We repeat the above analysis based on a pDOS + COHP approach for all Γ-point states and the results are summarized in Figure 9.10. We find that, with the exception of

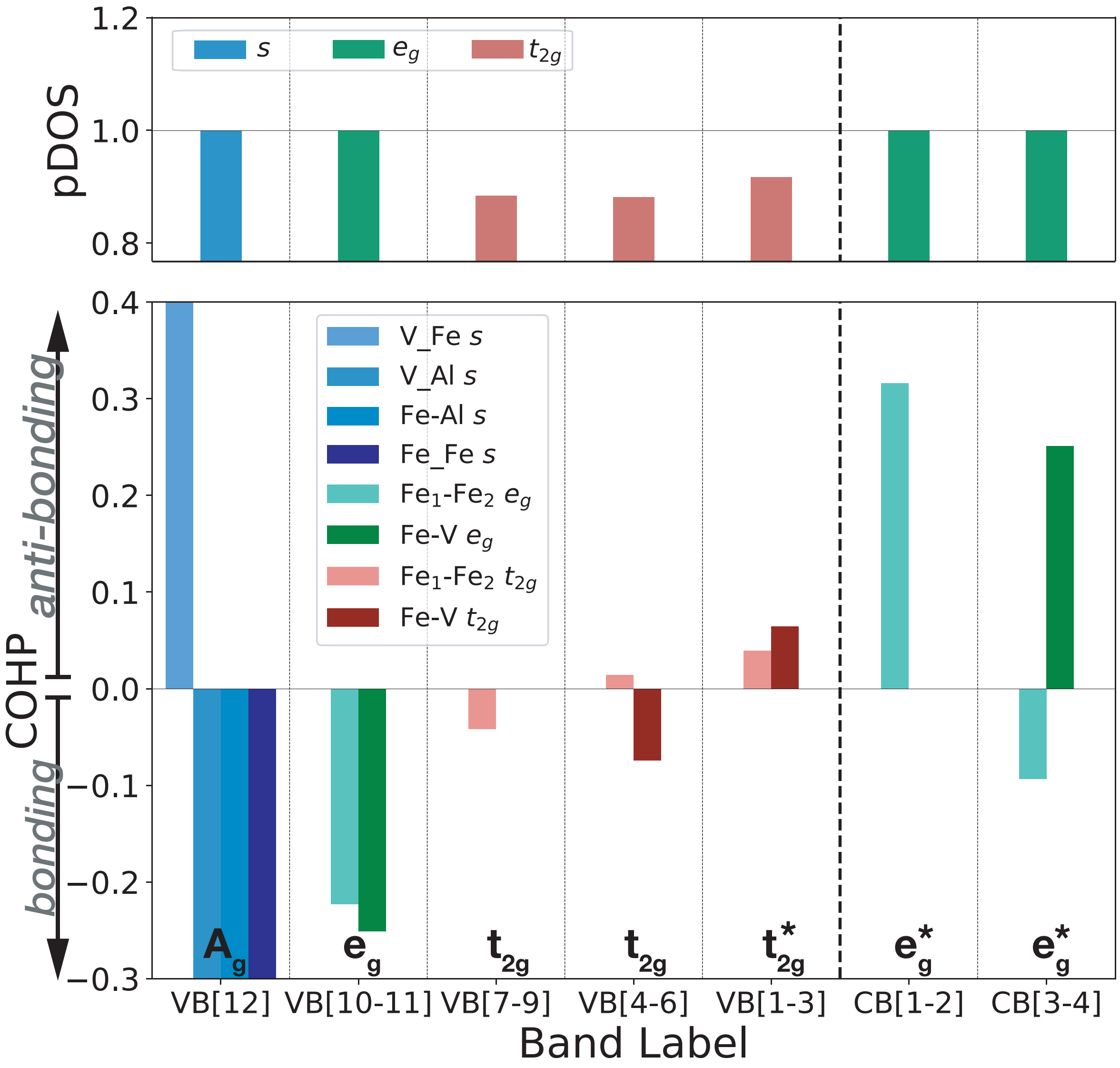

Figure 9.10: **Molecular orbital diagram construction requires both COHP *and* pDOS calculations.** Orbital projected partial Density of States (pDOS) and $k$-resolved Crystal Orbital Hamiltonian Population (COHP) of $\Gamma$-point states of $VFe_2Al$. The x-axis indicates the band index of the $\Gamma$-point state. The indices of the valence (VB) and conduction bands (CB) are counted with respect to the Fermi-level ($E_f$). Degenerate bands are indexed together. The pDOS are determined by adding contributions from $s$ (blue bar), $t_{2g}$-type ($d_{xy}$, $d_{yz}$, $d_{zx}$ red bars) and $e_g$-type ($d_{x^2-y^2}$, $d_{z^2}$, red bars) orbitals separately regardless of the atom type. pDOS value of 1 mean complete contribution from a particular set. The COHP values were determined by averaging across all inter-atomic interactions between orbitals of the same type (for example averaging between Fe $d_{z^2}$ - V $d_{z^2}$ and Fe $d_{x^2-y^2}$ - V $d_{x^2-y^2}$ COHP to obtain Fe-V $e_g$ COHP). Negative and positive COHP values indicate bonding and anti-bonding interactions respectively. COHP value of zero indicates the absence of any interaction. In general, interaction strength increases as $t_{2g} < e_g < s$.

the lowest valence band $A_g$, the valence band states and lowest conduction band states primarily arise from interactions between Fe and V $d$-states (see Figure 9.10). Since, both Fe and V are surrounded by a tetrahedral environment, their $d$-orbitals split into $t_{2g}$ ($d_{xy}$,$d_{yz}$ and $d_{zx}$) and $e_g$ ($d_{z^2}$ and $d_{x^2-y^2}$) orbitals. The three sets of $t_{2g}$ from V and the two Fe atoms interact to form three filled sets of $t_{2g}$ molecular orbitals in the valence band. The three sets of $e_g$ orbitals interact more strongly than the $t_{2g}$ orbitals pushing two sets above the Fermi-level and only one set lower in the valence band. The relative interaction strength of $t_{2g}$ and $e_g$ orbitals can be seen from their magnitude of COHP values for the conduction and valence band states (see Figure 9.10 and 9.11). Generally, the COHP values for $e_g$ interactions are considerably larger than those due to $t_{2g}$ interactions. The lowest valence band $A_g$ in the molecular orbital diagram has a predominantly bonding $s$-orbital type character with almost equal contributions from all atoms in the compound (see Figure 9.10).[72] The COHP of the $A_g$ largely reveals a very strong bonding interaction between the $s$-orbitals, indicating that it originates from interactions between high energy $s$-orbitals of the compound (see Figure 9.10 and 9.11).

In general, Al contribution to the valence band states is rather small. While the $A_g$ and the lowest $t_{2g}$ molecular orbitals (see Figure 9.9) show some Al contributions,[72] the content of Al $s$ and $p$-states are less than 25% and ∼5%, respectively. Among the three elements, Al is the most electropositive (Pauling electronegativity of 1.61) and the small Al content in the the valence bands indicates that the Al can be treated as a $\mathrm{Al}^{3+}$ cation within a valence balanced description [10] of this semiconductor compound. With Fe as the most electronegative element, we assign the $A_g$ states and the filled $e_g$ states to Fe giving each 9 electrons or a valence of $\mathrm{Fe}^{-1}$. V, on the other hand, only has its $t_{2g}$ states filled totaling 6 electrons or $\mathrm{V}^{-1}$. Thus the 24 electron/formula unit compound can be understood as valence balanced composition $\mathrm{V}^{-1}\mathrm{Fe}_2^{-1}\mathrm{Al}^{+3}$.

The full-Heusler structure is very similar to that of half-Heusler compounds with just an additional transition metal atom M’ occupying the vacant sub-lattice in the structure.

The molecular orbital picture of full-Heusler semiconductor allows for comparison with electronic structure of semiconductor half-Heusler compounds [220]. Similar to half-Heusler compounds, states on either side of the Fermi-level ($E_f$) in $VFe_2Al$ are formed from transition metal $d$-states (see Figure 9.11). In particular, the $\Gamma$ point states of the first conduction and valence bands show $d$-orbital character from Fe atoms which constitute the M' sub-lattice. Removing the M' atom from the structure would presumably decrease the number of states close to the $E_f$ and the $d$-$d$ interaction between transition metal atoms, thereby opening up the band-gap. From this understanding one can explain the larger band-gaps gneerally observed in half-Heusler compounds when compared to full-Heusler compounds such as $VFe_2Al$ and $VFe_2Ga$. The impact of adding atoms in the M' sub-lattice of the half-Heusler structure has been studied for TiNiSn. Ni solubility in TiNiSn introduces mid-gap defect states which impact the thermoelectric properties of the material significantly.[4] The main difference between half-Heusler and full-Heusler

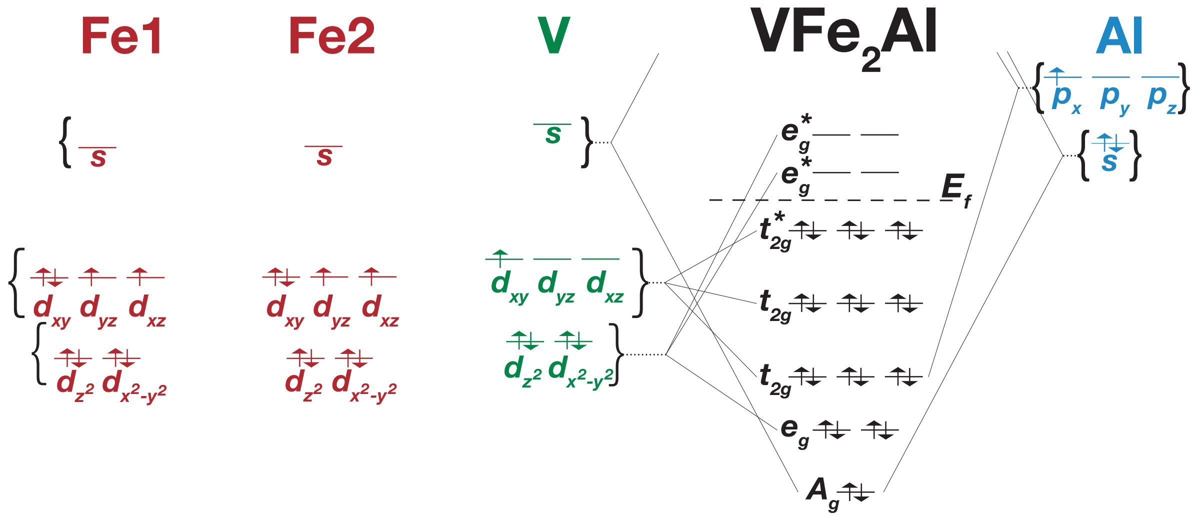

Figure 9.11: **Molecular orbital diagram of $VFe_2Al$.** Schematic illustration of the molecular orbital diagram in $VFe_2Al$. The bonding (example $e_g$) and anti-bonding (example $e_g*$) interactions are concluded from partial density of states and $k$-resolved Crystal Orbital Hamilton Population (COHP) analysis of states at the $\Gamma$ point in the electronic structure (see example in Figure 9.9 and Figure 9.8). States close to the Fermi-level ($E_f$) predominantly show $e_g$ and $t_{2g}$ charater from V and Fe atoms.

semiconductors is the electronegativity of the $X$-atom. While Al is the most electropositive atom in $VFe_2Al$ behaving as a +3 cation, in half-Heusler NbFeSb the Sb atom is the most electronegative and acts as a -3 anion within the Zintl description of the compound.[10]

### 9.4.1 Rationalizing trends in weighted mobility with electronic structure analysis

The reported electrical properties of different dopants in $VFe_2Al$ (see Figure 9.2 a and b) give somewhat different values for $\mu_w$, which could be due to differences in microstructure or changes in the bulk electronic properties. Weighted mobility values are known to be quite sensitive to grain boundaries and interfaces in materials with low dielectric constant such as the half-Heusler, and can be greatly altered depending on the synthesis conditions.[221, 139] Typically, samples with larger grain sizes tend to show larger $\mu_w$. We believe that the the variance in $\mu_w$ values of Si samples (400-650 $cm^2\ V^{-1}\ s^{-1}$) could be explained by such factors.

Changes to the bulk $\mu_w$ might be rationalized by considering the atomic contributions to conducting states in the electronic structure. Adding defects to atomic sites that contribute more to the conduction (valence) band are more likely to scatter electrons (holes) and reduce the $n$-type ($p$-type) $\mu_w$, as demonstrated in thermoelectric PbSe [191]. For example, the higher $\mu_w$ = 480 $cm^2V^{-1}s^{-1}$ for Ti doping on the V site when compared to Re-doping on the Fe site ($\mu_w$ = 300 $cm^2V^{-1}s^{-1}$, see Figure 9.2b) is expected because the valence band maximum is dominated by Fe states rather than V states. We further expect $p$-type samples with substitution on the Al site (e.g. Mg doping) to possibly show even higher $\mu_w$. To the best of our knowledge, this has not yet been investigated. Similarly, a high $\mu_w$ for Si and Ge doped $VFe_2Al$ is expected because these dopants should substitute on the Al site, which has little contribution to either conduction or valence band. Indeed the $\mu_w$ for Si and Ge doped $VFe_2Al$ is generally higher than the $\mu_w$ for Mo and Co doping (also $n$-type) where Mo and Co are expected to substitute on the Fe or V site. Mo and Co doping could also change the localized spin state of the transition metals which could lead to spin-disorder scattering of electrons that reduce $\mu_w$ [222].

# Bibliography

[1] Wolfgang G. Zeier, Shashwat Anand, Lihong Huang, Ran He, Hao Zhang, Zhifeng Ren, Chris Wolverton, and G. Jeffrey Snyder. Using the 18-electron rule to understand the nominal 19-electron half-heusler NbCoSb with Nb vacancies. *Chemistry of Materials*, 29(3):1210–1217, 2017.

[2] Saneyuki Ohno, Kazuki Imasato, Shashwat Anand, Hiromasa Tamaki, Stephen Dongmin Kang, Prashun Gorai, Hiroki K. Sato, Eric S. Toberer, Tsutomu Kanno, and G. Jeffrey Snyder. Phase boundary mapping to obtain n-type $Mg_3Sb_2$-based thermoelectrics. *Joule*, 2017.

[3] Yinglu Tang, Riley Hanus, Sinn-wen Chen, and G. Jeffrey Snyder. Solubility design leading to high figure of merit in low-cost Ce-$CoSb_3$ skutterudites. *Nature communications*, 6(1):1–7, 2015.

[4] Yinglu Tang, Xiaoshuang Li, Lukas H. J. Martin, Eduardo Cuervo Reyes, Toni Ivas, Christian Leinenbach, Shashwat Anand, Matthew Peters, G. Jeffrey Snyder, and Corsin Battaglia. Impact of Ni content on the thermoelectric properties of half-heusler TiNiSn. *Energy & Environmental Science*, 11(2):311–320, 2018.

[5] Mariette Hellenbrandt. The inorganic crystal structure database (ICSD)—present and future. *Crystallography Reviews*, 10(1):17–22, 2004.

[6] Romain Gautier, Xiuwen Zhang, Linhua Hu, Liping Yu, Yuyuan Lin, Tor O. L. Sunde, Danbee Chon, Kenneth R. Poeppelmeier, and Alex Zunger. Prediction and accelerated laboratory discovery of previously unknown 18-electron ABX compounds. *Nature chemistry*, 7(4):308, 2015.

[7] Hangtian Zhu, Jun Mao, Yuwei Li, Jifeng Sun, Yumei Wang, Qing Zhu, Guannan Li, Qichen Song, Jiawei Zhou, Yuhao Fu, et al. Discovery of TaFeSb-based half-heuslers with high thermoelectric performance. *Nature Communications*, 10(1):270, 2019.

[8] Scott Kirklin, James E. Saal, Bryce Meredig, Alex Thompson, Jeff W. Doak, Muratahan Aykol, Stephan Rühl, and Chris Wolverton. The Open Quantum Materials Database (OQMD): assessing the accuracy of DFT formation energies. *npj Computational Materials*, 1:15010, 2015.

[9] James E. Saal, Scott Kirklin, Muratahan Aykol, Bryce Meredig, and Christopher Wolverton. Materials design and discovery with high-throughput density functional theory: the open quantum materials database (OQMD). *Jom*, 65(11):1501–1509, 2013.

[10] Shashwat Anand, Kaiyang Xia, Vinay I. Hegde, Umut Aydemir, Vancho Kocevski, Tiejun Zhu, Chris Wolverton, and G. Jeffrey Snyder. A valence balanced rule for discovery of 18-electron half-Heuslers with defects. *Energy & Environmental Science*, 2018.

[11] N. Naghibolashrafi, S. Keshavarz, Vinay I. Hegde, A. Gupta, W. H. Butler, J. Romero, K. Munira, P. LeClair, D. Mazumdar, J. Ma, et al. Synthesis and characterization of Fe-Ti-Sb intermetallic compounds: Discovery of a new Slater-Pauling phase. *Physical Review B*, 93(10):104424, 2016.

[12] Shashwat Anand, Kaiyang Xia, Tiejun Zhu, Chris Wolverton, and G. Jeffrey Snyder. Temperature Dependent $n$-Type Self Doping in Nominally 19-Electron Half-Heusler Thermoelectric Materials. *Advanced Energy Materials*, 8(30):1801409, 2018.

[13] Shashwat Anand, Max Wood, Yi Xia, Chris Wolverton, and G Jeffrey Snyder. Double half-Heuslers. *Joule*, 3(5):1226–1238, 2019.

[14] Takeyuki Sekimoto, Ken Kurosaki, Hiroaki Muta, and Shinsuke Yamanaka. Thermoelectric and thermophysical properties of TiCoSb-ZrCoSb-HfCoSb pseudo ternary system prepared by spark plasma sintering. *Materials transactions*, 47(6):1445–1448, 2006.

[15] Wenjia Lu, Wenqing Zhang, and Lidong Chen. Thermoelectric properties of $(Fe_{1-x}Co_x)_2VAl$ Heusler-type compounds. *Journal of Alloys and Compounds*, 484(1-2):812–815, 2009.

[16] Hideaki Kato, Masaaki Kato, Yoichi Nishino, Uichiro Mizutani, and Shigeru Asano. Effect of silicon substitution on thermoelectric properties of Heusler-type $Fe_2VAl$ alloy. *Journal of Japanese Institute of Metals*, 65(7):652–656, 2001.

[17] M. Vasundhara, V. Srinivas, and V. V. Rao. Electronic transport in Heusler-type $Fe_2VAl_{1-x}M_x$ alloys (M= B, In, Si). *Physical Review B*, 77(22):224415, 2008.

[18] Y. Nishino, S. Deguchi, and U. Mizutani. Thermal and transport properties of the Heusler-type $Fe_2VAl_{1-x}Ge_x$ ($0 \leq x \leq 0.20$) alloys: Effect of doping on lattice thermal conductivity, electrical resistivity, and Seebeck coefficient. *Physical Review B*, 74:115115, 2006.

[19] Eric J. Skoug, Chen Zhou, Yanzhong Pei, and Donald T. Morelli. High thermoelectric power factor near room temperature in full-Heusler alloys. *Journal of Electronic Materials*, 38(7):1221–1223, 2009.

[20] Hitoshi Matsuura, Yoichi Nishino, Uichiro Mizutani, and Shigeru Asano. Doping effects on thermoelectric properties of the pseudogap $Fe_2VAl$ system. *Journal of Japanese Institute of Metals*, 66(7):767–771, 2002.

[21] Yoichi Nishino. Development of thermoelectric materials based on $Fe_2VAl$ Heusler compound for energy harvesting applications. *IOP Conference Series: Materials Science and Engineering*, 18:142001, 2011.

[22] Fuminori Kobayashi, Naoki Ide, and Yoichi Nishino. Effects of Re Substitution on Thermoelectric Properties of Pseudogap System $Fe_2VAl$. *Journal of Japanese Institute of Metals*, 71(2):208–212, 2007.

[23] Jeff W Doak, Kyle Jay Michel, and Chris Wolverton. Determining dilute-limit solvus boundaries in multi-component systems using defect energetics: Na in PbTe and PbS. *Journal of Materials Chemistry C*, 3(40):10630–10649, 2015.

[24] Anuj Goyal, Prashun Gorai, Haowei Peng, Stephan Lany, and Vladan Stevanović. A computational framework for automation of point defect calculations. *Computational Materials Science*, 130:1–9, 2017.

[25] G. Jeffrey Snyder and Eric S. Toberer. Complex thermoelectric materials. *Nature Materials*, 7(2):105, 2008.

[26] Lon E. Bell. Cooling, heating, generating power, and recovering waste heat with thermoelectric systems. *Science*, 321(5895):1457–1461, 2008.

[27] Hyun-Sik Kim, Zachary M. Gibbs, Yinglu Tang, Heng Wang, and G. Jeffrey Snyder. Characterization of Lorenz number with Seebeck coefficient measurement. *APL Materials*, 3(4):041506, 2015.

[28] Stephen Dongmin Kang and G. Jeffrey Snyder. Transport property analysis method for thermoelectric materials: material quality factor and the effective mass model. *arXiv preprint arXiv:1710.06896*, 2017.

[29] Andrew F. May and G. Jeffrey Snyder. *Introduction to Modeling Thermoelectric Transport at High Temperatures*, pages 1–18. CRC Press, 2012.

[30] Bolin Liao, Bo Qiu, Jiawei Zhou, Samuel Huberman, Keivan Esfarjani, and Gang Chen. Significant reduction of lattice thermal conductivity by the electron-phonon interaction in silicon with high carrier concentrations: A first-principles study. *Physical Review Letters*, 114(11):115901, 2015.

[31] Tyler J. Slade*, Shashwat Anand*, Max Wood, James P. Male, Kazuki Imasato, Dean Cheikh, Muath M. Al Malki, Matthias T. Agne, Kent J. Griffith, Sabah K. Bux, Chris Wolverton, Mercouri G. Kanatzidis, and G. Jeffrey Snyder. Charge-carrier-mediated Lattice Softening Contributes to High $zT$ in Thermoelectric Semiconductors. *Unpublished*, 2020.

[32] Zhiwei Chen, Binghui Ge, Wen Li, Siqi Lin, Jiawen Shen, Yunjie Chang, Riley Hanus, G. Jeffrey Snyder, and Yanzhong Pei. Vacancy-induced dislocations within grains for high-performance PbSe thermoelectrics. *Nature Communications*, 8(1):1–8, 2017.

[33] Zhiwei Chen, Zhengzhong Jian, Wen Li, Yunjie Chang, Binghui Ge, Riley Hanus, Jiong Yang, Yue Chen, Mingxin Huang, G. Jeffrey Snyder, et al. Lattice dislocations enhancing thermoelectric PbTe in addition to band convergence. *Advanced Materials*, 29(23):1606768, 2017.

[34] Yi Xia, Koushik Pal, Jiangang He, Vidvuds Ozoliņš, and Chris Wolverton. Particlelike Phonon Propagation Dominates Ultralow Lattice Thermal Conductivity in Crystalline $Tl_3VSe_4$. *Physical Review Letters*, 124(6):065901, 2020.

[35] Riley Hanus, Matthias T. Agne, Alexander J. E. Rettie, Zhiwei Chen, Gangjian Tan, Duck Young Chung, Mercouri G. Kanatzidis, Yanzhong Pei, Peter W. Voorhees, and

G. Jeffrey Snyder. Lattice softening significantly reduces thermal conductivity and leads to high thermoelectric efficiency. *Advanced Materials*, 31(21):1900108, 2019.

[36] Ramya Gurunathan, Riley Hanus, and G. Jeffrey Snyder. Alloy scattering of phonons. *Materials Horizons*, 7:1452–1456, 2020.

[37] Ramya Gurunathan, Riley Hanus, Maxwell Dylla, Ankita Katre, and G. Jeffrey Snyder. Analytical models of phonon–point-defect scattering. *Physical Review Applied*, 13(3):034011, 2020.

[38] G. Jeffrey Snyder, Alemayouh H. Snyder, Maxwell Wood, Ramya Gurunathan, Berhanu H. Snyder, and Changning Niu. Weighted mobility. *Advanced Materials*, page 2001537, 2020.

[39] Xinyue Zhang, Zhonglin Bu, Xuemin Shi, Zhiwei Chen, Siqi Lin, Bing Shan, Maxwell Wood, Alemayouh H. Snyder, Lidong Chen, G. Jeffrey Snyder, et al. Electronic quality factor for thermoelectrics. *Science Advances*, 6(46):eabc0726, 2020.

[40] Pierre Hohenberg and Walter Kohn. Inhomogeneous electron gas. *Physical Review*, 136(3B):B864, 1964.

[41] Wolfram Koch and Max C Holthausen. *A chemist's guide to density functional theory*. John Wiley & Sons, 2015.

[42] Walter Kohn and Lu Jeu Sham. Self-consistent equations including exchange and correlation effects. *Physical Review*, 140(4A):A1133, 1965.

[43] Walter Kohn, Axel D. Becke, and Robert G. Parr. Density functional theory of electronic structure. *The Journal of Physical Chemistry*, 100(31):12974–12980, 1996.

[44] Georg Kresse and Jürgen Furthmüller. Efficient iterative schemes for ab initio total-energy calculations using a plane-wave basis set. *Physical Review B*, 54(16):11169, 1996.

[45] Georg Kresse and Jürgen Hafner. Ab initio molecular-dynamics simulation of the liquid-metal–amorphous-semiconductor transition in germanium. *Physical Review B*, 49(20):14251, 1994.

[46] John P. Perdew, Kieron Burke, and Matthias Ernzerhof. Generalized gradient approximation made simple. *Physical Review letters*, 77(18):3865, 1996.

[47] Gus L. W. Hart and Rodney W Forcade. Algorithm for generating derivative structures. *Physical Review B*, 77(22):224115, 2008.

[48] Gus L. W. Hart, Lance J Nelson, and Rodney W Forcade. Generating derivative structures at a fixed concentration. *Computational Materials Science*, 59:101–107, 2012.

[49] Dat Do, Mal-Soon Lee, and Subhendra D Mahanti. Effect of onsite coulomb repulsion on thermoelectric properties of full-heusler compounds with pseudogaps. *Physical Review B*, 84(12):125104, 2011.

[50] Richard Dronskowski and Peter E. Blöchl. Crystal orbital Hamilton populations (COHP): energy-resolved visualization of chemical bonding in solids based on density-functional calculations. *The Journal of Physical Chemistry*, 97(33):8617–8624, 1993.

[51] Volker L. Deringer, Andrei L. Tchougréeff, and Richard Dronskowski. Crystal orbital Hamilton population (COHP) analysis as projected from plane-wave basis sets. *The Journal of Physical Chemistry A*, 115(21):5461–5466, 2011.

[52] Stefan Maintz, Volker L. Deringer, Andrei L. Tchougréeff, and Richard Dronskowski. Analytic projection from plane-wave and PAW wavefunctions and application to chemical-bonding analysis in solids. *Journal of Computational Chemistry*, 34(29):2557–2567, 2013.

[53] Shyue Ping Ong, William Davidson Richards, Anubhav Jain, Geoffroy Hautier, Michael Kocher, Shreyas Cholia, Dan Gunter, Vincent L. Chevrier, Kristin A. Persson, and Gerbrand Ceder. Python Materials Genomics (pymatgen): A robust, open-source python library for materials analysis. *Computational Materials Science*, 68:314–319, 2013.

[54] J. W. D. Connolly and A. R. Williams. Density-functional theory applied to phase transformations in transition-metal alloys. *Physical Review B*, 27(8):5169, 1983.

[55] Juan M. Sanchez, Francois Ducastelle, and Denis Gratias. Generalized cluster description of multicomponent systems. *Physica A: Statistical Mechanics and its Applications*, 128(1-2):334–350, 1984.

[56] L. G. Ferreira, Su-Huai Wei, and Alex Zunger. First-principles calculation of alloy phase diagrams: The renormalized-interaction approach. *Physical Review B*, 40(5):3197, 1989.

[57] G. Ceder. A derivation of the Ising model for the computation of phase diagrams. *Computational Materials Science*, 1(2):144–150, 1993.

[58] Alex Zunger. First-principles statistical mechanics of semiconductor alloys and intermetallic compounds. In *Statics and Dynamics of Alloy Phase Transformations*, pages 361–419. Springer, 1994.

[59] D. De Fontaine. Cluster approach to order-disorder transformations in alloys. In *Solid State Physics*, volume 47, pages 33–176. Elsevier, 1994.

[60] Chris Wolverton and Alex Zunger. Ising-like description of structurally relaxed ordered and disordered alloys. *Physical Review Letters*, 75(17):3162, 1995.

[61] Axel van de Walle and Gerbrand Ceder. Automating first-principles phase diagram calculations. *Journal of Phase Equilibria*, 23(4):348, 2002.

[62] Axel Van de Walle and M. Asta. Self-driven lattice-model Monte Carlo simulations of alloy thermodynamic properties and phase diagrams. *Modelling and Simulation in Materials Science and Engineering*, 10(5):521, 2002.

[63] Axel Van De Walle, M. Asta, and G. Ceder. The alloy theoretic automated toolkit: A user guide. *Calphad*, 26(4):539–553, 2002.

[64] Fei Zhou, Weston Nielson, Yi Xia, and Vidvuds Ozoliņš. Lattice anharmonicity and thermal conductivity from compressive sensing of first-principles calculations. *Phys. Rev. Lett.*, 113:185501, Oct 2014.

[65] Fei Zhou, Weston Nielson, Yi Xia, Vidvuds Ozoliņš, et al. Compressive sensing lattice dynamics. i. general formalism. *Physical Review B*, 100(18):184308, 2019.

[66] Atsushi Togo and Isao Tanaka. First principles phonon calculations in materials science. *Scripta Materialia*, 108:1–5, 2015.

[67] Wu Li, Jesús Carrete, Nebil A. Katcho, and Natalio Mingo. ShengBTE: a solver of the Boltzmann transport equation for phonons. *Comp. Phys. Commun.*, 185:1747–1758, 2014.

[68] Samuel A. Miller, Maxwell Dylla, Shashwat Anand, Kiarash Gordiz, G. Jeffrey Snyder, and Eric S. Toberer. Empirical modeling of dopability in diamond-like semiconductors. *npj Computational Materials*, 4(1):1–8, 2018.

[69] Anuj Goyal, Prashun Gorai, Shashwat Anand, Eric S Toberer, G Jeffrey Snyder, and Vladan Stevanović. On the dopability of semiconductors and governing materials properties. *Chemistry of Materials*, 2020.

[70] James Male, Matthias T. Agne, Anuj Goyal, Shashwat Anand, Ian T. Witting, Vladan Stevanović, and G. Jeffrey Snyder. The importance of phase equilibrium for doping efficiency: iodine doped PbTe. *Materials Horizons*, 6(7):1444–1453, 2019.

[71] Alexandre Berche, Martin Talla Noutack, Marie-Liesse Doublet, and Philippe Jund. Unexpected band gap increase in the $Fe_2VAl$ Heusler compound. *Materials Today Physics*, page 100203, 2020.

[72] Shashwat Anand, Ramya Gurunathan, Thomas Soldi, Leah Borgsmiller, Rachel Orenstein, and G. Jeffrey Snyder. Thermoelectric transport of semiconductor full-Heusler $VFe_2Al$. *Journal of Materials Chemistry C*, 8:10174–10184, 2020.

[73] Gangjian Tan, Shiqiang Hao, Riley C. Hanus, Xiaomi Zhang, Shashwat Anand, Trevor P. Bailey, Alexander J. E. Rettie, Xianli Su, Ctirad Uher, Vinayak P. Dravid, et al. High Thermoelectric Performance in SnTe–$AgSbTe_2$ Alloys from Lattice Softening, Giant Phonon–Vacancy Scattering, and Valence Band Convergence. *ACS Energy Letters*, 3(3):705–712, 2018.

[74] Joachim Maier. Defect chemistry and ionic conductivity in thin films. *Solid State Ionics*, 23(1-2):59–67, 1987.

[75] J. P. Goff, W. Hayes, S. Hull, M. T. Hutchings, and Kurt Nørgaard Clausen. Defect structure of yttria-stabilized zirconia and its influence on the ionic conductivity at elevated temperatures. *Physical Review B*, 59(22):14202, 1999.

[76] Jeffrey W. Fergus. Electrolytes for solid oxide fuel cells. *Journal of power sources*, 162(1):30–40, 2006.

[77] Julius Koettgen, Steffen Grieshammer, Philipp Hein, Benjamin O. H. Grope, Masanobu Nakayama, and Manfred Martin. Understanding the ionic conductivity maximum in doped ceria: trapping and blocking. *Physical Chemistry Chemical Physics*, 20(21):14291–14321, 2018.

[78] Shobit Omar, Eric D. Wachsman, Jacob L. Jones, and Juan C. Nino. Crystal structure–ionic conductivity relationships in doped ceria systems. *Journal of the American Ceramic Society*, 92(11):2674–2681, 2009.

[79] Liang Hong, Linsen Li, Yuchen-Karen Chen-Wiegart, Jiajun Wang, Kai Xiang, Liyang Gan, Wenjie Li, Fei Meng, Fan Wang, Jun Wang, Y-M Chiang, Song Jin, and Ming Tang. Two-dimensional lithium diffusion behavior and probable hybrid phase transformation kinetics in olivine lithium iron phosphate. *Nature Communications*, 8(1):1–13, 2017.

[80] Navaratnarajah Kuganathan, Apostolos Kordatos, Nikolaos Kelaidis, and Alexander Chroneos. Defects, lithium mobility and tetravalent dopants in the $Li_3NbO_4$ cathode material. *Scientific Reports*, 9(1):1–8, 2019.

[81] Liang Hong, Kaiqi Yang, and Ming Tang. A mechanism of defect-enhanced phase transformation kinetics in lithium iron phosphate olivine. *npj Computational Materials*, 5(1):1–9, 2019.

[82] Le Yang, Hao-Sen Chen, Wei-Li Song, and Daining Fang. Effect of defects on diffusion behaviors of lithium-ion battery electrodes: In situ optical observation and simulation. *ACS Applied Materials & Interfaces*, 10(50):43623–43630, 2018.

[83] Riley E. Brandt, Jeremy R. Poindexter, Prashun Gorai, Rachel C. Kurchin, Robert L. Z. Hoye, Lea Nienhaus, Mark W. B. Wilson, J. Alexander Polizzotti, Raimundas Sereika, Raimundas Zaltauskas, Lana C. Lee, Judith L. MacManus-Driscoll, Moungi G. Bawendi, Vladan Stevanović, and Tonio Buonassisi. Searching for “defect-tolerant” photovoltaic materials: combined theoretical and experimental screening. *Chemistry of Materials*, 29(11):4667–4674, 2017.

[84] Feng Wang, Sai Bai, Wolfgang Tress, Anders Hagfeldt, and Feng Gao. Defects engineering for high-performance perovskite solar cells. *npj Flexible Electronics*, 2(1):1–14, 2018.

[85] Kaiyang Xia, Pengfei Nan, Shihua Tan, Yumei Wang, Binghui Ge, Wenqing Zhang, Shashwat Anand, Xinbing Zhao, G. Jeffrey Snyder, and Tiejun Zhu. Short-range

order in defective half-heusler thermoelectric crystals. *Energy & Environmental Science*, 12(5):1568–1574, 2019.

[86] Jun Mao, Jennifer L. Niedziela, Yumei Wang, Yi Xia, Binghui Ge, Zihang Liu, Jiawei Zhou, Zhensong Ren, Weishu Liu, Maria K. Y. Chan, Gang Chen, Olivier Delaire, Qian Zhang, and Zhifeng Ren. Self-compensation induced vacancies for significant phonon scattering in InSb. *Nano Energy*, 48:189–196, 2018.

[87] Kaiyang Xia, Yintu Liu, Shashwat Anand, G. Jeffrey Snyder, Jiazhan Xin, Junjie Yu, Xinbing Zhao, and Tiejun Zhu. Enhanced Thermoelectric Performance in 18-Electron $Nb_{0.8}CoSb$ Half-Heusler Compound with Intrinsic Nb Vacancies. *Advanced Functional Materials*, 28(9):1705845, 2018.

[88] Chirranjeevi Balaji Gopal and Axel van de Walle. Ab initio thermodynamics of intrinsic oxygen vacancies in ceria. *Physical Review B*, 86(13):134117, 2012.

[89] Stephan Lany. Communication: The electronic entropy of charged defect formation and its impact on thermochemical redox cycles. *The Journal of Chemical Physics*, 148(7):071101, 2018.

[90] Yoshihiro Yamazaki, Peter Babilo, and Sossina M. Haile. Defect chemistry of yttrium-doped barium zirconate: A thermodynamic analysis of water uptake. *Chemistry of Materials*, 20(20):6352–6357, 2008.

[91] Rafael Schmitt, Andreas Nenning, Olga Kraynis, Roman Korobko, Anatoly I. Frenkel, Igor Lubomirsky, Sossina M. Haile, and Jennifer L. M. Rupp. A review of defect structure and chemistry in ceria and its solid solutions. *Chemical Society Reviews*, 49(2):554–592, 2020.

[92] Stephan Lany and Alex Zunger. Dopability, intrinsic conductivity, and nonstoichiometry of transparent conducting oxides. *Physical Review Letters*, 98(4):045501, 2007.

[93] Anubhav Jain, Shyue Ping Ong, Geoffroy Hautier, Wei Chen, William Davidson Richards, Stephen Dacek, Shreyas Cholia, Dan Gunter, David Skinner, Gerbrand Ceder, and Kristin A. Persson. Commentary: The materials project: A materials genome approach to accelerating materials innovation. *APL Materials*, 1(1):011002, 2013.

[94] Stefano Curtarolo, Wahyu Setyawan, Shidong Wang, Junkai Xue, Kesong Yang, Richard H. Taylor, Lance J. Nelson, Gus L. W. Hart, Stefano Sanvito, Marco Buongiorno-Nardelli, Natalio Mingo, and Ohad Levy. Aflowlib.org: A distributed materials properties repository from high-throughput ab initio calculations. *Computational Materials Science*, 58:227–235, 2012.

[95] Florian Tang and Bengt Hallstedt. Using the PARROT module of Thermo-Calc with the Cr–Ni system as example. *Calphad*, 55:260–269, 2016.

[96] Hans Lukas, Suzana G. Fries, and Bo Sundman. *Computational thermodynamics: the Calphad method*. Cambridge university press, 2007.

[97] Gregory S. Pomrehn, Eric S. Toberer, G. Jeffrey Snyder, and Axel van de Walle. Entropic stabilization and retrograde solubility in $Zn_4Sb_3$. *Physical Review B*, 83(9):094106, 2011.

[98] Stephan Lany and Alex Zunger. Accurate prediction of defect properties in density functional supercell calculations. *Modelling and Simulation in Materials Science and Engineering*, 17(8):084002, 2009.

[99] Samuel A Miller, Prashun Gorai, Umut Aydemir, Thomas O Mason, Vladan Stevanović, Eric S Toberer, and G Jeffrey Snyder. SnO as a potential oxide thermoelectric candidate. *Journal of Materials Chemistry C*, 5(34):8854–8861, 2017.

[100] B. Meredig and C. Wolverton. First-principles thermodynamic framework for the evaluation of thermochemical $h_2o$-or $co_2$-splitting materials. *Physical Review B*, 80(24):245119, 2009.

[101] S. Shahab Naghavi, Antoine A. Emery, Heine A. Hansen, Fei Zhou, Vidvuds Ozolins, and Chris Wolverton. Giant onsite electronic entropy enhances the performance of ceria for water splitting. *Nature Communications*, 8(1):1–6, 2017.

[102] Joachim Maier. Thermodynamics of electrochemical lithium storage. *Angewandte Chemie International Edition*, 52(19):4998–5026, 2013.

[103] Joachim Maier. Battery materials: why defect chemistry? *Journal of The Electrochemical Society*, 162(14):A2380, 2015.

[104] Prashun Gorai, Hai Long, Eric Jones, Shriram Santhanagopalan, and Vladan Stevanović. Defect chemistry of disordered solid-state electrolyte $Li_{10}GeP_2S_12$. *Journal of Materials Chemistry A*, 8(7):3851–3858, 2020.

[105] Prashun Gorai, Theodosios Famprikis, Baltej Singh Gill, Vladan Stevanovic, and Pieremanuele Canepa. The devil is in the defects: Electronic conductivity in solid electrolytes. *ChemRxiv*, 2020.

[106] Alexander G. Squires, David O. Scanlon, and Benjamin J. Morgan. Native defects and their doping response in the lithium solid electrolyte $Li_7La_3Zr_2O_{12}$. *Chemistry of Materials*, 32(5):1876–1886, 2019.

[107] Anderson Janotti and Chris G. Van de Walle. Oxygen vacancies in ZnO. *Applied Physics Letters*, 87(12):122102, 2005.

[108] Jiazhan Xin, Haijun Wu, Xiaohua Liu, Tiejun Zhu, Guanting Yu, and Xinbing Zhao. Mg vacancy and dislocation strains as strong phonon scatterers in $Mg_2Si_{1-x}Sb_x$ thermoelectric materials. *Nano Energy*, 34:428–436, 2017.

[109] Min Zhou, Zachary M. Gibbs, Heng Wang, Yemao Han, Caini Xin, Laifeng Li, and G. Jeffrey Snyder. Optimization of thermoelectric efficiency in SnTe: the case for the light band. *Physical Chemistry Chemical Physics*, 16(38):20741–20748, 2014.

[110] Zachary M. Gibbs, Hyoungchul Kim, Heng Wang, Robert L. White, Fivos Drymiotis, Massoud Kaviany, and G. Jeffrey Snyder. Temperature dependent band gap in PbX (X= S, Se, Te). *Applied Physics Letters*, 103(26):262109, 2013.

[111] Yanzhong Pei, Zachary M. Gibbs, Andrei Gloskovskii, Benjamin Balke, Wolfgang G. Zeier, and G. Jeffrey Snyder. Optimum carrier concentration in n-type PbTe thermoelectrics. *Advanced Energy Materials*, 4(13):1400486, 2014.

[112] Yanzhong Pei, Aaron LaLonde, Shiho Iwanaga, and G. Jeffrey Snyder. High thermoelectric figure of merit in heavy hole dominated PbTe. *Energy & Environmental Science*, 4(6):2085–2089, 2011.

[113] Anuj Goyal, Prashun Gorai, Eric S. Toberer, and Vladan Stevanović. First-principles calculation of intrinsic defect chemistry and self-doping in PbTe. *npj Computational Materials*, 3(1):1–9, 2017.

[114] Prashun Gorai and Vladan Stevanovic. Comment on "Understanding the Intrinsic p-Type Behavior and Phase Stability of Thermoelectric $\alpha$-Mg3Sb2". *ACS Applied Energy Materials*, 3(1):106–108, 2019.

[115] XiaoYu Chong, Pin-Wen Guan, Yi Wang, Shun-Li Shang, Jorge Paz Soldan Palma, Fivos Drymiotis, Vilupanur A. Ravi, Kurt E. Star, Jean-Pierre Fleurial, and Zi-Kui Liu. Correction to "Understanding the Intrinsic p-Type Behavior and Phase Stability of Thermoelectric $\alpha$-Mg3Sb2". *ACS Applied Energy Materials*, 3(1):1249–1252, 2020.

[116] William D. Richards, Stephen T. Dacek, Daniil A. Kitchaev, and Gerbrand Ceder. Fluorination of lithium-excess transition metal oxide cathode materials. *Advanced Energy Materials*, 8(5):1701533, 2018.

[117] Bin Ouyang, Nongnuch Artrith, Zhengyan Lun, Zinab Jadidi, Daniil A. Kitchaev, Huiwen Ji, Alexander Urban, and Gerbrand Ceder. Effect of fluorination on lithium transport and short-range order in disordered-rocksalt-type lithium-ion battery cathodes. *Advanced Energy Materials*, 10(10):1903240, 2020.

[118] Yinglu Tang, Yuting Qiu, Lili Xi, Xun Shi, Wenqing Zhang, Lidong Chen, Ssu-Ming Tseng, Sinn-wen Chen, and G. Jeffrey Snyder. Phase diagram of In–Co–Sb system and thermoelectric properties of In-containing skutterudites. *Energy & Environmental Science*, 7(2):812–819, 2014.

[119] Yinglu Tang, Sinn-wen Chen, and G. Jeffrey Snyder. Temperature dependent solubility of Yb in Yb–CoSb3 skutterudite and its effect on preparation, optimization and lifetime of thermoelectrics. *Journal of Materiomics*, 1(1):75–84, 2015.

[120] Saneyuki Ohno, Umut Aydemir, Maximilian Amsler, Jan-Hendrik Pöhls, Sevan Chanakian, Alex Zevalkink, Mary Anne White, Sabah K. Bux, Chris Wolverton, and G. Jeffrey Snyder. Achieving $zT > 1$ in inexpensive Zintl phase $\mathrm{Ca_9Zn_{4+x}Sb_9}$ by phase boundary mapping. *Advanced Functional Materials*, 27(20):1606361, 2017.

[121] Caitlin M. Crawford, Brenden R. Ortiz, Prashun Gorai, Vladan Stevanovic, and Eric S. Toberer. Experimental and computational phase boundary mapping of $\mathrm{Co_4Sn_6Te_6}$. *Journal of Materials Chemistry A*, 6(47):24175–24185, 2018.

[122] Daisuke Kato, Kouta Iwasaki, Masahito Yoshino, Tomoaki Yamada, and Takanori Nagasaki. Significant effect of Mg-pressure-controlled annealing: non-stoichiometry and thermoelectric properties of $\mathrm{Mg_{2-\delta}Si_{1-x}Sb_x}$. *Physical Chemistry Chemical Physics*, 20(40):25939–25950, 2018.

[123] Priyanka Jood, James P. Male, Shashwat Anand, Yoshitaka Matsushita, Yoshiki Takagiwa, Mercouri G. Kanatzidis, G. Jeffrey Snyder, and Michihiro Ohta. Na Doping in PbTe: Solubility, Band Convergence, Phase Boundary Mapping, and Thermoelectric Properties. *Journal of the American Chemical Society*, 142(36):15464–15475, 2020.

[124] Brenden R. Ortiz, Kiarash Gordiz, Lídia C. Gomes, Tara Braden, Jesse M. Adamczyk, Jiaxing Qu, Elif Ertekin, and Eric S. Toberer. Carrier density control in $Cu_2HgGeTe_4$ and discovery of $Hg_2GeTe_4$ via phase boundary mapping. *Journal of Materials Chemistry A*, 7(2):621–631, 2019.

[125] Xiaofang Li, Pengbo Yang, Yumei Wang, Zongwei Zhang, Dandan Qin, Wenhua Xue, Chen Chen, Yifang Huang, Xiaodong Xie, Xinyu Wang, et al. Phase Boundary Mapping in ZrNiSn Half-Heusler for Enhanced Thermoelectric Performance. *Research*, 2020:4630948, 2020.

[126] Max Wood, Micheal Toriyama, Shristi Dugar, James Male, Shashwat Anand, Vladan Stevanović, and G. Jeffrey Snyder. Phase Boundary Mapping of Tin-Doped ZnSb Reveals Thermodynamic Route to High Thermoelectric Efficiency. *Unpublished*, 2020.

[127] Rachel Orenstein, James P Male, Micheal Toriyama, Shashwat Anand, and G. Jeffrey Snyder. Using Phase Boundary Mapping to Resolve Discrepancies in the $Mg_2Si$-$Mg_2Sn$ Miscibility Gap. *Unpublished*, 2020.

[128] Xun Shi, Jiong Yang, James R Salvador, Miaofang Chi, Jung Y Cho, Hsin Wang, Shengqiang Bai, Jihui Yang, Wenqing Zhang, and Lidong Chen. Multiple-filled skutterudites: high thermoelectric figure of merit through separately optimizing electrical and thermal transports. *Journal of the American Chemical Society*, 133(20):7837–7846, 2011.

[129] Jeff W. Doak, Christopher Wolverton, and Vidvuds Ozoliņš. Vibrational contributions to the phase stability of PbS-PbTe alloys. *Physical Review B*, 92(17):174306, 2015.

[130] Xia Hua, Shiqiang Hao, and Chris Wolverton. First-principles study of vibrational entropy effects on the PbTe-SrTe phase diagram. *Physical Review Materials*, 2(9):095402, 2018.

[131] S. V. Barabash, V. Ozolins, and C. Wolverton. First-principles theory of competing order types, phase separation, and phonon spectra in thermoelectric $\mathrm{AgPb}_m\mathrm{SbTe}_{m+2}$ alloys. *Physical Review Letters*, 101(15):155704, 2008.

[132] Kuei Fang Hsu, Sim Loo, Fu Guo, Wei Chen, Jeffrey S. Dyck, Ctirad Uher, Tim Hogan, E. K. Polychroniadis, and Mercouri G. Kanatzidis. Cubic $\mathrm{AgPb}_m\mathrm{SbTe}_{2+m}$: bulk thermoelectric materials with high figure of merit. *Science*, 303(5659):818–821, 2004.

[133] Pierre F. P. Poudeu, Jonathan D'Angelo, Adam D. Downey, Jarrod L. Short, Timothy P. Hogan, and Mercouri G. Kanatzidis. High Thermoelectric Figure of Merit and Nanostructuring in Bulk p-type $\mathrm{Na}_{1-x}\mathrm{Pb}_m\mathrm{Sb}_y\mathrm{Te}_{m+2}$. *Angewandte Chemie International Edition*, 45(23):3835–3839, 2006.

[134] Pierre F. P. Poudeu, Aurélie Guéguen, Chun-I Wu, Tim Hogan, and Mercouri G. Kanatzidis. High figure of merit in nanostructured n-type $\mathrm{KPb}_m\mathrm{SbTe}_{m+2}$ thermoelectric materials. *Chemistry of materials*, 22(3):1046–1053, 2010.

[135] Kyunghan Ahn, Chang-Peng Li, Ctirad Uher, and Mercouri G. Kanatzidis. Thermoelectric properties of the compounds $\mathrm{AgPb}_m\mathrm{LaTe}_{m+2}$. *Chemistry of Materials*, 22(3):876–882, 2010.

[136] Tyler J. Slade, Jann A. Grovogui, Shiqiang Hao, Trevor P. Bailey, Runchu Ma, Xia Hua, Aurelie Gueguen, Ctirad Uher, Chris Wolverton, Vinayak P. Dravid, et al.

Absence of Nanostructuring in $NaPb_mSbTe_{m+2}$: Solid Solutions with High Thermoelectric Performance in the Intermediate Temperature Regime. *Journal of the American Chemical Society*, 140(22):7021–7031, 2018.

[137] Tyler J. Slade, Trevor P. Bailey, Jann A. Grovogui, Xia Hua, Xiaomi Zhang, Jimmy Jiahong Kuo, Ido Hadar, G. Jeffrey Snyder, Chris Wolverton, Vinayak P. Dravid, et al. High thermoelectric performance in PbSe–$NaSbSe_2$ alloys from valence band convergence and low thermal conductivity. *Advanced Energy Materials*, 9(30):1901377, 2019.

[138] Tyler J. Slade, Koushik Pal, Jann A. Grovogui, Trevor P. Bailey, James Male, Jason F. Khoury, Xiuquan Zhou, Duck Young Chung, G. Jeffrey Snyder, Ctirad Uher, et al. Contrasting SnTe–$NaSbTe_2$ and SnTe–$NaBiTe_2$ Thermoelectric Alloys: High Performance Facilitated by Increased Cation Vacancies and Lattice Softening. *Journal of the American Chemical Society*, 142(28):12524–12535, 2020.

[139] Tyler J. Slade, Jann A. Grovogui, Jimmy Jiahong Kuo, Shashwat Anand, Trevor P. Bailey, Maxwell Wood, Ctirad Uher, G. Jeffrey Snyder, Vinayak P. Dravid, and Mercouri G. Kanatzidis. Understanding the thermally activated charge transport in $NaPb_mSbQ_{m+2}$ (Q= S, Se, Te) thermoelectrics: weak dielectric screening leads to grain boundary dominated charge carrier scattering. *Energy & Environmental Science*, 2020.

[140] S. V. Barabash, V. Ozolins, and C. Wolverton. First-principles theory of the coherency strain, defect energetics, and solvus boundaries in the PbTe-$AgSbTe_2$ system. *Physical Review B*, 78(21):214109, 2008.

[141] Tanja Graf, Claudia Felser, and Stuart S. P. Parkin. Simple rules for the understanding of Heusler compounds. *Progress in Solid State Chemistry*, 39(1):1–50, 2011.

[142] Jun Mao, Zihang Liu, Jiawei Zhou, Hangtian Zhu, Qian Zhang, Gang Chen, and Zhifeng Ren. Advances in thermoelectrics. *Advances in Physics*, 67(2):69–147, 2018.

[143] Jian He and Terry M. Tritt. Advances in thermoelectric materials research: Looking back and moving forward. *Science*, 357(6358):eaak9997, 2017.

[144] Jiawei Zhou, Hangtian Zhu, Te-Huan Liu, Qichen Song, Ran He, Jun Mao, Zihang Liu, Wuyang Ren, Bolin Liao, David J. Singh, et al. Large thermoelectric power factor from crystal symmetry-protected non-bonding orbital in half-heuslers. *Nature Communications*, 9(1):1–9, 2018.

[145] S. Sakurada and N. Shutoh. Effect of Ti substitution on the thermoelectric properties of (Zr, Hf)NiSn half-Heusler compounds. *Applied Physics Letters*, 86(8):082105, 2005.

[146] G. Rogl, P. Sauerschnig, Z. Rykavets, V. V. Romaka, P. Heinrich, B. Hinterleitner, A. Grytsiv, E. Bauer, and P. Rogl. (V, Nb)-doped half heusler alloys based on {Ti, Zr, Hf}NiSn with high $zT$. *Acta Materialia*, 131:336–348, 2017.

[147] Chenguang Fu, Shengqiang Bai, Yintu Liu, Yunshan Tang, Lidong Chen, Xinbing Zhao, and Tiejun Zhu. Realizing high figure of merit in heavy-band p-type half-Heusler thermoelectric materials. *Nature Communications*, 6:8144, 2015.

[148] Hangtian Zhu, Ran He, Jun Mao, Qing Zhu, Chunhua Li, Jifeng Sun, Wuyang Ren, Yumei Wang, Zihang Liu, Zhongjia Tang, et al. Discovery of ZrCoBi-based half heuslers with high thermoelectric conversion efficiency. *Nature Communications*, 9(1):2497, 2018.

[149] Hangtian Zhu, Jun Mao, Yuwei Li, Jifeng Sun, Yumei Wang, Qing Zhu, Guannan Li, Qichen Song, Jiawei Zhou, Yuhao Fu, et al. Discovery of TaFeSb-based half-

Heuslers with high thermoelectric performance. *Nature Communications*, 10(1):1–8, 2019.

[150] Guodong Li, Qi An, Umut Aydemir, William A. Goddard III, Max Wood, Pengcheng Zhai, Qingjie Zhang, and G. Jeffrey Snyder. Enhanced ideal strength of thermoelectric half-heusler TiNiSn by sub-structure engineering. *Journal of Materials Chemistry A*, 4(38):14625–14636, 2016.

[151] M. M. Al Malki, Q. Qiu, T. Zhu, G. J. Snyder, and D. C. Dunand. Creep behavior and postcreep thermoelectric performance of the $n$-type half-heusler alloy $Hf_{0.3}Zr_{0.7}NiSn_{0.98}Sb_{0.02}$. *Materials Today Physics*, 9:100134, 2019.

[152] Wolfgang G. Zeier, Jennifer Schmitt, Geoffroy Hautier, Umut Aydemir, Zachary M. Gibbs, Claudia Felser, and G. Jeffrey Snyder. Engineering half-Heusler thermoelectric materials using Zintl chemistry. *Nature Reviews Materials*, 1(6):16032, 2016.

[153] W. Bockelmann and H-U. Schuster. Kristallchemische aspekte ternärer phasen des lithiums mit 3B-und 4B-elementen in elektrovalenter und nicht elektrovalenter zusammensetzung. *Zeitschrift für anorganische und allgemeine Chemie*, 410(3):241–250, 1974.

[154] Huixia Luo, Jason W. Krizan, Lukas Muechler, Neel Haldolaarachchige, Tomasz Klimczuk, Weiwei Xie, Michael K. Fuccillo, Claudia Felser, and Robert J. Cava. A large family of filled skutterudites stabilized by electron count. *Nature Communications*, 6:6489, 2015.

[155] Yuting Qiu, Lili Xi, Xun Shi, Pengfei Qiu, Wenqing Zhang, Lidong Chen, James R. Salvador, Jung Y. Cho, Jihui Yang, Yuan-chun Chien, et al. Charge-compensated compound defects in Ga-containing thermoelectric skutterudites. *Advanced Functional Materials*, 23(25):3194–3203, 2013.

[156] Xun Shi, Jiong Yang, Shengqiang Bai, Jihui Yang, Hsin Wang, Miaofang Chi, James R. Salvador, Wenqing Zhang, Lidong Chen, and Winnie Wong-Ng. On the design of high-efficiency thermoelectric clathrates through a systematic cross-substitution of framework elements. *Advanced Functional Materials*, 20(5):755–763, 2010.

[157] Stephanie L. Brock, Laura J. Weston, Marilyn M. Olmstead, and Susan M. Kauzlarich. Synthesis, structure, and properties of $A_{14}AlSb_{11}$ (A= Ca, Sr, Ba). *Journal of Solid State Chemistry*, 107(2):513–523, 1993.

[158] Lihong Huang, Ran He, Shuo Chen, Hao Zhang, Keshab Dahal, Haiqing Zhou, Hui Wang, Qinyong Zhang, and Zhifeng Ren. A new n-type half-heusler thermoelectric material NbCoSb. *Materials Research Bulletin*, 70:773–778, 2015.

[159] Hao Zhang, Yumei Wang, Lihong Huang, Shuo Chen, Heshab Dahal, Dezhi Wang, and Zhifeng Ren. Synthesis and thermoelectric properties of n-type half-heusler compound VCoSb with valence electron count of 19. *Journal of Alloys and Compounds*, 654:321–326, 2016.

[160] Lihong Huang, Yumei Wang, Jing Shuai, Hao Zhang, Siqi Yang, Qinyong Zhang, and Zhifeng Ren. Thermal conductivity reduction by isoelectronic elements V and Ta for partial substitution of Nb in half-Heusler $Nb_{(1-x)/2}V_{(1-x)/2}Ta_xCoSb$. *RSC Advances*, 5(124):102469–102476, 2015.

[161] Lihong Huang, Qinyong Zhang, Yumei Wang, Ran He, Jing Shuai, Jianjun Zhang, Chao Wang, and Zhifeng Ren. The effect of Sn doping on thermoelectric performance of n-type half-Heusler NbCoSb. *Physical Chemistry Chemical Physics*, 19(37):25683–25690, 2017.

[162] M. Gürth, G. Rogl, V. V. Romaka, A. Grytsiv, E. Bauer, and P. Rogl. Thermoelectric high $zT$ half-Heusler alloys $\mathrm{Ti}_{1-x-y}\mathrm{Zr}_x\mathrm{Hf}_y\mathrm{NiSn}$ ($0 \leq x \leq 1$; $0 \leq y \leq 1$). *Acta Materialia*, 104:210–222, 2016.

[163] Christoph B. H. Evers, Carolin G. Richter, Klaus Hartjes, and Wolfgang Jeitschko. Ternary transition metal antimonides and bismuthides with MgAgAs-type and filled NiAs-type structure. *Journal of Alloys and Compounds*, 252(1-2):93–97, 1997.

[164] P. I. Kripyakevich and V. Ya Markiv. Crystal structures of ternary compounds in the systems Ti (V)–Fe (Co, Ni)–Sn (Sb). *Dopov. Akad. Nauk Ukr. RSR*, 12:1606–1608, 1963.

[165] Heinrich Hohl, Art P. Ramirez, Claudia Goldmann, Gabriele Ernst, Bernd Wölfing, and Ernst Bucher. New compounds with MgAgAs-type structure: NbIrSn and NbIrSb. *Journal of Physics: Condensed Matter*, 10(35):7843, 1998.

[166] V. V. Romaka, P. Rogl, L. Romaka, Yu Stadnyk, N. Melnychenko, A. Grytsiv, M. Falmbigl, and N. Skryabina. Phase equilibria, formation, crystal and electronic structure of ternary compounds in Ti–Ni–Sn and Ti–Ni–Sb ternary systems. *Journal of Solid State Chemistry*, 197:103–112, 2013.

[167] Andriy Zakutayev, Xiuwen Zhang, Arpun Nagaraja, Liping Yu, Stephan Lany, Thomas O. Mason, David S. Ginley, and Alex Zunger. Theoretical prediction and experimental realization of new stable inorganic materials using the inverse design approach. *Journal of the American Chemical Society*, 135(27):10048–10054, 2013.

[168] Jianhua Ma, Vinay I. Hegde, Kamaram Munira, Yunkun Xie, Sahar Keshavarz, David T. Mildebrath, C. Wolverton, Avik W. Ghosh, and W. H. Butler. Computational investigation of half-heusler compounds for spintronics applications. *Physical Review B*, 95(2):024411, 2017.

[169] Takeshi Kanomata, Toshiyuki Igarashi, Hironori Nishihara, Keiichi Koyama, Kazuo Watanabe, Klaus-U Neumann, and Kurt R. A. Ziebeck. Magnetic properties of weak itinerant electron ferromagnet CoVSb. *Materials Transactions*, 47(3):496–500, 2006.

[170] L. Heyne, T. Igarashi, T. Kanomata, Klaus-Ulrich Neumann, B. Ouladdiaf, and K. R. A. Ziebeck. Atomic and magnetic order in the weak ferromagnet CoVSb: is it a half-metallic ferromagnet? *Journal of Physics: Condensed Matter*, 17(33):4991, 2005.

[171] Daniella A. Ferluccio, John E. Halpin, Kathryn L. MacIntosh, Robert J. Quinn, Eric Don, Ronald I. Smith, Donald A. MacLaren, and Jan-Willem G. Bos. Low thermal conductivity and promising thermoelectric performance in A$_x$CoSb (A= V, Nb or Ta) half-Heuslers with inherent vacancies. *Journal of Materials Chemistry C*, 7(22):6539–6547, 2019.

[172] Tiejun Zhu, Yintu Liu, Chenguang Fu, Joseph P. Heremans, G. Jeffrey Snyder, and Xinbing Zhao. Compromise and synergy in high-efficiency thermoelectric materials. *Advanced Materials*, 29(14):1605884, 2017.

[173] Jun Mao, Zihang Liu, Jiawei Zhou, Hangtian Zhu, Qian Zhang, Gang Chen, and Zhifeng Ren. Advances in thermoelectrics. *Advances in Physics*, 67(2):69–147, 2018.

[174] Yanzhong Pei, Xiaoya Shi, Aaron LaLonde, Heng Wang, Lidong Chen, and G. Jeffrey Snyder. Convergence of electronic bands for high performance bulk thermoelectrics. *Nature*, 473(7345):66, 2011.

[175] Joseph P. Heremans, Vladimir Jovovic, Eric S. Toberer, Ali Saramat, Ken Kurosaki, Anek Charoenphakdee, Shinsuke Yamanaka, and G. Jeffrey Snyder. Enhancement

of thermoelectric efficiency in PbTe by distortion of the electronic density of states. *Science*, 321(5888):554–557, 2008.

[176] A. H. Romero, E. K. U. Gross, M. J. Verstraete, and Olle Hellman. Thermal conductivity in PbTe from first principles. *Physical Review B*, 91(21):214310, 2015.

[177] Max Wood, Umut Aydemir, Saneyuki Ohno, and G. Jeffrey Snyder. Observation of valence band crossing: the thermoelectric properties of $CaZn_2Sb_2$-$CaMg_2Sb_2$ solid solution. *Journal of Materials Chemistry A*, 6(20):9437–9444, 2018.

[178] Eric S. Toberer, Alex Zevalkink, and G. Jeffrey Snyder. Phonon engineering through crystal chemistry. *Journal of Materials Chemistry*, 21(40):15843–15852, 2011.

[179] Michael R. Winter and David R. Clarke. Oxide materials with low thermal conductivity. *Journal of the American Ceramic Society*, 90(2):533–540, 2007.

[180] Eric S. Toberer, Catherine A. Cox, Shawna R. Brown, Teruyuki Ikeda, Andrew F. May, Susan M. Kauzlarich, and G. Jeffrey Snyder. Traversing the metal-insulator transition in a Zintl phase: rational enhancement of thermoelectric efficiency in $Yb_{14}Mn_{1-x}Al_xSb_{11}$. *Advanced Functional Materials*, 18(18):2795–2800, 2008.

[181] Sami Vasala and Maarit Karppinen. $A_2BBO_6$ perovskites: a review. *Progress in Solid State Chemistry*, 43(1-2):1–36, 2015.

[182] Mark T. Anderson and Kenneth R. Poeppelmeier. Lanthanum copper tin oxide ($La_2CuSnO_6$): a new perovskite-related compound with an unusual arrangement of B cations. *Chemistry of Materials*, 3(3):476–482, 1991.

[183] Pushkar Kanhere and Zhong Chen. A review on visible light active perovskite-based photocatalysts. *Molecules*, 19(12):19995–20022, 2014.

[184] Jiban Kangsabanik, Vipinraj Sugathan, Anuradha Yadav, Aswani Yella, and Aftab Alam. Double perovskites overtaking the single perovskites: A set of new solar

harvesting materials with much higher stability and efficiency. *Physical Review Materials*, 2(5):055401, 2018.

[185] K-I Kobayashi, T. Kimura, H. Sawada, K. Terakura, and Y. Tokura. Room-temperature magnetoresistance in an oxide material with an ordered double-perovskite structure. *Nature*, 395(6703):677, 1998.

[186] Alexander Page, Anton Van der Ven, P. F. P. Poudeu, and Ctirad Uher. Origins of phase separation in thermoelectric (Ti, Zr, Hf)NiSn half-Heusler alloys from first principles. *Journal of Materials Chemistry A*, 4(36):13949–13956, 2016.

[187] Feng Yan, Xiuwen Zhang, G. Yu Yonggang, Liping Yu, Arpun Nagaraja, Thomas O. Mason, and Alex Zunger. Design and discovery of a novel half-heusler transparent hole conductor made of all-metallic heavy elements. *Nature Communications*, 6:7308, 2015.

[188] Jesús Carrete, Wu Li, Natalio Mingo, Shidong Wang, and Stefano Curtarolo. Finding unprecedentedly low-thermal-conductivity half-heusler semiconductors via high-throughput materials modeling. *Physical Review X*, 4(1):011019, 2014.

[189] J. Toboła, L. Jodin, P. Pecheur, H. Scherrer, G. Venturini, B. Malaman, and S. Kaprzyk. Composition-induced metal-semiconductor-metal crossover in half-heusler $\mathrm{Fe}_{1-x}\mathrm{Ni}_x\mathrm{TiSb}$. *Physical Review B*, 64(15):155103, 2001.

[190] R. V. Skolozdra, L. P. Romaka, L. G. Aksel'rud, G. A. Mel'nik, and Ya T. Tatomir. New phases of MgAgAs, LiGaGe and TiNiSi structural types containing $d$-and $p$-elements. *Neorganicheskie Materialy*, 35(4):456–460, 1999.

[191] Heng Wang, Xianlong Cao, Yoshiki Takagiwa, and G. Jeffrey Snyder. Higher mobility in bulk semiconductors by separating the dopants from the charge-conducting band–a case study of thermoelectric PbSe. *Materials Horizons*, 2(3):323–329, 2015.

[192] Heng Wang, Aaron D. LaLonde, Yanzhong Pei, and G. Jeffery Snyder. The criteria for beneficial disorder in thermoelectric solid solutions. *Advanced Functional Materials*, 23(12):1586–1596, 2013.

[193] Kyoungdoc Kim, Logan Ward, Jiangang He, Amar Krishna, Ankit Agrawal, and C. Wolverton. Machine-learning-accelerated high-throughput materials screening: Discovery of novel quaternary Heusler compounds. *Physical Review Materials*, 2(12):123801, 2018.

[194] Joachim Barth, Gerhard H Fecher, Markus Schwind, Andreea Beleanu, Claudia Felser, Andrey Shkabko, Anke Weidenkaff, Jan Hanss, Armin Reller, and Martin Köhne. Investigation of the thermoelectric properties of LiAlSi and LiAlGe. *Journal of Electronic Materials*, 39(9):1856–1860, 2010.

[195] A. E. Dwight. Crystal structure of DyNiSb, DyPtSb and related compounds. Technical report, 1974.

[196] M. Vasundhara, V. Srinivas, and V. V. Rao. Low-temperature electrical transport in heusler-type $Fe_2V(AlSi)$ alloys. *Journal of Physics: Condensed Matter*, 17(38):6025, 2005.

[197] Jiangang He, Maximilian Amsler, Yi Xia, S. Shahab Naghavi, Vinay I. Hegde, Shiqiang Hao, Stefan Goedecker, Vidvuds Ozoliņš, and Chris Wolverton. Ultralow thermal conductivity in full heusler semiconductors. *Physical Review Letters*, 117(4):046602, 2016.

[198] Jiangang He, S. Shahab Naghavi, Vinay I. Hegde, Maximilian Amsler, and Chris Wolverton. Designing and discovering a new family of semiconducting quaternary heusler compounds based on the 18-electron rule. *Chemistry of Materials*, 2018.

[199] Ian T. Witting, Thomas C. Chasapis, Francesco Ricci, Matthew Peters, Nicholas A. Heinz, Geoffroy Hautier, and G. Jeffrey Snyder. The thermoelectric properties of Bismuth Telluride. *Advanced Electronic Materials*, 5(6):1800904, 2019.

[200] B. Hinterleitner, I. Knapp, M. Poneder, Yongpeng Shi, H. Müller, G. Eguchi, C. Eisenmenger-Sittner, M. Stöger-Pollach, Y. Kakefuda, N. Kawamoto, et al. Thermoelectric performance of a metastable thin-film heusler alloy. *Nature*, 576(7785):85–90, 2019.

[201] Hidekazu Okamura, J. Kawahara, Takao Nanba, S. Kimura, K. Soda, U. Mizutani, Yoichi Nishino, M. Kato, I. Shimoyama, H. Miura, et al. Pseudogap formation in the intermetallic compounds $(Fe_{1-x}V_x)_3Al$. *Physical Review Letters*, 84(16):3674, 2000.

[202] Chin-Shan Lue and Y-K Kuo. Thermoelectric properties of the semimetallic Heusler compounds $Fe_{2-x}V_{1+x}M$ (M= Al, Ga). *Physical Review B*, 66(8):085121, 2002.

[203] Yoichi Nishino, M. Kato, S. Asano, K. Soda, M. Hayasaki, and U. Mizutani. Semiconductorlike behavior of electrical resistivity in Heusler-type $Fe_2VAl$ compound. *Physical Review Letters*, 79(10):1909, 1997.

[204] Chin-Shan Lue, Joseph H. Ross, et al. Semimetallic behavior in $Fe_2VAl$: NMR evidence. *Physical Review B*, 58(15):9763, 1998.

[205] D. J. Singh and I. I. Mazin. Electronic structure, local moments, and transport in $Fe_2VAl$. *Physical Review B*, 57(22):14352, 1998.

[206] Ruben Weht and W. E. Pickett. Excitonic correlations in the intermetallic $Fe_2VAl$. *Physical Review B*, 58(11):6855, 1998.

[207] G. Y. Guo, G. A. Botton, and Y. Nishino. Electronic structure of possible $3d$ 'heavy-fermion' compound. *Journal of Physics: Condensed Matter*, 10(8):L119, 1998.

[208] Kiyoshi Ooiwa and Keizo Endo. Nuclear magnetic relaxation in Heusler alloys $Fe_2VGa$ and $Fe_2VAl$. *Journal of Magnetism and Magnetic Materials*, 177:1443–1444, 1998.

[209] Chin-Shan Lue, Joseph H. Ross Jr, C. F. Chang, and H. D. Yang. Field-dependent specific heat in $Fe_2VAl$ and the question of possible $3d$ heavy fermion behavior. *Physical Review B*, 60(20):R13941, 1999.

[210] Alex Zevalkink, David M. Smiadak, Jeff L. Blackburn, Andrew J. Ferguson, Michael L. Chabinyc, Olivier Delaire, Jian Wang, Kirill Kovnir, Joshua Martin, Laura T. Schelhas, Taylor D. Sparks, Stephen D. Kang, Maxwell T. Dylla, G. Jeffrey Snyder, Brenden R. Ortiz, and Eric S. Toberer. A practical field guide to thermoelectrics: Fundamentals, synthesis, and characterization. *Applied Physics Reviews*, 5(2):021303, 2018.

[211] Daniel I. Bilc, Geoffroy Hautier, David Waroquiers, Gian-Marco Rignanese, and Philippe Ghosez. Low-dimensional transport and large thermoelectric power factors in bulk semiconductors by band engineering of highly directional electronic states. *Physical Review Letters*, 114(13):136601, 2015.

[212] Zachary M. Gibbs, Hyun-Sik Kim, Heng Wang, and G. Jeffrey Snyder. Band gap estimation from temperature dependent Seebeck measurement—Deviations from the $2e|S|_{max}T_{max}$ relation. *Applied Physics Letters*, 106(2):022112, 2015.

[213] C. S. Lue, Y. Kuo, S. Horng, S. Y. Peng, and C. Cheng. Structural, thermal, and electronic properties of $Fe_2VSi_{1x}Al_x$. *Physical Review B*, 71:064202, 2005.

[214] Shivprasad S. Shastri and Sudhir K. Pandey. A comparative study of different exchange-correlation functionals in understanding structural, electronic and thermoelectric properties of $Fe_2VAl$ and $Fe_2TiSn$ compounds. *Computational Materials Science*, 143:316–324, 2018.

[215] Markus Meinert. Modified Becke-Johnson potential investigation of half-metallic Heusler compounds. *Physical Review B*, 87(4):045103, 2013.

[216] Shamim Sk, P. Devi, Sanjay Singh, and Sudhir K. Pandey. Exploring the best scenario for understanding the high temperature thermoelectric behaviour of $Fe_2VAl$. *Materials Research Express*, 6(2):026302, 2018.

[217] Bin Xu, Xingfu Li, Gongqi Yu, Jing Zhang, Shanshan Ma, Yusheng Wang, and Lin Yi. The structural, elastic and thermoelectric properties of $Fe_2VAl$ at pressures. *Journal of Alloys and Compounds*, 565:22–28, 2013.

[218] Daniel I. Bilc and Philippe Ghosez. Electronic and thermoelectric properties of $Fe_2VAl$: The role of defects and disorder. *Physical Review B*, 83(20):205204, 2011.

[219] Max Wood, Kazuki Imasato, Shashwat Anand, Jiong Yang, and G. Jeffrey Snyder. The Importance of the Mg-Mg Interaction in $Mg_3Sb_2$-$Mg_3Bi_2$ Shown Through Cation Site Alloying. *Journal of Materials Chemistry A*, 8:2033–2038, 2020.

[220] Maxwell T. Dylla, Alexander Dunn, Shashwat Anand, Anubhav Jain, and G. Jeffrey Snyder. Machine Learning Chemical Guidelines for Engineering Electronic Structures in Half-Heusler Thermoelectric Materials. *Research*, 2020:6375171, 2020.

[221] Jimmy Jiahong Kuo, Stephen Dongmin Kang, Kazuki Imasato, Hiromasa Tamaki, Saneyuki Ohno, Tsutomu Kanno, and G. Jeffrey Snyder. Grain boundary dominated charge transport in $Mg_3Sb_2$-based compounds. *Energy & Environmental Science*, 11:429–434, 2018.

[222] Shawna R. Brown, Eric S. Toberer, Teruyuki Ikeda, Catherine A. Cox, Franck Gascoin, Susan M. Kauzlarich, and G. Jeffrey Snyder. Improved thermoelectric performance in $Yb_{14}Mn_{1-x}Zn_xSb_{11}$ by the reduction of spin-disorder scattering. *Chemistry of Materials*, 20(10):3412–3419, 2008.

# Appendix A

# Derivation for Graphical solution of $\Delta H_{def}$

Consider the model binary compound $A_pB_q$ with $p+q$ atoms in its primitive cell. For the sake of simplicity, we assume that $A_pB_q$ is the only compound in the binary system $A-B$. To re-write the expression for $\Delta H_{def}$ given in 1.5, we assume that the defect is being created in a supercell which is $l$ times larger in volume than the primitive cell. Then the formation energies ($\Delta H_f^{pristine}$) of the pristine (defect-free) structure is given by

$$\Delta H_f^{pristine} = \frac{E_{pristine} - lp\,\mu_A - lq\,\mu_B}{l(p+q)} \tag{A.0.1}$$

where $E_{pristine}$ is the total energy of the pristine structure. Similarly, the formation energy on the defective structure $\Delta H_f^{defect}$ is given by

$$\Delta H_f^{defect} = \frac{E_{defect} - lp\,\mu_A - lq\,\mu_B - \sum \Delta N_i \mu_i}{l(p+q) + \sum \Delta N_i} \tag{A.0.2}$$

where $E_{defect}$ is the total energy of the defective structure. For the sake of generality we will write the chemical potential of the atomic species $i$ as

$$\mu_i = \mu_i^o + \Delta\,\mu_i \tag{A.0.3}$$

where $\mu_i^o$ is the chemical potential of the elemental phase and $\Delta\mu_i$ is the composition-dependent change in chemical potential. We rearrange the equations A.0.1 and A.0.2 to write down their total energies $E_{pristine}$ and $E_{defect}$ in terms of the formation energies ($\Delta H_f$) of the structures. We then substitute these expressions in equation 1.5 and simplify to get a general expression for $\Delta H_{def}$

$$\Delta H_{def} = (l(p+q) + \sum \Delta N_i) \left( [\Delta H_f^{defect} - \Delta H_f^{pristine}] + \frac{(\sum \Delta N_i) \Delta H_f^{pristine}}{l(p+q) + \sum \Delta N_i} \right) - \sum \Delta N_i \Delta\mu_i \tag{A.0.4}$$

We will further simplify this expression for interstitials anti-sites and vacancies on a case-by-case basis

### A.0.1 Frenkel and Schottky Defects

Consider the case of complex defects Schottky, Frenkel and anti-site swapping defects — all examples of stoichiometric defects which do not change the overall composition of the compound ($\sum \Delta N_i = 0$) — in which case the term $\sum \Delta N_i \Delta\mu_i$ in equation A.0.4 is independent of choice of chemical conditions a constant $(p+q)$ $\Delta H_f^{pristine}$. Following from equation A.0.4 the expression for $\Delta H_{def}$ becomes independent of chemical potential and the defect energy for these complex defects takes a constant value.

### A.0.2 Interstitial

Consider the case of A-interstitial defect in $A_pB_q$ for which $\Delta N_A = 1$ and $\Delta N_B = 0$. For the sake of simplicity let us assume that that $A_pB_q$ is in equilibrium with the the element

$A$ such that for $A-$rich conditions $\Delta\mu_A$ = 0. So Equation A.0.4 then becomes

$$\Delta H_{def} = (l(p+q)+1)\left([\Delta H_f^{defect} - \Delta H_f^{pristine}] + \frac{\Delta H_f^{pristine}}{l(p+q)+1}\right) \tag{A.0.5}$$

The factor $l(p+q)+1$ depends on the composition of the pristine and defective structures and can be written as this factor as

$$f_A^{interstitial} = (l(p+q)+1) = \frac{1 - x_A^{pristine}}{x_A^{defect} - x_A^{pristine}} \tag{A.0.6}$$

where $x_i$ is the percentage (for component $i$) composition of a particular structure. We call this factor $f_i^k$ as the "projection factor", where $k$ describes the type of defect in question. So $\Delta H_{def}$ becomes

$$\Delta H_{def} = f_A^{interstitial}\left([\Delta H_{defect} - \Delta H_{pristine}] + \frac{\Delta H_{pristine}}{f_A^{interstitial}}\right) \tag{A.0.7}$$

The second term in the expression, to which the projection factor is multiplied is the convex-hull distance ($E_{CH}$) of the defective structure. The convex-hull distance (see example in Figure 1.1 c) is the vertical energy distance of a point from the convex-hull. So the expression for $\Delta H_{def}$ can be written succinctly as

$$\Delta H_{def} = f_A^{interstitial}\, E_{CH}^{interstitial} \tag{A.0.8}$$

From the equation A.0.6 and A.0.8 it becomes clear that the factor $f_A^{interstitial}$ 'projects' the convex-hull distance on to the $A$-component axis. The example (p = q = 1) of such a graphical solution for $\Delta H_{def}$ is shown in 3.1 a. However, the generality of our derivation dictates that equation A.0.8 holds true even any case with $p \neq q$.

The graphical solution for $\Delta H_{def}$ in $A$-poor conditions can be understood by going back to equation 1.5. The difference in $\Delta H_{def}$ between $A$-rich and $A$-poor equilibrium conditions is simply given by the change in chemical potential $\Delta\mu_A$ between the two chemical conditions. Graphically this is taken care of by choosing chemical potentials pertaining to the $A$-poor equilibrium (see figure 3.1 a). Note that equation A.0.8 does not hold true only for $A$-poor chemical conditions. To define $\Delta H_{def}$ more generally regardless of chemical potentials, we replace $E_{CH}^{interstitial}$ with 'extended convex-hull distance' ($E_{eCH}^{interstitial}$). We define $E_{eCH}^{interstitial}$ as the vertical energy distance of the interstitial defective structure from the line drawn to determine the chemical potential on the convex-hull plot. So for the $A$-poor equilibrium $E_{eCH}^{interstitial}$ will be the energy distance of the interstitial defective structure from the common tangent to the $AB$-$B$ phase equilibria. The subtle difference between $E_{eCH}$ and $E_{CH}$ is that $E_{eCH}$ is chemical-potential-dependent, whereas $E_{CH}$ is not. We now re-write equation A.0.8 more generally as

$$\Delta H_{def} = f_A^{interstitial}\, E_{eCH}^{interstitial} \tag{A.0.9}$$

### A.0.3 Vacancy

For the case of $A-$vacancy defect $\Delta N_A = -1$ and $\Delta N_B = 0$. For $A$-rich conditions (assuming $\Delta\mu_A$ = 0) equation A.0.4 then becomes

$$\Delta H_{def} = (l(p+q)-1)\left([\Delta H_f^{defect} - \Delta H_f^{pristine}] - \frac{\Delta H_f^{pristine}}{l(p+q)-1}\right) \tag{A.0.10}$$

In this expression the projection factor can be written as

$$f_A^{vacancy} = (l(p+q)-1) = -\frac{1-x_A^{pristine}}{x_A^{defect} - x_A^{pristine}} \tag{A.0.11}$$

Notice the factor of -1 in front of the expression for $f_A^{vacancy}$ making it slightly different from $f_A^{interstitial}$. Graphically, this means that unlike $f_A^{interstitial}$, $f_A^{vacancy}$ will flip the sign of the quantity projected onto the $A$-component axis. The simplified expression for $\Delta H_{def}$ then becomes

$$\Delta H_{def} = f_A^{vacancy} \left( [\Delta H_f^{defect} - \Delta H_f^{pristine}] - \frac{\Delta H_f^{pristine}}{f_A^{vacancy}} \right) \tag{A.0.12}$$

Similar to the case of interstitial, the second term is the $E_{CH}$ of the vacancy defect structure ($E_{CH}^{interstitial}$) and $\Delta H_{def}$ becomes

$$\Delta H_{def} = f_A^{vacancy}\, E_{CH}^{vacancy} \tag{A.0.13}$$

For our $\Delta H_{def}$ derivation to hold regardless of choice of chemical potential we re-write the expression in terms of $E_{eCH}^{vacancy}$

$$\Delta H_{def} = f_A^{vacancy}\, E_{eCH}^{vacancy} \tag{A.0.14}$$

### A.0.4 Anti-site

For the case of $A_B$ anti-site defect $\Delta N_A = 1$ and $\Delta N_B = -1$. Assuming $A$-rich conditions we get $\Delta\mu_A$ = 0 and $\Delta\mu_B$ = $\frac{p+q}{q}\, H_{pristine}$. After substituting in equation A.0.4 and simplifying the expression

$$\Delta H_{def} = lp \left( [\Delta H_f^{defect} - \Delta H_f^{pristine}] + \frac{\Delta H_f^{pristine}}{lq} \right) + \\ lq \left( [\Delta H_f^{defect} - \Delta H_f^{pristine}] + \frac{\Delta H_f^{pristine}}{lq} \right) \tag{A.0.15}$$

we proceed to identify the relevant projection factors as follows

$$f_A^{interstitial} = lq = \frac{1 - x_A^{pristine}}{x_A^{defect} - x_A^{pristine}} \tag{A.0.16}$$

$$f_B^{vacancy} = lp = -\frac{1 - x_B^{pristine}}{x_B^{defect} - x_B^{pristine}} \tag{A.0.17}$$

Using these expressions for $f_A^{interstitial}$ and $f_B^{vacancy}$ we can re-write $\Delta H_{def}$ as

$$\Delta H_{def} = f_B^{vacancy} \left( [\Delta H_f^{defect} - \Delta H_f^{pristine}] + \frac{\Delta H_f^{pristine}}{f_A^{interstitial}} \right) + f_A^{interstitial} \left( [\Delta H_f^{defect} - \Delta H_f^{pristine}] + \frac{\Delta H_f^{pristine}}{f_A^{interstitial}} \right) \tag{A.0.18}$$

rewriting $\Delta H_{def}$ again in terms of convex-hull distance of defective structure ($E_{CH}^{anti-site}$) in question we get

$$\Delta H_{def} = f_B^{vacancy}\, E_{CH}^{anti-site} + f_A^{interstitial}\, E_{CH}^{anti-site} \tag{A.0.19}$$

The two terms in this expression can be obtained by projecting the convex-hull distance of the defective structure ($E_{CH}^{anti-site}$) on the $B$ and $A$-component axis respectively. For our $\Delta H_{def}$ derivation to hold regardless of choice of chemical potential we re-write the expression in terms of $E_{eCH}^{anti-site}$

$$\Delta H_{def} = f_B^{vacancy}\, E_{eCH}^{anti-site} + f_A^{interstitial}\, E_{eCH}^{anti-site} \tag{A.0.20}$$

$\Delta H_{def}$ in its most general form regardless of defect type and thermodynamic conditions can be written as

$$\Delta H_{def} = \Delta N_i^{added} f_i^{interstitial} E_{eCH}^{defect} - \Delta N_j^{removed} f_j^{vacancy} E_{eCH}^{defect} \tag{A.0.21}$$

where $\Delta N$ is the number of atoms added or removed in the defect for the component $i$ and $j$ respectively. $E_{eCH}^{defect}$ is the extended convex-hull distance of the defective structure. Equation A.0.21 can be used to derive all the equations on the panels of the Figure 3.1 (see bottom of the Figure 3.1).

### A.0.5 Interstitial defects in a ternary compound

For the case of interstitial $\mathrm{C}_i$ defects in the ternary compound $\mathrm{A}_p\mathrm{B}_q\mathrm{C}_r$ (see figure 3.3) consider the C-rich chemical conditions (two-phase region $\mathrm{A}_p\mathrm{B}_q\mathrm{C}_r$-C). In this case $\Delta N_C = 1$ and $\Delta\mu_C$ = 0. Using the general expression in equation A.0.4, $\Delta H_{def}$ can be written as

$$\Delta H_{def} = (l(p+q+r)+1)\left([\Delta H_{defect}^f - \Delta H_{pristine}^f] + \frac{\Delta H_{pristine}^f}{l(p+q+r)+1}\right) \tag{A.0.22}$$

this expression can further be written as

$$\Delta H_{def} = f_C^{interstitial} E_{eCH} \tag{A.0.23}$$

where $f_C^{interstitial}$ is the projection factor given by $f_C^{interstitial} = (l(p+q+r)+1)$

### A.0.6 Vacancy defects in a ternary compound

For the case of $C-$vacancy defects in the ternary compound $\mathrm{A}_p\mathrm{B}_q\mathrm{C}_r$ (see figure 3.3) consider the C-rich chemical conditions (two-phase region $\mathrm{A}_p\mathrm{B}_q\mathrm{C}_r$-C). In this case $\Delta N_C = -1$

and $\Delta\mu_C$ = 0. Using the general expression in equation A.0.4, $\Delta H_{def}$ can be written as

$$\Delta H_{def} = (l(p+q+r)-1)\left([\Delta H^f_{defect} - \Delta H^f_{pristine}] + \frac{\Delta H^f_{pristine}}{l(p+q+r)-1}\right) \tag{A.0.24}$$

this expression can further be simplified as

$$\Delta H_{def} = f_C^{interstitial}\ E_{eCH} \tag{A.0.25}$$

### A.0.7 Anti-site defects in a ternary compound

For the case of anti-site $C_B$ defects in the ternary compound $A_pB_qC_r$ (see figure 3.3) consider the B-poor chemical conditions (three-phase region $A_pB_qC_r$-A-C). Using the general expression in equation A.0.4, $\Delta H_{def}$ can be written as

$$\Delta H_{def} = l(p+q+r)\left([\Delta H^f_{defect} - \Delta H^f_{pristine}] + \frac{\Delta H^f_{pristine}}{lq}\right) \tag{A.0.26}$$

this expression can further be written as

$$\Delta H_{def} = l(p+q+r)\ E_{eCH} \tag{A.0.27}$$

This quantity can be visualized as a projection of the convex-hull distance of the defective structure as shown in the figure 3.3.

# Vita

### Personal Information

**Name:** Shashwat Anand, **Place of Birth:** $09^{th}$ July, 1990.

### Prior Education

- Post Graduate Diploma in Materials Science from Jawaharlal Nehru Center for Advanced Scientific Research (JNCASR)
  - Thesis Advisor: Prof. U. V. Waghmare
- Integrated Dual Degree (IDD) from the School of Materials Science and Engineering, Indian Institute of Technology - Banaras Hindu University (IIT-BHU)
  - Thesis Advisor: Prof. Akhilesh Kumar Singh

### Publications from PhD research

- **S. Anand**, K. Xia, V. I. Hegde, U. Aydemir, V. Kocevski, T. Zhu, C. Wolverton, G. J. Snyder, “A valence balanced rule for discovery of 18-electron half-Heuslers with defects", *Energy Environ. Sci.*, 11 (6), 1480-1488, 2018.
- **S. Anand**, K. Xia, T. Zhu, C. Wolverton, G. J. Snyder, “Temperature Dependent n-Type Self Doping in Nominally 19-Electron Half-Heusler Thermoelectric Materials", *Adv. Energy Mater.* 8 (30), 1801409, 2018.
- **S. Anand**, M. Wood, Y. Xia, C. Wolverton, G. J. Snyder, “Double Half-Heuslers", *Joule*, 3, 5, 1226-1238, 2019.

- **S. Anand**, R. Gurunathan, T. Soldi, L. Borgsmiller, R. Orenstein, G. J. Snyder, “Thermoelectric transport of semiconductor full-Heusler $VFe_2Al$", *J. Mater. Chem. C*, 8, 10174-10184, 2020.
- **S. Anand**, J. P. Male, C. Wolverton, G. J. Snyder “Visualizing Defect Energetics", *Mater. Today*, 2020 (Submitted).
- T. Slade*, **S. Anand***, M. Wood, J. P. Male, D. Cheikh, M. T. Agne, K. Imasato, C. Wolverton, M. G. Kanatzidis, G. J. Snyder, “Charge-carrier-mediated Lattice Softening Contributes to high $zT$ in Thermoelectric Semiconductors", 2020 (Completed, internal review). *equal contribution
- **S. Anand**, M. Toriyama, C. Wolverton, S. M. Haile, G. J. Snyder, “A Unified Understanding of Defects in Semiconductors and Insulators", 2020 (In Preperation).
- **S. Anand**, C. Wolverton, G. J. Snyder, “Predicting Solubility in Complex Materials with Pen-and-Paper Drawings", 2020 (In Preperation).
- **S. Anand**, G. J. Snyder, “Rationalizing the 21-electron Slater-Pauling semiconductor $TiFe_{1.5}Sb$ as a Valence Balanced Compound", 2020 (In Preperation).
- S. Ohno, K. Imasato, **S. Anand**, H. Tamaki, S. D. Kang, P. Gorai, H. K. Sato, E. S. Toberer, T. Kanno, G. J. Snyder, “Phase boundary mapping to obtain n-type $Mg_3Sb_2$-based thermoelectrics", *Joule*, 2 (1), 141-154, 2018.
- K. Xia, Y. Liu, **S. Anand**, G. J. Snyder, J. Xin, J. Yu, X. Zhao, T. Zhu, “Enhanced Thermoelectric Performance in 18-Electron $Nb_{0.8}CoSb$ Half-Heusler Compound with Intrinsic Nb Vacancies", *Adv. Func. Mater.* 28 (9), 1705845, 2018.
- Y. Tang, X. Li, L. H. J. Martin, E. C. Reyes, T. Ivas, C. Leinenbach, **S. Anand**, M. Peters, G. J. Snyder, C. Battaglia, “Impact of Ni content on the thermoelectric properties of half-Heusler TiNiSn", *Energy Environ. Sci.* 11 (2), 311-320, 2018.

- G. Tan, S. Hao, R. C. Hanus, X. Zhang, **S. Anand**, T. P. Bailey, A. J. E. Rettie, X. Su, C. Uher, V. P. Dravid, G. J. Snyder, C. Wolverton, M. G. Kanatzidis, “High Thermoelectric Performance in SnTe–$AgSbTe_2$ Alloys from Lattice Softening, Giant Phonon–Vacancy Scattering, and Valence Band Convergence", *ACS Energy Lett.* 3 (3), 705-712, 2018.

- W. Zeier, **S. Anand**, L. Huang, R. He, H. Zhang, Z. Ren, C. Wolverton, G. J. Snyder, “Using 18-Electron Rule To Understand the Nominal 19-Electron Half-Heusler NbCoSb with Nb Vacancies", *Chem. Mater.* 29, 3, 1210-1217, 2017.

- Z. Huang, S. A. Miller, B. Ge, M. Yan, **S. Anand**, T. Wu, P. Nan, Y. Zhu, W. Zhuang, G. J. Snyder, P. Jiang, X. Bao, “High Thermoelectric Performance of New Rhombohedral Phase of GeSe stabilized through Alloying with $AgSbSe_2$", *Angew. Chem.* 56 (45), 14113-14118, 2017.

- K. Xia, P. Nan, S. Tan, Y. Wang, B. Ge, W. Zhang, **S. Anand**, X. Zhao, G. J. Snyder, T. Zhu, “Short-range order in defective half-Heusler thermoelectric crystals", *Energy Environ. Sci.* 12, 1568-1574, 2019.

- M. T. Agne, K. Imasato, **S. Anand**, K. Lee, S. K. Bux, A. Zevalkink, A. J. E. Rettie, D. Y. Chung, M. G. Kanatzidis, G. J. Snyder, “Heat capacity of $Mg_3Sb_2$, $Mg_3Bi_2$, and their alloys at high temperature", *Mater. Today Phys.* 6, 83-88, 2018.

- J. P. Male, M. T. Agne, A. Goyal, **S. Anand**, I. T. Witting, V. Stevanović, G. J. Snyder, “The importance of phase equilibrium for doping efficiency: iodine doped PbTe", *Mater. Horizons*, 6 (7), 1444-1453, 2019.

- M. T. Dylla, A. Dunn, **S. Anand**, A. Jain, G. J. Snyder, “Machine Learning Chemical Guidelines for Engineering Electronic Structures in Half-Heusler Thermoelectric Materials", *Research*, 6375171, 2020.

- M. Wood, K. Imasato, **S. Anand**, J. Yang, G. J. Snyder, “The importance of the Mg–Mg interaction in $Mg_3Sb_2$–$Mg_3Bi_2$ shown through cation site alloying", *J. Mater. Chem. A*, 8 (4), 2033-2038, 2020.
- F. Reissig, B. Heep, M. Panthöfer, M. Wood, **S. Anand**, G. J. Snyder, W. Tremel, “Effect of anion substitution on the structural and transport properties of argyrodites $Cu_7PSe_{6x}S_x$", *Dalton Transactions*, 48 (42), 15822-15829, 2019.
- T. J Slade, J. A. Grovogui, J. J. Kuo, **S. Anand**, T. P. Bailey, M. Wood, C. Uher, G. J. Snyder, V. P. Dravid, M. G. Kanatzidis, “Understanding the thermally activated charge transport in $NaPb_mSbQ_{m+2}$ (Q = S, Se, Te) thermoelectrics: weak dielectric screening leads to grain boundary dominated charge carrier scattering", *Energy Environ. Sci.* 13, 1509-1518, 2020.
- S. A. Miller, M. Dylla, **S. Anand**, K. Gordiz, G. J. Snyder, E. S. Toberer, “Empirical modeling of dopability in diamond-like semiconductors", *npj Comput. Mater.* 4, 1, 1-8, 2018.
- A. Goyal, P. Gorai, **S. Anand**, E. S. Toberer, G. J. Snyder, V. Stevanović, “On the dopability of semiconductors and governing materials properties", *Chem. Mater.* 32, 11, 4467–4480, 2020.
- S. Guo, **S. Anand**, Y. Zhang, G. J. Snyder, “Vibrational entropy stabilizes distorted half-Heusler structures", *Chem. Mater.* 32, 11, 4767–4773, 2020.
- P. Jood, J. P. Male, **S. Anand**, Y. Matsushita, Y. Takagiwa, M. G. Kanatzidis, G. J. Snyder, and M. Ohta, “Na doping in PbTe- Solubility, Band Convergence, Phase Boundary Mapping, and Thermoelectric properties",*J. Am. Chem. Soc.* 142, 36, 15464–15475.
- S. Guo, Z. Liu, Z. Feng, T. Jia, **S. Anand**, G. J. Snyder, Y. Zhang, “Prediction of improved thermoelectric performance by ordering in double half-Heusler materials",

8, 23590-23598, 2020.

- M. T. Agne, **S. Anand**, G. J. Snyder, “Inherent anharmonicity of harmonic solids", (submitted to *Energy Environ. Sci.*).
- L. E. Borgsmiller, M. T. Agne, J. P. Male, **S. Anand**, G. Li, S. I. Morozov, G. J. Snyder, “Estimation of fracture toughness from quantum mechanical ideal-strength calculations", (submitted to *Acta Materialia*).
- M. Wood, M. Toriyama, S. Dugar, J. P. Male, **S. Anand**, A. Goyal, V. Stevanović, and G. J. Snyder, “Phase Boundary Mapping of Tin-Doped ZnSb Reveals Synthesis Route to High Thermoelectric Efficiency", (Completed, internal review).
- R. Orenstein, J. Male, M. Toriyama, **S. Anand**, and G. J. Snyder, “Phase Boundary Mapping of the $Mg_2Si$-$Mg_2Sn$ Ternary Phase Diagram", (Completed, internal review).